Dissertation

submitted to the
Combined Faculty of Natural Sciences and Mathematics
of Heidelberg University, Germany
for the degree of
Doctor of Natural Sciences

Put forward by
M. Sc. Jan-Hendrik Oelmann
born in: Hannover
Oral examination: 19.04.2023

Highly nonlinear light-matter interaction using cavity-enhanced frequency combs

Untersuchung hoch nichtlinearer Licht-Materie-Wechselwirkungen mit resonatorverstärkten Frequenzkämmen

In Resonatoren verstärkte Frequenzkämme sind ein leistungsstarkes Werkzeug zur Untersuchung hochgradig nichtlinearer Licht-Materie-Wechselwirkungen, wie beispielsweise Multiphotonenionisation (MPI) oder die Erzeugung hoher Harmonischer (HHG), mit vielversprechenden Aussichten für die Präzisionsspektroskopie jenseits des optischen Spektralbereichs. In dieser Arbeit wird ein metrologisch nutzbarer Frequenzkamm im extremen Ultraviolett (XUV) demonstriert, indem die Stabilität und Kohärenz eines Frequenzkamms im nahen Infrarot bei 1039 nm mittels HHG innerhalb eines Überhöhungsresonators in das XUV übertragen wird. Im Fokus des Resonators wird eine hohe Intensität von $\sim 10^{14}$ W cm^{-2} erreicht, um XUV-Strahlung bis zu 42 eV (30 nm) bei einigen Mikrowatt ausgekoppelter Leistung bereitzustellen. Langzeitmessungen werden durch ein geschlossenes Hochdruck-Edelgasrecycling- und Kompressionssystem ermöglicht. Darüber hinaus wurde eine neuartige polarisationsunempfindliche Kavität mit einem integrierten Geschwindigkeitsabbildungsspektrometer (VMI) entwickelt. Mit diesem werden 3D-Photoelektronen-Winkelverteilungen aus Xenon-MPI tomographisch rekonstruiert und resonante Rydberg-Zustände während des Ionisationsprozesses identifiziert. Zusätzlich werden polarisationsgeformte Pulspaare mit variabler Zeitverzögerung für Pump-Probe-Experimente bereitgestellt. Gegenläufig propagierende, im Fokus kollidierende Pulse produzieren intensive, stehende Femtosekundenlaserwellen, die im Nanometerbereich mit Hilfe von Photoemission aus einer nanometrischen Spitze untersucht werden. Photoelektronen erben die Kohärenz des Frequenzkammes, was zukünftige Präzisionsmessungen mit kohärenten Materiewellen ermöglicht. Diese Arbeit erweitert den Anwendungsbereich von resonatorverstärkten Frequenzkämmen und ermöglicht Starkfeldstudien mit einer Wiederholrate von 100 MHz.

Highly nonlinear light-matter interaction using cavity-enhanced frequency combs

Cavity-enhanced frequency combs are a powerful tool for studying highly nonlinear light-matter interactions, such as multiphoton ionization (MPI) and high-harmonic generation (HHG), with promising prospects for precision spectroscopy beyond the optical spectral range. In this work, a metrology-capable extreme ultraviolet (XUV) frequency comb is produced by transferring a near-infrared comb at 1039 nm to the XUV, using intra-cavity HHG. Intensities of $\sim 10^{14}$ W cm^{-2} are reached in the cavity focus, producing XUV radiation up to 42 eV (30 nm) and tens of microwatts of outcoupled power. A high-pressure closed-loop noble gas recycling and compression system enables long-term measurements. Additionally, a novel polarization-insensitive cavity with an integrated velocity-map imaging spectrometer was developed. 3D photoelectron angular distributions from xenon MPI are tomographically reconstructed, revealing resonant Rydberg states during ionization. Furthermore, polarization-shaped pulse pairs with a variable time delay are provided for pump-probe experiments. Intense femtosecond standing waves, produced by counter-propagating pulses colliding at the focus, are probed at the nanometer scale using photoemission from a nano-tip. The coherence of the frequency comb is imprinted on the photoelectrons, allowing future precision measurements with coherent matter waves. This work broadens the scope of cavity-enhanced frequency combs and enables strong-field studies at 100 MHz repetition rate.

Contents

Contents

List of Figures

List of Tables

Acronyms

AC	autocorrelation
ADK	Ammosov-Delone-Krainov
AR	anti-reflection
ATI	above-threshold ionization
BBO	β-barium borate
BS	beam splitter
CAS	compressed air supply
CC	channel closing
CEO	carrier-envelope offset
CEP	carrier-envelope phase
CF	ConFlat
CNC	computerized numerical control
COLTRIMS	cold-target recoil-ion momentum spectroscopy
CPA	chirped-pulse amplification
CryPTEx	Cryogenic Paul Trap Experiment
CS	compressor system
CT	computer tomography
CW	continuous wave
DDS	direct digital synthesizer
EBIT	electron beam ion trap
EOM	electro-optic modulator
FBP	filtered back-projection
FROG	frequency-resolved optical gating
FS	fused silica
fsEC	femtosecond enhancement cavity
FSR	free spectral range
FWHM	full width at half maximum
GD	group delay
GDD	group-delay dispersion
GNLSE	generalized nonlinear Schrödinger equation
GP	gas panel
GPS	Global Positioning System
GRISM	grating and prism
GTI	Gires-Tournois interferometer
GVD	group-velocity dispersion
HCI	highly charged ion
HHG	high-harmonic generation
HOD	higher-order dispersion
HPS	high-pressure system
HR	high reflection
HWP	half-wave plate
IBS	ion-beam sputtering
IC	input coupler

KF	Kleinflansch
KPD	potassium dihydrogenphosphate
LHCP	left-handed circularly polarized
LMA	large-mode-area
LPS	low-pressure system
MC	main chamber
MCP	microchannel plate
MPC	multipass cell
MPI	multiphoton ionization
MPIK	Max-Planck-Institut für Kernphysik
MRI	magnetic resonance imaging
NIR	near-infrared
NLSE	nonlinear Schrödinger equation
OAP	off-axis parabolic mirror
OBI	over-the-barrier ionization
PAD	photoelectron angular distribution
PBS	polarizing beam splitter
PCF	photonic-crystal fiber
PDH	Pound-Drever-Hall
PID	proportional-integral-derivative
PLO	phase-locked oscillator
PTB	Physikalisch-Technische Bundesanstalt
PTFE	polytetrafluoroethylene
QED	quantum electrodynamics
QWP	quarter-wave plate
REMI	reaction microscope
RF	radio frequency
RHCP	right-handed circularly polarized
SAD	split-and-delay
SBS	stimulated Brillouin scattering
SESAM	semiconductor saturable-absorber mirror
SFA	strong-field approximation
SHG	second-harmonic generation
SM	Standard Model of particle physics
SPM	self-phase modulation
SRS	stimulated Raman scattering
SVEA	slowly varying envelope approximation
TBP	time-bandwidth product
TI	tunnel ionization
TMP	turbomolecular pump
TOD	third-order dispersion
TSM	three-step model
UHV	ultra-high vacuum
UV	ultraviolet
VMI	velocity-map imaging
VNA	vector network analyzer
WC	tungsten carbide
XUV	extreme ultraviolet
YAG	yttrium aluminium garnet

1 Introduction

What does the traffic jam on the way to work have in common with stock market prices, the human nervous system, and the weather? They have as much in common as the propagation of water waves has with the internet, more specifically, with the fiber optic links that transmit the data in the form of laser pulses over long distances.

It is all about nonlinearities.

In simple words, a nonlinear system is one in which a small change in the input does not result in a proportionally small change in the output. The butterfly effect is a famous metaphorical example of a nonlinear effect, where the outcome is very sensitive to the initial conditions. The idea behind the butterfly effect is that small things can have nonlinear impacts on complex systems, just like a butterfly flapping its wings and causing a tornado. Mathematically, nonlinear systems are described by nonlinear differential equations. The dynamic behavior of nonlinear systems often appears counter-intuitive, unpredictable, or even chaotic. However, most systems are inherently nonlinear in nature, which is of interest to many scientific fields.

Nonlinearities have become indispensable in the field of optics. With the advent of the laser in 1960 [1], the field of nonlinear optics started to grow rapidly. Nonlinear optical processes can be used to generate light at new wavelengths. For instance, frequency doubling was demonstrated only one year after the invention of the laser [2]. Nonlinear optical techniques such as Raman spectroscopy can be adopted for sensitively detecting chemical and biological samples [3]. Nonlinearities are also crucial for the generation of nonclassical states of light [4, 5], which have applications not only in quantum computing [6] and quantum communication [7] but also in the search for gravitational waves [8]. This clearly underlines the importance of nonlinearities for many aspects of life today and in the future.

The motivation behind this thesis is to bridge the technological gap between the areas of high-precision laser spectroscopy and strong-field physics to study and utilize nonlinear light-matter interactions in intense laser fields. Up until now, the fields of frequency metrology and highly nonlinear optics were primarily treated independently, but recent experiments have shown that it is possible to transfer the coherence of stabilized lasers from the infrared to the extreme ultraviolet (XUV) spectral region using nonlinear frequency conversion of ultrashort waveform-stable laser pulses emitted from a device known as the frequency comb. Therefore, this thesis aims to advance these methods to enable long-term high-precision frequency spectroscopy in the XUV spectral region and additionally use the intense coherent light required to initiate these processes to study the underlying highly nonlinear light-matter interactions directly.

This introductory chapter starts with a description of how nonlinear processes are used as leverage for ultra-precise frequency measurements using frequency combs. Subsequently, it will be explained how nonlinear processes can be used to access different spectral domains for precision studies with atoms and highly charged ions (HCIs). Furthermore, the concept of multiphoton excitation by a train of coherent laser pulses and its experimental implementation are introduced. Finally, the nonlinear effects arising from intense counter-propagating pulses will be discussed, as well as the required experimental realization.

1.1 Precision spectroscopy

Physics relies on comparing theory to experimental data. The highest accuracy and reproducibility is currently achieved by laser spectroscopy of individual atoms. This technique allows for precise measurements of the properties of atomic and molecular systems, such as energy levels and transition probabilities. Knowledge gained in this way can be used not only to study fundamental physics and test the symmetries of nature but also to develop new technologies and applications, such as atomic clocks [9, 10], quantum simulation [11–14], atom trap trace analysis [15–17], computer network synchronization [18], and global navigation satellite systems [19].

The field of precision spectroscopy advanced rapidly after the invention of the first tunable, monochromatic laser sources [20]. Nonlinear spectroscopy techniques, such as Doppler-free two-photon spectroscopy [21], led to significant improvements in achievable precision [22]. Today, optical atomic clocks have fractional frequency uncertainties approaching or surpassing one part in 10^{18} [23–28].

To measure an absolute frequency, a comparison with a defined reference is necessary. Since 1967, the definition of time has been based on the unperturbed ground-state hyperfine transition frequency of the cesium-133 atom at 9 192 631 770 Hz. Thus, any absolute frequency determination needs to relate to this frequency. To establish an uninterrupted frequency chain from the optical part of the electromagnetic spectrum at around 500 THz to the radio frequency (RF) spectral region, a large gap has to be bridged. Before 2000, this had required a long and complex chain of frequency links filling several laboratory rooms. Therefore, these systems could only be installed at the most important national metrology institutes.

The frequency comb

The invention of the frequency comb revolutionized frequency metrology by providing a direct relation between the optical and RF frequencies, and it was awarded the Nobel prize in 2005 [29, 30]. The frequency comb developed out of mode-locked pulsed lasers, starting with the stabilization of the repetition rate f_{rep}, by controlling the cavity length. The pulse train emitted from such a mode-locked laser can be described as a superposition of phase-locked oscillating longitudinal laser modes that are equally spaced in frequency. Already with this comb-like spectrum, large frequency intervals within the optical range could be bridged and accurately measured [31]. However, the pulse-to-pulse phase slip f_{CEO} shifted the entire frequency spectrum, prohibiting absolute frequency measurements. A groundbreaking technological advance was made with the invention of a nonlinear self-referencing method using two different parts of the comb spectrum. In short, the laser spectrum is broadened in a highly nonlinear photonic-crystal fiber (PCF) to span more than an octave (a ratio of the high and low frequency of 2:1) [32–34]. In a subsequent f-to-$2f$ interferometer, the high-frequency part of the spectrum is brought to interference with the frequency-doubled low-frequency part to measure and control f_{CEO}, which allows establishing a stable comb of frequencies [35, 36]. The absolute frequency of the comb tooth with mode number n is described by [29, 30]

$$f_n = n f_{\mathrm{rep}} + f_{\mathrm{CEO}}. \tag{1.1}$$

The frequency comb has proven to be an essential tool in metrology for absolute frequency determination and phase-locking of lasers [32, 37–39], which were the prerequisites for the development of modern optical atomic clocks [10]. Furthermore, the frequency comb has found numerous other applications, for instance, in the fields of molecular spectroscopy [39, 40], laser ranging [41], exoplanet observations [42], attosecond science [43], and optical communication [44].

Noise properties play a major role for the relative precision of atomic frequency standards and clocks, and the Allan deviation is commonly used as a measure for the statistical errors of the frequency determination [9, 45]. When probing a resonance of N uncorrelated samples using the Ramsey method with a probe time T, the total averaging time τ, a perfect state detection efficiency, and the quantum projection noise being the dominant noise source, the Allan deviation is given by [10, 46]

$$\sigma_y(\tau) = \frac{1}{2\pi\nu_0\sqrt{N\tau T}}. \tag{1.2}$$

From this equation, it becomes clear that increasing the transition frequency ν_0 reduces the Allan deviation. Stated another way, fixing N and T, the time it takes to reach a certain measurement precision is proportional to $\tau \propto 1/\nu_0^2$ [10]. It shows the advantage of a high transition frequency. It is mainly for this reason that optical atomic clocks with terahertz transition frequencies outperform RF-driven Cs atomic clocks [47]. Currently, frequency metrology in the optical range progresses beyond what once appeared only imaginable, and the twentieth digit in accuracy seems within reach [28, 48]. Further improving the precision of frequency standards beyond the best of today's optical atomic clocks will drive future advancements in quantum communication, geodesy, and sensing applications.

1.2 Highly charged ions and the search for new physics

The number of atoms and (singly charged) ions that can be used to construct an atomic clock is limited by the number of atomic elements and technical constraints. HCIs, with the charge state as a freely selectable parameter, add a third dimension to the table of nuclides, which groups atoms by their number of neutrons and protons in the nucleus. Therefore, going from singly charged ions to HCIs offers novel systems to explore. The latter possess many forbidden transitions with narrow linewidths, making them ideal candidates for novel, more precise optical clocks. Recently, the survival of such a long-lived state with a predicted lifetime of 130 d was measured by detecting the relativistic mass increase of 202 eV of $^{187}\text{Re}^{29+}$ ions in a Penning trap [49]. As the charge of an ion increases, the energy separation between different principal quantum numbers (n) increases rapidly, shifting electronic transitions into the X-ray region and reducing the lifetime of the excited states. Furthermore, fine-structure transitions between electronic orbitals with the same n, which are caused by spin flips of electrons due to relativistic effects, typically occur in the optical or XUV ranges. Basing an atomic clock on transitions in the XUV instead of the optical spectrum reduces the averaging time to reach a certain measurement precision due to its much higher frequency. Another advantage of HCIs is that they suffer much less from external perturbations than neutral atoms. Thus, HCI clocks can surpass state-of-the-art optical clocks in accuracy if sufficiently narrow transitions can be addressed [50, 51].

However, there are technical challenges with frequency standards based on HCIs. Besides the significant obstacle of realizing a coherent and narrow-linewidth light source for frequencies far beyond the optical spectral region [52], which will be addressed in this work, the production and handling of HCIs is a hurdle, as this is much more challenging than for singly charged ions. Production of HCIs by stripping their electrons requires a lot of energy, which is why they are typically produced in an electron beam ion trap (EBIT), where a strong magnetic field focuses an energetic electron beam, and neutral atoms injected into the vacuum are ionized by electron-impact ionization. The negative space charge of the electron beam radially traps these ions. Longitudinal confinement is achieved by electrodes surrounding the trap region. In this way, the trapped ions get further ionized by the electron beam until the electron energy is insufficient

to reach the next charge state. Nevertheless, the continuous electron bombardment populates highly excited states and results in high ion temperatures in the range of 10^6 K.

Cold highly charged ions
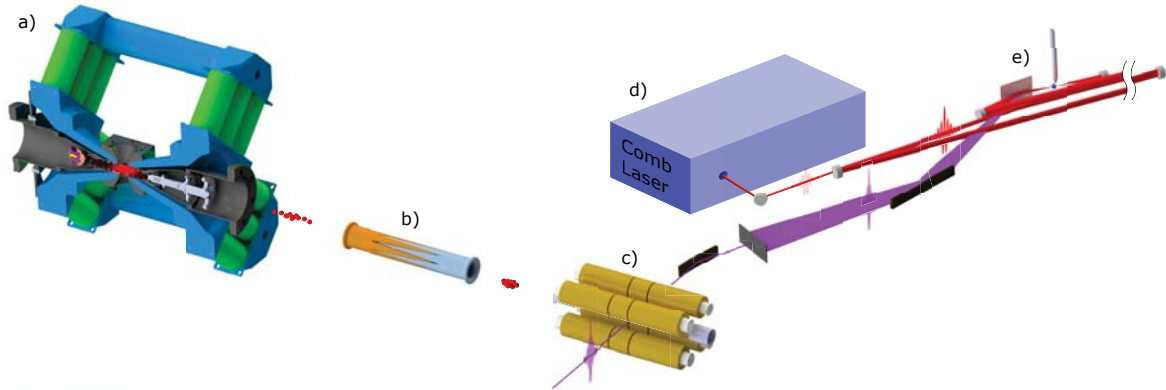
Figure 1.1: Schematic overview of the experimental setup for XUV comb spectroscopy of HCIs. The ions are produced in a compact EBIT, b) decelerated, and c) trapped in a linear Paul trap. d) The fundamental frequency comb spectrum is passively amplified in a e) resonant cavity to generate the XUV light for direct frequency comb spectroscopy of HCIs. Figure from [53].

Significant experimental progress has been made in recent years in the collaboration of our group led by J. R. Crespo López-Urrutia at the Max-Planck-Institut für Kernphysik (MPIK) and the group of P. O. Schmidt at the Physikalisch-Technische Bundesanstalt (PTB). Cooling of HCIs to millikelvin temperatures needed for frequency metrology was first demonstrated with Ar^{13+} at MPIK in 2015 [54]. Highly charged argon ions were produced at megakelvin temperatures in a superconducting EBIT [55] and extracted as bunches afterwards. The desired charge state of the ions was selected by their q/m mass ratio in an electrostatic bender using a kicker electrode to reject unwanted ions. Subsequently, serrated electrodes pulsed by high voltages were used to reduce the longitudinal velocity spread and average velocity of the ions. The Ar^{13+} ions were then guided into a cryogenic linear Paul trap with switchable mirror electrodes [56]. A large laser-cooled Be^+ ion crystal allowed multi-pass stopping and sympathetic cooling of the HCIs to millikelvin temperatures [57].

Soon after the successful proof-of-principle operation of the Cryogenic Paul Trap Experiment (CryPTEx), a new and improved version of this experimental setup was developed. HCIs are produced in a compact EBIT based on permanent magnets [58], while the trap is cooled to 4 K using a closed-cycle low-vibration cryostat [59]. Currently, two experiments, the CryPTEx-SC in our group in Heidelberg and the CryPTEx-PTB in Braunschweig, are in operation. However, there are a few differences between our setup and the CryPTEx-PTB. Figure 1.1 shows a schematic overview of our experimental setup for future direct XUV frequency comb spectroscopy of HCIs. Compared to the conventional miniature cryogenic Paul trap of the CryPTEx-PTB [60], we employ a novel superconducting Paul trap [61], which has the advantage of trapping the ions in a well-defined and highly stable RF field, reducing heating and micromotion. This enhanced stability is caused by the filtering effect of the trap, which is designed to serve as a high-Q cavity at 34.5 MHz. Additionally, the monolithic superconducting trap body completely encloses the trap center, which freezes a preexisting magnetic flux during cooldown below the critical temperature in place. The trapped magnetic field magnitude is stable over months, characterized using microwave spectroscopy of Be^+ hyperfine qubits [62]. Furthermore, not only high-frequency RF

fields but also low-frequency noise is shielded from the trapped ions due to the superconducting material. Co-trapping of HCIs and Be$^+$ ions has recently been demonstrated in this setup. Currently, the laser system for ground-state cooling is being installed.

After the first very successful experiments with the CryPTEx-PTB setup, where coherent laser spectroscopy of a cold HCI has been demonstrated [63] using the quantum logic spectroscopy method [64], advanced cooling techniques have been developed [65]. These allowed the first HCI atomic clock operation with a systematic frequency uncertainty of 2.2×10^{-17}, which is comparable with many state-of-the-art optical clocks in operation [66]. It demonstrates the feasibility of precision spectroscopy of forbidden narrowband transitions in HCIs for optical (and beyond) clocks, and future high-sensitivity searches for new physics beyond the Standard Model of particle physics (SM) [50, 51, 67–69].

Isotope-shift spectroscopy

The SM describes measurements of elementary particles exquisitely well. However, it is considered incomplete because it cannot account for certain phenomena, such as the existence of dark matter [70] and the asymmetry between matter and antimatter in the universe [71], and it does not incorporate gravity, which is a fundamental interaction in the universe. Isotope-shift spectroscopy has been proposed as a tabletop method to search for dark-matter candidates in the intermediate mass range [72]. An additional isotope shift from the interaction of a hypothetical new light boson can lead to a deviation from linearity in a so-called King-plot [73] and hint towards new physics [72, 74]. A King plot compares the normalized isotope shifts for two (or more) different transitions. However, higher-order SM effects can also lead to King-plot nonlinearities. Therefore, a generalized King-plot method, which allows eliminating the impact of higher-order SM effects by measuring additional electronic transitions, was proposed [75, 76], but it requires many stable isotopes. One example for such a study is highly charged calcium since this element has five stable isotopes with zero nuclear spin [77]. Recently, another advanced King-type formalism has been proposed that directly compares experimental and theoretical results of single isotope pairs of few-electron ions by modifying the King formalism to account for subleading standard model nuclear corrections [78].

To summarize, frequency metrology based on HCIs offers many advantages because plenty of narrow transitions from the optical up to the soft X-ray domain are promising for atomic clock operation and fundamental physics, by searching, for example, for King-plot nonlinearities.

1.3 Precision spectroscopy at high frequencies: The extreme ultraviolet frequency comb

At the beginning of the 2000s, when the frequency comb was invented, nonlinear optics was widely used to convert the central wavelength of the available laser sources to the spectral regions needed for laser spectroscopy. Continuous wave (CW) Ti:sapphire lasers or narrow-linewidth flash-lamp pumped dye lasers were often used. Nonlinear crystals for second-harmonic generation (SHG) or other low-order optical nonlinear effects had allowed covering the optical, the near-infrared (NIR), and the ultraviolet (UV) spectral region. However, the link to higher frequencies far beyond the optical was still missing.

Soon after the first frequency combs had been built, the research groups that were leading in its development started to nonlinearly transfer the near-infrared (NIR) comb spectrum to different spectral regions by making use of the improved efficiency of nonlinear processes enabled by the high peak intensity of ultrashort pulses. Although the principle of HHG had already been used to generate XUV light, it was only possible with amplified ultrashort laser pulses at a low
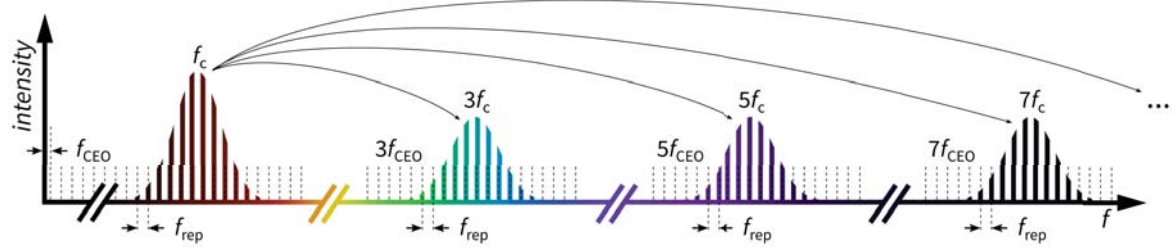
Figure 1.2: Illustration of the XUV frequency comb spectrum for the lowest harmonic orders. The fundamental NIR frequency comb spectrum is centered at f_c. The comb teeth are spaced by the repetition rate f_{rep} and offset from zero by f_{CEO}. Cavity-enhanced high-harmonic generation (HHG) is used to transfer the NIR comb to the XUV spectral region.

repetition rate since very high intensities are required for this highly nonlinear process [79–82]. Peak intensities of frequency comb lasers were orders of magnitude below what was necessary to start the highly nonlinear HHG process. This changed in 2005 when the intra-cavity generation of high-order harmonics in a xenon gas target was demonstrated, enabled by the passive amplification of the NIR frequency comb pulses in a femtosecond enhancement cavity (fsEC) [83, 84]. In this way, the fundamental comb spectrum was successfully extended to the XUV spectral region below 100 nm, providing the missing gear to directly link RF and the XUV frequencies.

The highly nonlinear process of high-harmonic generation (HHG) produces comb copies centered at odd multiples of the central wavelength of the original comb [83, 84], as shown in Figure 1.2. The resulting XUV comb can be described by a modified version of Equation 1.1

$$f_{n,q} = q f_{CEO} + n f_{rep}, \tag{1.3}$$

where q is the harmonic order. The generated electric field oscillates q-times as fast as the fundamental frequency, and thus, the carrier-envelope offset (CEO) frequency increases with the same factor. On the contrary, the spacing of the harmonic comb teeth is the same as that of the fundamental comb since it is determined by the repetition rate, which is the same for all harmonic orders. Soon after the invention of the XUV frequency comb, the first spectroscopy experiments, such as direct XUV comb spectroscopy of atomic xenon [85], were performed. However, the accessibility and availability of these systems have been, up to now, limiting factors on the route towards high-precision measurements. Nevertheless, compared to synchrotrons or other large-scale facilities that can produce XUV radiation, XUV frequency combs are quite accessible even though they were, and still are, no turnkey systems that can be easily operated over extended periods.

With the advent of ultrafast Yb-doped fiber-based frequency combs and high-power amplifier technology, reliability and generated XUV power have significantly improved. Nowadays, XUV frequency combs have matured, and a handful of systems are operated in the world by groups in Boulder [86–94], Garching [84, 93, 95–102], New York [103, 104], Tokyo [85, 105, 106], Vancouver [107–111], Vienna [112, 113], Wuhan [114], and recently, also in our lab in Heidelberg [53, 115–117]. The generated maximum photon energy has increased from ∼20 eV to above 100 eV in recent years [97, 99], and coherence times above one second have been realized [90].

The main advantages of the XUV frequency comb is the inherent coherence and phase stability of its pulse train of ultrashort laser pulses [90] that can be utilized for metrology by direct frequency comb spectroscopy to measure absolute frequencies and the high repetition rate, which results in a high XUV flux. Direct frequency comb excitation of a single trapped ion with a deep-UV frequency comb was demonstrated [118]. At higher energy, the 1*S*-2*S* two-photon resonance in He$^+$ is a narrow transition at 61 nm in a hydrogenic system that has a high potential

for accurately testing fundamental theories, such as quantum electrodynamics (QED). It has a high quality factor and can test higher-order QED corrections, which scale with large powers of the nuclear charge Z in hydrogenic systems [119]. Currently, experiments are being prepared at MPQ in Garching employing an XUV frequency comb and He^+ in a Paul trap [120]. Direct XUV frequency comb spectroscopy has also been proposed for direct laser excitation of the thorium nuclear isomeric state for a nuclear clock [94, 121], and experiments are currently being set up. A related method is XUV Ramsey-comb spectroscopy [122–124], where harmonics are generated by pairs of powerful amplified frequency comb pulses in a Ramsey-type [125] excitation scheme. Compared to intra-cavity HHG, it offers the advantage of easy tunability and simple upconversion. However, dynamic plasma effects affect the yield and add a time-dependent influence on the phase. Another relevant application of XUV combs is photoelectron spectroscopy of solid-state materials because the high repetition rate allows for space-charge-free measurements [101, 104, 105]. The exact and absolute frequency resolution of XUV frequency combs is promising for various other precision measurement tasks in the XUV. The temporal coherence of an XUV frequency comb pulse train can be determined at timescales several orders of magnitude longer than current state-of-the-art measurements by using narrow transitions in HCIs [126].

Experimental realization

For the onset of highly nonlinear processes, such as multiphoton ionization (MPI) and HHG, high laser intensities in the range of $10^{13}\,\mathrm{W\,cm^{-2}}$ are required. Conventionally, these ultrashort laser pulses are generated with low repetition rate amplifier systems operating in the kilohertz range. In order to measure frequencies absolutely and precisely by direct frequency comb spectroscopy, the comb line spacing needs to be larger than the width of the transition under study. Therefore, the repetition rate of the comb laser, which determines this frequency spacing (cf. Equation 1.3), needs to be large to enable precision spectroscopy in the XUV. However, an average power of many kilowatts is required to initiate highly nonlinear processes at repetition rates in the multi-megahertz range. Stabilized laser systems producing ultrashort pulses at such immense average power are yet to be developed. To overcome this technical obstacle, we utilize passive amplification in a fsEC.

Compared to the first XUV frequency combs, we have implemented a few significant changes and improvements to their designs to enable stable long-term operation: An astigmatism-compensated enhancement cavity [117], an ultra-high vacuum (UHV)-compatible vacuum system with advanced differential pumping [127], and a gas-catch, recycling, and high-pressure compression system [128]. These improvements are necessary for precision measurements requiring long-term operation over at least several days to record sufficient statistics. An astigmatism-compensated cavity design maximizes the intra-cavity laser intensity and generates a symmetric and non-elliptic XUV beam. Due to the high repetition rate of the XUV comb, plasma can easily accumulate in the generation volume if the gas velocity is too low, altering the phase matching of the HHG process. Therefore, a high-pressure gas nozzle enables a high gas replenishing rate, which allows efficient XUV generation. However, this introduces a significant gas load into the vacuum system. Consequently, a dedicated differential-pumping system encapsulating the interaction region is used for efficient gas removal. Even though this reduces the residual gas pressure inside the main chamber by several orders of magnitude, the consumption of the precious target gas is still high. Typically xenon is used, and its cost has been continuously increasing over recent years (without recycling ∼5000 €/d), prohibiting long experiments and motivating closed-loop operation. Therefore, we have developed a gas-catch and recycling system that allows recompressing the gas to high pressure, either for closed-loop operation or re-bottling.

1.4 Multiphoton ionization studies at 100 MHz repetition rate
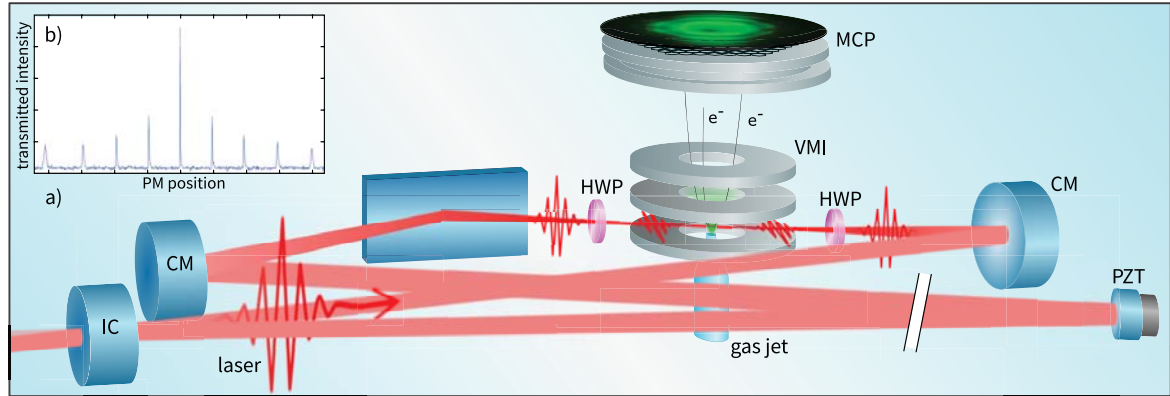
Figure 1.3: Schematic overview of the HHG cavity. Here, it is equipped with a velocity-map imaging (VMI) spectrometer and a microchannel plate (MCP) detector for the first demonstration of intra-cavity MPI. After this proof-of-principle experiment, the electrodes and the detector were removed for XUV frequency comb generation. a) Pulses enter the cavity through the input coupler (IC), and half-wave plates (HWPs) are used to adjust the polarization. The light is focused between two curved mirrors (CMs) to ionize gas-phase atoms, and photoelectrons are imaged using the VMI spectrometer. b) The cavity length can be tuned with a piezo-actuated mirror (PZT) to become resonant with the driving frequency comb, which leads to intra-cavity intensity enhancement. Adapted from [53, 129].

Apart from generating high-harmonics for high-precision measurements in the XUV, the cavity-enhanced NIR frequency comb is also utilized for directly studying nonlinear interactions of the intense laser pulses with atoms. In this way, atoms can be excited or even ionized by the simultaneous absorption of multiple photons, exploiting the coherence and absolute frequency resolution of the comb. MPI is a highly nonlinear process, with the ionization rate proportional to I^n, where I is the laser intensity, and n is the photon number. Therefore, high laser intensities are required, which are typically reached employing chirped-pulse amplification at kilohertz repetition rates.

Studying the onset of MPI at the lowest possible intensity is attractive because then the nonlinearities can be treated fully perturbatively. However, the count rate also drops dramatically at low intensity, which makes experiments with conventional kilohertz repetition rate systems impossible. Our laser and fsEC operate at a repetition rate of 100 MHz. Considering a fixed minimal count rate of a multiphoton event involving ten photons, we can study these processes at half the intensity ($10^{3/10} \approx 2$) of systems operating at 100 kHz, which has been considered a high repetition rate until recently [130–132]. The maximum obtainable count rate is limited by the onset of space-charge effects above approximately one electron per laser shot. To express it differently, low intensity MPI studies are only reasonable if the repetition rate is sufficiently high. Otherwise, the data acquisition time needed for good signal-to-noise ratios becomes very long since the acquisition of a single high-resolution spectrum can require up to 10^9 photoelectrons [133]. For that reason, we performed a proof-of-principle MPI experiment [53, 129] on our route towards the XUV comb [115, 116] to demonstrate the feasibility of such intra-cavity MPI studies. For this first intra-cavity VMI experiment, the HHG cavity was modified by adding electrodes and an MCP detector, as shown in Figure 1.2.

VMI is a technique to visualize and measure the momentum distribution of charged particles, such as photoelectrons, with an inhomogeneous electric field that maps their velocity vectors

onto a position on a detector. It is well suited and commonly utilized to study MPI and above-threshold ionization (ATI) [134], and has become a standard method to study charged particles within the last 25 years [135]. Eppink and Parker introduced the VMI technique [136] as an improvement of the product imaging technique from Chandler and Houston [137]. In VMI, an initial 3D particle velocity distribution is mapped onto the arrival position on a suitable 2D detector by integrating the distribution along the time-of-flight axis, which connects the interaction region and the detector. It was initially developed to study gas-phase molecular reaction dynamics and is now often employed in photo-fragmentation and inelastic-scattering experiments [138–142]. It utilizes the benefit of full 4π solid angle collection efficiency while having the capability to measure the kinetic energy and angular distribution of charged particles simultaneously [136, 143–146]. This is possible by an inhomogeneous electric extraction field, which focuses the particles onto the detector.

VMI has become a widely used tool in attosecond science [147–150] and has been used to study ionization time delays using the attoclock technique [151]. Compared to cold-target recoil-ion momentum spectroscopy (COLTRIMS) [152] with reaction microscopes (REMIs) [153], which allow coincidence measurements, it offers the benefits of reduced technical complexity, handling higher count rates and insensitivity to the size of the ionization volume. Nevertheless, it has been shown that coincidence measurements are also possible with VMI setups [154–158]. Therefore, VMI allows a practical and easy-to-use way to map 3D distributions, and it is well-suited for high repetition rate MPI experiments. Figure 1.4 shows a comparison of selected VMI experiments with femtosecond pulses at various repetition rates to benchmark the data acquisition time. It clearly shows the great advantage of studying MPI using enhancement cavities compared to conventional low repetition rate experiments.
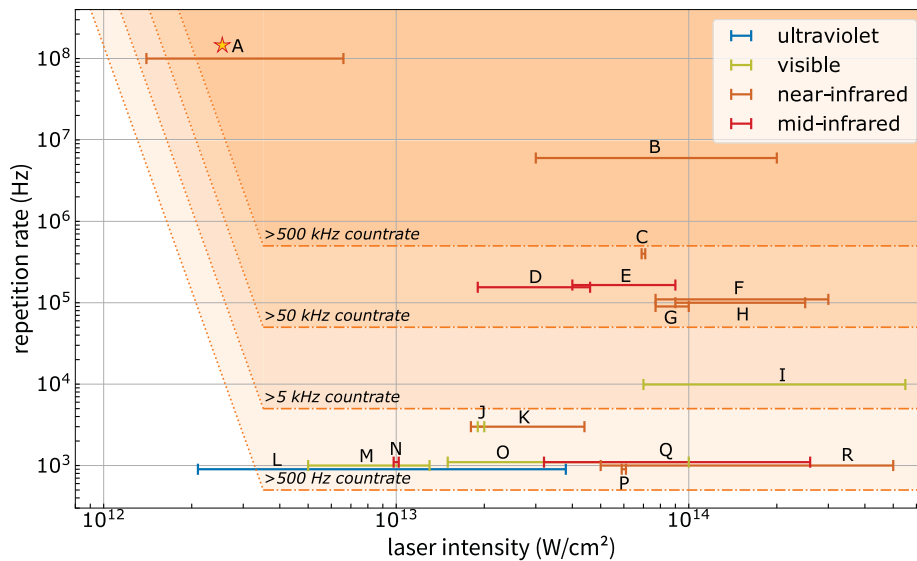
Figure 1.4: Comparison of selected published VMI experiments using ground-state noble gases in the short pulse regime. It underlines the importance of a high repetition rate for MPI studies since a high count rate allows short data acquisition times. Shaded regions indicate the achievable photoelectron count rate, limited either by a maximum yield of one electron per laser shot (dashed-dotted horizontal lines) or the ionization rate scaling with I^n, here illustrated for a ten-photon process (dotted angled lines). Clearly, this scaling depends strongly on the laser wavelength used. The letters refer to the literature: A (our work): [129], B: [159], C: [160], D: [161], E: [162], F: [133], G: [163], H: [164], I: [165], J: [146], K:[166], L: [167], M: [168], N: [169], O: [170], P: [171], Q: [172], and R: [173]. Adapted with permission from [129] ©The Optical Society.

The HHG enhancement cavity was designed for intra-cavity HHG and only supports s-polarized light, which is disadvantageous for versatile multiphoton excitation and ionization experiments. Additionally, inserting the differential pumping system for efficient target gas removal prohibited further MPI experiments. However, our first measurement demonstrated the feasibility of high repetition rate MPI experiments [53, 129], which resulted in the wish for a new cavity to advance the field of intra-cavity VMI studies. The construction of this novel cavity with a compact intra-cavity VMI spectrometer and its possibilities for future experiments are described in detail in this thesis.

Counter-propagating pulses

Using intense cavity-enhanced femtosecond laser pulses offers the compelling but still unexplored possibility of operating with counter-propagating pulses. When an atom is photo-ionized, the momentum $\Delta p = \hbar\omega/c$ is transferred from the photons to its fragments in the direction of light propagation [174]. However, a vastly unexplored scenario is the partitioning of the photon momentum between the electron and the nucleus in strong-field ionization. Experiments exploring this effect require a high momentum resolution because the transferred momentum is small. Additionally, the zero momentum position of the detector needs to be well known. In a recent experiment, counter-propagating pulses were used to calibrate the zero momentum position of the detector. Thereby it was possible to study the influence of the laser magnetic field on the electron in the classically forbidden tunnel barrier [175]. In a subsequent experiment with counter-propagating pulses, it has been shown that the partitioning of the linear photon momentum between electron and nucleus in strong-field ionization is drastically altered by the rescattering process [176]. The magnetic nondipole shift of the electron momentum distribution along the light propagation direction was found to be altered when the electron energy passed $2U_{\mathrm{p}}$, where U_{p} is the ponderomotive potential of the driving laser field as will be described in more detail in Section 2.5. In another experiment by the same group, it was shown that the forward-backward symmetry of electron emission in strong-field ionization is broken not only by the magnetic nondipole effect but also by an electric nondipole effect [177]. Counter-propagating pulses have also been utilized for improving the HHG phase-matching process [178–181].

Another exciting application is the diffraction of matter waves, such as electrons, by the standing wave of counter-propagating light. The diffraction of matter waves by a standing electromagnetic wave was already predicted in 1933 by P. L. Kapitza and P. A. M Dirac [182]. The Kapitza-Dirac effect is similar to light diffraction by a grating but with the wave and matter properties switched. At high laser intensities ($\sim 10^{13}\,\mathrm{W\,cm^{-2}}$), electrons could be deflected by the ponderomotive potential of a standing wave of picosecond pulses, and two classical scattering peaks, separated by about 1000 photon recoils, were observed [183]. The first quantum mechanical diffraction peaks (separated by two-photon recoils) were observed in 2001, demonstrating coherent interference, which characterizes wave diffraction [184]. Very recently, an atom interferometer directly driven by a frequency comb was demonstrated [185]. This experiment employs a frequency comb in counterpropagating-pulse geometry to coherently split and recombine cold rubidium wave packets by driving stimulated Raman transitions.

Another advantage of counter-propagating light is that it allows for Doppler-free excitation [21, 186]. The Doppler broadening is suppressed because the Doppler shift in one wave cancels that in the other if the target is irradiated by two laser pulses traveling in opposite directions [187]. Overall, the above descriptions demonstrate the multitude of possible experiments using counter-propagating pulses. Due to the high technical complexity, few of such experiments at high laser intensities have yet been realized.

Experimental realization

Employing intense counter-propagating laser pulses produced by laser systems with high-gain single-pass amplifier systems can only be realized with extreme caution because pulses propagate back into the amplifier at full power and can impair its performance or even cause critical damage. On the contrary, utilizing passive amplification at a high repetition rate in a fsEC results in the same intensity in the target region with the advantage of increased count rate and phase stability. A further advantage of this method is that the peak power of the pulses is only reached inside the resonant cavity when the field is enhanced. Outside the enhancement cavity, the laser power is reduced by the inverse enhancement factor $1/\beta_\epsilon$. Therefore, much less power travels back towards the amplifier, and optical isolators can be employed without restrictions. Typically, these isolators suppress the backward-traveling light by ~30 dB. The gain of our high-power rod-type fiber amplifier is on the order of ten, while low repetition rate systems often require higher gain. Thus, the combination of passive cavity enhancement and rather low-gain amplifiers with optical isolators at medium pulse energies facilitates colliding pulse operation.

Besides the possibility of having pulses colliding in the cavity, further control of the polarization and temporal fields inside the cavity will provide unique control of the investigated phase-coherent dynamic processes. Therefore, we have designed a novel fsEC that allows light of any polarization to be enhanced, as well as the possibility of sustaining pulses in both propagation directions, combined with a compact intra-cavity VMI spectrometer for detecting the photoelectrons. This cavity will be referred to as the VMI cavity. It allows tomographic reconstruction of photoelectron angular distributions (PADs) using the VMI spectrometer surrounding the cavity focus. In addition, the optical setup seeding the cavity can produce polarization-shaped pulse pairs for future pump-probe experiments or the generation of vortex-shaped PADs [188–190]. Thus, a Mach-Zehnder interferometer based split-and-delay (SAD)-box with polarization shaping enables large control over the high-intensity light field in the focus region. This setup could be applied, for instance, for aligning and coherently controlling molecules [191–194].

To reach even higher intensities, the pulse duration of the laser pulses needs to be decreased, which requires spectral broadening because for a given spectral width, the Fourier transform dictates a lower limit for the pulse duration. A multipass cell (MPC) based on pressure-tunable dispersion compensation has been developed to broaden the laser spectrum nonlinearly. This way, more comb lines can be used for spectroscopic applications. The pulses are temporally compressed, allowing for time-resolved experiments with better resolution and reduced plasma effects in HHG. Also, higher intensities can be reached with shorter pulses, allowing for higher photon energies with HHG, as well as enabling MPI studies in atoms with larger ionization potentials.

It is the first fsEC tailored for photoelectron tomography, but without losing flexibility for a wide range of future applications. It serves as a unique toolbox that has great potential because the phase coherence of the frequency comb laser pulses is combined with high intensity. The time structure of the comb is coherently imprinted in the photofragments at a high rate, producing coherent matter waves. It will undoubtedly find novel applications in atomic and solid-state physics and other fields. Furthermore, effects in intense pulsed standing light fields can be investigated, and polarization-shaped pump-probe experiments are possible.

1.5 Thesis organization

As we have seen, nonlinearities play a vital role in this thesis - in the investigated processes as well as in the experimental methods themselves. For this reason, we will encounter them at several places throughout this thesis, which is organized as follows:

Chapter 2 covers the theoretical background of ultrashort (frequency comb) laser pulses and its enhancement in fsECs. The concept of nonlinear temporal pulse compression is illustrated, and the numerical method to model the nonlinear pulse dynamics in the MPC is outlined. Furthermore, photoionization and HHG in strong laser fields are explained, and the tomographic reconstruction methods for 3D PADs is introduced. Chapter 3 deals with intra-cavity HHG for XUV comb production, starting with a description of the frequency comb laser source and the high-power amplifier system. The HHG cavity and the experimental setup, including the vacuum and gas system, are described before the results are shown at the end of the chapter. After that, in Chapter 4, the VMI cavity for intra-cavity photoionization studies is presented, including the complete optical setup to produce colliding pulses. The SAD-box for the generation of polarization-shaped double pulses with variable time delay, the MPC for temporal pulse compression, and the compact VMI spectrometer are detailed. Afterwards, the first intra-cavity tomographic photoelectron measurements are presented. Additionally, the possibility of producing highly intense pulses colliding at the cavity focus is elucidated. Finally, the concluding remarks with a discussion of the results and an outlook are given in Chapter 5.

2 Theoretical background

In the first part of this chapter, we will deal with ultrashort laser pulses in the time and frequency domain to understand the peculiarities of a particular type of laser - the frequency comb. Thereafter, theoretical aspects relevant to the different technologies developed in this thesis will be treated. Starting with the geometric propagation of Gaussian laser beams through optical elements, the ABCD-matrix formalism, which allows the formulation of geometric conditions for optical resonators, is introduced. Then, the field and energy relations in such optical cavities are described in more detail, and the effects of dispersion are explained. Since, in our experimental setup, it is possible generate double pulses with variable delay and shape the polarization freely, the Jones formalism for describing polarization effects is also introduced. Subsequently, a theoretical description of laser-atom interaction in strong laser fields is given with a focus on MPI and ATI. The PADs after ionization are characterized using the VMI technique that also allows the study of non-cylindrically symmetric distributions by tomographic reconstruction. Using the stabilized pulse train of a frequency comb to drive the HHG process leads to the generation of an XUV frequency comb that will be used for future precision spectroscopy of HCIs. The HHG process used to produce the XUV frequency comb is explained with a focus on phase-matching for efficient frequency conversion. At the end of this chapter, the concept of nonlinear temporal pulse compression in MPCs is introduced.

2.1 Ultrashort laser pulses

The basic properties of single ultrashort laser pulses are discussed in this section. It mainly follows the treatment of J.-C. Diels and W. Rudolph [195], and lecture notes of R. Trebino [196] and U. Morgner [197].

2.1.1 Wave equation

In the case of electromagnetic waves that propagate in isotropic media without free charges, the Maxwell equations lead to the wave equation

$$\nabla^2 \mathbf{E}(\mathbf{r}, t) - \frac{n^2}{c^2} \frac{\partial^2}{\partial t^2} \mathbf{E}(\mathbf{r}, t) = 0, \tag{2.1}$$

with the time t, the spatial coordinate $\mathbf{r}$, the refractive index $n^2 = \varepsilon_r$ that is linked to the relative permittivity ε_r, and the speed of light $c = 1/\sqrt{\varepsilon_0 \mu_0} = 299\,792\,458\,\mathrm{m\,s^{-1}}$, where ε_0 is the vacuum permittivity, and μ_0 is the magnetic permeability of free space. The relative permittivity is directly related to the electric susceptibility χ by $\varepsilon_r = (1 + \chi^{(1)})$ and couples the time-dependent electric field $\mathbf{E}(\mathbf{r}, t)$ to the (linear) polarization density $\mathbf{P}_L(\mathbf{r}, t)$ such that $\mathbf{P}_L(\mathbf{r}, t) = \varepsilon_0 \chi^{(1)} \mathbf{E}(\mathbf{r}, t)$.

At high field strengths, the nonlinear susceptibility leads to a nonlinear polarization of the medium $\mathbf{P}_{NL}(t)$, given by the Taylor expansion

$$\mathbf{P}(\mathbf{r}, t) = \varepsilon_0 \chi^{(1)} \mathbf{E}(\mathbf{r}, t) + \mathbf{P}_{NL}(\mathbf{r}, t) = \varepsilon_0 \left(\chi^{(1)} \mathbf{E}(\mathbf{r}, t) + \chi^{(2)} \mathbf{E}^2(\mathbf{r}, t) + \chi^{(3)} \mathbf{E}^3(\mathbf{r}, t) + \dots \right), \tag{2.2}$$

with the n-th-order susceptibilities $\chi^{(n)}$ of the medium. In general, $\chi^{(n)}$ is a tensor, but here we consider it as a scalar for simplicity, assuming a homogeneous isotropic material. It leads to the

standard nonlinear wave equation

$$\nabla^2 \mathbf{E}(\mathbf{r}, t) - \frac{n^2}{c^2} \frac{\partial^2}{\partial t^2} \mathbf{E}(\mathbf{r}, t) = \frac{1}{\varepsilon_0 c^2} \frac{\partial^2}{\partial t^2} \mathbf{P}_{\mathrm{NL}}(\mathbf{r}, t). \tag{2.3}$$

Equation 2.3 is the basis of nonlinear optics and this treatment becomes useful for describing nonlinear frequency mixing such as SHG or self-phase modulation (SPM).

2.1.2 Electric field

Plane waves are the most simple solution of the wave equation

$$\mathbf{E}(\mathbf{r}, t) = \mathbf{E}_0 \cos\left(\omega t - \mathbf{k}\mathbf{r} + \phi\right), \tag{2.4}$$

with the angular frequency $\omega = 2\pi f$, the wave vector $\mathbf{k}$, and a constant phase ϕ. The electric field $\mathbf{E}(\mathbf{r}, t)$ is a real function and can be measured experimentally.

To simplify the calculations, a complex electric field is introduced

$$\mathcal{E}(z, t) = \mathcal{E}_0(z, t) \, e^{i(\omega t - kz + \phi(t))}, \tag{2.5}$$

where the spatial dependence is reduced to a single dimension along the propagation direction z, and $\phi(t)$ is the time-dependent phase. From now on, the complex electric field is written as a calligraphic $\mathcal{E}$. The real electric field $E(z, t)$ is given by the real part

$$E(z, t) = \Re\{\mathcal{E}\} = \frac{1}{2}\left(\mathcal{E}(z, t) + c.c.\right), \tag{2.6}$$

where $c.c.$ denotes the complex conjugate.

A complete description of the electric field can be given either in the time or the frequency domain. They are linked through the complex Fourier transform

$$\mathcal{E}(\omega) = \mathcal{F}\{E(t)\} = \int_{-\infty}^{\infty} E(t) \, e^{-i\omega t} \, dt = |\mathcal{E}(\omega)| \, e^{i\varphi(\omega)}, \tag{2.7}$$

with the spectral amplitude $|\mathcal{E}(\omega)|$ and the spectral phase $\varphi(\omega)$. The z-dependence has been dropped for a simpler notation. In the same way, the temporal electric field is obtained from the spectral field by the inverse Fourier transform $(\mathcal{F}^{-1})$

$$E(t) = \mathcal{F}^{-1}\{\mathcal{E}(\omega)\} = \frac{1}{2\pi} \int_{-\infty}^{\infty} \mathcal{E}(\omega) \, e^{i\omega t} \, d\omega, \tag{2.8}$$

using $\mathcal{E}(\omega) = \mathcal{E}^*(-\omega)$, because $E(t)$ is real.

An intuitive picture is that a temporal pulse can be formed by adding many waves of different frequencies in the spectral domain, as illustrated in Figure 2.1. When the waves are in phase at $t = 0$, they add constructively, and a pulse centered at $t = 0$ is formed. This is the concept behind mode-locking of laser resonators [199, 200]. Experimentally, nonlinear effects are used for locking the longitudinal laser modes inside the laser resonator because the high peak intensity of a pulse needs to be favored with regards to CW operation. Therefore, semiconductor saturable-absorber mirrors (SESAMs) [201], nonlinear polarization rotation [202] or Kerr lens mode-locking [203] are widely used techniques to add nonlinear gain or loss to the circulating laser field.

Note that in Equation 2.7, negative frequencies result from the Fourier transform, and it is convenient to find a complex representation of the electric field that contains only positive frequencies

$$\mathcal{E}^+(\omega) = \int_{-\infty}^{\infty} \mathcal{E}^+(t) \, e^{-i\omega t} \, dt = \begin{cases} \mathcal{E}(\omega) & \text{for } \omega \geq 0 \\ 0 & \text{for } \omega < 0 \end{cases}, \tag{2.9}$$
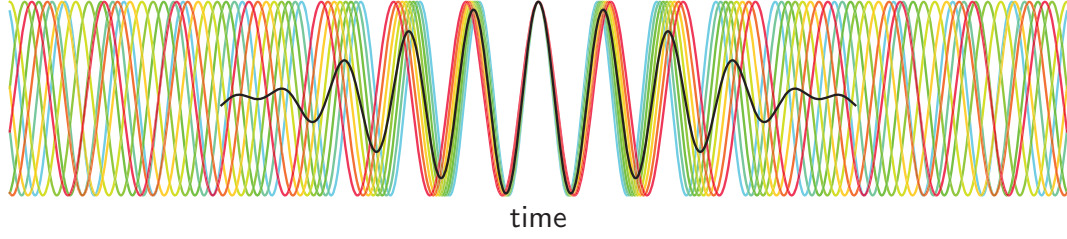
time

Figure 2.1: Illustration of mode-locking in the time domain. A phase-stable relationship of the longitudinal laser resonator modes with different frequencies (drawn in color) results in constructive interference, and a short pulse (normalized pulse drawn in black) is generated. Graphical representation inspired by [198].

related through the inverse Fourier transform to

$$\mathcal{E}^+(t) = \frac{1}{2\pi} \int_{-\infty}^{\infty} \mathcal{E}^+(\omega) \, e^{i\omega t} \, d\omega. \tag{2.10}$$

The corresponding quantities $\mathcal{E}^-(t)$ and $\mathcal{E}^-(\omega)$ are defined in the same way for the negative frequencies. The real field $E(t)$ is obtained from Equations 2.9 and 2.10 by

$$E(t) = \mathcal{E}^+(t) + \mathcal{E}^-(t) \tag{2.11}$$

and the complex spectral field is given by

$$\mathcal{E}(\omega) = \mathcal{E}^+(\omega) + \mathcal{E}^-(\omega). \tag{2.12}$$

For the treatment of short laser pulses, it is convenient to introduce a carrier frequency ω_c and separate the complex field into a fast oscillating part and a slowly varying envelope

$$\mathcal{E}^+(t) = \frac{1}{2} A(t) \, e^{i\varphi_{\mathrm{CEP}}} \, e^{i\varphi(t)} \, e^{i\omega_c t} = \frac{1}{2} \mathcal{A}(t) \, e^{i\omega_c t}, \tag{2.13}$$

where $\varphi(t)$ is the time-dependent phase, $A(t)$ is the real field envelope, and $\mathcal{A}(t)$ is the complex field envelope. The constant phase term $e^{i\varphi_{\mathrm{CEP}}}$ refers to the carrier-envelope phase (CEP), which is important for few-cycle pulses and frequency combs, as described in Section 2.2. The factor 1/2 results from the fact that here only the positive frequency part of the spectrum is considered. The separation of the field into a fast oscillating part and an envelope within the slowly varying envelope approximation (SVEA) is valid when the spectral bandwidth is only a small fraction of the carrier frequency

$$\frac{\Delta\omega}{\omega_c} \ll 1, \tag{2.14}$$

which requires small temporal variations of $A(t)$ and $\varphi(t)$ within an optical cycle.

The complex temporal envelope $\mathcal{A}(t)$ defines the temporal shape of short laser pulses, and it is used to describe (nonlinear) pulse propagation. It is given by the inverse Fourier transform of the frequency-shifted (positive) spectral field

$$\mathcal{A}(t) = A(t) \, e^{i(\varphi(t) + \varphi_{\mathrm{CEP}})} = \frac{1}{2\pi} \int_{-\infty}^{\infty} 2\mathcal{E}^+(\omega + \omega_c) \, e^{i\omega t} \, d\omega. \tag{2.15}$$

The complex spectral envelope $\mathcal{A}(\omega)$ is centered around the origin $\omega = 0$ by choice of ω_c and defines the spectral shape of the pulse. The reason is that we have dropped the rapid oscillations at ω_c by considering only the temporal envelope of the pulse. As a result, the complex envelope

needs to be stated in terms of the shifted frequency and is given by the Fourier transform of the complex temporal envelope $\mathcal{A}(t)$ defined in Equation 2.15

$$\mathcal{A}(\omega) = \int_{-\infty}^{\infty} \mathcal{A}(t)\,e^{-i\omega t}\,dt = 2\int_{-\infty}^{\infty} \mathcal{E}^{+}(t)\,e^{-i(\omega+\omega_c)t}\,dt. \tag{2.16}$$

The most common temporal pulse shapes are the Gaussian pulse

$$\mathcal{A}(t) = \mathcal{A}_0\,e^{-(t/\tau_{\text{Gauss}})^2}, \tag{2.17}$$

the hyperbolic secant pulse

$$\mathcal{A}(t) = \mathcal{A}_0\,\text{sech}(-t/\tau_{\text{sech}}), \tag{2.18}$$

and the Lorentzian pulse

$$\mathcal{A}(t) = \frac{\mathcal{A}_0}{1 + (t/\tau_{\text{L}})^2}, \tag{2.19}$$

where the durations $\tau_{\text{Gauss}} = \tau_{\text{FWHM}}/\sqrt{2\ln 2} \approx \tau_{\text{FWHM}}/1.177$, $\tau_{\text{sech}} \approx \tau_{\text{FWHM}}/1.763$, and $\tau_{\text{L}} \approx \tau_{\text{FWHM}}/1.287$ are related to the full width at half maximum (FWHM) of the temporal intensity profile $|\mathcal{A}(t)|^2$. In the spectral domain, the width $\Delta\omega_{\text{FWHM}}$ is defined in a similar way as the FWHM of the spectral intensity $|\mathcal{A}(\omega)|^2$, unless noted otherwise.

The temporal and spectral widths are related through the Fourier transform and thus a time-bandwidth product (TBP)

$$TBP = \tau_{\text{FWHM}}\Delta\omega_{\text{FWHM}} \geq 2\pi C_{TBP} \tag{2.20}$$

is defined with the constant C_{TBP}, which is specific for the pulse shape. It is given by $C_{TBP,\text{Gauss}} = 0.441$, $C_{TBP,\text{sech}} = 0.315$, and $C_{TBP,\text{Lorentz}} = 0.142$ [195]. Pulses are bandwidth-limited if Equation 2.20 holds, meaning they have the shortest possible pulse duration for a given spectral width. A nonlinear spectral phase of the pulses causes the instantaneous frequency to change during the pulse, called chirped pulses. In that case, the pulses are longer than their bandwidth limit.

2.2 Frequency comb

This section illuminates the difference between the spectrum of a single laser pulse and a sequence of temporally equally spaced pulses. A mode-locked laser oscillator emits a train of ultrashort pulses at a fixed repetition rate $f_{\text{rep}} = 1/T_{\text{rep}}$, where the repetition time $T_{\text{rep}} = c/L$ is given by the speed of light c and optical path length of the laser resonator L. The following derivation follows the treatment of S. T. Cundiff [204]. By combining Equations 2.13 and 2.15, the electric field of a pulse train of N pulses, spaced by T_{rep}, can be expressed as

$$\mathcal{E}_{\text{pt}}(t) = \sum_n A(t - nT_{\text{rep}})\,e^{i(\omega_c t + n(\varphi_{\text{CEP}} - \omega_c T_{\text{rep}}) + \varphi_0)}, \tag{2.21}$$

with the pulse-to-pulse phase shift φ_{CEP}, also known as the CEP. When $\varphi_{\text{CEP}} = 0$, the electric fields of all pulses are identical and centered under the envelope.

In the general case with $\varphi_{\text{CEP}} \neq 0$, the electric field slips under the envelope by φ_{CEP} from one
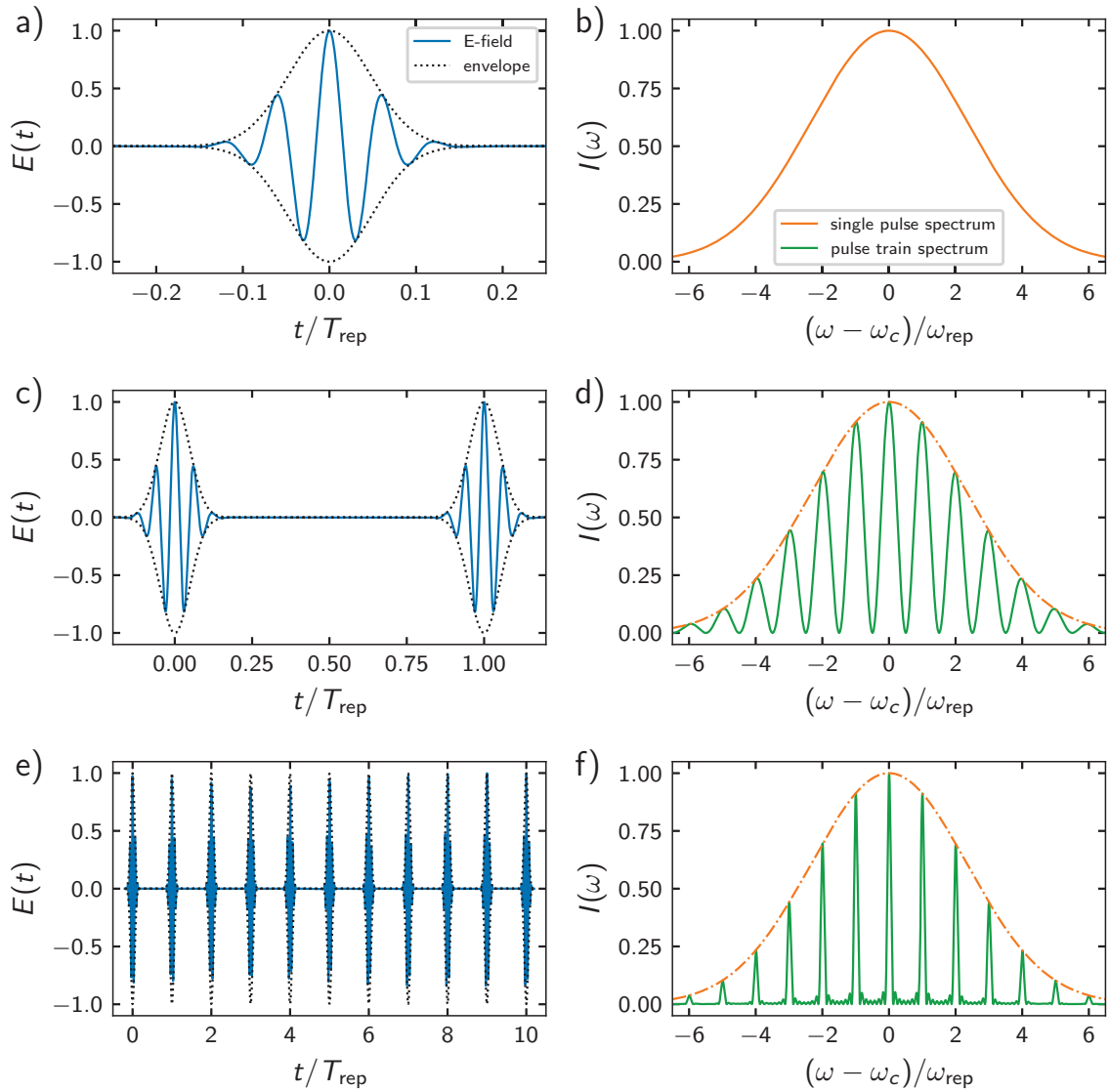
Figure 2.2: A train of ultrashort pulses results in a modulated spectrum. a), c), and e) show the electric field $E(t)$ in blue color and its temporal envelope $\pm A(t)$ with a dotted black line, assuming $\varphi_{\text{CEP}} = 0$. The Fourier transform links the time domain (left column) to the spectral domain (right column). b), d), and f) show the spectrum of the temporal pulses shown in a), c), and e), respectively. a), b) The spectrum of an isolated Gaussian pulse is smooth. c), d) Adding a second pulse in the time domain results in spectral modulation of the intensity distribution at the repetition rate $\omega_{\text{rep}} = 2\pi f_{\text{rep}}$. e), f) A spectrum consisting of a series of equidistant sharp peaks is obtained for a pulse train. Figure adapted from [53].
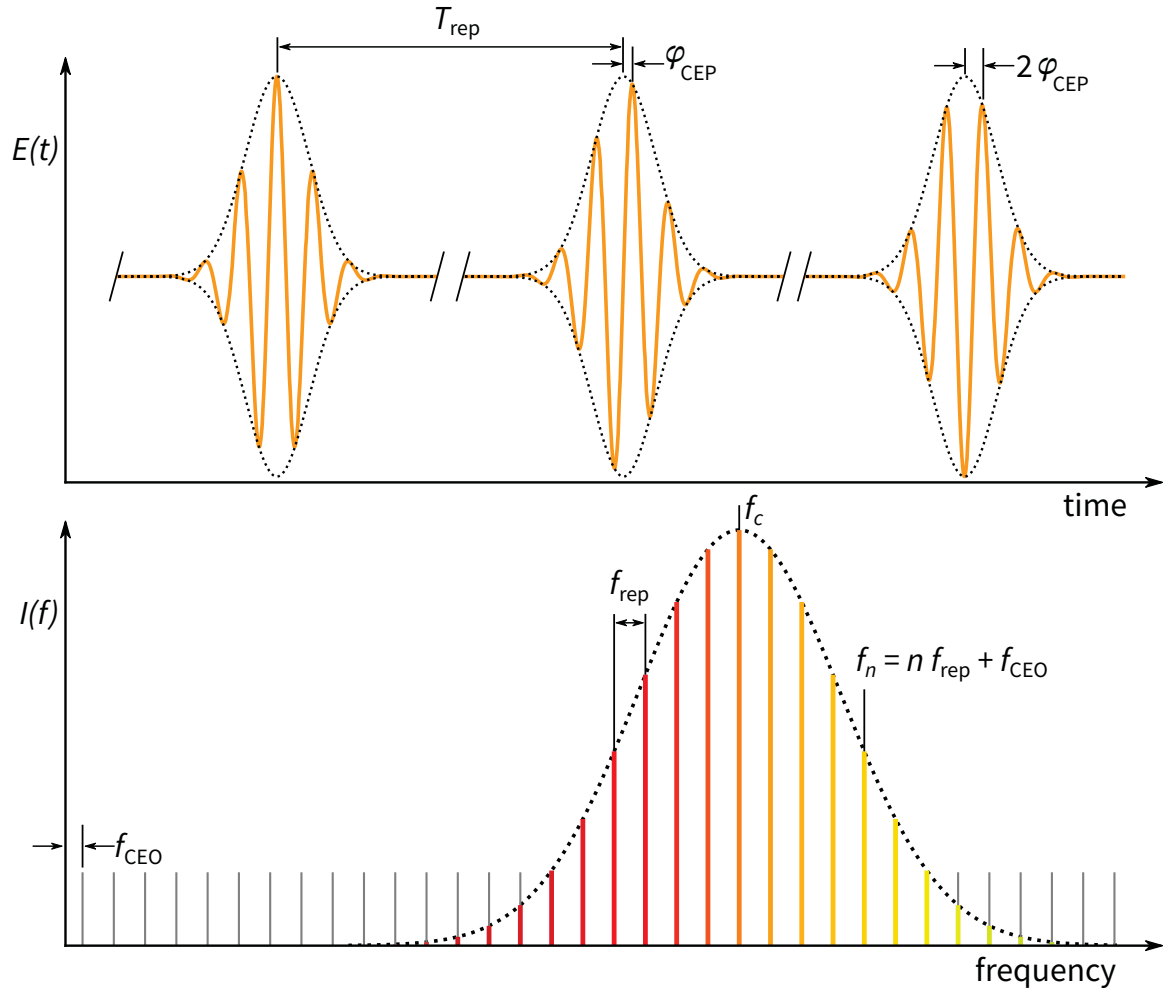
Figure 2.3: Frequency comb schematic in the time (top) and frequency (bottom) domain. Between consecutive pulses, which are spaced by the repetition time $T_{rep} = 1/f_{rep}$, the carrier phase slips under the envelope by φ_{CEP}. The frequency comb spectrum consists of sharp frequency peaks - the comb teeth. The spectral envelope is centered at $f_c = \omega_c/(2\pi)$.

pulse to the next. The Fourier transform of Equation 2.21 yields the spectrum of the pulse train

$$\mathcal{E}_{\text{pt}}(\omega) = \int_{-\infty}^{\infty} \sum_n A(t - nT_{\text{rep}}) \, e^{i(\omega_c t + n(\varphi_{\text{CEP}} - \omega_c T_{\text{rep}}) + \varphi_0)} \, e^{-i\omega t} dt \tag{2.22}$$

$$= e^{i\varphi_0} \sum_n e^{in(\varphi_{\text{CEP}} - \omega_c T_{\text{rep}})} \int_{-\infty}^{\infty} A(t - nT_{\text{rep}}) \, e^{-it(\omega - \omega_c)} \, dt \tag{2.23}$$

$$= e^{i\varphi_0} \sum_n e^{in(\varphi_{\text{CEP}} - \omega_c T_{\text{rep}})} \, e^{-in(\omega - \omega_c)T_{\text{rep}}} \, \mathcal{E}(\omega - \omega_c) \tag{2.24}$$

$$= e^{i\varphi_0} A(\omega - \omega_c) \sum_n e^{in(\varphi_{\text{CEP}} - \omega T_{\text{rep}})}, \tag{2.25}$$

where the identity $\int f(x - a)e^{-i\alpha x}dx = e^{-i\alpha a} \int f(x)e^{i\alpha x}dx$ was used in the second, and the definition of the real spectral envelope was used in the last step.

Figure 2.2 shows an exemplary single pulse temporal field in a) and its spectrum in b). When a second pulse is added, the spectrum is modulated with the inverse repetition time, as shown in c) and d). A pulse train with ten pulses is shown in e) and f), where the modulation produces sharp spectral features.

For an infinitely long pulse train, the Poisson summation formula connects $f(x)$ to its Fourier transform $F(y)$ by

$$\sum_{m=-\infty}^{\infty} f(x - mp) = \sum_{n=-\infty}^{\infty} \frac{1}{p} F(k/p) \, e^{2\pi i n x / p} \,. \tag{2.26}$$

Together with Equation 2.25 and the relation $\int 1 e^{2\pi i a x} dx = \delta(a)$, the frequency comb spectrum is derived

$$\mathcal{E}_{\text{comb}}(\omega) = e^{i\varphi_0} A(\omega - \omega_c) \sum_{n=0}^{\infty} \frac{1}{2\pi} \int_{-\infty}^{\infty} e^{2\pi(\varphi_{\text{CEP}} - \omega T_{\text{rep}} - 2\pi n)} \, e^{-i\omega t} d\omega \tag{2.27}$$

$$= e^{i\varphi_0} A(\omega - \omega_c) \sum_{n=0}^{\infty} \delta(\varphi_{\text{CEP}} - \omega T_{\text{rep}} - 2\pi n). \tag{2.28}$$

It yields a spectrum consisting of sharp lines spaced by f_{rep}. The amplitude of each line is given by the envelope $A(\omega - \omega_c)$ of the single pulse spectrum. With

$$f_{\text{CEO}} = \frac{\varphi_{\text{CEP}}}{2\pi T_{\text{CEP}}}, \tag{2.29}$$

the well-known definition of the frequency comb spectrum is obtained [29, 30, 32, 37]

$$f_n = n f_{\text{rep}} + f_{\text{CEO}}. \tag{2.30}$$

The frequency comb spectrum is illustrated in Figure 2.3

Mode-locking leads to the emission of a train of ultrashort pulses out of a laser oscillator, as shown in Figure 2.1. The measurement and stabilization of the repetition rate, which is typically in the range of 10^6 to 10^9 Hz, is straightforward with standard RF electronics and a feedback loop. Locking the CEP is demanding because f_{CEO} is directly related to the phase of the fast optical carrier frequency, which is way too fast to be directly measured with electronics. Producing a heterodyne beat signal by nonlinear self-referencing of the two ends of the comb spectrum enables measuring and stabilizing f_{CEO} [35, 36]. Frequency doubling the low end of the laser spectrum and interference with the fundamental light at the high-frequency end of the spectrum results in a beat note of

$$2f_n - f_{2n} = 2(n f_{\text{rep}} + f_{\text{CEO}}) - (2n f_{\text{rep}} + f_{\text{CEO}}) = f_{\text{CEO}}. \tag{2.31}$$

The mathematics of this technique are simple but experimentally, optical spectra that span at least one octave (a ratio of the high and low frequency of 2:1) are required [205]. If the femtosecond pulses emitted from the laser oscillator are not already octave-spanning by itself [206–208], spectral broadening needs to be applied [32–34]. Experimentally, an f-to-$2f$ interferometer takes the spectrum as the input and splits it into two arms. A nonlinear crystal is used for SHG in one arm. Then the pulses of both arms are recombined. The interference pattern is detected with a fast photodiode and compared to a reference signal that is phase coherent with the repetition rate. It yields the measured frequency f_{CEO}, which can also be stabilized using a feedback loop.

As described by the frequency comb Equation 2.30, it is sufficient to know the two RF frequencies f_{rep} and f_{CEO} to determine the absolute frequency of each comb tooth. Then, a beat note of the comb with a narrow-linewidth CW laser yields the absolute frequency of the latter. It is also possible to phase-lock several lasers at different frequencies. In this way, the short-time stability of a cavity-referenced ultra-narrowband laser can be transferred to other lasers. For example, the clock laser that is used to probe the clock transition of an optical atomic clock benefits from this short-time stability. Optical atomic clocks have become possible only with the development of the frequency comb because it provides the missing gear between optical and RF frequencies.

After its invention, frequency comb laser sources quickly became more accessible. Nowadays, they are not only used in metrology for absolute frequency determination and phase-locking of lasers [29, 30, 37–39] but also for laser ranging [41], astrophysics [42], and dual-comb molecular spectroscopy [40]. Because they offer the benefit of emitting coherent and phase-stable pulse trains, they can be enhanced in passive cavities to reach very high intra-cavity intensities.

2.3 Optical resonators

When free space is confined by impenetrable barriers, as in the 'particle in a box' problem in quantum mechanics, only a discrete set of energy values and wavenumbers are allowed inside the system. It is the same for an optical cavity resonator, where light is confined in well-defined longitudinal and transversal modes between highly reflective mirrors, which form the potential barrier. In the case of an optical cavity, only these distinct frequency modes are resonant and oscillate with much greater amplitude than all other (nonresonant) frequencies. Depending on the desired application of the enhancement cavity, specific aspects of the geometrical design must be considered. The theory behind enhancement cavities will be explored in this chapter, starting with the geometric design.

2.3.1 Gaussian beam propagation by ABCD-matrix formalism

The propagation of light rays through optical elements and systems can be treated with the ABCD-matrix formalism. However, wave optics are needed to describe the geometric properties of laser resonators. The resonator acts as a waveguide, and not only the fundamental transverse electromagnetic mode TEM_{00}, but also higher-order modes can be resonant [209, 210]. In cylinder-symmetric systems, such as optical fiber (lasers), Laguerre-Gaussian modes denoted as TEM_{pl} are typically well suited. There, the transverse mode pattern is described by a combination of a Gaussian beam profile with a Laguerre polynomial of order p and index l. On the contrary, systems with rectangular symmetry, such as typical free-space laser resonators, are well described by Hermite-Gaussian modes TEM_{mn}. The indices m and n are the horizontal and vertical orders of the pattern, i.e. the number of nodes. The fundamental TEM_{00} mode is identical for both descriptions as Laguerre-Gaussian and Hermite-Gaussian modes.

The TEM$_{00}$ mode follows the paraxial approximation and can therefore be modeled by the ABCD-matrix formalism [211, 212]. For these calculations, it is convenient to use the complex beam parameter $q(z)$ (also named complex radius)

$$\frac{1}{q(z)} = \frac{1}{R(z)} - i\frac{\lambda}{\pi w^2(z)}, \tag{2.32}$$

with the beam radius $w(z)$, where the transversal intensity has dropped to $1/e^2$ of its maximum

$$w(z) = w_0\sqrt{1 + \frac{z^2}{z_R^2}}, \tag{2.33}$$

with a minimum waist size w_0. The radius of curvature of the wavefronts is given by

$$R(z) = z + \frac{z_R^2}{z}, \tag{2.34}$$

with the Rayleigh range

$$z_R = \frac{\pi w_0^2}{\lambda}. \tag{2.35}$$

The beam radius does not change much within the Rayleigh range, and the wavefronts are almost flat. The divergence in the far-field is given by $\Theta_{div} = w_0/z_R$. Far away from the beam waist, the beam radius and the radius of the phase fronts increase linear with the distance from the waist. Furthermore, the Gouy phase φ_G describes the phase shift of a focused Gaussian laser beam in the propagation direction z

$$\varphi_G = -\arctan\left(\frac{z}{z_R}\right), \tag{2.36}$$

compared to the shift of an unfocused plane wave with the same frequency [213].

A ray-transfer ABCD-matrix of the whole optical system can be defined as

$$M_{\text{tot}} = \begin{pmatrix} A & B \\ C & D \end{pmatrix}. \tag{2.37}$$

It is obtained by matrix multiplication of all n elements of the optical system

$$M_{\text{tot}} = M_n M_{n-1} \dots M_1. \tag{2.38}$$

The ABCD-matrix of the system transforms the complex q-parameter by multiplication with the matrix components A, B, C and D of M_{tot} [214]

$$q_{\text{out}} = \frac{Aq_{\text{in}} + B}{Cq_{\text{in}} + D}. \tag{2.39}$$

The ray matrices for common optical elements can be found in literature [215], and the most relevant matrices are listed in Table 2.1. For an intuitive understanding of the influence of the individual matrix entries, it is helpful to consider what effect the ray transfer matrix has on an incoming ray with position x_{in} and angle θ_{in} when these parameters are set to zero. If component A is zero, x_{out} is independent of x_{in}. Therefore, the incident rays undergo parallel-to-point focusing. If $B = 0$, the system images an object by point-to-point focusing with the magnification A, because $x_{\text{out}} = Ax_{\text{in}}$ is independent of the input angle θ_{in}. Components C and D describe parallel-to-parallel (telescope) and point-to-parallel imaging (collimation), respectively.

For stable cavity operation, the q-parameter must not change after transformation with the ABCD-matrix of the whole cavity M_{cav}, since the beam has to reproduce itself after each round

Optical element	ABCD matrix
Free space (refractive index n)	$\begin{pmatrix} 1 & z/n \\ 0 & 1 \end{pmatrix}$
Thin lens (focal length f)	$\begin{pmatrix} 1 & 0 \\ -1/f & 1 \end{pmatrix}$
Curved mirror, tangential plane (radius of curvature R, angle of incidence θ)	$\begin{pmatrix} 1 & 0 \\ -2/(R\cos(\theta)) & 1 \end{pmatrix}$
Curved mirror, sagittal plane (radius of curvature R, angle of incidence θ)	$\begin{pmatrix} 1 & 0 \\ -2\cos(\theta)/R & 1 \end{pmatrix}$

Table 2.1: Most important ABCD ray transfer matrices used in this work. Replacing the focal length of the lens by $f = R/2$, yields the matrix for a curved mirror with zero angle of incidence θ and the lower three entries become equal. In the convention used here, R is negative for concave mirrors. Cylindrical elements can be treated by performing separate transformations for each transverse direction.

trip in order to sustain a stable mode. From this fact, a stability criterion can be derived from the trace of M_{cav} [211]

$$0 < \frac{A+D}{2} < 1. \tag{2.40}$$

From an experimental perspective, at least one concave mirror is needed in a stable cavity to fulfill this condition.

For the graphical representation of the stability criterion for two-mirror resonators, it is helpful to define the so-called g-parameters $g_1 = 1 - d/R_1$ and $g_2 = 1 - d/R_2$, where d is the curved mirror distance, and R_1 and R_2 are the radii of curvature. With that, Equation 2.40 can be rewritten in terms of the g-parameter 2.41

$$0 \le g_1 g_2 \le 1. \tag{2.41}$$

Figure 2.4 illustrates different regimes of two-mirror cavities. Here, the g-parameters form the coordinate axes, and stable resonators are located within the color-shaded area bounded by the line $g_1 g_2 = 1$.

In practice, laser resonators often consist of more than two mirrors, producing a folded cavity design. Using two focusing elements, a cavity can be constructed in different geometries, such as a (folded) concave-concave linear cavity, a triangular ring cavity with two concave mirrors and one flat mirror, or a bow-tie ring cavity. A ring (i. e. traveling-wave) cavity offers the advantage of a single interaction of the light with a target every round trip, which is essential for the efficient use of high-harmonics. Additionally, it offers easy access to the reflected light and even allows to independently send light into both propagation directions (clockwise vs. anti-clockwise) of the cavity. Usually, a pair of curved mirrors form a confocal section and a quasi-collimated long arm. In all of these geometries except the linear layout, the tangential plane needs to be treated separately from the sagittal plane because of non-zero angles of incidence at the curved optics. The bow-tie ring cavity offers the best possibilities to manipulate the cavity mode for astigmatism compensation [216].

A stability zone can be defined as the range of focusing mirror distances where the stability criterion is fulfilled. Bow-tie cavities have a single stability zone for each plane, and the mode radii diverge at both edges of it. However, only at one of the edges the alignment sensitivity also diverges, whereas it reaches a minimum on the other stability edge [216]. Stable cavity operation
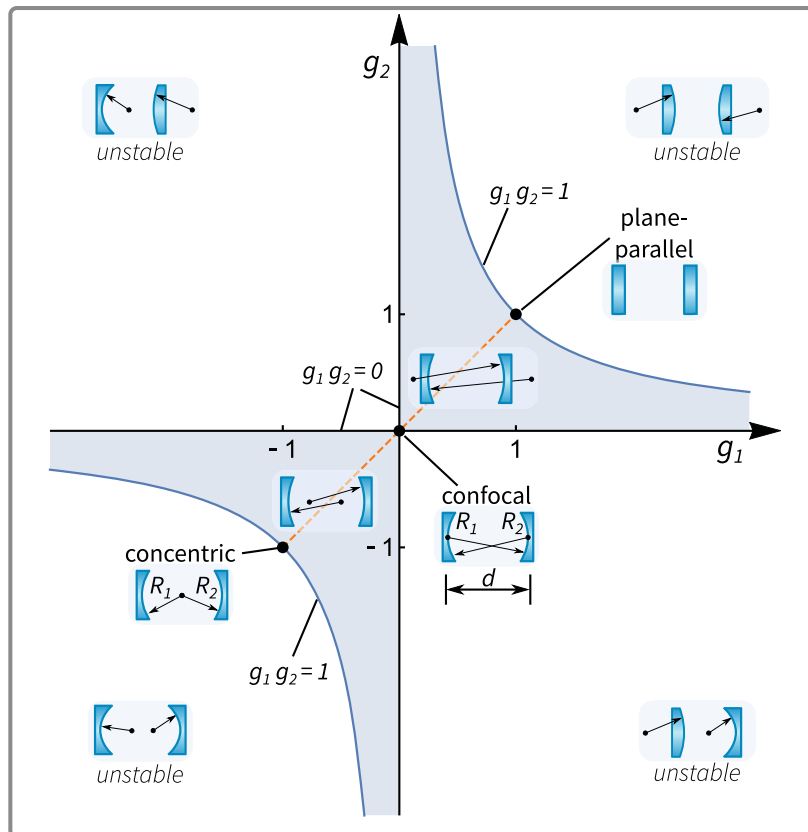
Figure 2.4: Schematic cavity stability diagram for two-mirror linear cavities. According to Equation 2.41, stable resonators are located within the colored area. Symmetrical resonators are located on the orange diagonal line. Insets illustrate main cavity geometries, where small arrows indicate the mirror's radii of curvature R. The angle of the arrows is for illustration only and has no physical relevance. Three famous geometries are concentric ($R_1 = R_2 = d/2$), confocal ($R_1 = R_2 = d$), and plane-parallel ($R_1 = R_2 = \infty$). Adding flat mirrors and unfolding the linear cavity to a ring cavity does not change the basic concept, and the stability criterion must still be fulfilled. Graphical representation inspired by [211].

is possible in the region where the tangential and sagittal curves overlap. The smallest possible waist size can be achieved by moving to the edge of the stability region. However, astigmatism is increased there.

2.3.2 Field and energy relations in optical resonators
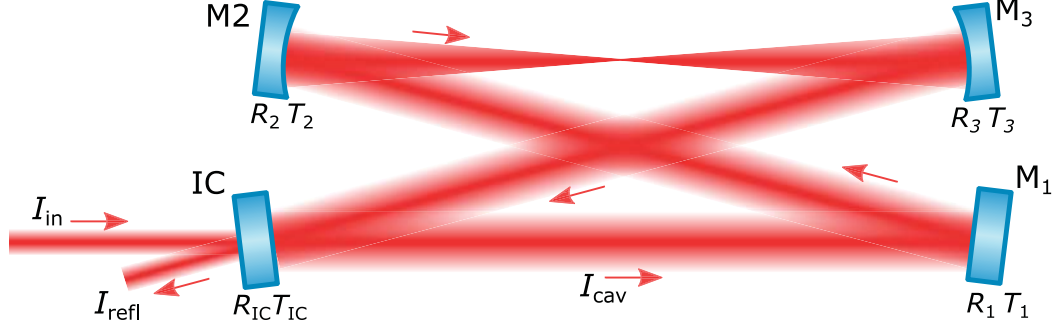
Figure 2.5: Schematic representation of a four mirror bow-tie ring resonator with mirror reflectivity and transmission coefficients R_n and T_n, respectively. Light with intensity I enters the resonator through the input-coupler mirror (IC) and is guided by high-reflective mirrors M_n. M_2 and M_3 are curved to focus the light to a small spot and are necessary to establish a stable resonator (cf. Section 2.3.1).

In this subsection, the relations for the electric field and the energy in an optical cavity are derived, building upon the treatments of C. Benko, N. Hodgson, W. Nagourney, J. Nauta, and D. C. Yost [53, 209, 217–219]. A typical geometry for an optical enhancement cavity is the bow-tie cavity with three high reflection (HR) mirrors plus one partially transmissive input coupler (IC) mirror aligned in a ring configuration, as shown schematically in Figure 2.5. The amplitude of the electric field in the spectral domain is given by $E(\omega)$ and is linked to the intensity $I(\omega) = |E(\omega)|^2$. The intensity reflectivity and transmission coefficients of mirror i are given by $R_i(\omega) = r_i(\omega)^2$ and $T_i(\omega) = t_i(\omega)^2$, respectively. $r_i(\omega)$ and $t_i(\omega)$ are the field reflectivity and transmission, respectively. For better readability, the explicit writing out of the ω dependence is omitted in the following. With these definitions, the intra-cavity field changes each round trip n according to

$$E_{\text{cav}, n+1} = t_{\text{ic}}E_{\text{in}} + r_{\text{cav}}E_{\text{cav}, n}e^{i\phi_{\text{cav}}}, \tag{2.42}$$

with an incident electric field E_{in} and the fraction of the electric field remaining in the cavity after one round trip r_{cav}. The latter includes the combined transmission losses of the cavity mirrors $T_{\text{tot}} = 1 - \prod_n R_n$ and all other losses due to scattering and absorption, but it excludes IC mirror transmission. The spectral phase acquired in one round trip is denoted as ϕ_{cav}. It results from the propagation distance and (mirror) dispersion ϕ_d

$$\phi_{\text{cav}} = kL + \phi_d, \tag{2.43}$$

with the wave number $k = \omega/c = 2\pi/\lambda$ and the cavity path length L. Contributions from nonlinearities and ionization-induced plasma effects are not included at this point. These intensity-dependent effects act on the temporal phase and are considered in Section 4.1.5. The effective cavity reflectivity r_{cav} allows us to write the intra-cavity circulating field as a coherent superposition of several round trips in a geometric series

$$E_{\text{cav, circ}} = E_{\text{in}}t_{\text{ic}}\left(1 + r_{\text{ic}}r_{\text{cav}}\,e^{i\phi_{\text{cav}}} + \left(r_{\text{ic}}r_{\text{cav}}\,e^{i\phi_{\text{cav}}}\right)^2 + \dots\right)$$

$$= E_{\text{in}}\frac{t_{\text{ic}}}{1 - r_{\text{ic}}r_{\text{cav}}\,e^{i\phi_{\text{cav}}}}. \tag{2.44}$$

The expression for the intra-cavity intensity is obtained by using the relation $\cos(\phi) = 1 - 2\sin^2(\phi/2)$

$$I_{\text{cav, circ}} = |E_{\text{cav, circ}}|^2 = I_{\text{in}} \frac{t_{\text{ic}}^2}{\left(1 - r_{\text{ic}}r_{\text{cav}}\right)^2 + 4r_{\text{ic}}r_{\text{cav}}\sin^2\left(\phi_{\text{cav}}/2\right)}. \tag{2.45}$$

The terms for the field and intensity of the reflected light are obtained in a similar way and are given by

$$E_{\text{cav, refl}} = E_{\text{in}} \frac{r_{\text{cav}}\,e^{i\phi_{\text{cav}}} - r_{\text{ic}}}{1 - r_{\text{ic}}r_{\text{cav}}\,e^{i\phi_{\text{cav}}}}, \tag{2.46}$$

and

$$I_{\text{cav, refl}} = I_{\text{in}} \frac{\left(r_{\text{ic}} - r_{\text{cav}}\right)^2 + 4r_{\text{ic}}r_{\text{cav}}\sin^2\left(\phi_{\text{cav}}/2\right)}{\left(1 - r_{\text{ic}}r_{\text{cav}}\right)^2 + 4r_{\text{ic}}r_{\text{cav}}\sin^2\left(\phi_{\text{cav}}/2\right)}. \tag{2.47}$$

Efficient coupling of incident light into the cavity can be achieved if the electric fields of the incident and circulating light interfere constructively at the IC mirror. To enhance a train of ultrashort pulses in a cavity, not only intra-cavity dispersive (and nonlinear) effects but also the pulse-to-pulse time delay and CEP slip $\Delta\phi_{\text{CEP}}$ of the incident pulses need to be considered. To simplify the expressions, dispersive and nonlinear (phase) effects are not considered in the rest of this subsection but are discussed in more detail in Section 2.3.3 and 2.7.3. As shown in Equa-
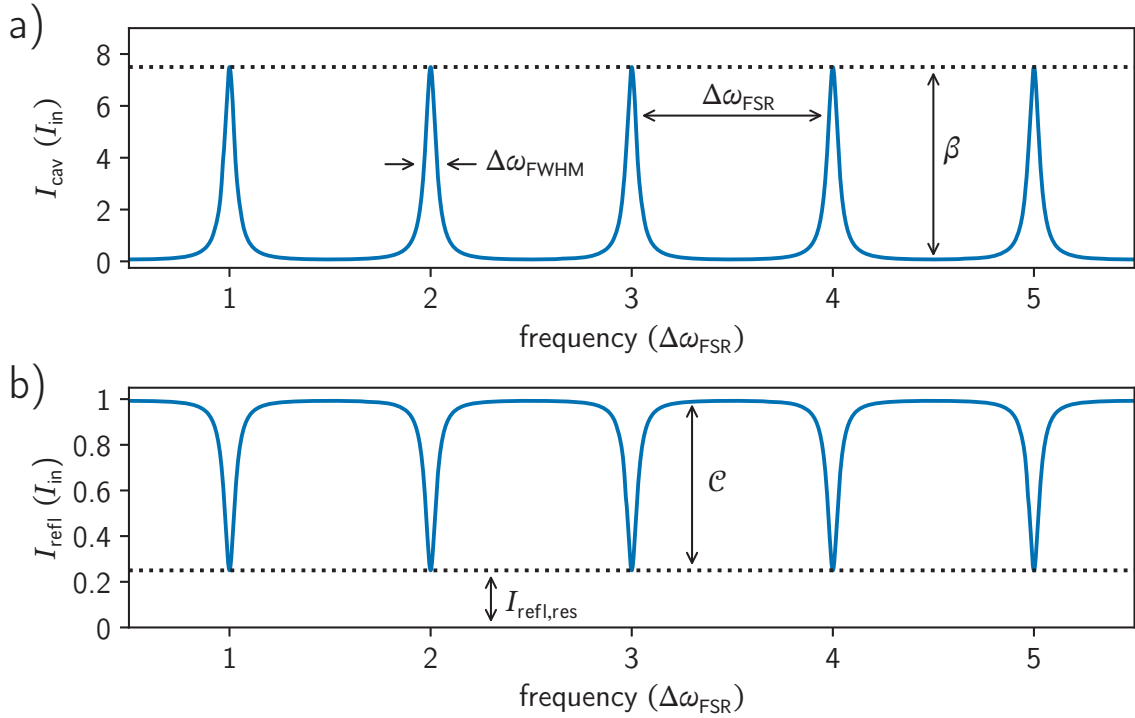
Figure 2.6: Cavity resonances as a function of frequency, with $R_{\text{ic}} = 0.7$, $R_{\text{cav}} = 0.9$ and ideal mode-matching ($\varepsilon = 1$). a) At resonance, the intra-cavity intensity is enhanced by a factor of β within the cavity line-width $\Delta\omega_{\text{FWHM}}$. Resonances are separated by the FSR. b) The cavity contrast $\mathcal{C}$ is the depth ratio of the resonance dips. It becomes optimal in the mode- and impedance-matched case, when the reflected intensity at resonance $I_{\text{refl,res}}$ vanishes. Figure adapted from [53].

tion 2.45 and 2.53, the intra-cavity and reflected intensities are periodic functions of ϕ_{cav}. The resonance condition is met when the cavity round-trip phase accumulates to an integer multiple

of 2π. This yields the free spectral range (FSR) $\Delta\omega_{\text{FSR}}$, which is the frequency spacing between adjacent cavity resonances

$$\Delta\omega_{\text{FSR}} = \frac{2\pi c}{L}. \tag{2.48}$$

From Equation 2.45 and under the assumption of a low-loss cavity ($\phi_{\text{cav,FWHM}} \ll \pi$), the line width of the cavity defined as the FWHM of the intensity resonance peaks is given by

$$\Delta\omega_{\text{FWHM}} = \frac{2(1 - r_{\text{ic}}r_{\text{cav}})}{\sqrt{r_{\text{ic}}r_{\text{cav}}}} \frac{c}{L}. \tag{2.49}$$

With this, the cavity finesse $\mathcal{F}$, which is a measure of the cavity quality factor, is defined as the ratio of the cavity FSR to the FWHM of the intensity resonances

$$\mathcal{F} = \frac{\Delta\omega_{\text{FSR}}}{\Delta\omega_{\text{FWHM}}} = \frac{\pi\sqrt{r_{\text{ic}}r_{\text{cav}}}}{1 - r_{\text{ic}}r_{\text{cav}}}. \tag{2.50}$$

Assuming small mirror transmissions $T_{\text{ic}} = 1 - R_{\text{ic}} \ll 1$, $T_{\text{cav}} = 1 - R_{\text{cav}} \ll 1$ and plugging it in Equation 2.50 simplifies the expression to

$$
\begin{aligned}
\mathcal{F} &= \frac{\pi\sqrt[4]{R_{\text{ic}}R_{\text{cav}}}}{1 - \sqrt{R_{\text{ic}}R_{\text{cav}}}} && (\sqrt[4]{R} \approx 1,\ T_{\text{ic}}T_{\text{cav}} \approx 0), \\
&\approx \frac{\pi}{1 - \sqrt{1 - (T_{\text{ic}} + T_{\text{cav}})}} && (\sqrt{1-x} \approx 1 - \frac{x}{2} + ...), \\
&\approx \frac{2\pi}{T_{\text{ic}} + T_{\text{cav}}}.
\end{aligned}
\tag{2.51}
$$

The finesse is inversely proportional to the IC transmission and the combined total losses of the cavity. The consequence of this is that high finesse can be achieved at high mirror reflectivities and minimized losses, leading to intra-cavity intensity enhancement at resonance. For illustration, resonances are plotted in Figure 2.6 for an exemplary cavity with rather low mirror reflectivities of $R_{\text{ic}} = 0.7$ and $R_{\text{cav}} = 0.9$. Typically, reflectivities are much higher for any real enhancement cavity ($R_{\text{ic}} > 0.95$, $R_{\text{cav}} > 0.99$) resulting in much higher and narrower resonance features.

The enhancement factor β provides a measure for the intra-cavity intensity enhancement. It is defined as the ratio of intra-cavity to incident laser intensity at resonance, where $\phi_{\text{cav}} = 0$

$$\beta = \frac{I_{\text{cav,circ}}}{I_{\text{in}}} = \frac{t_{\text{ic}}^2}{\left(1 - r_{\text{ic}}r_{\text{cav}}\right)^2 + 4r_{\text{ic}}r_{\text{cav}}\sin^2\phi_{\text{cav}}/2} \approx \frac{4T_{\text{ic}}}{(T_{\text{ic}} + T_{\text{cav}})^2} = \frac{T_{\text{ic}}\mathcal{F}^2}{\pi^2}. \tag{2.52}$$

While the cavity enhancement is maximal at resonance, the reflected intensity becomes minimal

$$I_{\text{cav, refl}} \overset{\phi_{\text{cav}}=0}{=} I_{\text{in}} \frac{\left(r_{\text{ic}} - r_{\text{cav}}\right)^2}{\left(1 - r_{\text{ic}}r_{\text{cav}}\right)^2} \approx I_{\text{in}} \frac{4\left(T_{\text{ic}} - T_{\text{cav}}\right)^2}{\left(T_{\text{ic}} + T_{\text{cav}}\right)^2}. \tag{2.53}$$

It vanishes for the impedance-matched case when the input-coupler transmission equals the combined losses in the rest of the cavity ($T_{\text{ic}} = T_{\text{cav}}$). Starting from the impedance-matched case, the enhancement factor β is not very sensitive to slight variations of the input-coupler transmission, and a change of a factor of two modifies the intra-cavity intensity typically only by about 10 % [218].

Placing an element in the cavity, such as a nonlinear medium (e. g. a crystal or HHG gas target) or adding mirror dispersion results in modification of the intra-cavity phase ϕ_{cav}. This spectrally

dependent phase limits the enhancement of femtosecond laser pulses because then only a fraction of the spectrum can be resonant at the same time [109]. To minimize this spectral-filtering effect, the finesse can be reduced by increasing the IC transmission (instead of introducing losses elsewhere) [217]. If the net cavity loss is dominated by the IC transmission, the cavity is operated in the so-called over-coupled regime. Compared to the impedance-matched case with $\beta \approx \mathcal{F}/\pi$, it offers the advantage of twice the enhancement ($\beta \approx 2\mathcal{F}/\pi$) [109]. It is a counterintuitive result that reducing the finesse by lowering the IC reflectivity minimizes spectral filtering and thus maximizes the attainable intra-cavity intensity for non-CW light.

Even for a perfectly impedance-matched cavity without any additional losses or dispersion, light is still reflected if the incoming light is not mode-matched. This means that the incident light needs to spatially overlap the (fundamental) cavity mode, implying that the beam size and divergence match. This overlap is quantified by the mode-matching factor ϵ, providing a measure for the fraction of reflected light at the IC, which effectively reduces the attainable intra-cavity intensity by lowering the enhancement

$$\beta_\epsilon = \epsilon \frac{I_{\text{cav,circ}}}{I_{\text{in}}} = \epsilon T_{\text{ic}} \frac{\mathcal{F}^2}{\pi^2}. \tag{2.54}$$

The enhancement can be determined experimentally by measuring the light leaking through one of the cavity mirrors with a photodiode. To account for the mirror reflectivity of this cavity mirror, the IC mirror is temporarily removed, and the photodiode signal is recorded for a known incident laser power. Re-inserting the IC closes the cavity again, and the enhancement factor is directly obtained from the increase of the photodiode signal, i. e. $\beta_\epsilon = P_{\text{resonant cavity}}/P_{\text{open cavity}}$. Including the mode-matching factor into Equation 2.53 yields the total reflected intensity

$$I_{\text{refl, total}} = \epsilon I_{\text{cav, refl}} + (1 - \epsilon) I_{\text{in}}. \tag{2.55}$$

Consequently, it is useful to define the cavity contrast $\mathcal{C}$ as

$$\mathcal{C} = \frac{I_{\text{in}} - I_{\text{refl, total}}}{I_{\text{in}}} = \epsilon \left(1 - \left((T_{\text{cav}} - T_{\text{ic}}) \frac{\mathcal{F}}{2\pi} \right)^2 \right), \tag{2.56}$$

which can be measured by recording the reflected intensity on- and off-resonance with a photodiode. It describes how much of the incident light is coupled into the cavity.

The parameters $\mathcal{F}$, $\mathcal{C}$ and β are suitable to characterize the cavity. However, the latter two depend on the mode-matching factor ϵ, which is not a property of the cavity itself but depends on the properties of the incident beam. Therefore, the cavity finesse is the best parameter to compare cavities. A direct method to measure the finesse is rapidly switching off the laser with a fast switch, such as an acousto-optical modulator or a pockels-cell with a polarizer when the cavity is at resonance. In both cases, the light stored in the cavity leaks out through the cavity mirrors with a time constant τ_{cav}. The intra-cavity intensity decays by

$$I_{\text{cav, circ}}(t) = I_0 \exp\left(-t/\tau_{\text{cav}}\right) = I_0 \exp\left(-tL/(c\mathcal{L})\right). \tag{2.57}$$

The decay time is given by the total intensity loss per round trip $\mathcal{L} = T_{\text{ic}} + T_{\text{cav}}$. Using the definition of the finesse given in Equation 2.50, the above expression simplifies to

$$\mathcal{F} = 2\pi\tau_{\text{cav}} c/L. \tag{2.58}$$

Alternatively, this so-called ring-down measurement can be performed by scanning the laser frequency at a much higher rate than the cavity lifetime, i.e. $f_{\text{scan}} \gg 1/\tau_{\text{cav}}$. On resonance, interference between the fixed-frequency light leaking out of the cavity and the variable-frequency

reflected light leads to a heterodyne beat note [220]. It can be detected by recording the reflected light with a fast photodiode and fitting a damped cosine to the signal [53, 219]. Such a measurement of the finesse is shown in Figure 4.9 in Section 4.1.3. The mode-matching factor ϵ is obtained by plugging the measured value of $\mathcal{F}$ into Equation 2.54 and comparing it with the measured value of β_ϵ.

2.3.3 Femtosecond enhancement cavities
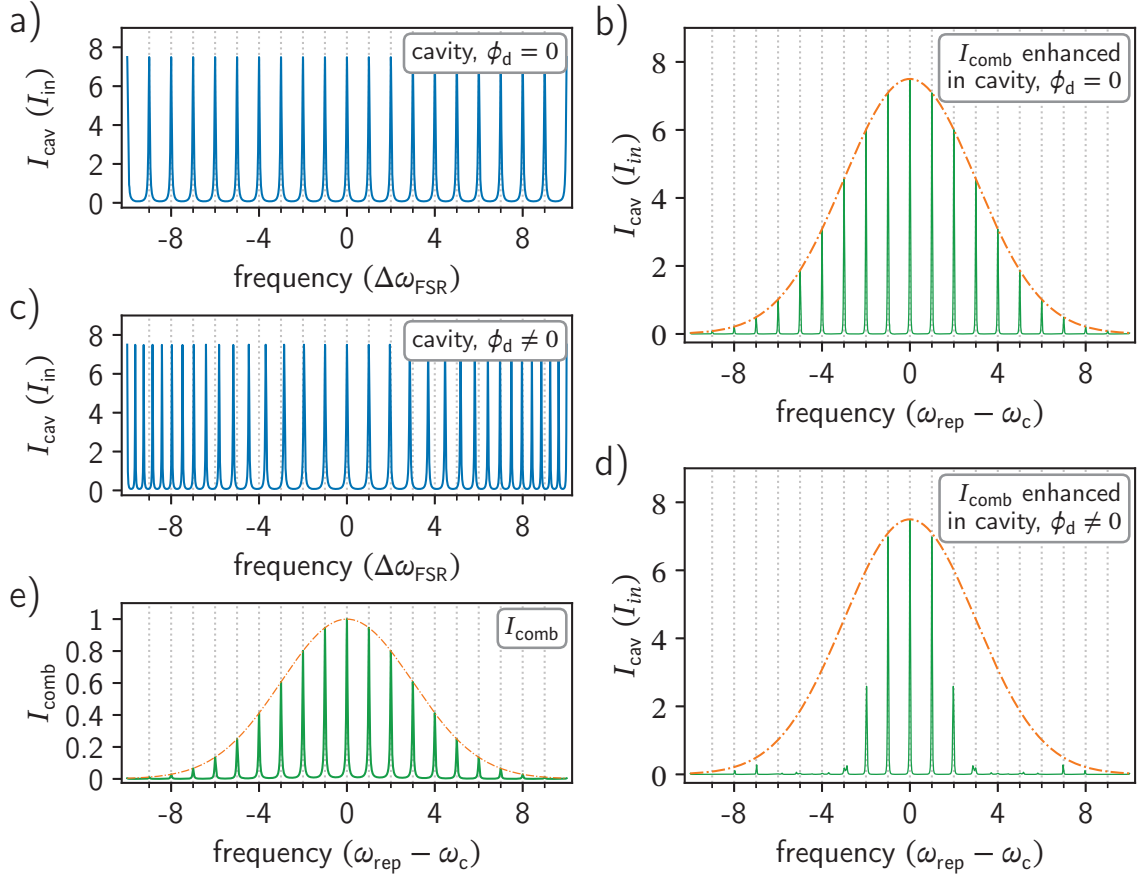
Figure 2.7: Dispersion reduces the achievable intra-cavity intensity enhancement of a frequency comb. a) Cavity resonances of the same cavity as in Figure 2.6 with $R_{ic} = 0.7$, $R_{cav} = 0.9$ and $\epsilon = 1$. c) Adding dispersion to the cavity, shifts the resonance positions and the frequency spacing is no longer constant. e) A normalized frequency comb spectrum ($\omega_{rep} = \Delta\omega_{FSR}$, $\omega_{CEO} = 0$) is used as the input for both cavities. The central frequency comb mode at ω_c is enhanced in both situations ($\beta = 7.5$), but the whole spectrum is only enhanced in the cavity without dispersion, as shown in b). d) The mismatch of comb modes and cavity resonances in the dispersive cavity leads to narrowing of the intra-cavity spectrum and thus a reduced total intensity.

Dispersion in an enhancement cavity causes the cavity FSR to vary as a function of frequency, limiting the spectral bandwidth of the pulses that can be enhanced [83, 221]. This effect is illustrated in Figure 2.7. When sending laser pulses of a frequency comb with a spectrum, shown in Figure 2.7 e), to an enhancement cavity without any dispersion, and thus, equally spaced resonances, as shown in a), the whole spectrum is enhanced, as shown in b). Adding (strong) dispersion to the cavity round-trip phase shifts the resonance positions, as shown in c). This results

in spectral narrowing of the enhanced spectrum, which is shown in d). The further the comb lines are away from the central frequency ω_c, the worse the enhancement gets. Therefore, cavity dispersion should be minimized to reach maximum enhancement of the full spectral bandwidth [222].
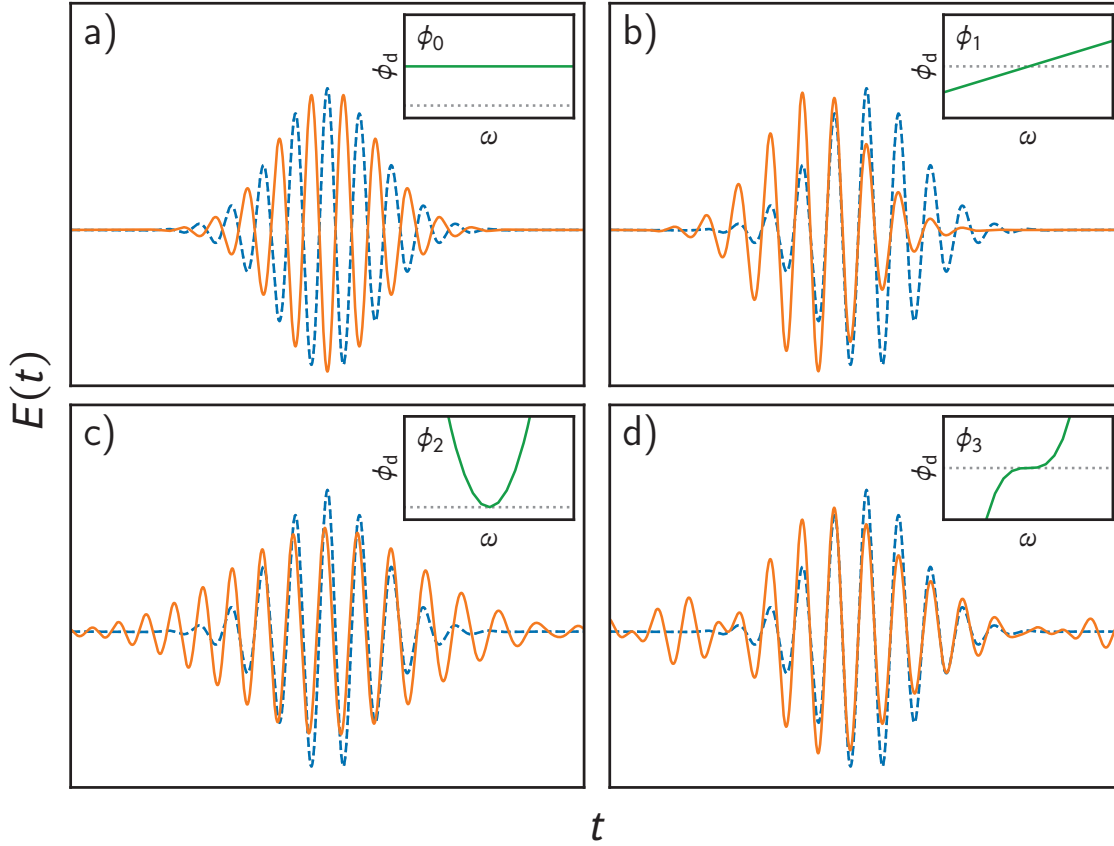
Figure 2.8: The individual dispersion orders, as defined in Equation 2.59, modify the (temporal) shape of a short laser pulse differently. The blue dotted line shows a ten-cycle ultrashort laser pulse without dispersion. The spectral phase $\phi_d(\omega)$ modifies the electric field in the spectral domain resulting in a modified (temporal) electric field $E(t)$, drawn as a solid orange line. a)-d) show the pulse after adding the individual dispersion terms ϕ_0 to ϕ_3. The insets show the resulting spectral phase of the corresponding component.

In the previous section, the field and intensity relations of enhancement cavities were derived for CW light by setting dispersive or nonlinear effects to zero. By starting from Equation 2.43, we now add dispersion in the form of a phase contribution to the cavity round-trip phase $\phi_{cav} = kL + \phi_d$. Expanding ϕ_d in a Taylor series around the central comb frequency ω_c leads to

$$\phi_d = \underbrace{\phi_0}_{\text{PS}} + \underbrace{\phi_1 (\omega - \omega_c)}_{\text{GD}} + \underbrace{\frac{1}{2!}\phi_2 (\omega - \omega_c)^2}_{\text{GDD}} + \underbrace{\frac{1}{3!}\phi_3 (\omega - \omega_c)^3}_{\text{TOD}} + \dots, \qquad (2.59)$$

with each dispersion order affecting the intra-cavity laser pulse differently. The effect of each of the dispersion orders on the electric field of an initially unchirped ultrashort laser pulse is the following:

PS The first term ϕ_0 causes a phase-shift (PS) of the electric field relative to the envelope without affecting the envelope position, as shown in Figure 2.8 a). This behavior can be

accounted for by matching the CEP of the driving frequency comb to the round-trip phase, such that $\phi_0 = \omega_c/\omega_{rep}$. Then, the pulse-to-pulse phase-slip of the circulating intra-cavity pulse and the incident pulses are balanced. In this way, interference at the IC mirror stays constructive even after multiple round trips. In the spectral domain, this corresponds to a uniform frequency shift of all cavity and comb modes.

GD The second term ϕ_1, known as the group delay (GD) and shown in Figure 2.8 b), delays the envelope in time without changing the CEP. It acts as an effective change of the cavity-path length, which can be accounted for by adapting the repetition rate of the comb.

GDD The third term ϕ_2, known as group-delay dispersion (GDD), symmetrically broadens the pulse in time and leads to a chirp, which is shown in Figure 2.8 c). It is a quantitative measure for the frequency dependence of the phase velocity and describes the phase shift of each spectral component of the circulating pulse after one round trip.

TOD Third-order dispersion (TOD), as shown in Figure 2.8 d), and higher-order dispersion (HOD) cause the pulse to broaden temporarily in more complex ways.

Recalling Equation 2.43 and the fact that the phase shift between the circulating pulse and the incident pulses needs to be a multiple of 2π after one round trip yields the resonance condition

$$2\pi n_{cav} = \phi_{cav} = \frac{\omega L}{c} + \phi_d, \tag{2.60}$$

with an integer n_{cav} indexing the enhancement cavity mode. Using the definition of the frequency comb spectrum (cf. Equation 2.30) and solving for the mode number n_{comb} gives

$$n_{comb} = \frac{\omega - \omega_{CEO}}{\omega_{rep}}. \tag{2.61}$$

Using Equation 2.60 and 2.61, the mode numbers of the comb are related to those of the cavity by

$$p = n_{cav} - n_{comb} \tag{2.62}$$

$$= \frac{\omega L}{2\pi c} + \frac{\phi_d}{2\pi} - \frac{\omega - \omega_{CEO}}{\omega_{rep}}, \tag{2.63}$$

where p is an integer labeling the resonance fringe [53, 222, 223]. Solving for $L(\omega)$ yields the cavity length, where the comb frequencies ω are resonant

$$L(\omega) = \frac{2\pi c}{\omega_{rep}} - \frac{2\pi c}{\omega}\left(\frac{\omega_{CEO}}{\omega_{rep}} - p\right) - c\frac{\phi_d}{\omega}. \tag{2.64}$$

For the simplified situation without dispersion $\phi_d = 0$ and nonlinearities and with zero offset frequency of the comb $\omega_{CEO} = 0$, all frequencies are resonant when the enhancement cavity length L matches the cavity length of the frequency comb laser $L_{comb} = 2\pi c/\omega_{rep}$, as shown in Figure 2.9. In this case, maximum amplification is achieved at $p = 0$.

Adding second-order dispersion (group-delay dispersion (GDD)) to the cavity round trip phase causes a quadratic curvature of the central fringe ($L_{cav} = L_{comb}$) in the resonance map. As a result, only a fraction of the whole spectrum can be simultaneously resonant, as indicated by the vertical lines in Figure 2.10, and the maximum attainable enhancement is decreased compared to the cavity without dispersion.

a)

b)
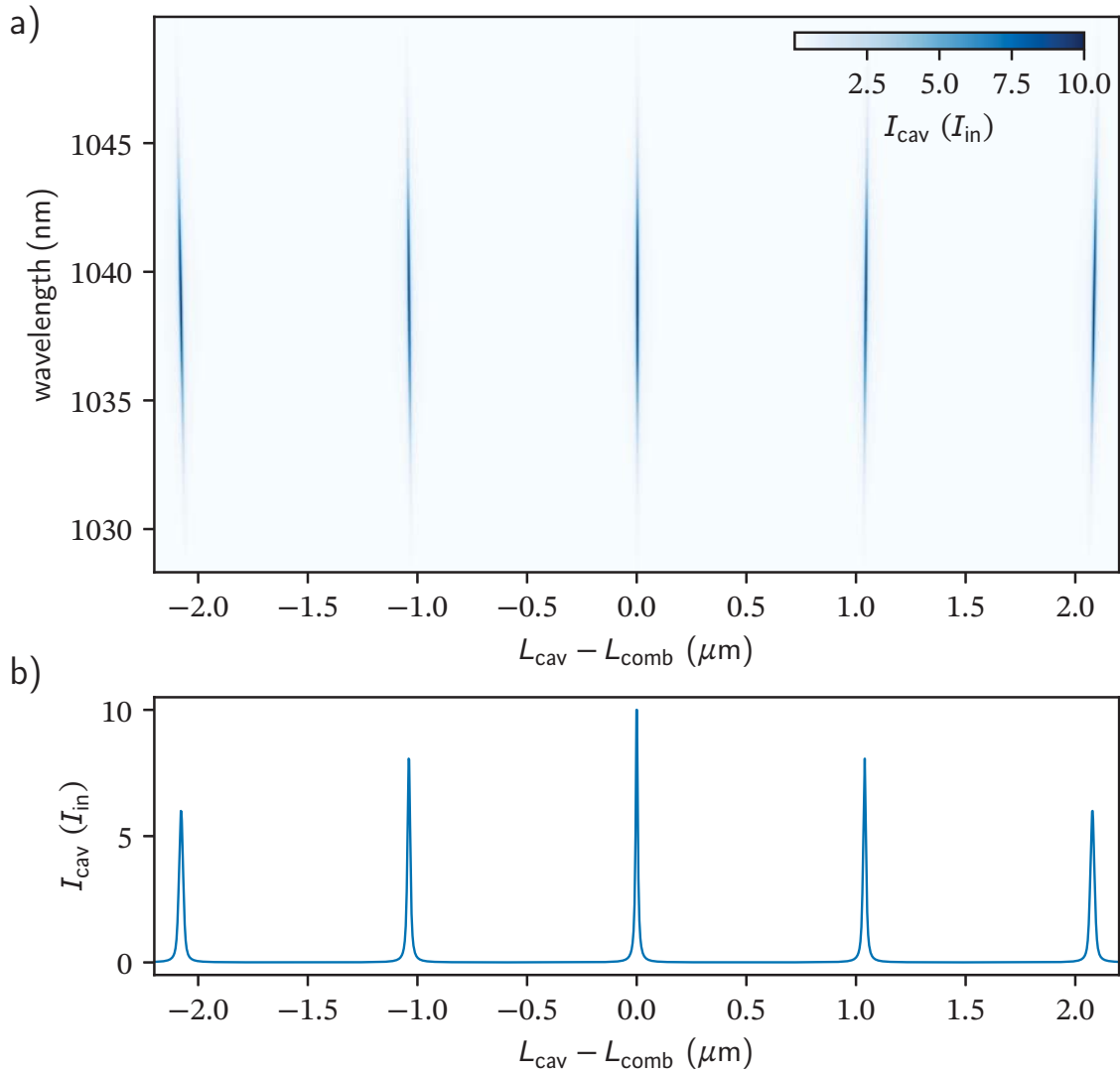
Figure 2.9: Simulated dispersion-free enhancement cavity with $T_{ic} = T_{cav} = 0.1$, $f_{CEO} = 0$ MHz, $\phi_D = 0$, $\mathcal{F} \approx 31.4$, fed with 200 fs pulses centered around 1039 nm at a rate of 100 MHz. a) The resonance map shows the spectrally resolved intra-cavity intensity distribution, while scanning the cavity length around the central fringe ($L_{cav} = L_{comb}$). On the central fringe, all frequencies are simultaneously resonant. For mismatched lengths the fringes tilt, resulting in a reduced intra-cavity intensity, as shown in b). A maximum enhancement of $\beta = 10$ is reached. Graphical representation inspired by [53, 109, 223].
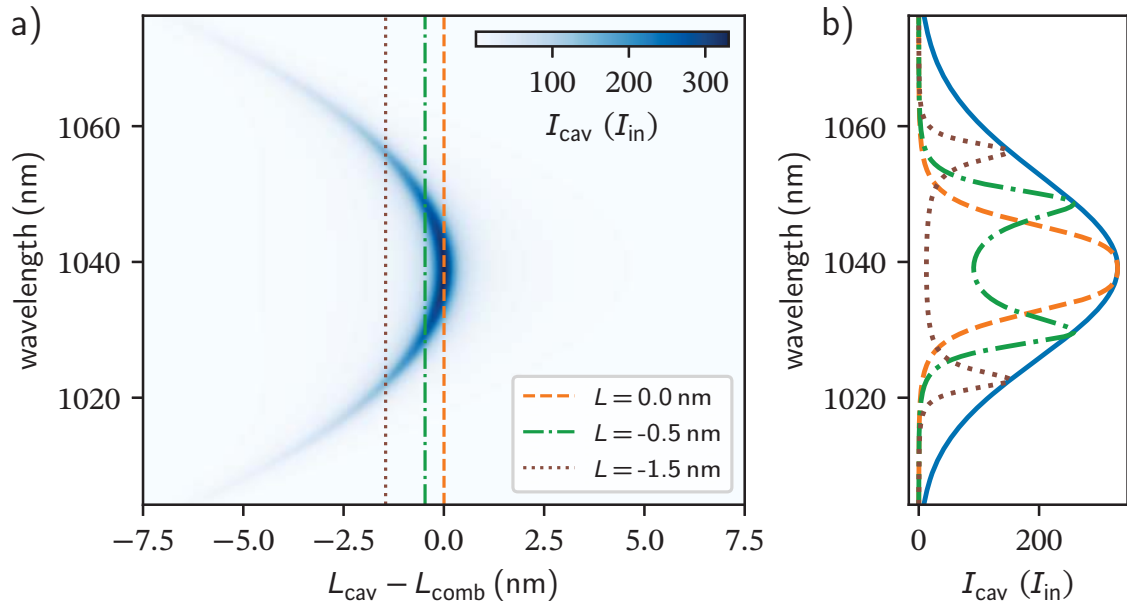
Figure 2.10: Simulated enhancement cavity with $T_{ic} = 0.01$, $T_{cav} = 0.001$, $f_{CEO} = 0$ MHz, $\phi_D = 0$, $\mathcal{F} = 571$, fed with 50 fs pulses centered around 1039 nm at a rate of 100 MHz and a round-trip GDD of 10 fs². a) Second-order dispersion causes a quadratic curvature of the central fringe ($L_{cav} = L_{comb}$). Now, only a fraction of the whole spectrum can be simultaneously resonant, as indicated by the vertical lines. b) The circulating spectra for different cavity lengths are narrowed compared to the incident spectrum (solid blue line). The maximum attainable enhancement drops from $\beta = 330$ for a cavity without dispersion to 166. Graphical representation inspired by [53, 109, 223].

2.3.4 Jones calculus

Fully polarized light can be described using the Jones calculus [224–226]. Jones matrices represent optical elements, and the Jones vector describes the polarization state of the light. Assuming propagation along z, the two transversal components of the electric field along the x and y direction are given by

$$\mathcal{E}_x(z,t) = \mathcal{E}_{0,x}\, e^{i(\omega t - kz + \phi_x)} \tag{2.65}$$

$$\mathcal{E}_y(z,t) = \mathcal{E}_{0,y}\, e^{i(\omega t - kz + \phi_y)}. \tag{2.66}$$

The Jones vector $\mathcal{J}$ includes the x and y components of the electric field and dropping the fast carrier oscillation of the laser field yields

$$\mathcal{J} = \frac{1}{\mathcal{E}_0}\begin{pmatrix} \mathcal{E}_{0,x}\, e^{i\phi_x} \\ \mathcal{E}_{0,y}\, e^{i\phi_y} \end{pmatrix}, \tag{2.67}$$

with $\mathcal{E}_0 = \sqrt{\mathcal{E}_{0,x}^2 + \mathcal{E}_{0,y}^2}$ and the phase of the x and y components ϕ_x and ϕ_y, respectively. Adding the Jones vectors of two superimposed light beams yields their combined polarization state. In this way, it is straightforward to obtain the relationship that the sum of right- and left-handed circularly polarized light of equal amplitude results in linearly polarized light. Note that here the convention of polarization handedness as defined from the receiver's point of view is used. Table 2.2 lists the Jones vectors of linearly and circularly polarized light.

The change of the polarization state $\mathcal{J}$ through an optical element is described by the Jones matrix $\mathcal{M}$. The Jones vector at the output of that optical element is the product of the Jones matrix with the input Jones vector

$$\mathcal{J}_{\text{out}} = \mathcal{M}\mathcal{J}_{\text{in}}. \tag{2.68}$$

The Jones matrices of important optical elements are listed in Table 2.3. P-polarized light has the electric field parallel to the plane of incidence, while s-polarized light is polarized perpendicular to that plane. This means that since the beam plane is typically parallel to the optical table, p-polarized light is horizontally polarized. All polarizers used in this work transmit p-polarized light and reflect s-polarized light.

Waveplates are used to shift the horizontal and vertical electric field components of the light against each other in phase. This effect can be utilized to rotate the polarization in the case of a HWP or convert linearly polarized light into circularly or elliptically polarized light with a quarter-wave plate (QWP). The resulting handedness of the circularly polarized light corresponds to the same direction it would take to rotate the initially linearly polarized light through the smallest angle into alignment with the slow axis of a QWP [225]. A general waveplate can be described as

$$\begin{pmatrix} e^{i\varphi_x} & 0 \\ 0 & e^{i\varphi_y} \end{pmatrix}, \tag{2.69}$$

with the fast axis aligned in the horizontal or vertical direction. The fast axis of the waveplate is the axis in which the refractive index of the birefringent material is the lowest. Therefore, the phase velocity along this axis is ahead of the slow axis. For a QWP it results in a phase-shift of $\delta = \varphi_y - \varphi_x = \pi/2$. Note that it is useful to shift the phases symmetrically such that $\varphi_x = -\varphi_y = \pi/4$ because common phase factors can be omitted.
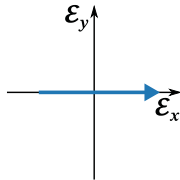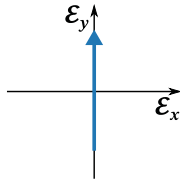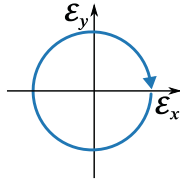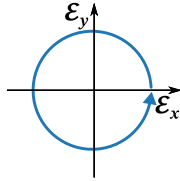
Polarization state	Illustration	Jones vector
Horizontally linearly polarized (p-polarized)		$\begin{pmatrix} 1 \\ 0 \end{pmatrix}$
Vertically linearly polarized (s-polarized)		$\begin{pmatrix} 0 \\ 1 \end{pmatrix}$
Right-handed circularly polarized (RHCP)		$\frac{1}{\sqrt{2}} \begin{pmatrix} 1 \\ -i \end{pmatrix}$
Left-handed circularly polarized (LHCP)		$\frac{1}{\sqrt{2}} \begin{pmatrix} 1 \\ i \end{pmatrix}$

Table 2.2: Jones vectors describe the polarization states of fully polarized light as defined from the point of view of the receiver [224, 225].

Optical element	Jones matrix
Horizontal linear polarizer	$\begin{pmatrix} 1 & 0 \\ 0 & 0 \end{pmatrix}$
Vertical linear polarizer	$\begin{pmatrix} 0 & 0 \\ 0 & 1 \end{pmatrix}$
Rotation by angle θ	$\begin{pmatrix} \cos(\theta) & -\sin(\theta) \\ \sin(\theta) & \cos(\theta) \end{pmatrix}$
Linear polarizer at angle θ	$\begin{pmatrix} \cos^2(\theta) & \cos(\theta)\sin(\theta) \\ \cos(\theta)\sin(\theta) & \sin^2(\theta) \end{pmatrix}$
Right circular polarizer	$\frac{1}{2}\begin{pmatrix} 1 & i \\ -i & 1 \end{pmatrix}$
Left circular polarizer	$\frac{1}{2}\begin{pmatrix} 1 & -i \\ i & 1 \end{pmatrix}$
HWP, fast axis at angle θ	$e^{-\frac{i\pi}{2}}\begin{pmatrix} \cos^2\theta - \sin^2\theta & 2\cos\theta\sin\theta \\ 2\cos\theta\sin\theta & \sin^2\theta - \cos^2\theta \end{pmatrix}$
QWP, fast axis at angle θ	$e^{-\frac{i\pi}{4}}\begin{pmatrix} \cos^2\theta + i\sin^2\theta & (1-i)\sin\theta\cos\theta \\ (1-i)\sin\theta\cos\theta & \sin^2\theta + i\cos^2\theta \end{pmatrix}$

Table 2.3: Jones matrices for selected optical elements [224, 225]. The angle θ is defined with respect to the horizontal axis.

The Jones calculus is only applicable to fully polarized light. To cover partially polarized and unpolarized light, this formalism can be extended resulting in Stokes vectors and Müller matrices [225]. Since we are dealing mostly with coherent light, the Jones formalism is sufficient. In Section 4.2, this formalism is used in the design process of a SAD line. It is based on a Mach-Zehnder interferometer and splits pulses into two copies with a variable temporal delay of τ, and polarization shaping is employed to generate a pulse pair with variable polarization.

2.4 Velocity-map imaging

As described in Chapter 1, VMI is a technique to measure the momentum distribution of charged particles, such as photoelectrons, with an inhomogeneous electric field that maps their velocity vectors onto a detector [135, 136]. It is commonly utilized in MPI and ATI experiments [134].

However, because in VMI only 2D detector images are obtained, reconstruction of the original 3D distribution is necessary, posing constraints in the choice of possible laser polarization geometries. For measurements with linear polarization, the cylindrical symmetry of the distributions can be exploited to reconstruct the original distribution if the polarization vector, i. e. the symmetry axis, is parallel to the detector. The same is true for purely circular polarized light, where the symmetry axis is along the laser beam propagation axis [227]. There are numerous ways to recover the original 3D distribution from such detector images because cylindrically symmetric distributions are uniquely related to their projection by the Abel transform [228]. It has been demonstrated that it is also feasible to directly slice the photoion [143, 229] and photoelectron [155, 230] clouds by application of a short-time gate pulse to the detector, the camera, or even directly recording time-resolved images [157, 231]. The expansion of the photoelectron/ion sphere typically takes place within several hundred nanoseconds in these schemes, which is much longer than the 10 ns repetition time of our system. Therefore, these methods are not suited for high repetition rates.

Alternatively, tomographic reconstruction allows retrieval of 3D PADs from photoionization of atoms [151, 232, 233] and molecules [234, 235], also for non-cylindrically symmetric distributions. Recently, vortex-shaped PADs were produced by polarization-shaped ultrashort laser pulses and tomographically reconstructed utilizing VMI [188–190]. As a result, 3D free-electron wave-packet distributions, which are generated by polarization-shaped ultrashort laser pulses, can be retrieved, regardless of any symmetry assumptions [188, 190].

2.4.1 Reconstruction of 3D photoelectron angular distributions by Abel inversion
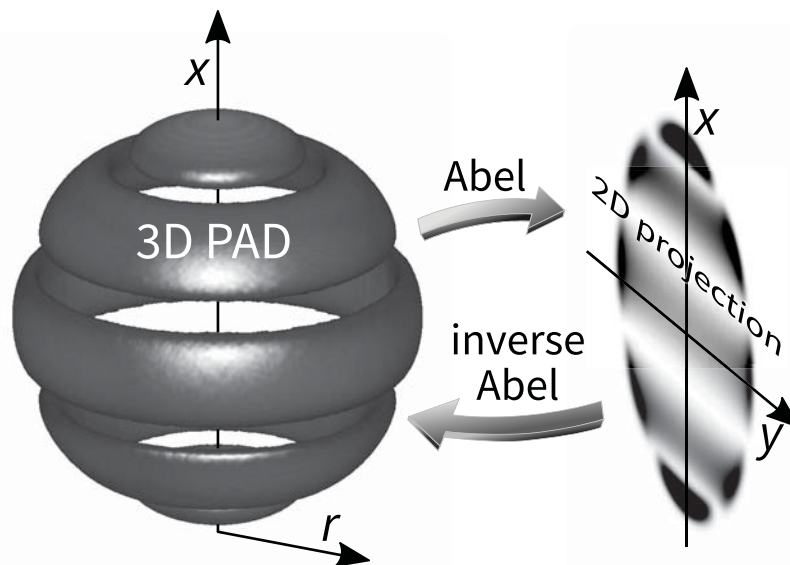

Figure 2.11: Illustration of the Abel inversion. A cylindrically symmetric 3D PAD is projected onto a detector. The inverse Abel transform can be used to reconstruct the original 3D distribution.

Provided that the 3D image possesses cylindrical symmetry with the symmetry axis aligned parallel to the detector plane, Abel inversion can be applied to reconstruct the original 3D PAD

[228, 236, 237]. For a cylindrically symmetric 3D function $f(r, x)$, the (forward) Abel transform is defined as

$$F(x, y) = 2 \int_y^\infty \frac{f(r, x)r}{\sqrt{r^2 - y^2}} dr, \tag{2.70}$$

where x, y, and r are the spatial coordinates, as shown in Figure 2.11. The inverse Abel transform is given by

$$f(r, x) = -\frac{1}{\pi} \int_r^\infty \frac{dF(x, y)}{dy} \frac{1}{\sqrt{y^2 - r^2}} dy, \tag{2.71}$$

where $F(x, y)$ is the intensity projection on the 2D plane, i. e. the detector image.

Over the years, several algorithms have been developed for the numerical implementation of the inverse Abel transform, and the basis-set expansion (BASEX) has become the *de facto* standard in photoelectron spectroscopy [237]. For Abel inversion, we use the BASEX method implemented by Hickstein and coworkers in the PyAbel Python software package [238].

Analytic reconstruction of 3D objects without cylinder symmetry from their 2D projections is only possible if multiple object images are recorded over a range of various projection angles, requiring tomographic reconstruction methods. Recently, a reconstruction approach based on deep learning has been reported, but prior knowledge of the main features of the 3D distribution is required for the design of the training set [239]. Besides being a promising method, it is not suitable for reconstructing *a priori* unknown PADs with complicated structures and several ATI rings.

2.4.2 Tomographic reconstruction of 3D photoelectron angular distributions

Tomography is used in many areas - both in science and other fields. Various techniques such as computer tomography (CT) or magnetic resonance imaging (MRI) are used in medical imaging to image internal organs and structures at various angles. Slices through the patient's body are obtained by tomographic reconstruction of the recorded images and can then be used for diagnostics [240]. All tomographic reconstruction algorithms are based on the Radon transform [227, 241].

We utilize tomography to retrieve 3D PADs from photoionization of atoms [151, 232, 233]. The process of data acquisition and tomographic reconstruction is illustrated in Figure 2.12, where also the used coordinate system is shown. Using VMI, several projections of the original 3D distribution $f(x, y, z)$ are projected at a series of angles θ along the time-of-flight axis onto the detector, which is parallel to the xy-plane. Experimentally, instead of rotating the detector around the object as in medical imaging, we rotate the object and keep the detector stationary. This is performed by rotating the laser polarization with a waveplate, as discussed in Section 4.5.2. The projected images $P_\theta(x, y)$ are related to the Radon transform of $f(x, y, z)$, which is given by integration of the rotated original distribution along the time-of-flight axis z, as shown in Figure 2.13 a). The set of 1D Radon transforms obtained from the 2D slices of $f(x_0, y, z)$ are given by [227]

$$RT\{f(x_0, y, z)\} = P_{x_0}(\theta, u) = \int_{-\infty}^\infty \int_{-\infty}^\infty f(x_0, y, z)\delta(u - z\cos(\theta) - x\sin(\theta))dxdz, \tag{2.72}$$

where u is the distance from the origin to a line parallel to the z axis for a given x-coordinate. The detector images $P_\theta(x, y)$ are stacked to a 3D array, where $P_{x_0}(\theta, u)$ are extracted as vertical slices for each y-pixel. These slices are called the sinograms of $f(x, y, z)$, and from them the original distribution $f(x, y_0, z)$ can be reconstructed by applying the inverse Radon transform [242]. However, this reconstruction is an inverse problem that can only be solved analytically
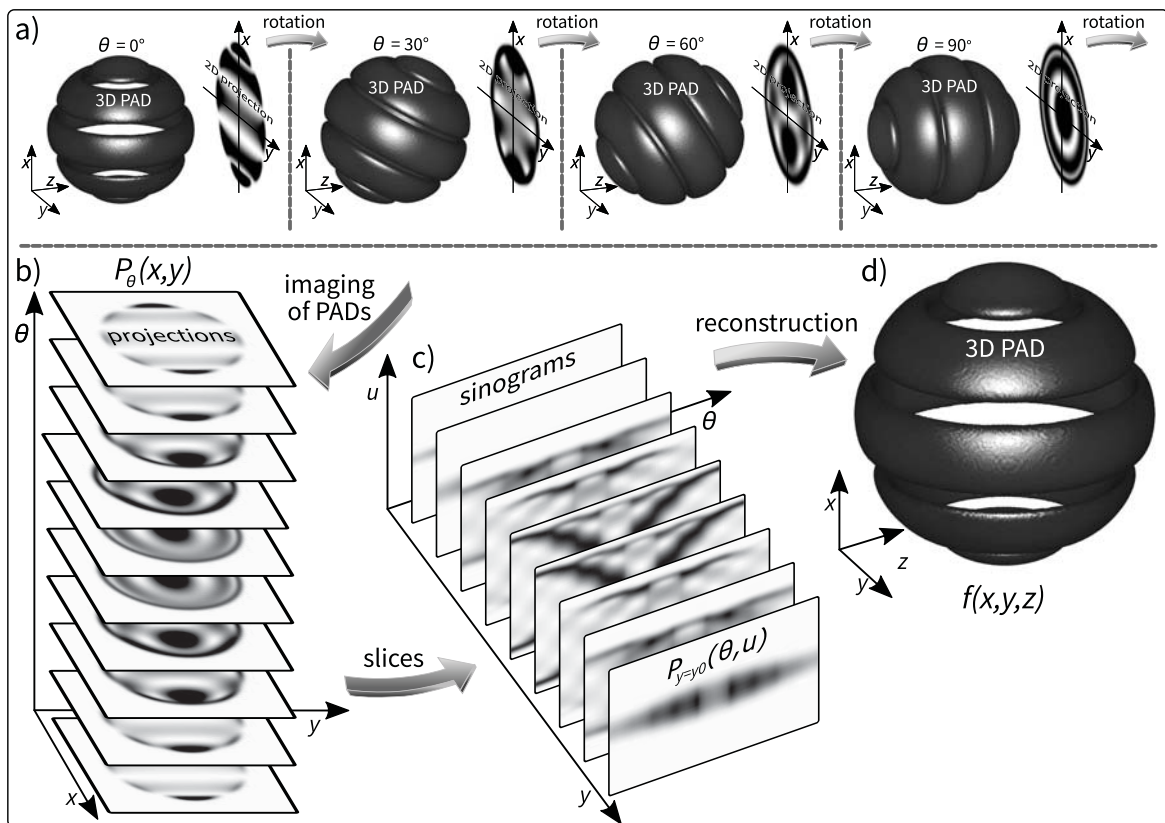
Figure 2.12: Illustration of the data collection and tomographic reconstruction method of a typical PAD. a) Several projections of the 3D distribution are recorded by rotating it by an angle θ with respect to the detector (xy) plane. Projections of the distribution are recorded for several angles θ with respect to the detector (xy) plane and b) stacked together into a single array. c) Slices of this array (the sinograms) are extracted for each y-pixel. d) These are tomographically reconstructed one by one, and stacked to a 3D array, yielding the reconstructed 3D PAD, visualized as an isosurface plot.

using the Fourier-slice theorem if the sinogram is known exactly. The Fourier-slice theorem can be stated as

$$\mathcal{F}_{1D}\{P_{x_0}(\theta, u)\} = \mathcal{S}_\theta \mathcal{F}_{2D}\{f(x_0, y, z)\}, \tag{2.73}$$

where $\mathcal{F}_{1D}$ and $\mathcal{F}_{2D}$ denote the 1D and 2D Fourier transform, respectively, and $\mathcal{S}_\theta$ is a slice operator, which extracts a 1D slice through the origin at angle θ [242]. Therefore, the Fourier-slice theorem relates the Fourier transform of each line of constant θ of the sinogram with an angular slice through the 2D Fourier transform of the original image [227].
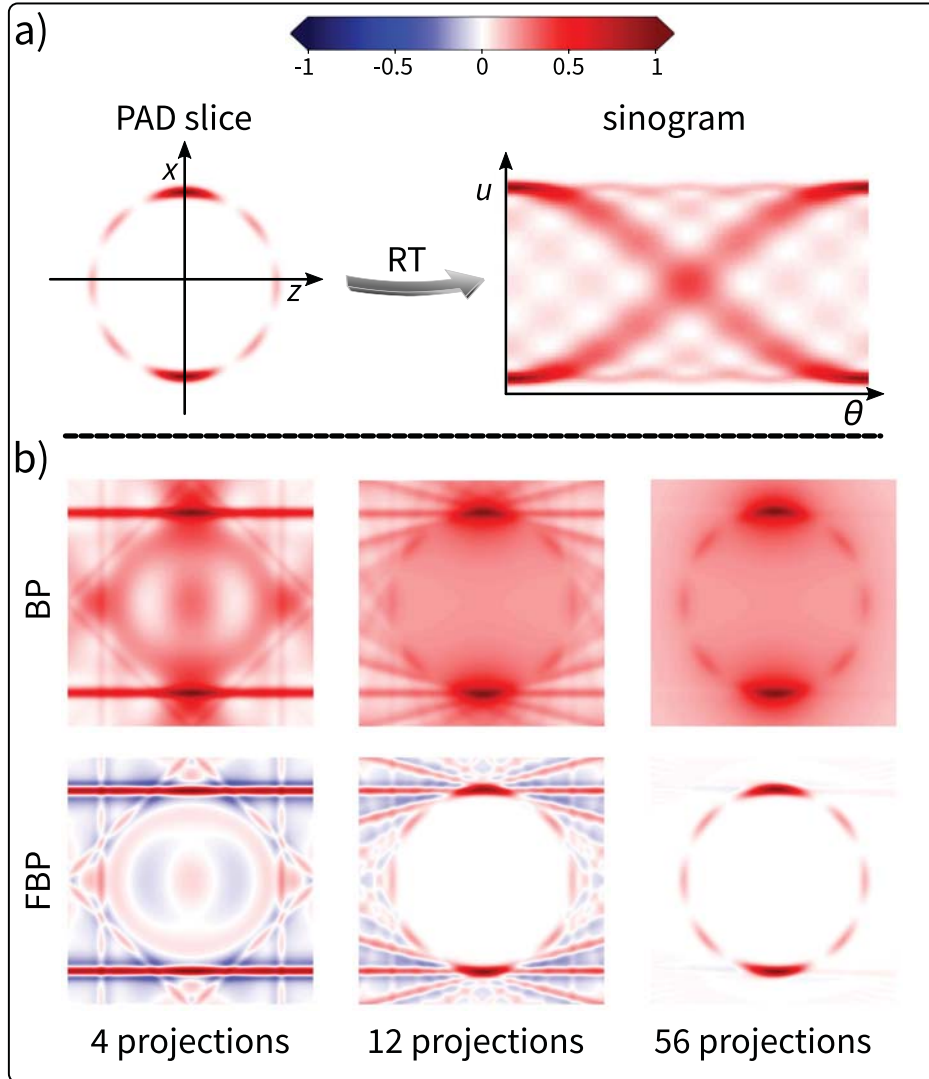
Figure 2.13: Illustration of the filtered back-projection (FBP) method. a) A slice through the 3D PAD (cf. Figure 2.12) is converted into a sinogram by the Radon transform (RT). b) The inverse Radon transform is implemented using the simple back-projection (BP) and the filtered back-projection (FBP) algorithm. The reconstructed slices are shown for 4, 12, and 56 projection angles. The angle $\theta = 0$ corresponds to a horizontal back-projection. The simple back projection method always produces blurry images, even for many projections. On the contrary, the filtered back-projection reproduces the original slice of the PAD if enough projection angles are used. Graphical representation inspired by [227].

In reality, however, a perfect measurement of the sinogram is impossible because only a finite number of projections can be recorded. Additionally, the pixelated devices used to detect the

projections (typically a camera imaging a fluorescent screen) use the Cartesian coordinate system. In contrast, polar coordinates have to be used for the reconstruction, which results in blurry reconstructions due to the transformation between the Cartesian and polar coordinate systems. A straightforward reconstruction method is the (simple) back-projection algorithm, where each 1D Radon transform of the sinogram is back-projected (extruded) along its specific projection angle θ, and summing together the series of rotated images yields the reconstructed slice [227]. However, low-frequency components are over-sampled, which leads to blurring, as shown in figure 2.13 b).

A much-improved method is the filtered back-projection algorithm [241]. This method enhances high-frequency components, which avoids over-sampling at low frequencies but can introduce high-frequency noise. Figure 2.13 b) compares the (simple) back-projection and the filtered back-projection method. We use the filtered back-projection method implemented in the iradon Python package [243] for tomographic reconstruction. Even though this method is very reliable, it was recently demonstrated that more advanced tomographic reconstruction methods provide better performance [227]. The Nyquist-Shannon sampling theorem and simulations suggest that the number of recorded angles should be similar to the number of x and y pixels of the detector [244].

2.5 Photoionization in strong laser fields

Albert Einstein hypothesized in his famous paper to explain the photoelectric effect that light is quantized and discontinuously distributed in space, resulting in three laws for photoionization [245]:

1. The incident light cannot release photoelectrons below a material-dependent cut-off frequency.

2. Above this cut-off frequency, the maximum kinetic energy of the photoelectrons is independent of the intensity of the incident light.

3. Above the cut-off frequency, the number of released electrons is proportional to the intensity of the light.

Using these findings, the maximum kinetic energy of the photoelectrons is given by

$$E_e = hf - I_\mathrm{p}, \tag{2.74}$$

where h is the Planck constant, f is the frequency of the light, and I_p is the ionization potential of the atom (or the work function of the material).

However, this simple model is modified at high laser intensities, where nonlinearities arise and several photons can be absorbed simultaneously. A few years after Albert Einstein's explanation of the photoelectric effect in 1905, the possibility of two-photon absorption was predicted [246]. It was realized experimentally [247] shortly after the invention of the laser 1960 [1, 248]. This section describes the main effects in the interaction between light and atoms for strong laser fields with intensities above $\sim 1 \times 10^{12} \, \mathrm{W \, cm^{-2}}$.
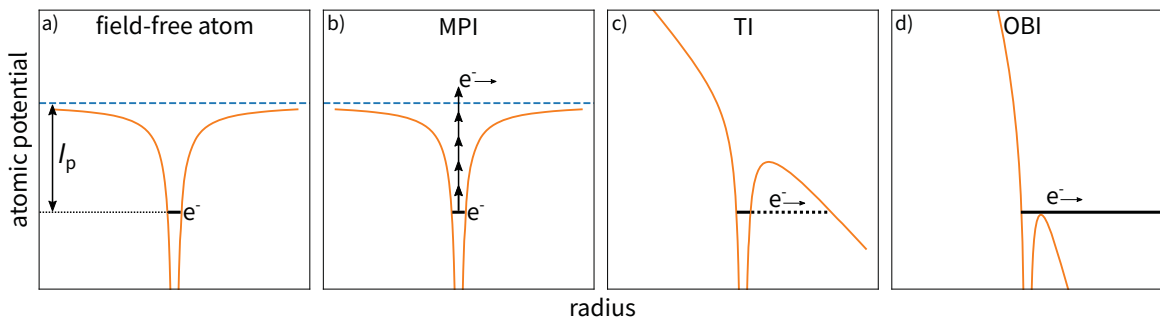
Figure 2.14: Illustration of atomic potentials in laser fields of different intensity. a) Without a laser field, the atomic potential is unperturbed. b) Increasing the intensity can lead to absorption of multiple photons and ionization (MPI). c) At higher intensity, the atomic potential is modified by the strong laser field and electrons can tunnel through the barrier (TI). d) At even higher intensities, the potential is modified so much that the electrons can leave the atom over the barrier (OBI).

2.5.1 Multiphoton and above-threshold ionization

Considering atoms in intense laser fields, their Coulomb potential is perturbed by the high electric field strengths. Qualitatively, the regime of laser-matter interaction is classified by the well-known Keldysh parameter into three different mechanisms: MPI, tunnel ionization (TI), and over-the-barrier ionization (OBI), as shown in Figure 2.14 [249]. The Keldysh parameter is defined as [250]

$$\gamma = \frac{\omega\sqrt{2m_e I_p}}{eE_0},$$
(2.75)

where $\omega = 2\pi f$ is the angular frequency of the light, e is the electron charge and m_e its mass, and E_0 is the maximum electric field of the laser as defined in Equation 2.4. Essentially, γ gives the ratio of the laser frequency and the tunneling frequency, indicating whether electrons ionize mainly by multiphoton absorption $\gamma \gg 1$ or tunneling through the potential barrier $\gamma \ll 1$. For even higher intensities, the barrier of the Coulomb potential is lowered so much that the electron can escape without tunneling. Therefore, MPI and TI are two limiting cases of the universal process of nonlinear ionization, and the Keldysh parameter defines the borderline between the weak- and strong-field regimes of light–matter interactions.
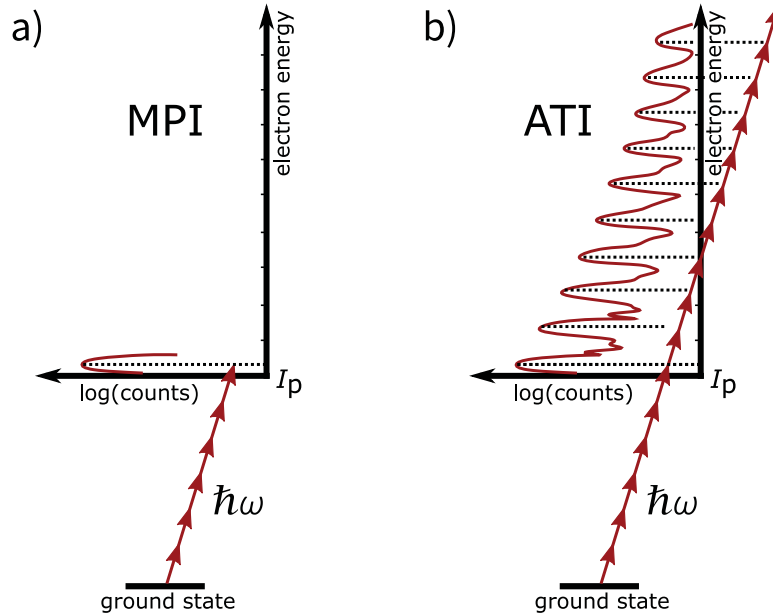
Figure 2.15: Illustration of the MPI and ATI processes. a) At high laser intensity, several photons are absorbed simultaneously to overcome the ionization potential I_p. b) When the intensity increases further, additional absorption of photons in the continuum leads to free-free transitions, and distinct peaks spaced by the photon energy arise in the photoelectron energy spectrum [134]. Graphical representation inspired by [251].

The MPI process is illustrated in Figure 2.15 a). MPI describes the transition of an electron from a bound state into the continuum by absorption of several photons, which can be modeled by perturbation theory in the photon picture. The ionization rate in the multiphoton limit follows

$$\omega_{\mathrm{MPI}} \propto I^n,$$
(2.76)

where I is the laser intensity and n is the minimum number of photons needed for ionization [249]. If the intensity is increased further, additional photons can be absorbed in the continuum, which leads to free-free transitions. Distinct peaks spaced by the photon energy arise in

the photoelectron energy spectrum, a phenomenon known as ATI [134, 252]. The ATI process is illustrated in Figure 2.15 b). The measured width of the ATI peaks depends on the spectral bandwidth of the light and other effects, such as the spectrometer resolution.

2.5.2 AC-Stark shift
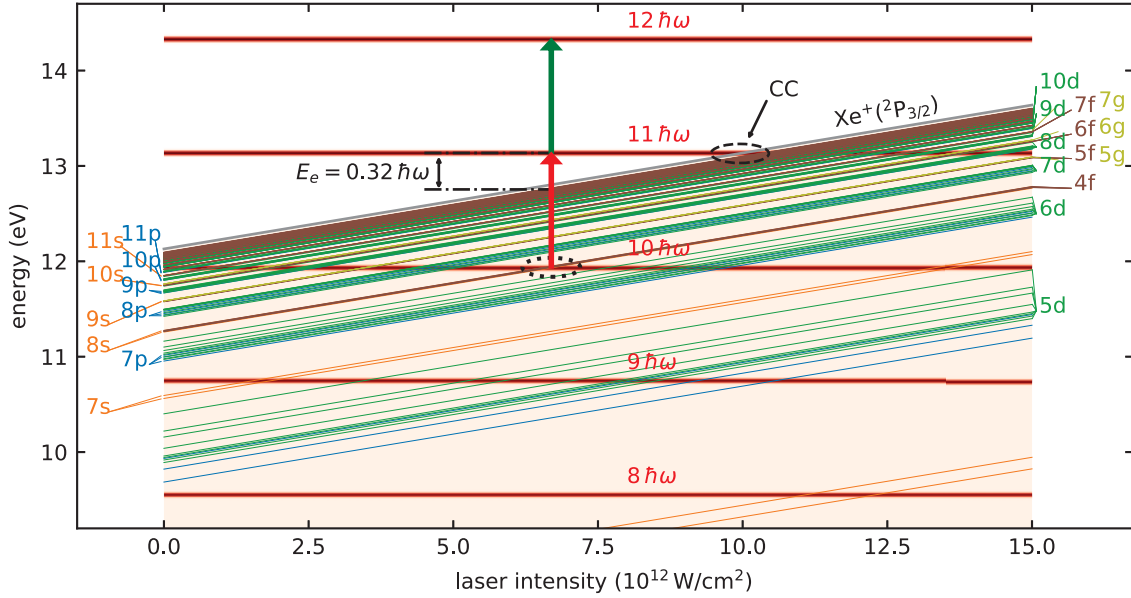
Figure 2.16: Illustration of the ponderomotive shifting of Rydberg states of xenon that are accessible from the $^1S_0\, 5p^6$ ground state [253]. These states can become resonant by simultaneous absorption of n photons, as indicated by red horizontal lines labeled with $n\,\hbar\omega$. The dotted ellipse marks the laser intensity, where the $5p^5(^2P_{3/2})4f$ state can be reached by ten photons. From this state, photoionization by absorption of a photon (red arrow) leads to the first ATI peak ($E_e = 0.32\hbar\omega$) and an additional photon (green arrow) causes a second peak in the ATI electron spectrum and so on. The dashed ellipse indicates the laser intensity ($\sim 1 \times 10^{13}\,\mathrm{W\,cm^{-2}}$), where eleven photons are not sufficient anymore to overcome the ionization threshold, and thus, this ionization channel closes (CC), and twelve photons are necessary for ionization.

The time-averaged quiver energy of a free electron in a laser field is given by the ponderomotive energy

$$U_\mathrm{p} = \frac{e^2 E_0^2}{4 m_\mathrm{e} \omega_c^2} = \frac{e^2 I_\mathrm{peak}}{2 c \varepsilon_0 m_\mathrm{e} \omega_c^2}, \tag{2.77}$$

with the laser peak intensity $I_\mathrm{peak} = c\varepsilon_0 E_0^2/2$. Consequently, the Keldysh parameter defined in Equation 2.75 simplifies to [250, 254]

$$\gamma = \sqrt{\frac{I_\mathrm{p}}{2 U_\mathrm{p}}}. \tag{2.78}$$

The energy of the photoelectrons at a given laser intensity after absorption of n photons is reduced by the ponderomotive energy because the ponderomotive potential effectively increases the ionization potential. Therefore, the photoelectron energy is given by

$$E_e = n\hbar\omega - (I_\mathrm{p} + U_\mathrm{p}). \tag{2.79}$$

The ponderomotive force acts along the gradient of the beam intensity and is independent of the light polarization. It pushes the photoelectrons out of the interaction region into regions of low laser intensity. Thus, for long laser pulses, the ponderomotive energy of a photoelectron is converted into kinetic energy, which compensates for the peak shifting in the electron energy spectrum described in Equation 2.79. Therefore, ultrashort laser pulses <500 fs are necessary to observe ponderomotive shifts in the photoelectron angular distribution and energy spectrum.

Channel switching

In the short-pulse regime, not only does the ionization threshold shift ponderomotively, but due to the AC-Stark effect, also Rydberg states shift and can be resonantly excited. As a rule of thumb, the ponderomotive shift at our laser wavelength ($\lambda_c = 1039$ nm) is given by ~ 1 eV/10^{13} W cm^{-2}. The lower energy levels of more tightly bound electrons are less polarizable, and therefore, they are only minimally affected by these shifts. It leads to a rich structure in the ATI electron spectra because intermediate bound states shift into momentary resonance during the pulse [255]. Thus, the ATI peaks have smaller peaks corresponding to the excited, bound states, and the spectrum becomes sensitive to the atomic structure. These features in the electron energy spectrum are known as Freeman resonances, and they reflect the characteristics of the intermediate states [170, 256]. Additionally, it results in a considerable enhancement of the absorption probability through this new ionization channel. Therefore, this mechanism is known as channel switching and indicated with a dotted ellipse in Figure 2.16, where the ponderomotive shifting of xenon Rydberg states is shown. In the figure, the energies reachable by absorption of eight to twelve photons are indicated as red horizontal lines with the thickness representing the spectral bandwidth. We assume a negligible influence of the laser field on the ground state.

Xenon is often used to study MPI and ATI [145, 170, 257–260] because it has the lowest ionization threshold of the nonradioactive noble gases, as shown in Table 2.4.

Element	I_p(eV)
He	24.59
Ne	21.56
Ar	15.76
Kr	14.00
Xe	12.13

Table 2.4: Ionization energies of the nonradioactive noble gases used to study photoionization in strong laser fields [261].

Channel closing

As soon as U_p exceeds the energy of a single photon $\hbar\omega$, photoionization that previously occurred with a minimum number of photons n is no longer possible. This process, called channel closing (CC) [257, 258, 262, 263], is indicated with a dashed ellipse in Figure 2.16, where the ponderomotively shifted ionization potential of xenon equals the combined energy of eleven photons. Simultaneous absorption of eleven NIR photons is sufficient to overcome the ionization potential of xenon at low laser intensities. At intensities above $\sim 1 \times 10^{13}$ W cm^{-2}, the combined energy of eleven photons is not sufficient anymore, and twelve photons become necessary. However,

this ionization channel is still possible in less intense areas in the inhomogeneous experimental laser intensity distribution. Nevertheless, MPI with eleven photons becomes unlikely, CC starts, and the first (resonance) peaks are suppressed.

2.5.3 Tunnel ionization

At higher laser intensities ($\gamma \ll 1$, which for xenon corresponds to $I \approx 10^{14}\,\mathrm{W\,cm^{-2}}$ at our wavelength), the photoionization process cannot be explained using perturbation theory in the photon picture anymore. A non-perturbative quantum mechanical model is required for an in-depth understanding [264]. In this approach, the laser field is described as a classical field that modifies the Coulomb potential of the atom, where the electron can tunnel through. The ionization rate, which had followed a power law in the multiphoton limit (cf. Equation 2.76), is modified and increases exponentially [265]

$$\omega_{\mathrm{tunnel}} \propto \exp\left(-\frac{2(2I_{\mathrm{p}})^{3/2}}{3E}\right), \tag{2.80}$$

where E is the electric field strength and I_{p} is the unperturbed ionization potential of the atom. The latter is listed in Table 2.4 for the nonradioactive noble gases.

In general, the ATI photoelectron energy spectrum is consistent with the semiclassical viewpoint of the intuitive three-step model (TSM), which explains the most important phenomena of the HHG process, as described in Section 2.6. The discrete peaks visible in the ATI spectrum in the multiphoton regime disappear for TI. The overall photoelectron signal drops fast from the origin until $\sim 2U_{\mathrm{p}}$, where a plateau is formed up to $\sim 10U_{\mathrm{p}}$ [266]. This distribution can be explained by the kinetic energy the electron acquires while drifting in the laser field after TI, as described in Section 2.6. The cutoff can be explained by non-sequential double ionization, which happens in addition to sequential double ionization, where two electrons are removed from an atom independently after each other during a laser pulse [267, 268].

Including the tunneling rates of the atoms in a quasi-static field completes the semiclassical approach [172]. The ionization rates can be calculated using the Ammosov-Delone-Krainov (ADK) theory [265, 269]. However, ADK theory overestimates the ionization rates in the barrier-suppression regime, where OBI ionization occurs. Therefore, the ADK theory was extended from TI to OBI using an empirical formula [270]. It yields the instantaneous ionization rate ω_{ADK}, and the analytical form can be found in literature [270]. Numerical calculations can be performed using public code [271]. Integration over time yields the ionization fraction from the laser field

$$\eta = 1 - \exp\left(-\int_{-\infty}^{\infty} \omega_{\mathrm{ADK}}(t)dt\right). \tag{2.81}$$

A corresponding quantum approach is provided by the Keldysh-Faisal-Reiss theory [250, 272, 273]. Further increasing the laser intensity distorts the atomic potential so much that the maximum of it is below the binding energy, and thus, OBI occurs. However, such high laser intensities are not reached in our experiments.

2.6 High-harmonic generation

In the tunneling regime ($\gamma \ll 1$) ionization can be approximated by tunneling, and high-order harmonics can be generated to produce XUV light. The TSM provides an intuitive understanding of the HHG process, which is illustrated in Figure 2.17 [274]. In the first step, an electron can tunnel through the barrier of the Coulomb potential of the atom that is modified in the intense laser
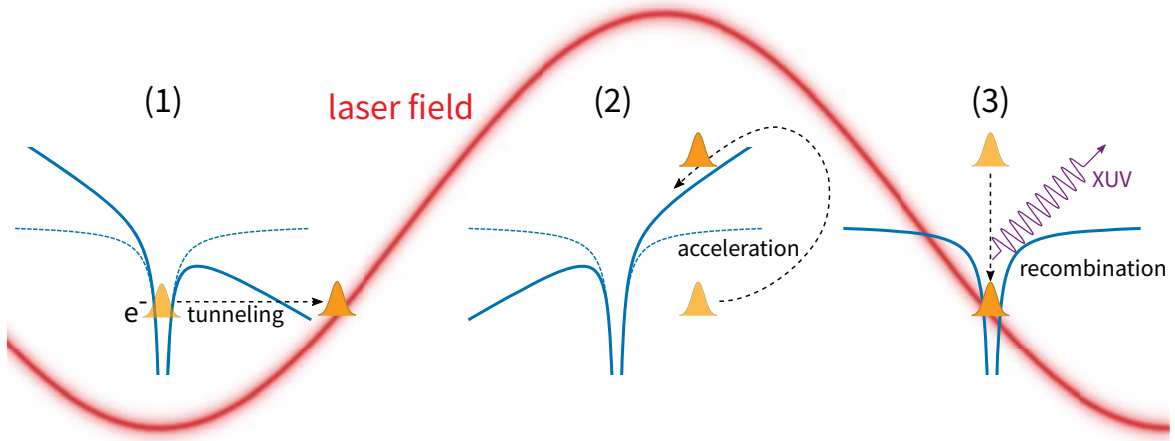
Figure 2.17: Illustration of the HHG process in three steps: In the first step, the intense laser field modifies the Coulomb potential of the atom so that the electron can tunnel out. In the second step, the electron is accelerated by the oscillating fundamental laser field. In the third and last step, the electron can recombine with the parent ion emitting an XUV photon.

field. In the second step, after launching, the electron is accelerated by the steep electric field gradient of the oscillating laser field following a classical trajectory. The trajectory which yields the maximum kinetic energy is followed by electrons tunneling shortly after the fundamental field maximum ($\sim T_{osc}/20$), where $T_{osc} \approx 3.5$ fs is the oscillation period of the fundamental laser at a central wavelength of 1039 nm [275]. Electrons launched before that time follow so-called long trajectories, while the electrons tunneling afterwards follow short trajectories. In the third step, the electron can recombine and release the acquired energy as a high-energy XUV photon. The energy of the XUV photon is determined by the sum of the ionization potential and the momentary kinetic energy of the electron at the time of recollision. Each instant of ionization is linked to a moment of recollision by a classical trajectory. This process happens twice per laser cycle in isotropic media. Since the electrons are launched at around $T_{osc}/20$ and recombine at a well-defined time later, the emitted XUV pulse train consists of attosecond bursts [82, 275, 276].

For describing the electron trajectory, it is helpful to express the ionization time t_i as the corresponding phase $\phi_i = \omega_c t_i$ of the oscillating laser field $E = E_0 \cos(\phi)$, with $\phi = \omega_c t$. The position $z(\phi)$ of the electron is given by [277]

$$z(\phi) = E_0/\omega_c^2 \left(\cos(\phi) - \cos(\phi_i) + (\phi - \phi_i)\sin(\phi_i) \right), \tag{2.82}$$

with the initial condition that the electron is launched with zero velocity at the ionization time from $z(\phi_i) = 0$. The kinetic energy of the electrons is then given by

$$E_{kin}(\phi) = 2U_p \left(\sin(\phi) - \sin(\phi_i) \right)^2. \tag{2.83}$$

Figure 2.18 shows the trajectories for $0 < \phi_i < \pi/2$. For larger or smaller ionization phases, the electron does not return to the parent ion and flies away. At $\phi_i = 0.31$ ($t_i \approx T_{osc}/20$), which corresponds to a recombination phase of $\phi_r = 4.4$ ($t_r \approx 0.7 T_{osc}$), the maximum kinetic energy is reached. When recombining, these electrons yield the maximum photon energy (cutoff) energy [274]

$$E_{cutoff} = I_p + 3.17 U_p. \tag{2.84}$$

For every pair of solutions ϕ_i and ϕ_r, also $\phi_i + \pi$ and $\phi_r + \pi$ are solutions as well. Therefore, the long and short trajectories can happen every half-cycle of the laser field, only with an opposite sign, which leads to harmonic emission twice per laser cycle. In the frequency domain, only odd harmonics of the driving center frequency ω_c are generated.
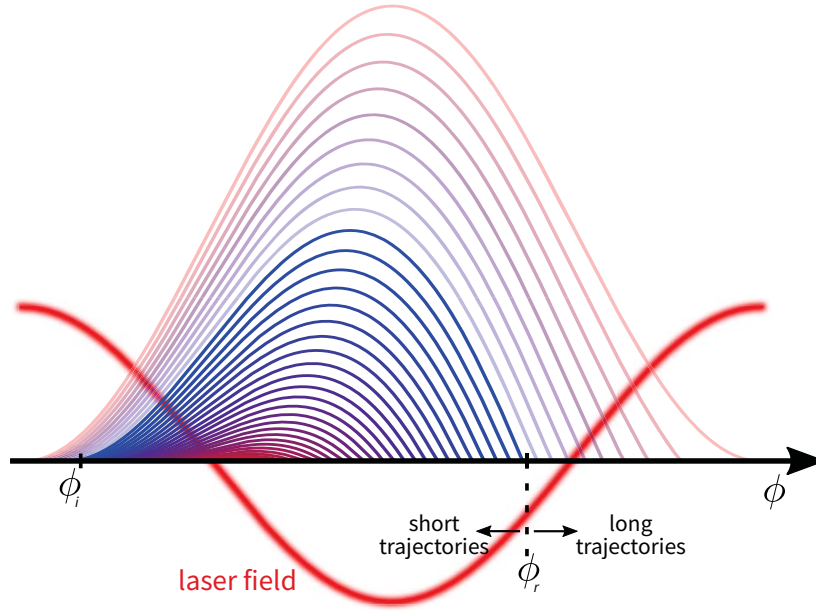
Figure 2.18: Illustration of electron trajectories in the HHG process. The recollision phase ϕ_r of the electrons depends on their ionization phase ϕ_i. The trajectories are described classically within the TSM. Electrons emitted at $\phi_i > 0.31$, recombine at $\phi_r < 4.4$ and follow short trajectories, while electrons that are emitted before $\phi_i = 0.31$, follow long trajectories and recombine at $\phi_r > 4.4$. The color code represents the electron energy at recollision, where red is low and blue is high energy. The long trajectories are grayed in the illustration.

2.6.1 Quantum theory of HHG

The preceding intuitive description of the trajectories was entirely semi-classical and provided an intuitive understanding. Furthermore, it explains most experimental findings and reproduces the key features of an analytical quantum mechanical treatment, as given by the Lewenstein model [278]. This model is briefly summarized here, following [53, 277].

The time-dependent Schrödinger equation in the length gauge describes the laser-atom interaction of linearly polarized light by

$$i\frac{\partial \Psi(r,t)}{\partial t} = \left[-\frac{1}{2}\nabla^2 + V(r) + zE(t)\right]\Psi(r,t), \tag{2.85}$$

where $V(r)$ denotes the atomic potential and $E(t) = E_0 \cos(\omega_c t)$ the laser field. We employ the widely used strong-field approximation (SFA) with the following three assumptions:

- The contribution of all excited bound states can be neglected.

- The motion of the continuum electron is independent of the atomic potential.

- The depletion of the ground state can be neglected.

Using the SFA [278], the time-dependent dipole moment $x(t) = \langle \Psi(x,t)|x|\Psi(x,t)\rangle$ is given by

$$x(t) = i \int_{-\infty}^{t} dt' \int d^3\mathbf{p} E_0 \cos(\omega_c t') d(\mathbf{p} + \mathbf{A}(\mathbf{t}')) e^{(-iS(\mathbf{p},t,t'))} d^*(\mathbf{p} + \mathbf{A}(t)) + c.c., \tag{2.86}$$

where $\mathbf{p}$ is the canonical momentum, $d(\mathbf{p})$ is the dipole transition matrix element from the ground state to the continuum, $\mathbf{A}(t) = -\int \mathbf{E}(t)dt = (-E_0/\omega_c \sin(\omega_c t), 0, 0)$ denotes the vec-

tor potential of the laser field, and the semi-classical action is defined as

$$S(\mathbf{p}, t, t') = \int_{t'}^{t} dt'' \left(\frac{(\mathbf{p} - \mathbf{A}(t''))^2}{2} + I_p \right).$$ (2.87)

Equation 2.86 can be interpreted as the probability amplitudes for the following processes, which are linked to the TSM. The first term $E_0 \cos(\omega_c t') d(\mathbf{p} + \mathbf{A}(t'))$ describes the probability amplitude for an electron to tunnel into the continuum at time t' with the canonical momentum $\mathbf{p}$. The tunneled electron wave function propagates and acquires a phase factor of $e^{(-iS(\mathbf{p}, t, t'))}$ until time t, where the electron wave packet recombines with the parent ion with a probability amplitude $d^*(\mathbf{p} + \mathbf{A}(t))$.

An analysis of Equation 2.86 shows that in the quasi-classical limit, the integral becomes a sum over all relevant electron paths, which are the trajectories known from the TSM. The electron wave packets acquire an intensity-dependent dipole phase in the continuum, given by

$$\phi_i(q, k) = q\omega_c t' - S(\mathbf{p}, t, t'),$$ (2.88)

where q denotes the harmonic order. Therefore, the accumulated phase during the laser-driven propagation of the electron strongly depends on the trajectory and the space- and time-dependent laser intensity $I(r, z, t)$. Mainly two of these trajectories play a dominant role, one with a return time t_1 and the other with a longer return time t_2, which relate to the short and long trajectory, respectively [278]. Taking only these two return times into account, reduces Equation 2.88 to [279]

$$\phi_i(q, I) = -\alpha_i I(r, z, t),$$ (2.89)

where α_i is the slope of the phase as a function of the laser intensity for each of the two quantum path components. $\phi_i(q, I)$ greatly influences the spatial and spectral properties of the generated high-harmonics. However, the coherence time of the harmonic field is reduced by the temporal variation of the laser intensity, caused by a changing instantaneous frequency $\Delta\omega_i(t) = \partial\phi_i(t)/\partial t$, also called chirp. Furthermore, the radial variation of the intensity $I(r)$ introduces a curvature of the phase front. This curvature is much larger for the longer trajectories α_2 than for the short trajectories α_1. Therefore, the short trajectories are preferred for frequency metrology due to their smaller divergence and longer coherence time.

2.6.2 XUV frequency comb by HHG

The HHG process, which generates attosecond pulse trains within each laser pulse of the driving laser, has been shown to produce phase-locked harmonic orders [90]. However, using conventional laser systems to drive the HHG process leads to significant pulse-to-pulse variations in the phase of the XUV light resulting in the well-known harmonic spectrum, as shown in Figure 2.19 a). When driving the HHG process with few-cycle pulses, the waveform of the driving laser field plays an important role. Stabilization of the CEP of the driving lasers enabled electric-field-sensitive strong-field experiments and produced attosecond pulses for time-resolved spectroscopic applications [275]. However, the repetition rate of these kilohertz systems is typically not stabilized, which leads to the washed-out spectrum.

The HHG process is phase coherent, and thus, the stability of the driving laser field can be transferred to the XUV spectral region. Figure 2.19 b) shows the high-harmonic spectrum of a frequency comb driving laser with stabilized CEP and f_{rep}. The envelope of the spectrum is governed by the harmonic spectrum of a single femtosecond laser pulse. Since the attosecond bursts produced by each laser pulse of the fundamental pulse train are generated at the same rate as the repetition rate of the driving laser, the HHG spectrum becomes modulated, and narrow
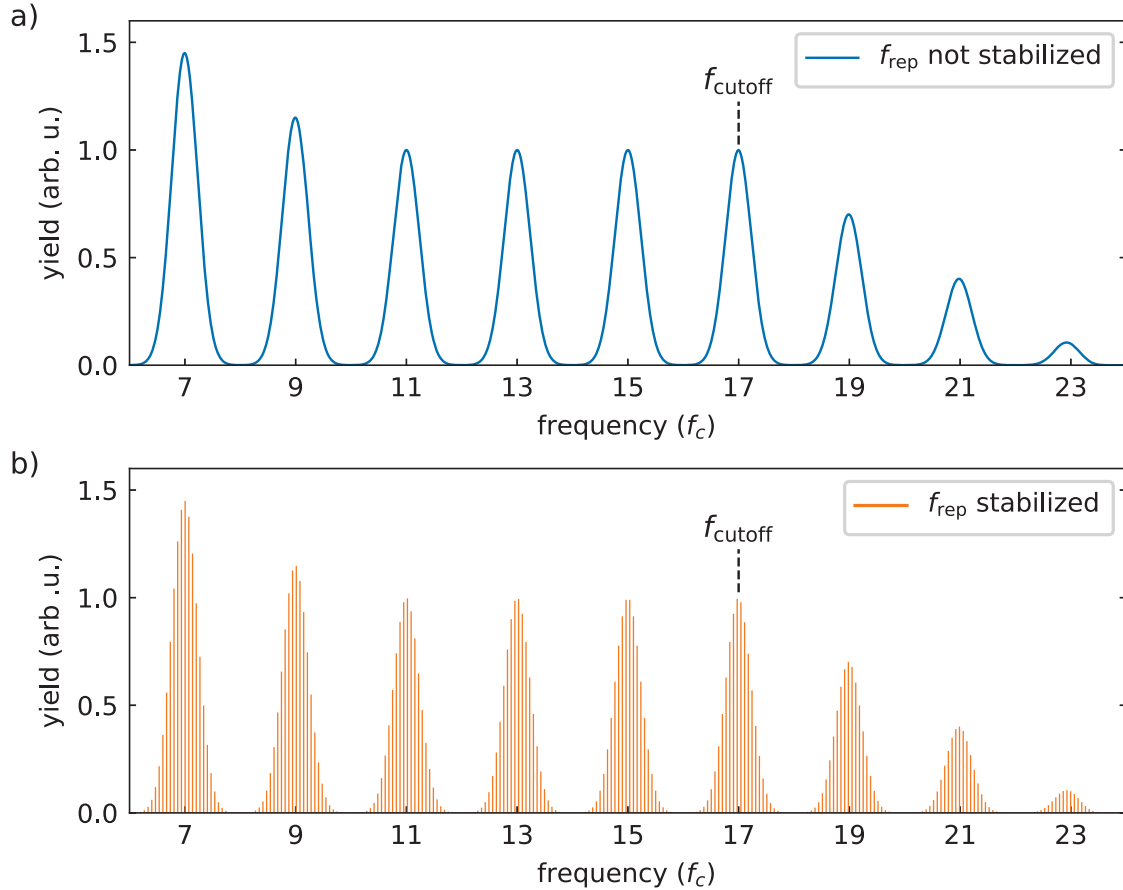
Figure 2.19: HHG spectrum of a driving pulse train. a) Without a stable pulse-to-pulse phase relationship of the driving laser, a broadband spectrum of harmonic orders centered at odd multiples of the fundamental laser frequency f_c extend up to the cutoff frequency $f_{cutoff} = E_{cutoff}/h$. b) When the repetition rate f_{rep} and the CEO of the laser are stabilized, a frequency comb structure emerges under the envelope. The repetition rate of the fundamental laser gives the frequency spacing of these narrow peaks. Adapted from [53].
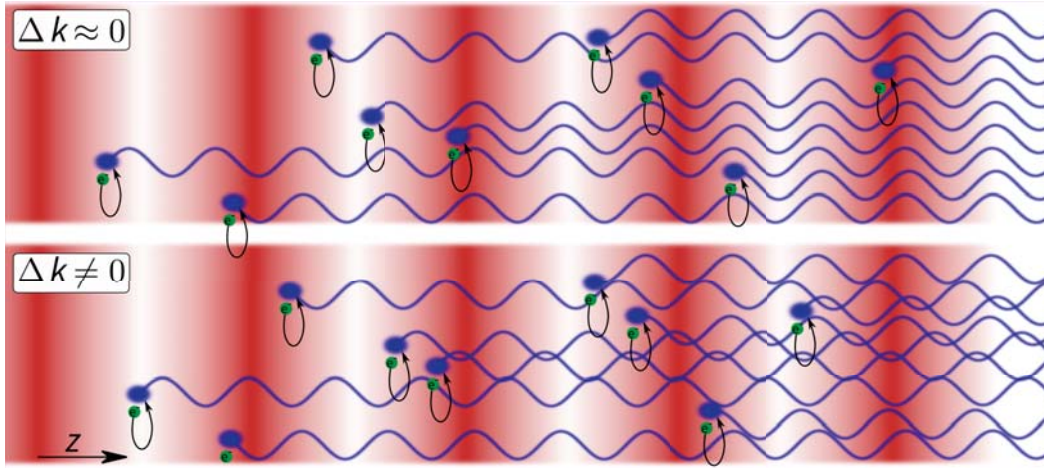
Figure 2.20: Illustration of the HHG phase-matching process for the fifth harmonic. The instantaneous absolute value of the real part of the driving laser electric field amplitude is indicated in red, thus showing two peaks for each positive wavefront. In the case of phase matching ($\Delta k \approx 0$), the harmonic fields (blue) of individual atomic emitters interfere constructively and the total harmonic signal grows. On the contrary, without phase matching ($\Delta k \neq 0$), the XUV yield is small. Graphical representation inspired by [280].

peaks emerge, which are spaced in frequency by f_{rep}. However, the electric field of harmonic order q oscillates q times as fast as the fundamental, causing the CEO of the harmonic orders to increase by the same factor. The resulting spectrum of the XUV frequency comb can be described by

$$f_{n,q} = q f_{CEO} + n f_{rep}, \tag{2.90}$$

which is a modified version of Equation 2.30 describing the spectrum of the fundamental frequency comb.

2.6.3 Phase matching of the HHG process

HHG is a phase-sensitive process, and thus, constructive interference of the single-atom emitters is required for observing a macroscopic signal. This means that phase matching between the induced and driving field is required in addition to strong single-atom emission to make the process most efficient [79, 180, 281–283]. The wave vector mismatch between the fundamental and the q-th harmonic beam can be written as

$$\Delta k(q) = qk - k_q. \tag{2.91}$$

The effect of phase matching is illustrated in Figure 2.20.

Driving the HHG process with a Gaussian laser beam, focused on a gas target, four phase terms between the harmonic and fundamental field need to be balanced [284]

$$\Delta k = \Delta k_g + \Delta k_d + \Delta k_n + \Delta k_p. \tag{2.92}$$

The first term Δk_g describes the wave vector mismatch due to the Gouy phase and depends on the focusing geometry. The second term Δk_d is the mismatch induced by the dipole phase, arising from the electron trajectory. The third and fourth term include the effects of dispersion from neutral gas Δk_n and plasma-induced dispersion Δk_p.

a)

b)
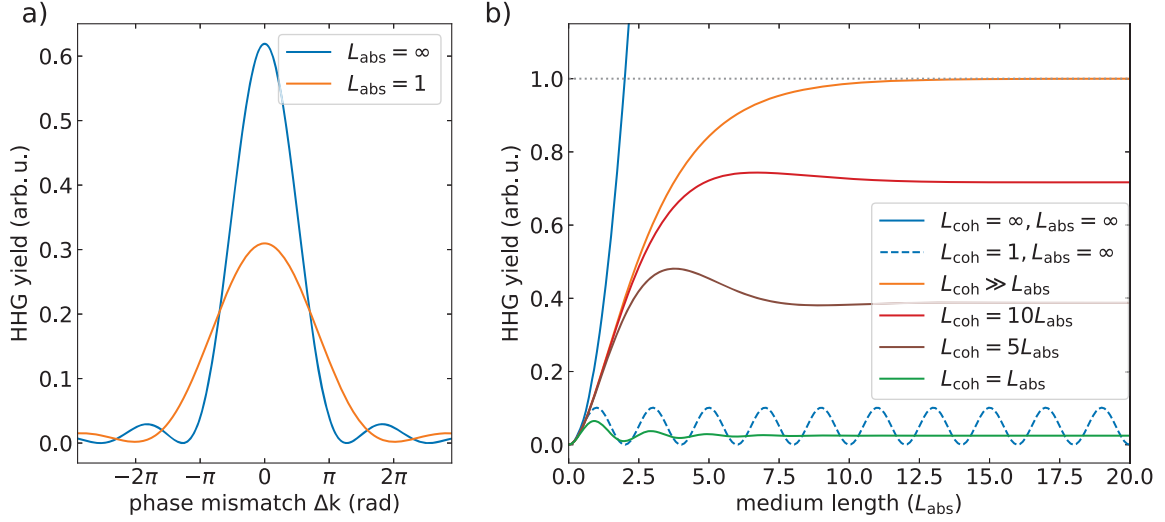
Figure 2.21: HHG yield for different phase-matching conditions. a) A macroscopic output signal is only achieved for phase matching $\Delta k = 0$. The HHG signal is shown after the generation medium length $L_{med} = L_{abs}$. b) The total XUV photon yield is plotted for different phase-matching conditions $L_{coh} = \pi/\Delta k$. The HHG yield grows quadratically to infinity for perfect phase matching without re-absorption, while the signal oscillates if $\Delta k = \pi$.

Macroscopic HHG response

Before explaining the individual phase-matching contributions in more detail, the influence of phase matching on the total HHG yield is described. The role of group-velocity matching in the macroscopic build-up of the harmonic signal becomes relevant for long wavelength ultrashort driving laser pulses and can be neglected in our case [285].

The HHG yield S_q for each harmonic order q is the coherent sum over all single-atom emitters within the length L_{med} of the nonlinear medium

$$S_q \propto \rho^2 A_q^2 \frac{4L_{abs}^2}{1 + 4\pi^2 \left(L_{abs}/L_{coh}\right)^2} \left[1 + \exp\left(-\frac{L_{med}}{L_{abs}}\right) - 2\cos\left(\frac{\pi L_{med}}{L_{coh}}\right)\exp\left(-\frac{L_{med}}{2L_{abs}}\right)\right], \quad (2.93)$$

where A_q denotes the amplitude of the atomic response at the harmonic frequency ω_q and L_{abs} is the absorption length [53, 280, 286]. This length $L_{abs} = 1/(\rho\sigma)$ depends on the gas density ρ and the ionization cross-section σ for the harmonic radiation [287]. A_q and L_{abs} are both assumed to be constant along the propagation axis [286]. In the absorption-limited case, the coherence length $L_{coh} = \pi/\Delta k$ defines the parameter range in which the yield is at least half of its maximum value.

In the absence of absorption ($L_{abs} = \infty$), Equation 2.93 simplifies to [288]

$$|S_q|^2 \propto \left|\frac{\sin\left(\Delta k L_{med}/2\right)}{\Delta k}\right|^2, \quad (2.94)$$

as shown in blue color in Figure 2.21 a) with the well-known sinc^2 shape found in nonlinear optics [289].

The evolution of the harmonic signal as a function of the medium length L_{med} is plotted in Figure 2.21 b). Even if the coherence length L_{coh} is infinite, the generated harmonic signal saturates after a few L_{abs} because of re-absorption. As a rule of thumb, the coherence length should be at least $L_{coh} > 5L_{abs}$ and the medium length $L_{med} > 3L_{abs}$ to achieve more than half of the maximum XUV output [286].

Description of phase-matching components

To understand the influence of the individual components from Equation 2.92 better, these are discussed in more detail below. The divergence of the generated harmonic beam is much smaller than that of the fundamental light and the resulting Gouy phase shift can thus be set to zero. The resulting on-axis ($r = 0$) Guoy phase contribution to the phase matching between the fundamental and the qth harmonic is given by

$$\Delta k_g = -q \frac{\partial}{\partial z} \left[\arctan\left(\frac{z}{z_R}\right) - \frac{kr^2}{2R(z)} \right] \xrightarrow{(r, z \to 0)} \Delta k_g = -\frac{q}{z_R}, \tag{2.95}$$

with w_0 denoting the beam waist size at the focus, z_R is the Rayleigh range, r is the radial coordinate and $R(z)$ is the beam radius of curvature, as introduced in Section 2.3.1. The Gouy phase contribution reaches a maximum at the waist position where $z = 0$ and has a negative sign. Therefore, adjusting the gas nozzle position with respect to the laser focus allows to fine-tune the HHG phase matching.

The dipole phase contribution (cf. Equation 2.89) is approximated to be linearly dependent on the laser intensity I, which yields [290]

$$\Delta k_d = -\alpha_i(q) \frac{\partial I(r, z)}{\partial z}. \tag{2.96}$$

This approximation is usually sufficient to describe phase matching of individual harmonic orders but does not provide the correct relative phase across the harmonic spectrum [284]. When the medium is placed before the focus at $z < 0$, the phase-matching contribution is negative (positive for $z > 0$), and its magnitude strongly depends on the spatial position because of the intensity dependence. Within the laser focus and for short trajectories, the contribution of Δk_d is small and can be neglected [291].

The neutral gas dispersion term of Equation 2.92 is given by

$$\Delta k_n = qp \frac{\omega_c}{c} (1 - \eta)(n_1 + n_2 I - n_q), \tag{2.97}$$

where p is the gas pressure, η is the ionization fraction, n_1 and n_q are the refractive indices of the gas medium at the fundamental laser frequency ω_c and the harmonic frequency $q\omega_c$, respectively [283, 292]. As opposed to solid materials, the intensity-dependent refractive index n_2 is typically small in gases [293, 294], and its influence on HHG phase matching can be neglected. Values for n_1 and n_q can be found in the literature [295, 296].

The HHG process is inefficient in the sense that the recombination probability of the tunnel-ionized electrons is small, and most electrons miss their originating ion and stay free for an extended time. If the time between consecutive laser pulses is much larger than this time, no plasma is present at the beginning of the pulse, and the ionization fraction η increases during the ionization process, starting from zero. However, this is only sometimes the case for high-repetition rate systems, as plasma can accumulate over many pulses. Replacing the refractive indices n_1 and n_q of Equation 2.97 with the plasma refractive indices n_1^e and n_q^e yields [280]

$$\Delta k_p = q \frac{\omega_c}{c} (n_1^e - n_q^e), \tag{2.98}$$

with

$$n_q^e = \sqrt{1 - \frac{N_e}{N_c}}. \tag{2.99}$$

The free electron density is denoted as N_e and can be calculated by ADK theory [269]. $N_c = \varepsilon_0 \omega^2 / e^2$ is the critical density at which the plasma frequency [297] $\omega_p = \sqrt{N_e e^2 / (m\varepsilon_0)}$ equals

the laser frequency and below which the plasma becomes opaque to electromagnetic waves of frequency ω [284]. Because of this, the free-electron dispersion mainly affects the fundamental light and the plasma dispersion of the harmonic field can be neglected due to its much higher frequency. The dispersion of the ions can also be neglected for small ionization fractions of $\eta < 10\,\%$ and it only becomes important for very high driving intensities, which are beyond cavity-enhanced frequency combs [298]. Rewriting Equation 2.98 in terms of η [282, 283] and assuming constant gas temperature leads to

$$\Delta k_{\mathrm{p}} \approx -qp\eta N_a r_e \lambda_{\mathrm{c}}, \tag{2.100}$$

with p, N_a, r_e, and $\lambda_{\mathrm{c}} = 2\pi c/\omega_{\mathrm{c}}$ being the gas pressure, atomic number density per pressure unit, the classical electron radius, and the central wavelength of the driving laser field, respectively.

The phase-matching contribution of the neutral gas is positive, while the plasma dispersion is negative. Neglecting geometric effects and comparing Equation 2.97 and 2.100, it becomes clear that phase matching is only possible if the ionization fraction stays below the critical ionization fraction [283, 299] which is defined as

$$\eta_{\mathrm{crit}} = \left(\frac{\lambda_{\mathrm{c}}^2 N_a r_e}{2\pi(n_1 - n_q)} + 1 \right)^{-1}. \tag{2.101}$$

Typically, the ionization fraction η is in the range of a few percent for the laser parameters used to generate XUV frequency combs [53, 91, 280].

Pressure-induced phase matching

If the ionization fraction is below the critical value ($\eta < \eta_{\mathrm{crit}}$), phase matching is possible by tuning the gas pressure. Recalling Equation 2.92, this leads to [291]

$$p_{\mathrm{match}} \left[\frac{\partial \Delta k_{\mathrm{n}}}{\partial p} + \frac{\partial \Delta k_{\mathrm{p}}}{\partial p} \right] + \Delta k_{\mathrm{g}} = 0, \tag{2.102}$$

and the solution yields the phase-matching pressure [300]

$$p_{\mathrm{match}} = p_0 \frac{\lambda_{\mathrm{c}}}{2\pi^2 w_0^2 \left(n_1 - n_q\right)\left(1 - \eta/\eta_c\right)}, \tag{2.103}$$

with the standard pressure $p_0 = 101.3\,\mathrm{kPa}$. This means that the phase-matching pressure as well as the Gouy phase scale inversely to the square of the beam radius w_0.

Figure 2.22 a) shows the phase-matching pressure for typical target gases and selected harmonics as a function of η. At low ionization fractions, p_{match} depends only weakly on the harmonic order and it is possible to phase-match a large part of the harmonic spectrum. As the ionization level approaches η_{crit}, p_{match} increases rapidly and the spectral window for HHG phase matching narrows.

From Equation 2.103 it becomes clear that high pressure is required for phase matching in the tight focusing regime (which is typically the case for XUV combs). This is illustrated in Figure 2.22 b), where the required xenon gas pressure for phase matching the 15th harmonic is plotted as a function of focus waist size and ionization fraction. This means that in order to achieve the required phase matching pressure in the generation region, backing pressures in the range of several bars are typically used for XUV frequency comb generation [53, 91, 93, 99, 101, 117]. The reason for this is that the gas pressure drops rapidly after leaving the end-firing gas nozzle and only about ten percent of the backing pressure is available at the laser focus.
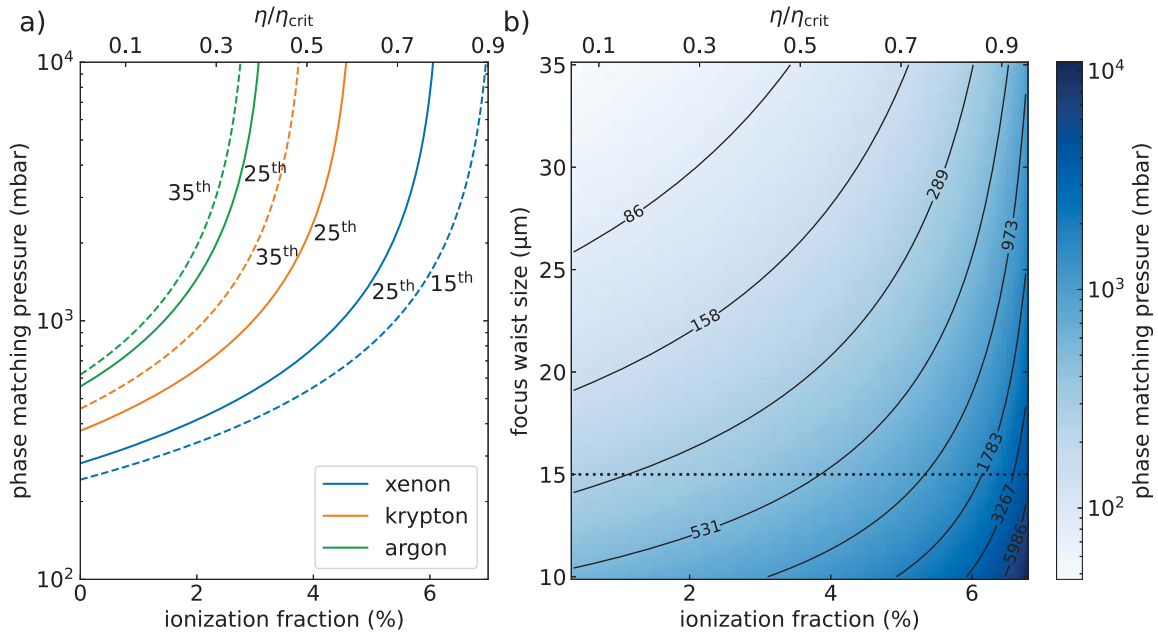
Figure 2.22: HHG phase matching can be achieved by tuning the target gas pressure. a) The phase-matching pressure p_{match} depends on the gas (shown: Ar, Kr and Xe) and the harmonic order q. Calculations are performed for a driving field centered at $\lambda_c = 1039$ nm and a focus waist size of $w_0 = 15\,\mu$m. b) A phase matching pressure map is shown for the 15th harmonic of xenon, as a function of ionization fraction η and focus waist size w_0. The horizontal dotted line indicates the waist size of the XUV-comb cavity, also used for calculating a). For such tight focusing conditions and significant ionization, phase-matching pressures in the range of a few bar are required. Figure adapted from [53].

2.7 Nonlinear temporal pulse compression

MPI and HHG are highly nonlinear processes, so a slight increase in laser intensity strongly affects their yield. Additionally, the HHG efficiency increases for shorter pulses because fewer cycles of the electric field contribute to the target gas ionization prior to the intensity maximum of the pulse [282]. Furthermore, shorter pulses have broader spectra, which increases the spectral coverage for spectroscopic applications. However, it requires more care in the optics' design of the experiment because dispersion management becomes essential.

With a wider spectrum, HHG transfers a broader fundamental spectrum to the XUV, so that more transitions in HCIs can be studied there. Additionally, we plan to utilize the field enhancement at sharp nano-tips to excite the ^{229m}Th nuclear isomeric state of thorium atoms deposited on a tungsten tip by simultaneous absorption of multiple photons. Direct laser excitation of this isomeric state at a wavelength of 148.71 ± 0.42 nm [301], corresponding to an excitation energy of $E_{is} \approx 8.3$ eV, is promising for future highly accurate nuclear clock operation [121, 302, 303]. This energy is very close to seven photons from our frequency comb laser, and broadening our laser spectrum nonlinearly enables us to cover the current uncertainty range of the thorium transition completely.

As the grating compressor of our fiber amplifier almost completely compensates dispersion, nonlinear spectral broadening enables further temporal compression of our pulses. Nonlinear pulse compression is based on spectral broadening by nonlinear interactions between the intense laser pulses and a nonlinear medium and compensation of the induced phases. Presented below is a comparison of methods used for spectral broadening and temporal compression, followed by our design of a flexible, continuously dispersion-compensated MPC for spectral broadening and nonlinear pulse compression [304].

2.7.1 Design considerations for a nonlinear pulse compressor

For optimized nonlinear pulse compression, it is important to accumulate significant nonlinear phase. On the one hand, a material with a high nonlinear refractive index n_2 can be used for this purpose. On the other hand, the intensity needs to be as high as possible and has to be maintained for a certain propagation distance. The high repetition rate of 100 MHz in combination with a pulse energy of $\sim 0.75\,\mu$J yields a high average power of 75 W, which results in constraints on the pulse compressor design. Assuming 200 fs pulses at the compressor input, the peak power is then ~ 4 MW.

Waveguides (optical fibers) offer the advantage of a small core in which the light propagates over extended distances. There is a distinction between solid and hollow-core fibers with different subtypes, such as conventional step-index fibers, gradient index fibers, solid or hollow-core PCFs, capillaries, and more. All these fibers have different mechanisms of how the light is confined and guided inside the core.

One of the most common techniques for few-cycle pulse generation is using a noble gas-filled hollow-core waveguide (stretched capillary) followed by dispersion compensation, typically with chirped mirrors [305–308]. These capillaries require millijoule pulse energies and, thus, are only used at relatively low repetition rates. Additionally, they have the disadvantage of high loss because the light is only weakly guided inside the hollow core.

PCFs, however, confine the light by exploiting the physics of photonic bandgaps with hollow microchannels running along the length of the fiber, thus producing an anti-resonant two-dimensional photonic crystal that prevents the light from escaping the core [309, 310]. Hollow-core PCFs can be used to compress few-μJ pulses to sub-10 fs and have reduced losses. Their nonlinearity and dispersion can be tuned by varying the pressure and gas mixture [311]. Typically, noble gases are used for pulse compression [312–315], but molecular gases can also be used

[316]. The Kagomé-type is the most used hollow-core PCF geometry. Contrary to true photonic bandgap guiding, Kagomé fibers use a low density of states separated from each other by a high density of states to confine the light instead of full bandgaps around the hollow-core [317, 318]. Even though it was demonstrated that pulse compressors based on these fibers could be operated in the 100 W average power regime [319], they are typically only used up to a few watts of power to avoid burning of the end-facets.

PCFs with small solid cores are often used for supercontinuum generation because of their strongly enhanced nonlinearities [320, 321]. The ability to engineer the dispersion profile allows the exploitation and study of highly nonlinear dynamics inside these fibers already at low input pulse energies [322–327]. Large mode-area PCFs can be used at elevated power [328, 329]. However, when coupling more than ~50 W into a fiber, minor misalignment or a contaminated end-facet can lead to the destruction of the system. To reduce this effect, it is possible to splice end-caps on the fiber ends to enlarge the illuminated surface at the glass-air interface. This reduces the chance of damaging the fiber at high power, but these systems are still not very robust. Even though temporal compression of 1 μJ pulses, at 250 W of average power, was demonstrated using a large-pitch fiber with a mode-field diameter of 59 μm, the ultimate limitation for dielectric waveguides is catastrophic self-focusing, which is a result of the optical Kerr effect. This nonlinear effect induces an intensity-dependent focusing lens. Therefore, the peak intensity keeps increasing as the pulse travels through the medium until medium damage interrupts this process. It happens at more than ~4 MW peak power (not intensity!) in fused silica with linearly polarized light. Hence, it is impossible to reduce the peak power by increasing the mode-field diameter, and temporal stretching is required. All in all, fibers are not the ideal choice for stable operation at high power.

Another simpler method for pulse compression is to use free-space beam interaction with the nonlinear medium. Nonlinear pulse compression based on spectral broadening in solid-state multi-plate materials and subsequent temporal compression with chirped mirrors allows the generation of supercontinuum-spanning spectra and few- and even single-cycle pulse duration even at high average power [330–333]. A disadvantage is that the input pulses are typically already below ~100 fs in duration and care must be taken to avoid excessive spatio-temporal couplings in the output beam.

A recent development that builds upon the multi-plate (single-pass) compression approach in a wide range of laser parameters is the Herriott-type MPCs, named after its inventor Donald R. Herriott [334, 335] who also co-invented the He:Ne laser [336]. These cells are commonly used for spectroscopy of gaseous targets due to the large interaction length of the medium with the laser light [337–339]. They have also been used inside femtosecond laser cavities to extend the cavity path length to increase the pulse energy by reducing the repetition rate [340, 341]. Beside these applications, Herriott cells can also be used for nonlinear spectral broadening of high intensity laser pulses in gases. Typically, at least 85 % transmission and five to ten-fold temporal compression down to tens of femtoseconds can be reached in a single stage [342, 343]. These cells can handle kilowatt-average-power levels [344] and millijoule pulse energies over extended periods of time. In addition, it is possible to integrate a transparent solid-state material plate into the cell to exploit the enhanced nonlinear refractive index n_2, which is about three orders of magnitude higher than in gases [345, 346].

A very advantageous property of MPCs is that the nonlinearity is distributed over many passes and is thus spatially homogenized. If the spatial phase induced by the Kerr effect in the nonlinear medium is much smaller than the phase-contributions from the propagation in the cell itself, spatial effects are washed out, and the temporal nonlinear phase is homogeneous over the whole beam profile [347, 348]. Provided that the medium is shorter than the self-focusing distance, this is still valid for peak powers above the self-focusing threshold. In addition, unlike

fibers, MPCs are rather insensitive to beam pointing fluctuations and it is possible to control the pulse propagation in a wide range by the choice of the nonlinear medium and mirror dispersion. Using multiple plates instead of just a single plate is advantageous because it leads to significantly higher spectral broadening factors and suppresses adverse features of single-pass bulk broadening [349, 350].

2.7.2 Multipass cell geometry

Herriott cells are constructed either from two spherically curved mirrors or a curved and a flat mirror, resulting in a cavity-like for a beam propagating on the optical axis. However, light is coupled in off-axis at the position (x_0, y_0) with a coupling angle of θ_x and θ_y through a hole or gap in the mirror or by means of a small so-called scraper mirror. An ABCD-matrix of a MPC can be defined according to the methods described in Section 2.3.1. The incoming beam only remains confined in the cell for multiple bounces if the same stability criterion as for optical cavities $|(A + D)/2| \leq 1$ is fulfilled. The ray-transfer matrix of a cell after n round trips then becomes

$$M_{\mathrm{MPC}}^n = \begin{pmatrix} \frac{A-D}{2} \frac{\sin(n\varphi)}{\varphi} + \cos(n\varphi) & \frac{B \sin(n\varphi)}{\sin(\varphi)} \\ \frac{C \sin(n\varphi)}{\sin(\varphi)} & \frac{D-A}{2} \frac{\sin(n\varphi)}{\sin(\varphi)} + \cos(n\varphi) \end{pmatrix}, \tag{2.104}$$

where φ is the change in angular position of the spots in the circle formed by successive bounces of the beam after each round trip [340]. Using the above expression, the transverse displacements x_n, y_n after n round trips are given by

$$x_n = x_0 \cos(n\varphi) + \left(\frac{x_0 (A - D) + 2B\theta_x}{2 \sin(\varphi)} \right) \sin(n\varphi) \tag{2.105}$$

$$y_n = y_0 \cos(n\varphi) + \left(\frac{y_0 (A - D) + 2B\theta_y}{2 \sin(\varphi)} \right) \sin(n\varphi), \tag{2.106}$$

as illustrated in Figure 2.23 a.
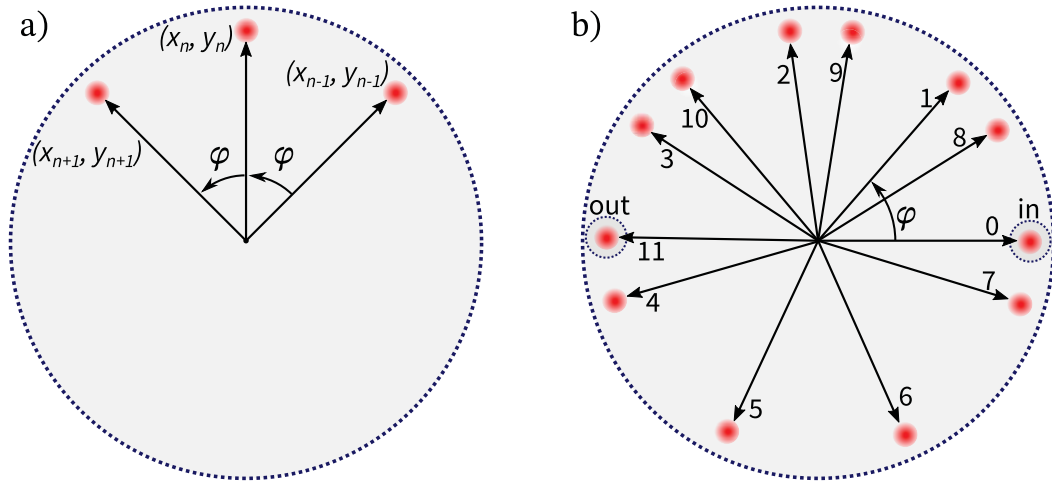
Figure 2.23: Laser spot pattern on the first MPC mirror. a) The spots on the mirror advance by φ after each round trip n, as defined in Equation 2.107. b) The spot pattern on the end mirror is shown for 22 passes through the crystal. This corresponds to $m = 3, n = 11$ and an angle of $\varphi = 49.1°$ between the spots on the mirror. Small dotted circles indicate the position of the scaper mirrors directly in front of the curved mirror used for in- and out coupling.

In order to preserve the complex q-parameter of the incident beam (cf. Section 2.3.1), the ABCD-matrix of the cell must be $M_{\text{MPC}}^n = (-1)^m M_{\text{I}}$, where M_{I} is the unity matrix and the integer m gives the number of semicircular arcs that the beam traverses on one of the mirrors before q is transformed back to its initial value [334, 340]. This yields the most important design rule for a q-preserving cell with n round trips

$$n\varphi = m\pi. \tag{2.107}$$

In a q-preserving cell, the re-entrant condition is met, and a replica of the incoming beam exits the cell, which reduces the sensitivity to beam pointing fluctuations [351].

For a given mirror radius of curvature R and integer n, the integer m determines the length of the cell L, and it is useful to define a constant representing the geometry

$$\xi = L/R = 1 - \cos(\varphi/2) = 1 - \cos(m\pi/2n). \tag{2.108}$$

Using this constant, the focal waist w_0 and the spot radius on the mirror w_{m} is given by [351]

$$w_0^2 = \frac{R\lambda}{2\pi}\sqrt{\xi(2-\xi)} = \frac{R\lambda}{2\pi}\sin(m\pi/2n) \tag{2.109}$$

$$w_{\text{m}}^2 = \frac{R\lambda}{\pi}\sqrt{\frac{\xi}{2-\xi}} = \frac{R\lambda}{\pi}\tan(m\pi/4n). \tag{2.110}$$

In the experiment, self-focusing modifies the spot sizes and needs to be accounted for in mode-matching.

The spot pattern of a cell design with 22 passes through the crystal is shown in Figure 2.23 b). Using the above Equation 2.107, this corresponds to $m = 3$ and $n = 11$ resulting in an angle of $\varphi = 49.1°$ between the spots on the mirror. Small scraper mirrors directly in front of the surface of the first curved mirror are used to couple the beam in and out. The beam is coupled out after the 22nd pass. Note that the beam passes the crystal twice on its way to and from the second end mirror, so the number of passes is twice the number of spots on the first end mirror.

2.7.3 Numerical modeling

Numerical simulations of the underlying linear and nonlinear propagation effects inside MPCs allow a deeper understanding of the physics and thus make it possible to optimize the design. The best simulations include both spatial and temporal effects, as well as their interaction, and are performed in 3D for the field $\mathcal{E}(x, y, t)$ for propagation along z [348]. These models often include many effects, such as dispersion, wavelength-dependent diffraction, SPM, self-focusing, self-steepening, Raman scattering, and plasma effects. In cases where spatio-temporal couplings can be neglected, simpler models which describe the pulse only in the time domain are sufficient [352]. These simple models allow fast parameter scanning and produce reliable results for cells with only modest nonlinearities for pulse compression, which is the case for our cell. Therefore, our simulations build upon available code for the propagation of ultrashort pulses in optical fibers. In our simulation code [304], we include a python open-source generalized nonlinear Schrödinger equation (GNLSE)-solver [353], based on code from J. M. Dudley and J. R. Taylor initially used to study supercontinuum generation in nonlinear optical fibers [354].

In the following text, the theory underlying the numerical simulations is briefly summarized. For that, we recall the definition of the slowly-varying envelope $\mathcal{A}(z)$ with respect to the carrier frequency ω_0 [324] (cf. Equation 2.13)

$$\mathcal{E}(z, t) = \mathcal{A}(z, t)e^{-i\omega_0 t}. \tag{2.111}$$

The propagation constant $\beta(\omega)$ can be Taylor-expanded similarly as the intra-cavity phase (cf. Equation 2.59)

$$\beta(\omega) = \beta_0 + \beta_1(\omega - \omega_0) + \frac{1}{2}\beta_2(\omega - \omega_0)^2 + \frac{1}{6}\beta_3(\omega - \omega_0)^3 + \cdots, \tag{2.112}$$

with the coefficients

$$\beta_n = \left(\frac{\partial^n k(\omega)}{\partial\omega^n}\right)_{\omega_0}. \tag{2.113}$$

A new reference frame moving along with the pulse at the group velocity $v_g = 1/\beta_1$ is defined by introducing $T = t - z/v_g$. Neglecting higher-order ($n > 2$) dispersion and self-steepening leads to the nonlinear Schrödinger equation (NLSE)

$$i\frac{\partial}{\partial z}\mathcal{A}(z,T) - \frac{\beta_2}{2}\frac{\partial^2}{\partial T^2}\mathcal{A}(z,T) + \gamma|\mathcal{A}(z,T)|^2\mathcal{A}(z,T) = 0, \tag{2.114}$$

where the second-order term β_2 accounts for the group-velocity dispersion (GVD) and the strength of the nonlinearities depends on the nonlinear parameter γ [289].

GVD has an important impact on pulse propagation because pulses always have a certain spectral bandwidth leading to different propagation velocities. In the normal dispersion regime, higher-frequency components travel slower, which results in an increase of the instantaneous frequency with time, called (positive) chirp. The instantaneous frequency is defined as

$$\omega(t) = \frac{d\varphi(t)}{dt}, \tag{2.115}$$

with the unwrapped (temporal) phase $\varphi(t)$. Vice versa, anomalous dispersion causes negatively chirped pulses. In dispersive media, initially unchirped pulses are stretched in time. The total chromatic dispersion properties of MPCs are defined by the combination of material (e. g. air, glass) and mirror dispersion. Therefore, a careful choice of the mirror coating is important for successful operation. Otherwise, the pulses get too long and the peak intensity drops, which results in the weakening of nonlinear effects.

The nonlinearities in Equation 2.114 are governed by the optical Kerr effect. Its physical origin is the generation of a nonlinear polarization by the light field (cf. Equation 2.2). It results in a change of the refractive index as a function of intensity that acts back on the propagation properties of the light itself [289]. The nonlinear parameter γ is defined as

$$\gamma(\omega_0) = \frac{\omega_0 n_2}{c A_{\text{eff}}}, \tag{2.116}$$

with the effective mode area A_{eff} and the intensity dependent refractive index

$$n = n_0 + n_2 I, \tag{2.117}$$

where n_0 denotes the linear and n_2 the nonlinear part of the refractive index n. The nonlinear index $n_2 = 3\chi^{(3)}/(4n_0^2\epsilon_0 c)$ is linked to the $\chi^{(3)}$ nonlinearity of the material and is determined experimentally [293, 294, 355].

The nonlinear change of the refractive index is directly related to a nonlinear phase delay with the same temporal shape as the laser pulse, which leads to the generation of new frequencies and is called SPM. It leads to an approximately linear and positive chirp over a large central region for typical pulse shapes (e. g. Gaussian or hyperbolic secant). As a result, the chirp introduced by SPM can be compensated by anomalous dispersion, which enables stable soliton solutions of the NLSE.

For ultrashort (few cycle) pulses, the simple picture of pure Kerr nonlinearities breaks down and further perturbations have to be considered [324]. Because the refractive index depends on the intensity, pulses will be distorted during propagation because the peak of the pulse travels slower than the leading and trailing edges, known as self-steepening [356]. This leads to the formation of a shock at the trailing edge of the pulse, where new frequencies are generated and the spectrum is broadened asymmetrically [357, 358]. Additionally, since ultrashort pulses also have a large spectral bandwidth, higher order dispersion needs to be considered.

The GNLSE extends the NLSE (cf. Equation 2.114) by including higher-order dispersion terms and the above mentioned self-steepening as well as the Raman response. Its validity range is extended down to few-cycle pulses [321, 324, 359]

$$
\left(\frac{\partial}{\partial z} + \frac{\alpha}{2} - \sum_{k \geq 2} \frac{i^{k+1}}{k} \beta_k \frac{\partial^k}{\partial T^k} \right) \mathcal{A}(z, T)
$$
$$
= i\gamma \left(1 + i\tau_{\text{shock}} \frac{\partial}{\partial T} \right) \left(\mathcal{A}(z, T) \int_{-\infty}^{+\infty} R(T') |\mathcal{A}(z, T - T')|^2 \mathrm{d}T' \right),
$$

(2.118)

where α accounts for the losses during propagation. The Raman response function $R(T)$ describes the instantaneous and delayed material response [360]. The most important difference to the NLSE is the time derivative on the right hand side of Equation (2.118). It accounts for dispersion of the nonlinearity and describes effects such as self-steepening and shock formation on the time scale $\tau_{\text{shock}} = 1/\omega_0$.

We apply the split-step (Fourier) method to solve the GNLSE [324], and the crystal is divided in several small steps of size dz. In our case, a step size of d$z = 0.1$ mm proved to be sufficient. The method to simulate the nonlinear dynamics inside the cell is illustrated in Figure 2.24.

First, the nonlinear step is calculated in the time domain. In this way, the nonlinearities can be added as simple phase terms by multiplication in the time domain, whereas in the spectral domain a computationally more costly convolution would be needed. Then, the signal is transformed to the spectral domain by the Fourier transform and the linear term (dispersion) is added. In the end, the signal is transformed back to the time domain and the process starts again. At our pulse parameters, the nonlinearities of the crystal are dominating and we can neglect nonlinearities in the gas medium. Therefore, it is sufficient to treat the propagation in the gas only once per pass by adding the corresponding phase term in the spectral domain. Mirror dispersion is added in the same way.

The results from a simulation of an evacuated MPC propagation with 22 passes through 10 mm of fused silica (FS) and two mirrors with a negative GDD of $-125\,\text{fs}^2$ each are shown in Figure 2.25. Pulses are compressed by a factor of ~ 5 from initially 200 fs to 38 fs. The spectral width increases from $\Delta\lambda_{\text{in}} = 3.4$ nm to $\Delta\lambda_{\text{out}} = 57$ nm. The spectral bandwidth $\Delta\lambda$ is stated in terms of the root mean square bandwidth [361]. Using a chirped-mirror pulse compressor behind the cell with a total GDD of $\sim -250\,\text{fs}^2$, it is possible to shorten the pulses to sub-30 fs.

This larger bandwidth is beneficial not only for spectroscopic applications where it increases the number of accessible transitions but also greatly enhances the efficiency of highly nonlinear processes such as MPI and HHG. In Section 4.3, we use these theoretical findings for the experimental realization of a MPC for nonlinear pulse compression.
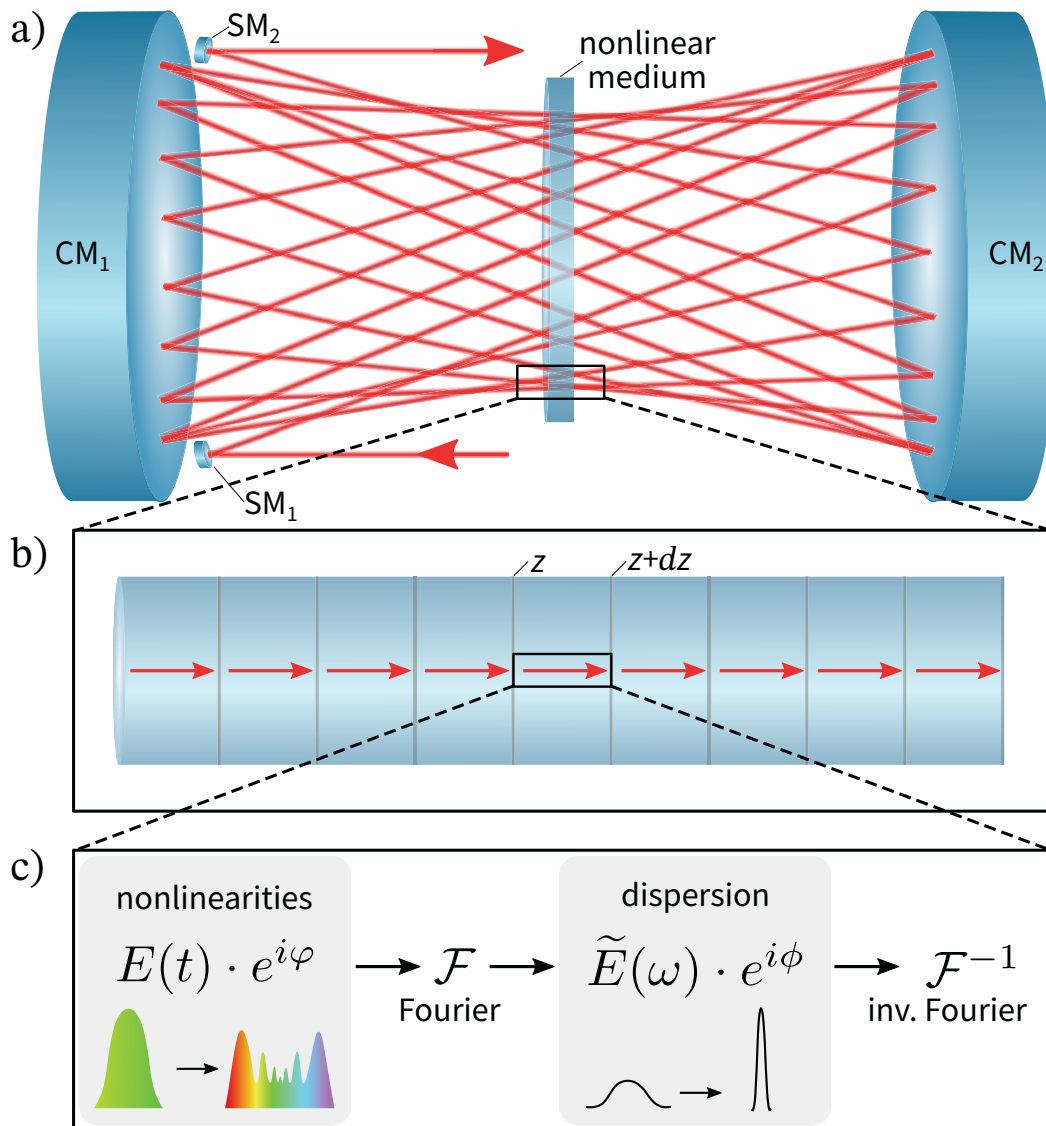
Figure 2.24: Illustration of the working principle and the split-step Fourier method used for the simulations of the MPC. a) The beam is coupled in with a small scraper mirror SM$_1$ and bounces back and forth between large curved mirrors M$_{1,2}$ while passing through the nonlinear medium. The beam is coupled out after the last round trip by SM$_2$. b) For the simulations, the crystal is split in small steps with size dz. c) In each increment, the nonlinearities are added first in the time domain and the spectrum is broadened by SPM. The dispersion is applied in the spectral domain and affects the pulse duration. A Fourier transform links the time and frequency domains. Graphical representation inspired by [304, 351].
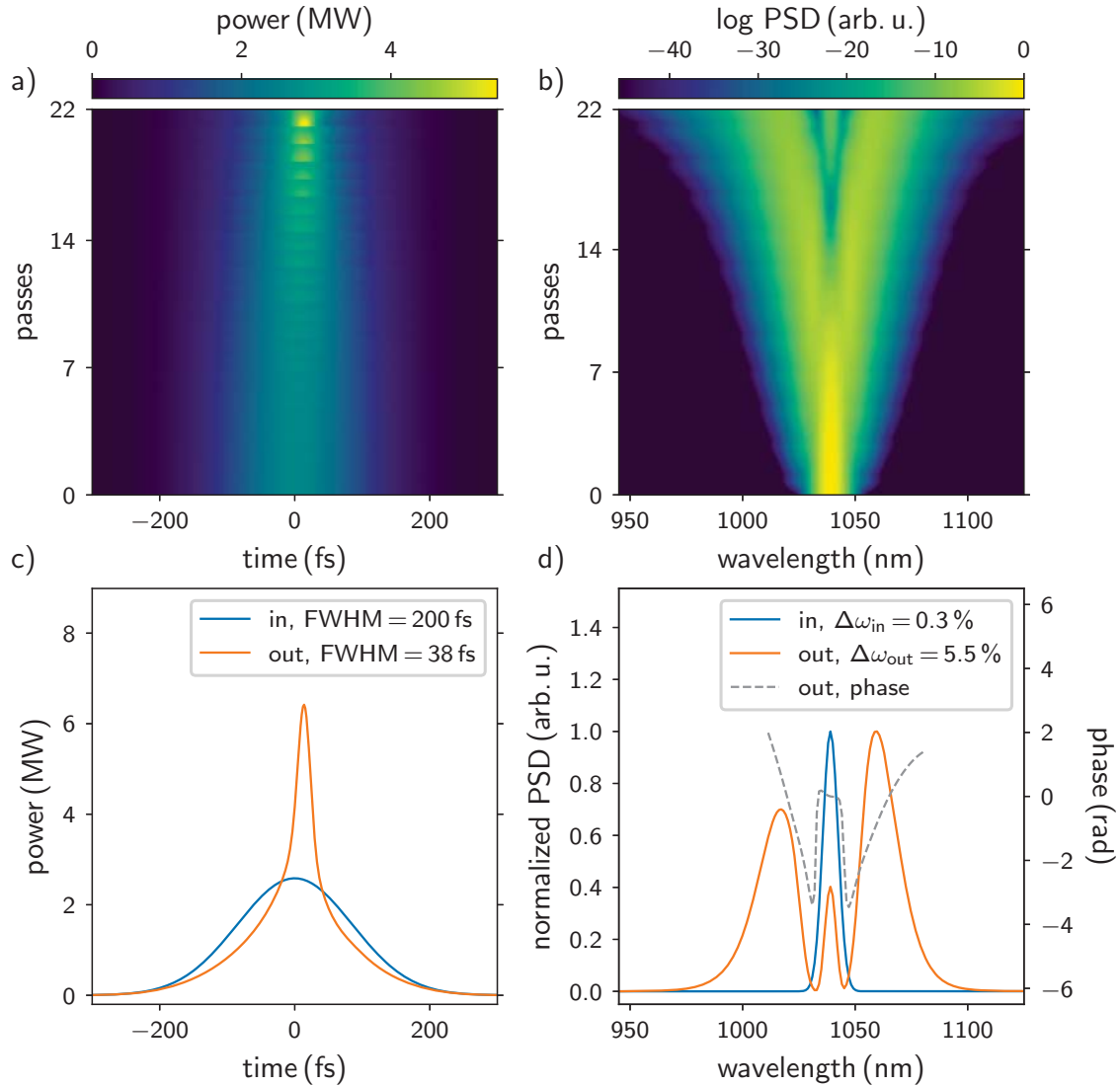
Figure 2.25: Simulation of the nonlinear dynamics inside a MPC with incident 200 fs pulses with an energy of 750 nJ focused to a 75 μm waist. The initial peak power of 2.6 MW increases to 6.4 MW after 22 passes through 10 mm of FS. The cell is evacuated, and two mirrors with a negative GDD of −125 fs^2 each are used. The evolution of the pulse in the temporal and spectral domains are shown in a) and b), respectively. c) After propagation through the cell, the pulses are compressed to 38 fs FWHM pulse duration, and the spectrum broadens from $\Delta\omega_{in} = 0.3\%$ to $\Delta\omega_{out} = 5.5\%$, as shown in d).

3 Intra-cavity high-harmonic generation

In this chapter, the different parts of the experimental setup used for intra-cavity HHG are described and characterized. First, the frequency comb laser source, amplifier, and compressor are treated. Afterwards, the optical and mechanical setup of the fsEC used for XUV frequency comb generation, named HHG cavity, is explained. Furthermore, the vacuum system and differential pump system with gas-recycling for closed-loop long-time XUV comb operation is presented.

3.1 Laser system

Conventional systems for HHG and MPI studies are based on titanium-doped sapphire lasers (Ti:sapph) [362]. Mode-locked Ti:sapph lasers have long been known as the workhorse for ultrashort pulse generation due to their ability to emit few-cycle pulses with octave-spanning spectra directly out of their oscillators [206–208]. This is the reason why the first frequency combs developed out of mode-locked Ti:sapph lasers [29, 30, 32–34, 37]. The main reason behind that is the large gain bandwidth and the robustness of the crystal material, which allows straightforward Kerr-lens mode-locking by tuning the spatial overlap between the pump beam and the cavity mode [203, 363, 364]. Usually, the megahertz repetition rate of the pulses from the oscillator is decreased by a pulse-picker. Then, the low repetition rate pulses on the order of a few kilohertz are amplified by chirped-pulse amplification [198, 365] to high pulse energy and used for experiments. Often, stretched capillaries are used after the amplifier to broaden the spectrum and produce intense few-cycle pulses [305–308]. A method to reach high intensity also at a high repetition rate is the enhancement of the pulses in a high-finesse cavity. Indeed, the first XUV frequency combs were based on intra-cavity HHG of cavity-enhanced Ti:sapph lasers [83, 84, 108]. A significant drawback of Ti:sapph-based laser systems is reliability. They require frequent re-alignment - as everybody who has ever worked with one of these systems can confirm. Additionally, expensive high-power CW pump lasers with excellent beam quality are required for operation.

On the contrary, considerable progress was made in developing Yb-based fiber technology. Today, high-power and low-noise Yb:fiber lasers and their components are commercially available [103]. They offer the advantage of insensitivity to the environment, which results in high stability even at high power operation, enabled by the geometry, which allows effective cooling of the active fiber core. These are the main reasons why Yb:fiber lasers are nowadays used in high power and high repetition-rate laser systems. To study highly nonlinear processes, such as HHG in cavities, it is more convenient to use a higher input power and a lower finesse, as opposed to the early high-finesse femtosecond enhancement cavities because plasma instabilities complicate the operation of those [109, 217]. Therefore, we also chose such a system to drive our enhancement cavities. In this section, the frequency comb laser is introduced first, followed by the description of our home-built amplifier and compressor system.

3.1.1 Frequency comb laser source

The frequency comb laser system has already been described in the PhD thesis of J. Nauta [53]. Following that description, a brief overview of the system will be given here for completeness. We use a commercial frequency comb laser (Menlo Systems, FC1000-250) with a 14 nm FWHM
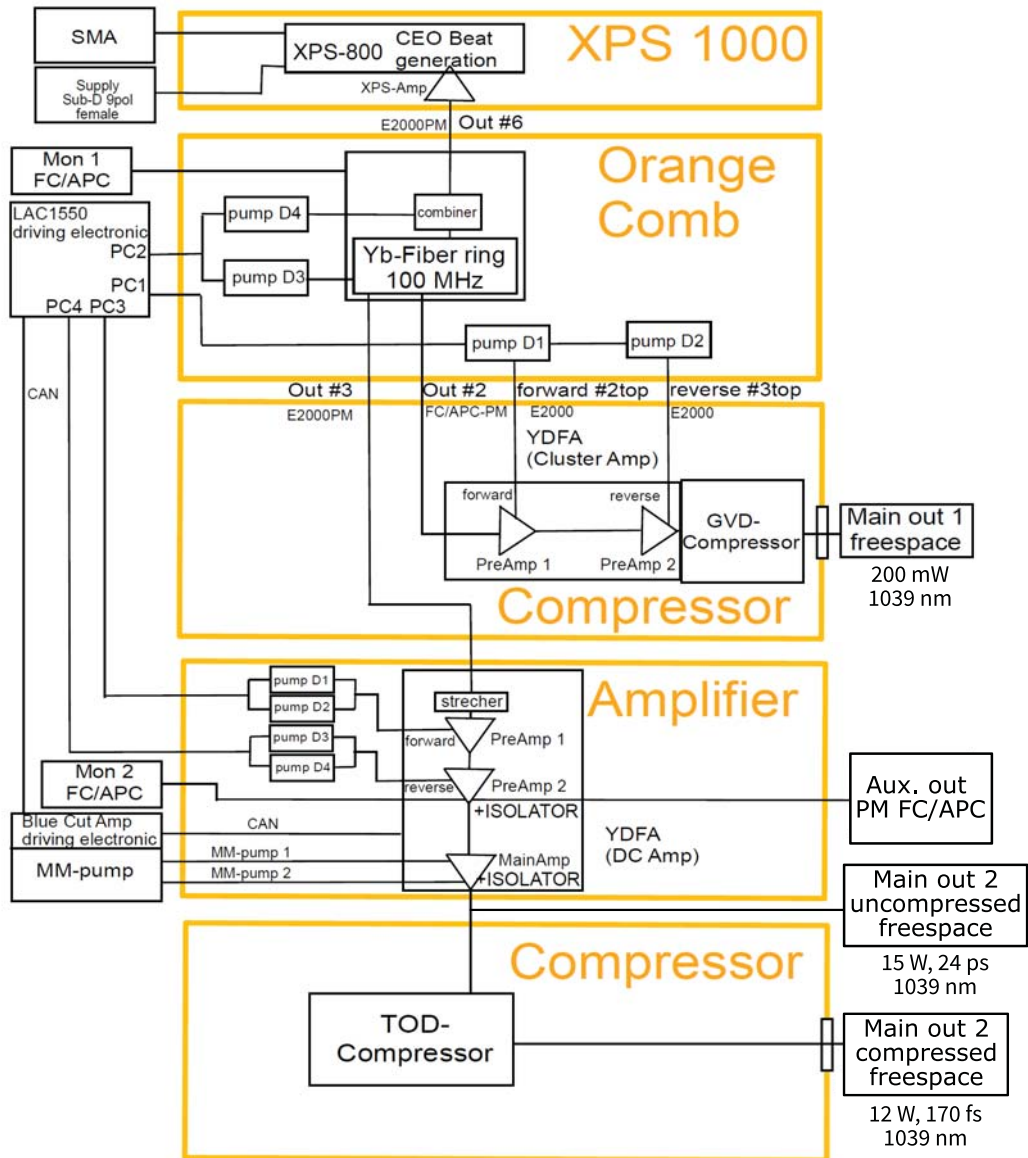
Figure 3.1: Schematic overview of the commercial frequency comb laser system. The light from the first main output can be used to detect a beating with a CW laser. The uncompressed output from the second main output is used to seed our home-built amplifier. Additionally, a third-order dispersion (TOD) pulse compressor can be used to output 10 W, 170 fs pulses, centered around 1039 nm. Figure provided by the manufacturer Menlo Systems GmbH.

spectral bandwidth centered around 1039 nm. A schematic overview of the system is given in Figure 3.1. The Yb:fiber-based oscillator has a free-space section, where the CEO and the repetition rate can be changed with motorized translation stages. The repetition rate can be adjusted by 1 %, which corresponds to a path length change of 30 mm of the fiber ring cavity at the 100 MHz repetition rate of our system. Fast feedback and locking of the cavity length can be achieved with the piezo-actuated cavity mirror, and fast changes of the CEO are performed by pump current modulation.

The repetition rate is detected with a fast photodiode. The 10th harmonic of this signal ($\sim$1 GHz) is mixed with the signal of a 980 MHz phase-locked oscillator (PLO), which is a low-noise fixed frequency synthesizer. The relative phase between this mixed signal and the $\sim$20 MHz signal from a direct digital synthesizer (DDS) are detected with a phase detector. A proportional-integral-derivative (PID) control loop then acts on the repetition rate. Figure 3.2 shows a schematic overview of the locking electronics. The CEO is detected with an f-to-$2f$ interferometer in the XPS-800 unit, as described in Section 2.2. The signal is amplified and transmitted through a 20 MHz band-pass filter, and the phase is compared to the DDS signal. An integrated PID control loop then modifies the pump current of the pump laser diodes of the oscillator. The 20 MHz band-pass filter allows CEO-locking only at this value. In practice, the free-running stability of the CEO is good enough to manually compensate for the slow drifts from time to time during experiments.
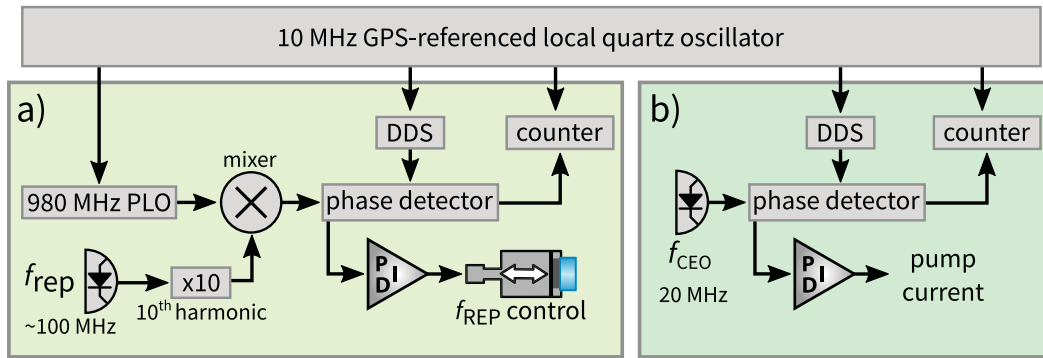
Figure 3.2: Schematic overview of the used locking electronics of the commercial frequency comb laser system. The electronics for locking the repetition rate are shown in a), and for f_{CEO} in b). A 10 MHz Global Positioning System (GPS)-referenced quartz oscillator is used as a frequency reference.

The DDS has a tunable output frequency with a resolution of 10 μHz and is locked to the 10 MHz GPS-referenced oscillator. With our setup it is currently possible to stabilize the repetition rate to a fractional uncertainty of 10×10^{-12} within 1 s but our system is already prepared for locking it to an optical reference to further improve the stability.

Besides a few auxiliary fiber-coupled outputs that we use to monitor the laser system, it has two main free-space outputs that have their own fiber amplifiers: A compressed low power output for optical beating with CW lasers and a high power output, as shown in Figure 3.1. The light exiting the first main output is broadened in a highly nonlinear PCF and superimposed with a CW laser on a fast photodiode. The beat-signal can then be used to lock the laser to the comb or the other way round, or determine the absolute frequency of the laser, as it was done with the 441 nm spectroscopy laser of the ALPHATRAP experiment for the first optical excitation of a HCI in a Penning trap [366].

For the high power output, a two-stage pre-amplifier followed by a single-stage main amplifier boosts the output power of the stretched 24 ps long pulses up to 15 W of average power. Two

optical isolators prevent the laser system from back-reflected light that could lead to instabilities and damage of the oscillator. A grating and prism (GRISM) compressor compensates dispersion and produces up to 12 W of average power pulses at a duration of 170 fs. This output was used for our very first intra-cavity MPI experiments [129]. A removable mirror is used to bypass the TOD compressor and allows to directly use the uncompressed pulses as the seed for our home-built high power amplifier, which is described in the following.

3.1.2 Amplifier and compressor

For MPI-studies and XUV comb generation, the pulses of our commercial frequency comb fiber laser need to be amplified prior to further enhancement inside a cavity. For optimal phase stability of the frequency comb, nonlinear effects in the amplification chain have to be omitted. Besides adding excess noise, nonlinearities impose fundamental limitations on fiber amplifier systems, which may lead to severe spatial and temporal pulse distortions and even damage to the fiber. Especially, the small mode size and the long interaction length inside the elongated fiber core can lead to the onset of nonlinearities, even at rather low power levels [324]. This effect can be desired, for example in supercontinuum generation in photonic crystal fibers, where nonlinear effects are intentionally enhanced [321].

It has been shown that SPM in a gain fiber can broaden the spectrum at high power and even produce shorter pulses than the input pulses [367–369], but at the expense of robustness and system stability. Aside from that, the balance of pre-chirp and nonlinear phase requires to operate these amplifiers always at the same (maximum) power level.

For fiber amplifiers, the most detrimental nonlinear effects are stimulated Brillouin scattering (SBS) and stimulated Raman scattering (SRS) [370]. SBS arises from the interaction of guided light with acoustical phonons inside the fiber. After a certain power threshold, laser power is transferred from the signal to frequency down-shifted light propagating in the opposite direction, which can destabilize or even damage the seed laser [371]. Fortunately, the SBS gain is inversely proportional to the spectral bandwidth and not of concern to us. On the other hand, SRS is an optical-phonon-based nonlinear effect that is utilized in broadband Raman fiber amplifiers as the gain effect but, at the same time, limits the performance of high-power amplifiers. In SRS, the laser frequency is downshifted by an amount determined by the vibrational modes of the medium, which is ~13 THz in fused silica [372]. In our case, no SRS components arise in the spectrum at 1087 nm.

To avoid nonlinear effects during amplification, we apply the concept of chirped-pulse amplification (CPA), which was awarded the Nobel Price in 2019 [198, 365]. In CPA, pulses are temporally stretched by dispersion prior to amplification. After amplification, temporal re-compression yields pulses with high peak power after the amplification process. To further minimize the peak intensity at a given pulse energy, it is not only necessary to stretch the pulse temporally but also spatially by using a large beam diameter. Fibers with large mode areas have proven well suited for high average-power applications and are nowadays commercially available [373–375].

Using the above concepts to minimize nonlinearities, fiber amplifiers offer significant advantages over bulk solid-state amplifiers, especially at high repetition rates. The waveguide structure guides the light stably over long distances and enables large single-pass gain because of the long interaction length with the active medium. It leads to high average output power and an excellent beam quality that is essentially power independent [376].

In our home-built amplifier system, which is shown in Figure 3.3, we use a rod-type large-mode-area (LMA) fiber with a length of 800 mm (aeroGAIN rod module 2.0 PM85, NKT photonics). The fiber is equipped with high-power anti-reflection (AR)-coated end caps and is mounted in a stable aluminum mount with integrated water cooling for thermal management. The signal core is doped with Yb and guides the light with a mode-field area of $3300\,\mu m^2$. The backwards
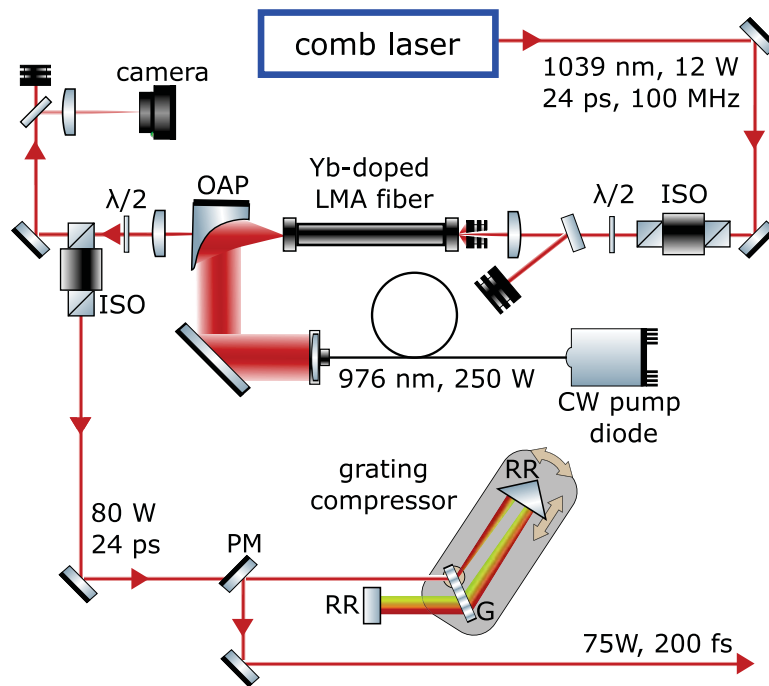
Figure 3.3: Schematic overview of the home-built amplifier and grating compressor setup. Stretched pulses from the commercial comb laser are amplified in an Yb-doped rod-type fiber amplifier, reversely pumped by a 250 W multi-mode fiber-coupled laser diode that is focused by an off-axis parabolic mirror (OAP). To enable counter-propagating pulses in the cavity, high-power optical isolators (ISOs) are placed before and after the active fiber to remove backwards-propagating light and prevent it from being sent back into the comb laser. The grating compressor can be rotated around the point where the incident light is transmitted through the grating. Retroreflectors (RRs) reflect the beam by 180° with a beam offset. The picking mirror (PM) with a vertical offset reflects the beam towards the experiments after compression.

pumping method is chosen because it can generate the highest pulse energies with the lowest losses through amplified spontaneous emission while minimizing nonlinear effects in the fiber [377]. Nonlinearities are weakened in backward pumping operation due to a lower spatially integrated peak power than forward pumping, where signal peak power rises quicker and stays higher for longer.

A high power fiber-coupled laser diode (D4F2S22-976.3-250C-IS58.1, DILAS) offers 250 W of CW pump power at a wavelength of 976 nm. Pumping at 976 nm has a higher quantum efficiency than often used 915 nm laser diodes with the advantage of high amplifier efficiency. After a fiber collimator with $f = 58$ mm and two dichroic turning mirrors, the pump light is coupled to the rod-type fiber with a gold-coated off-axis parabolic mirror (OAP) (MPD229H-M03, Thorlabs) with a 3 mm diameter central hole for signal light transmission. As a result of the hole being in the center of the mirror, a fraction of the 19 mm diameter pump beam profile is cut away. Furthermore, pump-light absorption of the gold coating is rather high, and thus, only 230 W are sent to the fiber. The OAP is mounted on a water-cooled adapter on a three-axis stage for alignment. Compared to conventional setups with a lens and dichroic mirror for combined signal and pump light, the main advantage of this coupling setup is the absence of pump light-induced thermal lensing effects in the signal beam path. On the signal entrance end of the fiber, a water-cooled annular beam dump with a hole for the signal light cuts away the highly divergent exiting pump light [103]. Additionally, a dichroic mirror and a second water-cooled beam dump filter and block the remaining pump light.

A high-power Faraday isolator (PAVOS Ultra-05–I-1015-1065, Soliton) is used between the amplifier and source to protect the comb laser from unwanted back-reflections. This single isolator proved sufficient for stable intra-cavity HHG operation [53]. However, a second isolator of the same kind was added between the rod-type fiber output and the compressor to enable intra-cavity colliding pulse operation with arbitrary polarization. The reason is that the reflected incident light of one propagation direction propagates collinearly with the other propagation direction but in the opposite direction. It is thus sent back directly into the laser. Nonlinearities in the Faraday rotator crystal are minimized by placing it in the uncompressed beam path. Zero-order HWPs (WPH10M-1030, Thorlabs) are used before and after the fiber to match the signal polarization light to the polarization axis of the gain fiber and maximize transmission through the second isolator, respectively.

Amplifier interlock and monitoring system

To prevent the amplifier from damage, we developed an interlock system. It quickly shuts down the pump power supply, if the seed is interrupted. Additionally it is used to monitor parameters, such as temperature and cooling water flow at several places.

The interlock system consists of a fast analog and a slower part based on a microcontroller (Arduino Mega 2560). The fluorescence decay time of Yb-doped glass is typically around 0.8 ms, but can be as low as 0.2 ms for high Yb doping concentrations [378, 379]. Therefore, the fast interlock needs to shut down the 250 W pump at a similar time in the case of interrupted seed light. Otherwise, a behavior similar to Q-switched laser operation can occur. Since the rate of stimulated emission drops to zero, when the seed is interrupted, the energy stored in the fiber increases during pumping until it saturates. Because of the large amount of energy stored in the gain medium, the first pulse of the seed laser is amplified rapidly to a giant pulse with very high peak intensity, which could cause fatal damage to the fiber and subsequent optics.

In the fast part of the interlock, a photodiode (VBPW34SR, Vishay) detects a small portion of the seed beam reflected from the dichroic mirror before the incoupling lens. A transimpedance amplifier (OP27) with a variable amplification factor amplifies the photodiode signal, and this value is then compared to a threshold voltage. The potentiometers (DS1845) used to set the

amplification factor, and the threshold voltage of the comparator (LM311) are programmable by the same microcontroller, which is also used to monitor the water flow and temperature at several locations. The interlock is triggered when the seed power drops below ~ 2 W, and the laser diode output is switched off within 1.5 ms. An integrated display shows the current status, and all parameters can be logged with a connected computer.

Pulse compressor

A grating compressor compresses the pulses exciting the rod-type fiber. The compressor consists of an AR-coated 1000 grooves mm^{-1} transmission grating made of 6.35 mm thick fused silica with a free aperture of 28 x 18 mm^2 (1158 2818 6.35 H, Gitterwerk GmbH), followed by a retroreflector mounted on a translation stage (PT1/M, Thorlabs). The grating is operated under the Littrow angle of incidence ($\Theta_{AOI} = 31°$) to reach the specified maximum grating efficiency of ≥ 98.5 % at 1030 nm. After the first pass of the beam through the grating, different frequency components of the pulses are fanned out due to the angular dispersion introduced by the grating.

A two-mirror retroreflector guides the beam back towards the grating while inverting the horizontal orientation of the different frequency components. At the second pass through the grating, the angular dispersion of the grating parallelizes the propagation directions of all frequency components. In order to have a round beam profile with all frequency components overlapping, a second vertically oriented retroreflector sends the beam back through the compressor with a slight vertical displacement of the beam, which enables pick-up after the compressor. For optimal alignment, the grating is mounted on a gimbal mount with three axes of tilt adjustment (UGP-1, Newport). At the same time, the whole compressor assembly sits on a rotatable plate, with the pivot point below the grating, as shown in Figure 3.3. This degree of freedom of rotation, in combination with the free adjustability of the grating angle, makes it possible to easily adjust the angle of the laser with respect to the grating. The mounting position of the translation stage of the first retroreflector can be changed by a dovetail guide integrated into the rotatable baseplate.

Due to the high diffraction efficiency of the grating, a total compressor efficiency of 95 % is reached, which is a significant improvement compared to other grating-based systems with only 65-85 % total efficiency [103, 380, 381]. The performance of the amplifier and the compressor is shown in Figure 3.4.

Before implementing the high-efficiency grating compressor, we designed and implemented a GRISM compressor [382, 383]. The advantage of a GRISM compressor compared to a pure grating- or pure prism-based compressor is that it enables compensation of GDD and TOD simultaneously. This is possible because both introduce negative GDD but with opposite signs of TOD. Thus, cascading a grating- and a prism compressor enables GDD and TOD compensation [384]. It has been shown that this setup can be simplified by integrating a grating and a prism into a single compression unit [385, 386]. We adapted this concept with a 800 grooves mm^{-1} volume phase grating and an SF11 prism. It allowed compression down to 150 fs, outperforming the commercial compressor integrated into our frequency comb laser system.

Unfortunately, strong thermal effects prohibited using the GRISM compressor for high-power cavity operation. Thermal lensing became noticeable when attempting to compress pulses with more than ~ 10 W of average laser power. Heating of the grating to over 100 °C and of the prism to 32 °C at full amplifier power was observed with a thermal camera [383]. In the future, a revised GRISM design based on a new highly efficient grating and a larger prism with AR coating on both sides could deliver shorter pulses to the experiment, with the cost of a more complicated geometric design and higher losses than in our current grating compressor. Additionally, optimizing the GRISM compressor is more delicate than a single grating compressor because of the many degrees of freedom. A better solution is the temporal post-compression of our pulses by
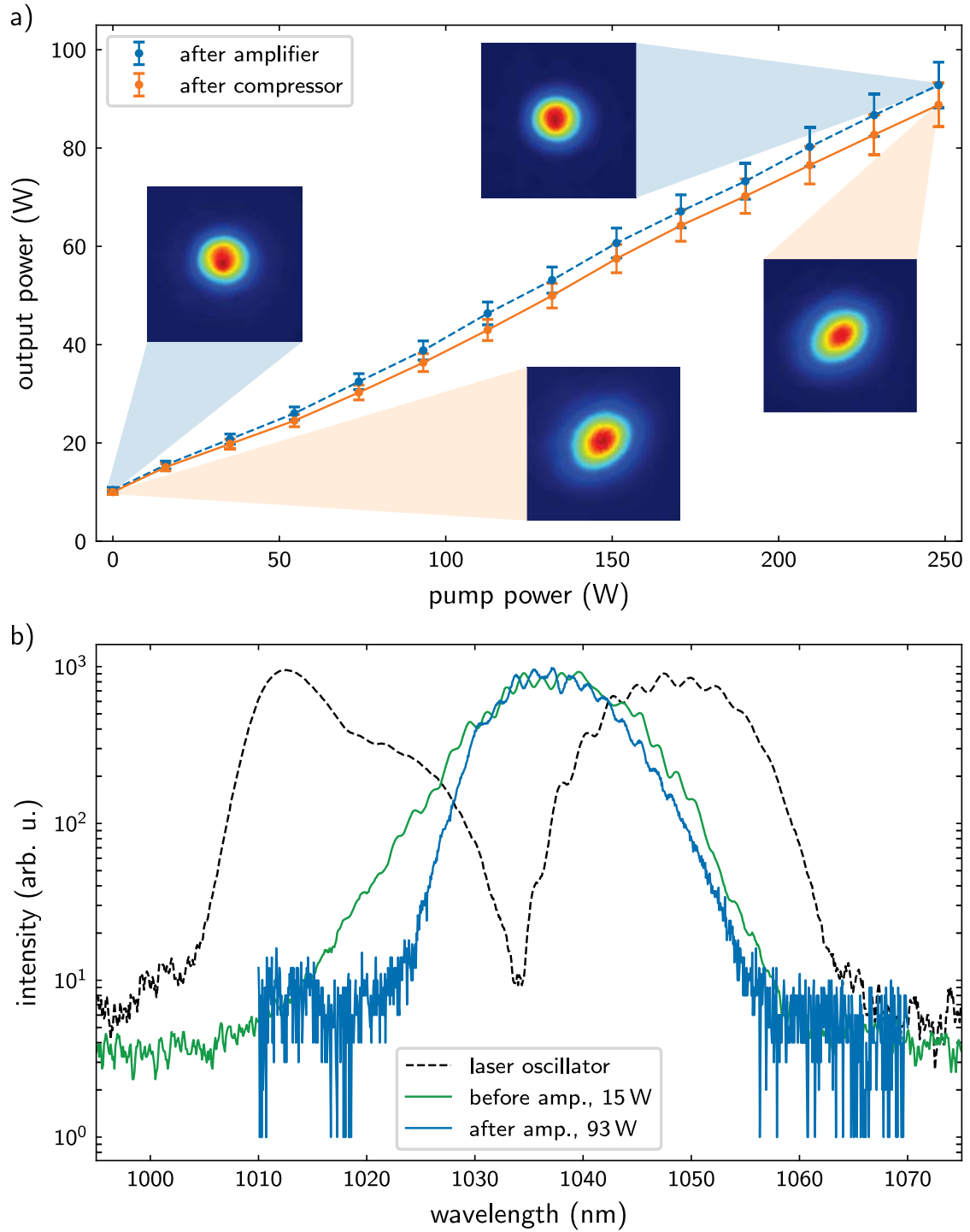
Figure 3.4: High-power rod-type fiber amplifier performance. a) The optical output power after the amplifier fiber and after the compressor is measured as a function of pump power at 976 nm. The insets show far-field beam profiles. The compressor reaches a power-transmission efficiency of 95 %. b) Spectra are measured at different positions in the laser system. The spectrum from the oscillator narrows significantly in the built-in amplifiers of the commercial comb laser system. The high-power fiber amplifier reduces the spectral width only slightly. Adapted from [53].

nonlinear spectral broadening, as explained in Section 4.3.

The pointing stability of our complete laser system, including the frequency comb oscillator, the fiber amplifier, and the compressor, is excellent. Only minor optimization of the seed and pump light coupling into the high-power fiber amplifier is necessary every few weeks at most. The great advantage of the fiber-based high-power amplifier is that it serves as an ideal beam reference and decouples the components of the laser system. Even if the coupling into the amplifier fiber is lost, the beam path after the fiber would keep its alignment, and the coupling into the enhancement cavities is never lost. All in all, the system is very reliable, and its turnkey operation makes daily lab work pleasant.

3.2 HHG cavity

For the generation of high-harmonics, high laser intensities in the range of $10^{13}\,\mathrm{W\,cm^{-2}}$ are required. Conventionally, these ultrashort intense laser pulses are generated with low repetition rate amplifier systems in the kilohertz range. However, to initiate these processes at repetition rates in the megahertz range, extremely high average power in the range of many kilowatts of the laser systems is required, which is not yet technically possible. Therefore, we employ a fsEC to passively amplify the frequency comb pulses of our high-power fiber amplifier.

In this section, general design criteria for fsECs are explained, which are then applied to the design of a cavity for XUV frequency comb generation (HHG cavity). The optical system necessary for intra-cavity HHG will be described, as well as the vacuum and gas system, including a new closed-loop gas recycling system.

3.2.1 Cavity design considerations

The fsEC is the central part of the experimental setup used for studying MPI and XUV comb generation at high repetition rates. The most critical geometrical property is the size and shape of the cavity focus because this defines the volume where the laser interacts with the target.

A round focus is desired to maximize the laser intensity, implying a similar waist size in the sagittal (vertical) and tangential (horizontal) plane. However, the standard bow-tie cavity geometry with two curved and two flat mirrors leads to astigmatism and an asymmetrical focal volume, arising from non-normal angles of incidence on the curved focusing mirrors. At normal incidence, a concave mirror has the focal length $f = R/2$. Increasing the angle of incidence θ on a spherical mirror with a radius of curvature R shifts the focus positions in the sagittal and tangential plane by

$$f_{\mathrm{tan}}(\theta) = \frac{R}{2}\cos(\theta),\tag{3.1}$$

$$f_{\mathrm{sag}}(\theta) = \frac{R}{2}\frac{1}{\cos(\theta)},\tag{3.2}$$

where the tangential plane is the plane of incidence, as described in Section 2.3.1. Several methods have been proposed to reduce astigmatism in enhancement cavities. One method is inserting a Brewster plate into the cavity [387]. Introducing material into the cavity can be beneficial, for example, for intra-cavity nonlinear spectral broadening and temporal pulse compression [388]. On the contrary, the plate adds dispersion that needs to be compensated, and thermal lensing effects have to be taken into account as well [389, 390]. Thus, it is unsuitable for use at very high intra-cavity powers.

The use of parabolic focusing mirrors avoids these problems, but comes at the cost of alignment complications because the rotation angle of the mirror must be considered in addition to position and tilt angle [391]. Additionally, parabolic mirrors are costly and not readily available with high surface quality. That is why, using spherical optics is preferable, as they can be obtained in various formats with very high quality. Typically, optical systems are set up in a single plane to avoid polarization rotation. Using standard spherical components and moving the optics out of this plane allows to compensate astigmatism, but polarization-rotation effects need to be considered in the design process [112, 392]. A cylindrical mirror pair avoids the polarization rotation effects and allows fine-tuning of the focus shape [393]. However, more cavity mirrors result in enhanced dispersion and scattering losses.

For this reason, we have introduced a new cavity design with a single cylindrical input-coupling mirror that entirely compensates astigmatism near the focal volume, thereby not increasing the

number of cavity mirrors [53, 117, 129]. This method is used for our XUV cavity as well as the VMI cavity, the latter being detailed in Section 4.1.

The incident NIR frequency comb pulses are resonantly overlapped and tightly focused on a gas target, where the light-matter interaction produces high-order harmonics. To initiate the HHG process, exceptionally high peak intensities are required in the target region, where the focused light interacts with the gas jet. Therefore, the XUV cavity consists of only five optical elements. The XUV light is generated collinearly with the NIR pulses, and is coupled out employing a nano-grating etched into the surface of a flat cavity mirror [86].

Even though it is desirable for a large HHG yield to maximize the cavity focal volume [89], it comes at the cost of reduced NIR intensity and, thus, decreased HHG yield. A high cavity finesse or a very powerful driving laser would be required in this case to reach the necessary intra-cavity peak intensity. In contrast to this, reducing the sensitivity of the cavity mode to disturbing effects of the target gas plasma, it is preferable to keep the finesse low, $\mathcal{F} < 1000$ [394]. Further, a small focus size is advantageous for HHG phase matching because ions leave the interaction region within a shorter time, and steady-state plasma is reduced [100]. To conclude, a rather low-finesse enhancement cavity with tight focusing is optimal for HHG with limited incident laser power.

When applying the XUV frequency comb for precision spectroscopy, only a single comb tooth needs to interact with the ion. Therefore, spatial separation of the different harmonic orders is required to select the suitable wavelength for the HCI. Compared to other methods, such as Brewster plates [83, 84, 395], or geometrical output coupling [92, 97], using a grating mirror for outcoupling of the XUV [86] offers the advantage of complete separation of the XUV from the fundamental NIR light in the diffracted beam, thus making the use of metallic filters unnecessary. As opposed to the VMI cavity, polarization-independent enhancement in the HHG cavity is unnecessary, and s-polarization is desired because the diffraction efficiency of the grating is increased. After the XUV light has been coupled out from the cavity, it can be guided to a Paul trap with cold HCIs [61] or a different target. As illustrated in Figure 1.3, we also used this cavity for a first MPI experiment[129], which motivated the design of a dedicated second cavity - the VMI cavity - because the grating mirror acts as an intra-cavity polarizer. Today the HHG cavity is used for its actual purpose and generates XUV light [53, 117].

As described in Section 2.6.3, using target gas mixtures with several bars of backing pressure reduces plasma effects and significantly improves the HHG yield. A differential pump system around the nozzle allows a high target gas backing pressure, and a subsequent gas-recycling and compression system will allow continuous operation even with rare target gases such as krypton or xenon.

3.2.2 HHG cavity optics setup

The optical setup is the most crucial part of the fsEC, and its most important parameter is the size and shape of the NIR focus it produces. A cylindrical IC mirror is used for astigmatism compensation in the focus region. An overview of the *in vacuo* optical elements is shown in Figure 3.5 a).

The asymmetric bow-tie cavity has one short arm with the focus in between the curved mirrors, and the cylindrical IC mirror is positioned in the collimated long arm. The cavity length is 2997.9 mm to match the 100 MHz repetition rate of the comb laser. The cavity is aligned with UHV-compatible piezo-actuated mirror mounts (N-480 PiezoMike, Physik Instrumente) in the long cavity arm while the vacuum chamber is closed. Around the interaction volume, a differential pump system for efficient target gas removal is implemented [127]. The transverse profile of the cavity mode is monitored with a CCD camera (DCC1240M, Thorlabs) that detects a small cavity leakage through CM1, and a typical image is shown in Figure 3.5 d). A photodiode (PDA 100A, Thorlabs) measures the intra-cavity power.
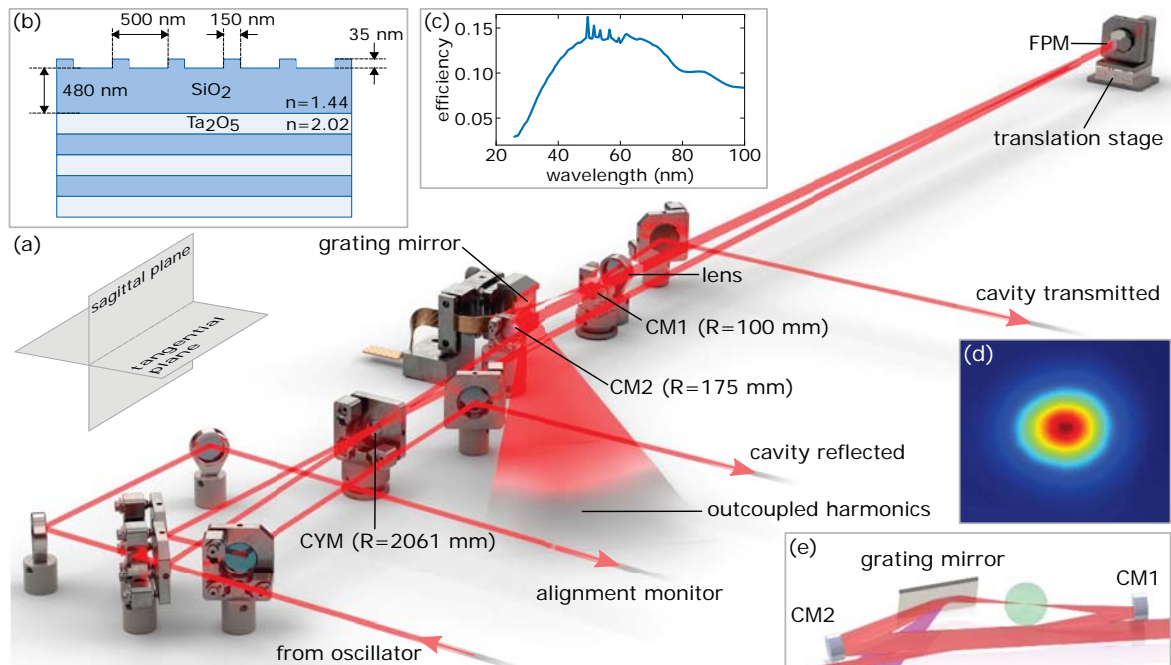
Figure 3.5: a) Schematic overview of the *in vacuo* optical elements of the enhancement cavity. The oscillator beam is directed through the cylindrical input coupler (CYM) with a single mirror reflection. The transmitted leakage from the mirror before the CYM is guided out of the vacuum and used to monitor the alignment of the incident beam. The beam reflected from the input coupler is used for locking the cavity length using the PDH technique, correcting the cavity length with a piezo behind the flat cavity mirror (FPM). The short cavity arm is formed by two curved mirrors (CM1, CM2) and the grating mirror. The intra-cavity mode profile and circulating power can be monitored via a small leakage through CM1. The direction of the out-coupled harmonics is also indicated. b) Illustration of the grating mirror design. The IR mirror consists of a quarter-wave dielectric stack with a thicker top layer, in which a grating structure is etched to diffract impinging XUV radiation. c) Calculated diffraction efficiency of the grating mirror for the wavelengths of interest. d) A beam profile capture of the Gaussian cavity mode, recorded with a CCD camera from the cavity transmitted beam at a distance of 0.78 m after the mirror. e) Close-up of the focus region. The free space around the cavity focus is illustrated by a green sphere with a radius of 10 mm. Reprinted with permission from [117] ©The Optical Society.
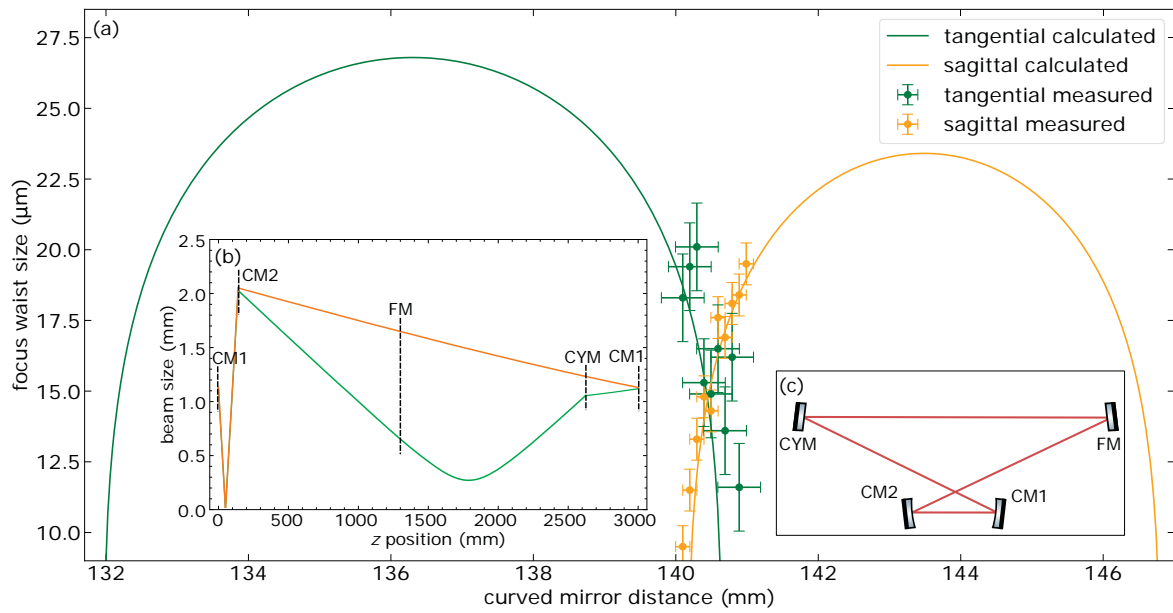
Figure 3.6: a) Focus waist size of the final cavity design. Due to the large incidence angles of 11° and 8° on the curved mirrors with $R = 100$ mm and $R = 175$ mm, respectively, both stability regions are pulled apart, and only a small section of overlap remains for operating the cavity. In the center of that region, an astigmatism-free focus is achieved. Measurements confirm stable cavity operation with a waist of 14.7 μm in both planes. The overall geometry is shown in the inset c) for clarity. b) Calculated waist size of the cavity beam, with indicated mirror positions. A secondary tangential focus is apparent in the long cavity arm. Reprinted with permission from [117] ©The Optical Society.

The focus waist size in the tangential and sagittal plane depends on the distance between the two curved mirrors, as shown in Figure 3.6 a). It is adjusted with a closed-loop translation stage (Q-521.24U, Physik Instrumente) under the first curved mirror (CM1). A waist size of $14.7\,\mu\text{m}$ is reached, and the cavity mode in the long arm is elliptical, as shown in inset b).

Directly after the focus, separation of the generated XUV from the fundamental light is achieved with a grating mirror, as shown in Figure 3.5 b). The beam impinges on that mirror ($35 \times 20 \times 2\,\text{mm}^3$, Ibsen Photonics) under a 75° grazing-incidence angle. While the grating is designed to have a high NIR reflectivity of 99.999 % with a low GDD ($< 2\,\text{fs}^2$), the XUV diffraction efficiency is optimized to above 10 % for wavelengths between 40 and 100 nm using simulation software (PCGrate), as shown in Figure 3.5 c). A $10\,\text{mm}^2$ copper braid is glued to the backside of the grating mirror to transport heat away. After diffraction by the grating mirror, the spatially dispersed harmonics are detected with a sodium salicylate-coated glass screen.

3.2.3 Titanium mounting structure

For resonant operation, the cavity length needs to be stabilized within a fraction of the central wavelength $\Delta L \ll 1039\,\text{nm}$. At a repetition rate of 100 MHz, this length corresponds to $L = c/f_{\text{rep}} \approx 3\,\text{m}$, which means that a fractional length stability on the order of 10^{-9} needs to be achieved to keep the cavity resonant. If the highest possible stability is already achieved in the mechanical design of the mounting structure that holds the mirrors, the requirements for the fast feedback loop are relaxed. Furthermore, the structure needs to be UHV compatible.

For this reason, we designed a rigid titanium rod structure that mounts the cavity optics. Titanium offers the advantage of a vacuum-compatible material with high strength that is non-magnetic. It has a much lower density than stainless steel, which makes the overall structure lighter and reduces the load on the optical table. At the same time, thermal expansion of titanium ($9 \times 10^{-6}\,\text{K}^{-1}$) is lower than type 1.4301 stainless steel ($17 \times 10^{-6}\,\text{K}^{-1}$) or aluminum ($23 \times 10^{-6}\,\text{K}^{-1}$). Titanium can be machined with high precision on our in-house computerized numerical control (CNC) machining centers.

The overall size of the rod structure was chosen to simultaneously accommodate two cavities and still provide enough space for future upgrades and changes. In our design, four massive $\varnothing 55\,\text{mm}$ rods with a length of $l = 1925\,\text{mm}$ surround the optical axis of the XUV cavity and are held in place by three monolithic supports. They are arranged symmetrically, reducing the sensitivity of the cavity length to accelerations and vibrations. Diagonal $\varnothing 25\,\text{mm}$ rods stabilize the structure in the rotational degree of freedom. Bridges with threaded M6 holes are used as small optical tables to accommodate the optics of the XUV cavity with a beam height of 50 mm. The titanium rod structure as a whole is placed in a large vacuum chamber, as described in the following subsection. The VMI cavity, which was installed after the XUV cavity was already operating, is mounted on a single titanium breadboard to allow for setting up the optics outside the vacuum chamber.

Figure 3.7 shows the titanium rod structure. The laser beams of both cavities are drawn in different colors (red and orange) to distinguish both beam paths even though they share the same driving laser at the same wavelength. The generated XUV light is angularly dispersed by the grating mirror, and the harmonic order is selected by a translatable flat gold mirror and guided towards future experiments.
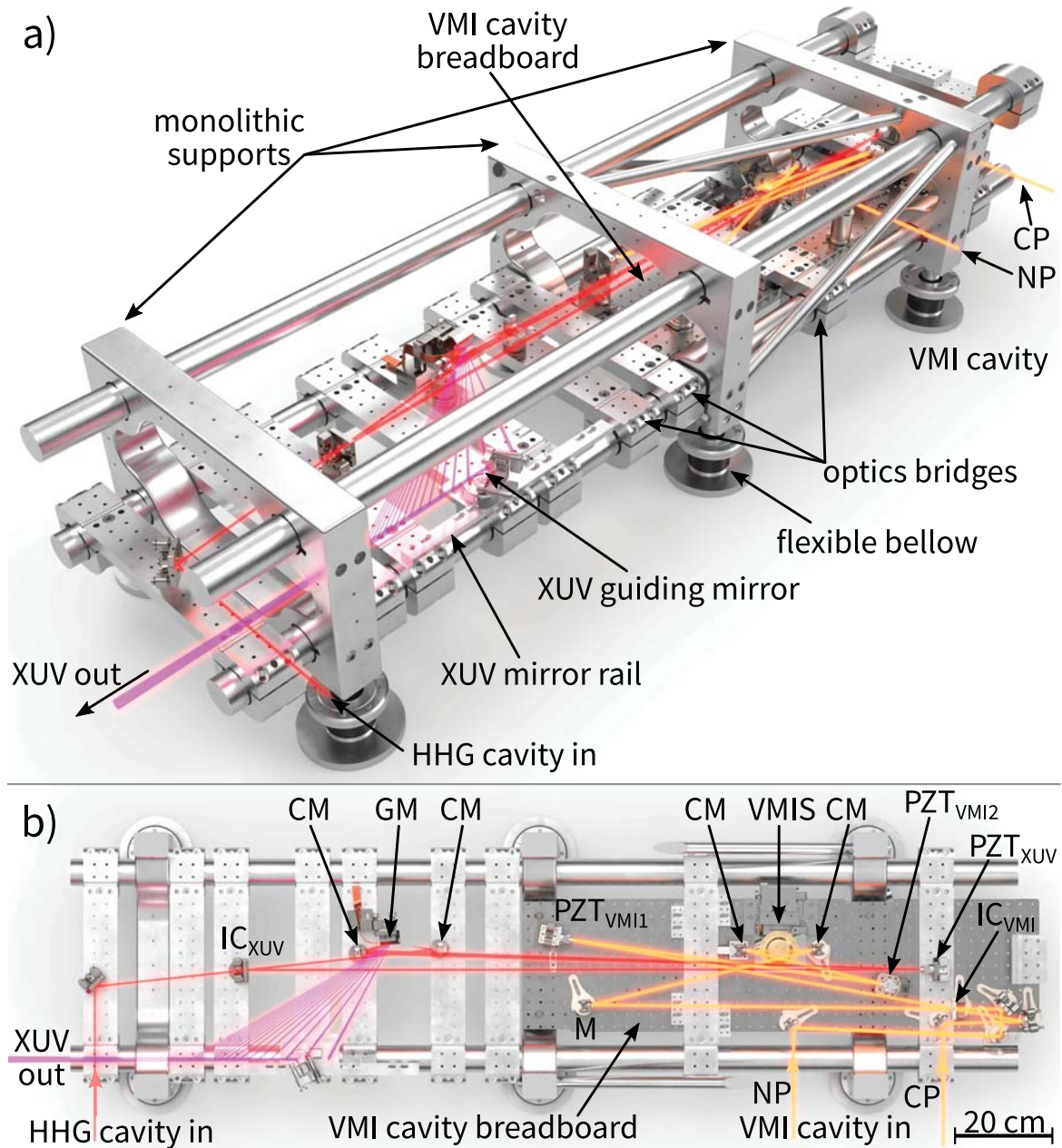
Figure 3.7: Overview of the titanium mounting structure showing the main HHG and VMI cavity optics shown as an a) 3D and b) top view with the upper components cut away. Three monolithic supports hold four rigid titanium rods, onto which the optics bridges for the HHG cavity can be mounted. The whole titanium structure sits on six feet, which are rigidly connected to the optical table, while flexible bellows connect the vacuum chamber. All metal parts (apart from screws, optic mounts and flexible bellows) are fabricated from titanium. The breadboard for the VMI cavity is drawn in darker grey, with the VMI spectrometer (VMIS) placed between the curved mirrors. The laser beam of the VMI cavity is drawn in dark orange (NP: normal-propagation direction, CP: counter-propagation direction). The HHG cavity beam is drawn in red, and the XUV beam in violet color to visualize the different beam paths. The cavity optics are denoted as: mirror (M), curved mirror (CM), grating mirror (GM), input coupler (IC), and piezo mirror (PZT). More details about the VMI cavity are given in Chapter 4.

3.3 Vacuum and gas system

For the various experiments that are conducted with the fsECs, it is necessary to guarantee stable and undisturbed operation. For the generation of XUV light, vacuum is required due to the high absorption of air. Furthermore, ionization of the ambient air would occur due to the high intensities reached within the cavities. In addition, air turbulence leads to fluctuations in intra-cavity power, which is caused by the high average power of the cavities.

For MPI experiments, a vacuum of below 10^{-6} mbar is necessary since, at higher pressures, the MCP detector can no longer be operated. The better the vacuum, the fewer residual gas atoms are ionized and detected, which improves the signal-to-noise ratio. The contamination level must be as low as possible for operating the cavity at high power. This is particularly relevant for intra-cavity HHG, as the high-energy XUV photons can crack hydrocarbons and deposit them on the mirror surfaces [91, 396]. This would be fatal on the grating mirror, the first optical element after the gas jet, as no more XUV light can be coupled out when the fine grooves fill up. For this reason, we have developed an UHV-compatible vacuum chamber, which is described in Subsection 3.3. Furthermore, our main vacuum chamber is connected in a direct line of sight to the cryogenic Paul trap, where a pressure of $\sim 10^{-14}$ mbar is required [61, 115]. Therefore, good vacuum conditions are already required in our chamber during HHG to bridge the large pressure gap and avoid charge exchange of the trapped HCI with the background gas.

On the contrary, a high target gas pressure is needed for phase matching the HHG process, as described in Subsection 2.6.3. For this reason, we have developed a differential pumping system that effectively removes and collects the gas from the interaction region [127]. The captured gas can then be recompressed, filtered, and reused. The gas injection and compression system are described in detail at the end of this chapter, for which we are preparing a publication [128].

Main vacuum chamber and differential pumping system

The titanium mounting structure with the cavity optics is placed inside a large rectangular UHV chamber ($2.1 \times 0.6 \times 0.4 \, \text{m}^3$), as shown in Figure 3.8. Several ConFlat (CF) flanges sealed with copper gaskets are attached to the sides and the top of the custom-made chamber for optical access and electrical feedthroughs. The complete top lid of the chamber can be lifted using a home-build lifting construction. The vertical sides of the short ends can also be opened completely. These three large flanges are sealed with two FKM O-rings each with a differentially pumped channel in between to improve the vacuum in the main chamber. The main chamber is pumped using a $2100 \, \text{L s}^{-1}$ magnetically levitated turbomolecular pump (TMP) (TMP_0, not depicted in the figure) to generate a vacuum of 8×10^{-8} mbar. The vibrations from the TMP are transmitted to the whole chamber. The chamber sits on pneumatic vibration isolators to minimize the transmission towards the cavities and the optical table. The titanium mounting structure is directly mounted on the optical table, which sits on six large vibration-insulating pistons. Flexible bellows are used at the feet position of the titanium structure for mechanical decoupling of the chamber. More details of the differentially-pumped and mechanically-decoupled vacuum system can be found in [53, 127, 397].

The efficiency of the HHG process depends on the gas density in the interaction region due to phase matching as discussed in Section 2.6.3. Furthermore, the ionization fraction needs to be as small as possible for phase matching, which is difficult to achieve using high repetition rate systems because steady-state plasma accumulates. Gas cells are often used in low repetition rate HHG [398] but are not suited for high repetition rate because the gas-refreshing rate is low and efficient gas removal is difficult. Therefore, most XUV combs use end-fire nozzles to inject the gas. Typically, xenon or krypton is used as the HHG target gas. Mixing these heavy gases with helium increases the average velocity of the gas atoms, which enables reducing the accu-
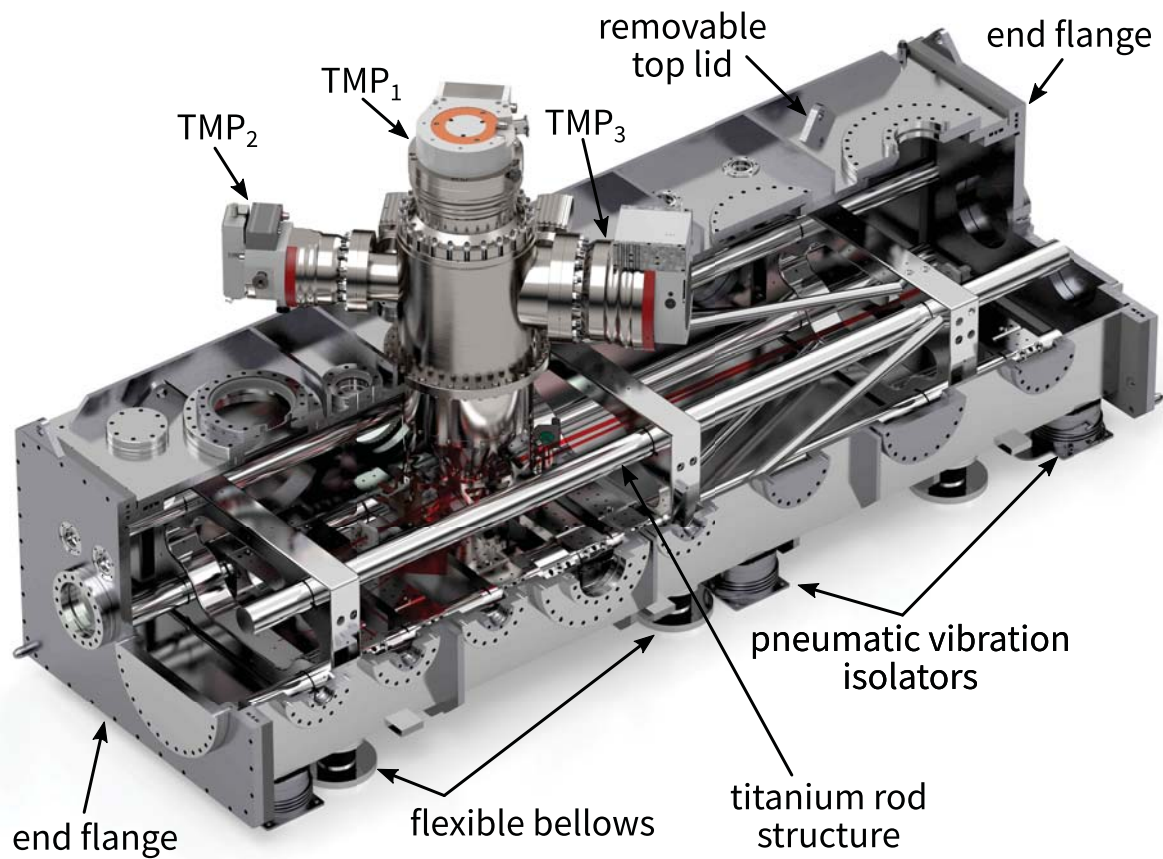
Figure 3.8: Overview of the main vacuum chamber with the three-stage differential-pump system. A cut-away view reveals the titanium mounting structure. The complete upper section of the chamber and the two short sides are closed with large removable flanges. The differential pump system is pumped by three TMPs (TMP_{1-3}). The TMP of the main chamber is not depicted.

mulating steady-state plasma and allows phase matching [91]. However, using a xenon partial pressure of 5 bar in a 9:1 He:Xe gas mixture results in a backing pressure of ~50 bar and a correspondingly high gas load. A single-stage cone-shaped gas-catching construction opposite the nozzle removes most of the injected gas, thus improving the vacuum [399]. In our setup, we take this concept to a new level by adding two shells to the gas catch, which enclose the interaction volumes entirely. Furthermore, the system is not only pumped with fore-vacuum pumps but also with TMPs, which improves the pressure in the main chamber by two orders of magnitude. Figure 3.9 shows the differential-pumping system at the focus position.
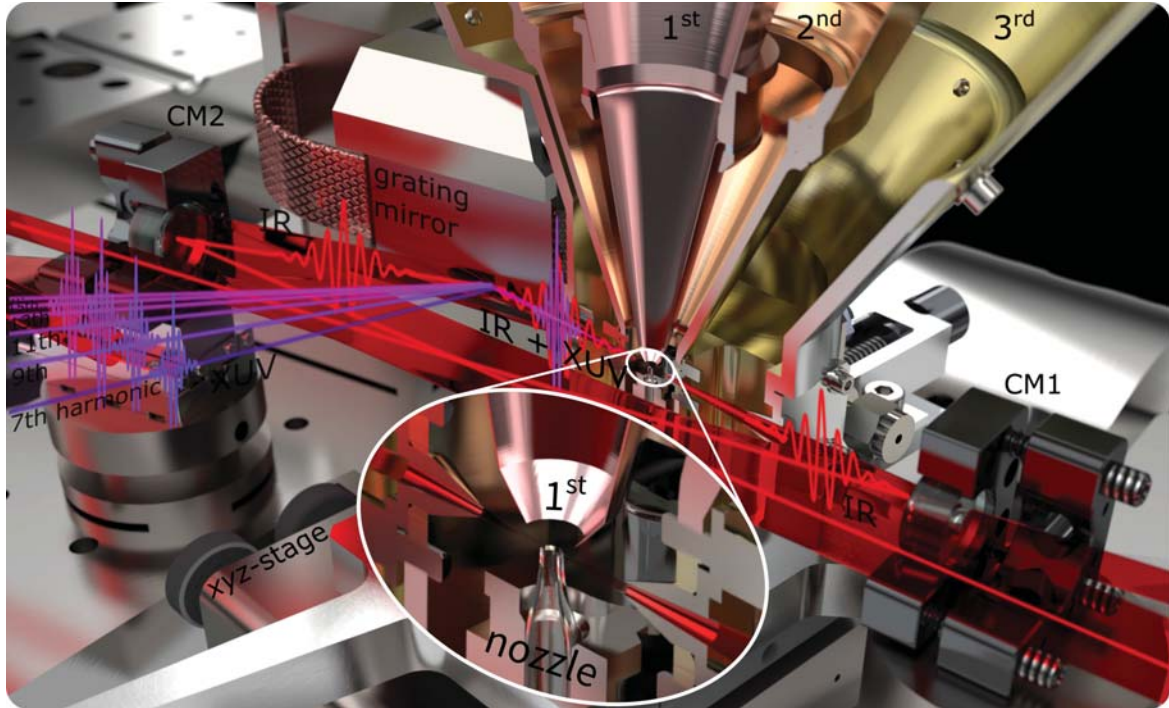
Figure 3.9: Overview of the focus region of the HHG cavity with a cut-away view of the differential pumping system. The three stages of the system encapsulate the interaction region. The zoomed inset shows the gas nozzle and the entrance of the first differential pumping stage. The system is inserted into the tight space between the curved mirrors (CMs) and the grating mirror. Generated harmonics are diffracted at the grating mirror and coupled out of the cavity angularly dispersed. Adapted from [53].

The gas is injected using quartz nozzles with an outer diameter of ~0.5 mm and an inner diameter between 20 to 100 μm. The skimmer of the first differential pumping stage is placed ~100 μm above the nozzle to catch most of the gas, as shown in the inset of Figure 3.9. Cone-shaped walls increase the pumping speed further away from the focus, where more space is available. The second and third stages encapsulate the focus region and have small holes along the laser propagation axis. The whole part of the system shown in the figure can be moved using a piezo-driven five-axis stage. In the upper section, overlapping metal sheets at a distance of 2 mm avoid the transmission of vibrations from the TMPs to the lower section. A large CF 250 flange above the focus position of the HHG cavity is used to insert the differential-pumping system, as shown in Figure 3.8.

Each stage is connected to a separate turbo pump with TMP_1: 300 L s^{-1}, TMP_2: 440 L s^{-1} and TMP_3: 1300 L s^{-1} pumping speed for the first, second and third stage, respectively. All turbo pumps have magnetic bearings for reduced vibrations. The pressure in the main vacuum chamber is in the range of 8×10^{-8} mbar without gas injection. Injecting gas with a backing pressure
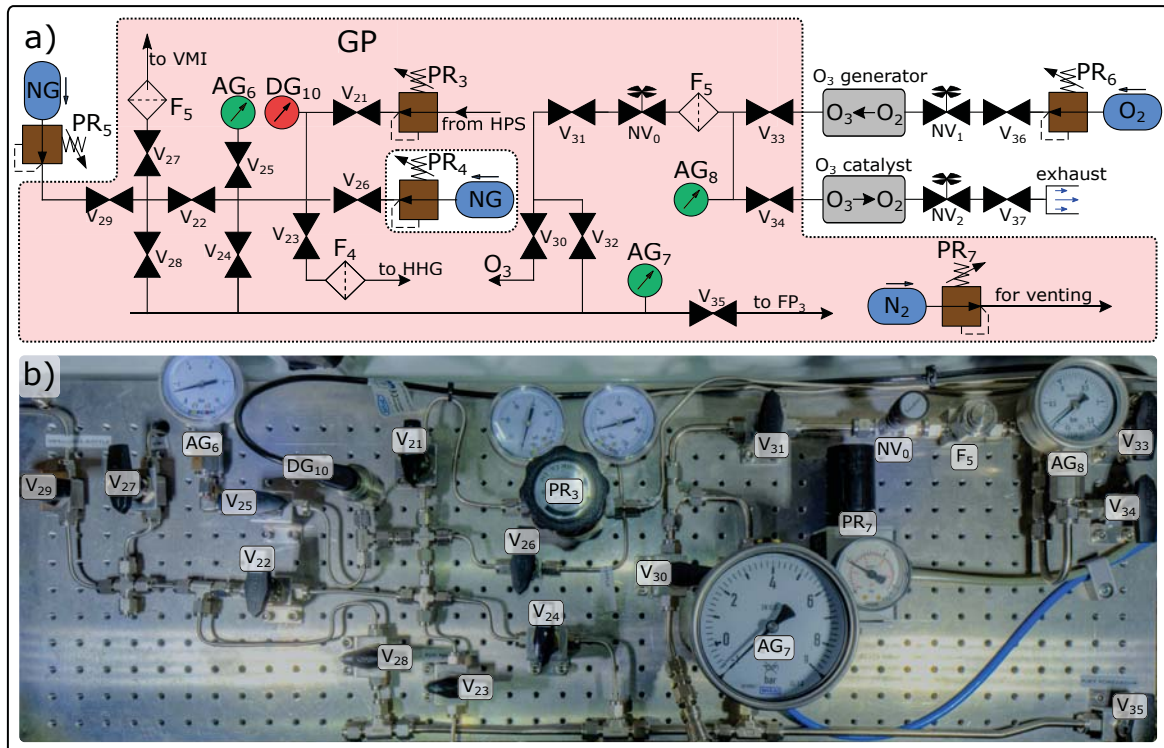
Figure 3.10: Gas distribution and injection system for the main vacuum chamber. It is used to supply the MPI and HHG target gases, for ozone (O_3) injection, and for venting the chamber with nitrogen (N_2). a) A circuit diagram and b) photograph of the gas injection system is shown with the main components of the gas panel (GP) labeled: valve (V), Needle valve (NV), pressure regulator (PR), filter (F), neutral gas tank (NG), fore-vacuum pump (FP), analog/digital pressure gauge (AG/DG), and ozone injection.

of several bar through the $\varnothing 40\,\mu$m nozzle results in a pressure rise to 9×10^{-5} mbar. The pressures on the UHV side of the setup are monitored with digital gauges (DG_{0-3}) in combination with a controller (Agilent, XGS600) connected to the experimental control system.

3.3.1 Target gas and ozone injection system

A gas distribution system was developed to inject the target gas at high pressure, shown in Figure 3.10. It is used to supply the HHG and VMI cavities with noble gases. The components are mounted on an aluminum board with M5 holes in a 20×20 mm grid. The board is mounted directly next to the main vacuum chamber. Stainless steel tubes and double ferrule fittings (Swagelock) are used for stable, leak-proof, and low-contamination connections. For high pressure, we use mainly $\varnothing 1/8$-inch tubes because of the small inner volume, which is advantageous when the gas inside the system is changed. Inside the main chamber, we use $\varnothing 1/16$-inch tubing. Several valves and pressure regulators can be used to either inject low gas pressure from laboratory gas bottles (1 L, 12 bar) with a pressure regulator (PR_5), which is mainly used to supply the target gas for VMI experiments. For experiments requiring high pressure, we either use the gas from high-pressure bottles or the gas-recycling system, with pressure regulators PR_4 and PR_3, respectively. Analog and digital pressure gauges are used to monitor the pressure. The whole system can be emptied using a fore-vacuum pump.

As mentioned before, hydrocarbon contamination of the optics was limiting XUV comb operation [91, 104, 111], as hydrocarbon molecules are cracked by the high energy of the XUV

photons and stick to mirror surfaces. This hydrocarbon contamination layer is hard to remove, and the filling of the grating-mirror grooves must be avoided. Therefore, we minimize this by exclusively using UHV-compatible components inside the main vacuum chamber, which brings the accumulated hydrocarbon contamination to well below 1×10^{-11} mbar partial pressure. The vacuum level in the main chamber ($\sim 8 \times 10^{-8}$ mbar) is mainly limited by water vapor, which is evaporating from the large surfaces of the vacuum chamber, the titanium mounting structure and the breadboard of the VMI cavity, as we confirmed with a mass-spectrometer analysis.

Injecting ozone and guiding it towards the cavity mirrors is a well-known trick to remove surface contamination and is also used in other XUV frequency comb experiments[91, 109, 400, 401]. Ozone can be produced from oxygen using ultraviolet light or by electrical discharge. Because it is such a strong oxidizing agent, it is also used in various areas of everyday life, such as the food industry. We use a commercial ozone generator (Ozotech Poseidon 220). A needle valve on the gas panel (NV_0) regulates the ozone flow into the chamber as shown in Figure 3.10. $\varnothing 400\,\mu$m nozzles direct the ozone to the grating mirror, the second curved mirror, and the IC mirror. Oxygen is passed through the generator at a flow rate of $\sim 0.5\,$L min^{-1} to produce about 2 % ozone O_3. The oxygen/ozone mixture is fed into a $\varnothing 6\,$mm stainless steel tube to the gas panel and back outside, forming a loop so that a constant flow of ozone is passed through. The constant flow is necessary because ozone is unstable and decays back into oxygen. An ozone-destruction catalyst converts the ozone back to oxygen, which is released into the atmosphere. A pressure regulator (PR_6) and needle valves ($NV_{1,2}$) at the in- and outlet of the ozone line are used to regulate the flow and pressure. A mass spectrometer measurement confirmed a relative contribution of ozone compared to oxygen of ~ 0.6 %.

3.3.2 Gas recycling and compression

Long measurement times on the order of weeks of continuous operation are required for precision experiments. Prices and availability of noble gases are strongly influenced by the prevailing political situation since some noble gases are very rare (e.g. xenon abundancy on earth ~ 87 ppb) and are only produced in a few regions worldwide. For high repetition rate systems, such as XUV frequency combs, the gas consumption approaches several hundred SL per day. The unit standard liter (SL) describes the amount of gas with the volume of one liter at standard temperature and pressure. For instance, using a $\varnothing 40\,\mu$m nozzle with a backing pressure of 20 bar results in a consumption of $>200\,$SL d^{-1}. Using xenon at this high flow rate prevents the use over an extended time because of the high cost (>10 €/SL) and limited availability. Therefore, it is not only economical to catch and recycle the gas for later use but simply necessary.

Only a few lab-scale gas recycling systems have been demonstrated and used for HHG target gases. Chiang and coworkers [402] injected xenon through a 30 μm nozzle at a backing pressure of 5 bar, resulting in a background pressure of about 1×10^{-2} mbar in the generation chamber. A fore-vacuum pump compressed the xenon to atmospheric pressure, followed by a dry-membrane compressor to compress the gas up to 10 bar and store it in an expansion tank. The gas is fed to a pressure regulator and then back to the nozzle, enabling closed-loop operation. After one week of continuous operation, a slight increase of CO of ~ 10 % is observed in the mass spectrum. A single xenon loading was sufficient to operate the system for over half a year. After that, the contamination level became too high, requiring filtering of the xenon (e.g. in an adsorption trap). Wallauer and coworkers [403] used a 30 μm nozzle with a backing pressure of 4 bar and a cryopump to freeze the xenon at the outlet of a turbo pump. After several days of operation, the xenon from the cryopump was defrosted into a 50 L stainless steel vessel and then liquefied in a gas cylinder cooled by liquid nitrogen. The authors state that they could recover almost all of the xenon without further quantification. However, none of these systems could recompress the gases to high pressure $\gg 10$ bar.

Table 3.1: Components of the gas-recycling system, which is shown in Figure 3.11, are listed by their acronyms and sorted by type. More details in the text.

Vacuum pumps and compressors			Filters, gauges, detectors		
Abbr.	Company	Type	Abbr.	Company	Type
TP_0	Leybold	Turbo pump MAG W 2200	F_0	Agilent	Particle filter SCRINTRPNW25
TP_1	Edwards	Turbo pump STPH 301C	F_1	Vacom	Adsorption trap FT25KF-J
TP_2	Edwards	Turbo pumo STP 451-3	F_2	Parker Balston	Particle filter Model 95S6
TP_3	Leybold	Turbo pump MAG W 1300	F_3	Parker Balston	Activated carbon filter Model EU37/12
FP_0	Edwards	Scroll pump XDS35i	F_4	Swagelock	Particle filter $0.5\,\mu m$
FP_1	Pfeiffer	Roots pump A100L	$DG_{0,1,2,3}$	Agilent	FRG-730 full range Pirani Bayard-Alpert
FP_2	Edwards	Scroll pump XDS7i	$DG_{4,5,6}$	Agilent	ConvecTorr thermocouple gauge
DP_0	Hyco	Diaphragm pump MP65-GD-W14	$DG_{7,10}$	RS PRO	Model 175-4981 (-1 + 24 bar)
C_0	Haskel	Gas booster AAD-5-HD	DG_9	RS PRO	Model 175 - 4995 (0 - 250 bar)
C_1	Haskel	Gas booster AAD-30	DG_8	RS PRO	Model 175 - 4992 (0 - 25 bar)
			RGA	MKS	Residual gas analyzer Microvision 2

Therefore, we developed a gas-recycling system that allows recompressing the gas to high pressure (up to 200 bar). Our system can operate in a closed-loop configuration, or the compressed gas can be rebottled and stored. The outlets of the TMPs are connected to the fore-vacuum system. For a better description of the experimental realization of the gas recycling system, it is convenient to divide it into segments, which differ by the pressure range: main chamber (MC): $\ll 1\,bar\,(abs.)$, low-pressure system (LPS): $\leq 1\,bar\,(abs.)$, compressor system (CS): $\leq 200\,bar$, and high-pressure system (HPS): $\leq 200\,bar$, and gas panel (GP): $< 50\,bar$. A circuit diagram showing the main components and connections of the gas-recycling system is depicted in Figure 3.11, and the most important components are listed in Table 3.1.

Low pressure system

After entering the differential-pumping system, the collected gas is directed to one of the fore-vacuum pumps ($FP_{0,1}$), depending on the setting of the valves (V_{0-3}, see Figure 3.11). To recycle all of the injected gas, V_2 is closed and $V_{0,1,3}$ are opened, and FP_1 is used as the only fore-vacuum pump for all TMPs. It is a multi-stage roots pump with a large pumping capacity of $100\,m^3\,h^{-1}$ (at 3 mbar). When ozone is injected into the chamber, the ozone/oxygen/noble-gas mixture in the main chamber is not recycled by closing V_0, and opening V_2, and only the inner two or all three differential-pumping stages are used for recycling. Furthermore, we flush the TMPs of the main chamber with nitrogen when ozone is injected. FP_0 is a scroll pump, also with a large pumping capacity of $35\,m^3\,h^{-1}$ (at 10 mbar).
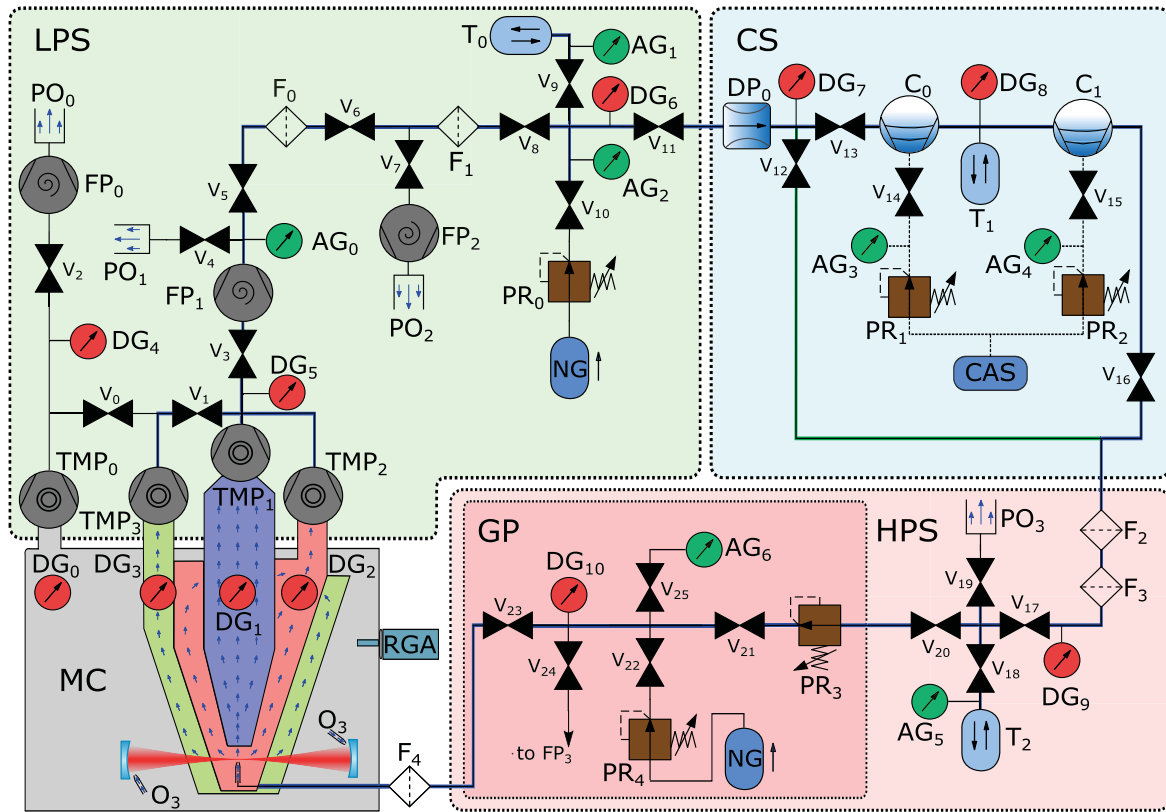
Figure 3.11: Circuit diagram and flowchart of the gas recycling system. The setup is divided into several sections: low-pressure system (LPS), compressor system (CS), high-pressure system (HPS), and gas panel (GP). The components are labeled: main vacuum chamber (MC), turbomolecular pump (TMP), fore-vacuum pump (FP), diaphragm pump (DP), filter (F), pump outlets (PO), storage/buffer tank (T), valve (V), compressor (C), compressed air supply (CAS), residual gas analyzer (RGA), analog/digital pressure gauges (AG/DG), neutral gas supply (NG), and ozone injection (O_3). Table 3.1 provides a detailed list of the used components. The blue line indicates the flow path of the gas when gas is caught in the differential pumping system and recompressed up to 200 bar using the high-pressure gas boosters ($C_{0,1}$). For compression up to ~4 bar using only DP_0, the high-pressure components ($C_{0,1}$, T_1) of the CS can be skipped, as indicated in green. More details in the text. Adapted from [404].

In the next step, the gas is either directed to an external exhaust port $PO_{0,1}$ (and therefore lost) or confined in the low-pressure system (LPS), which is mainly built of a 20 L stainless steel tank to store gas between 0 and 1 bar (abs.) of pressure, connector bellows and digital (DG_{4-6}) as well as analog pressure gauges (AG_{0-2}). Before entering the LPS, the gas passes through a particle filter (F_0) and an adsorption trap (F_1). The latter is a zeolite-based water and oil filter with a built-in heating element for regenerating the zeolite pellets. The total volume of the LPS amounts to 22.2 L. It ends at (V_{11}), before the compressor system (CS). The storage tank (T_0) can be decoupled from the system by closing V_9. All connections of the fore-vacuum system are based on ISO-K or ISO-Kleinflansch (KF) connections, ensuring a low leakage rate. In order to fill the system with a utility gas, a gas bottle can be connected to it with a pressure regulator (PR_0) in between.

Table 3.2: Summary of the volumes distributed across the different parts. *Calculated from fit values in Figure 3.13; †reduced by unknown volume of filter element.

Position	Volume	Pressure range
LPS + T_0	22.2 L	0 - 1 bar (abs.)
C_0 cylinder capacity	0.32 L	0 - 10 bar
T_1	2.04 L	0 - 10 bar
C_1 cylinder capacity	0.05 L	0 - 200 bar
C_1 cylinder dead volume*	0.06 L	0 - 200 bar
T_2	0.075 L	0 - 200 bar
C_1 outlet to V_{17} (excluding F_2, F_3)	0.04 L	0 - 200 bar
F_2 housing volume†	0.02 L	0 - 200 bar
F_3 housing volume†	0.17 L	0 - 200 bar
GP	0.02 L	0 - 200 bar

Compressor system

Inside the compressor station (HD Tech, custom model), two gas boosters driven by the in-house compressed air supply (CAS) are used to compress the gas to high pressure. The main advantage of the boosters is a hydrocarbon-free separation between air and gas sections using graphite-based seals. Because these compressors are based on air-driven pistons which compress the gas, they can stall at any predetermined pressure, hold the fixed pressure without consuming power, and continue operation without venting the high-pressure side. A rod-driven diaphragm pump (MP_0) is used as an input booster for the compressor station. It has FKM seals, with a leakage rate specified to 1×10^{-3} mbar L s^{-1}, and it boosts the output pressure by about 4 bar. The first booster (CS_0) is a single-acting dual-stage compressor, which boosts the gas pressure up to 10 bar. The second stage (CS_1) is a single-acting single-stage booster able to increase the pressure up to 200 bar. A schematic of a gas-driven booster is shown in Figure 3.12, including a brief description of the compression cycle. The output pressure of both stages is manually regulated with two pressure reducers (PR_1 and PR_2). Between the diaphragm pump and the input of CS_0 and at the position of the intermediate storage tank T_1 with a volume of 2 L, digital pressure gauges DG_7 and DG_8 monitor the pressure. The 4-20 mA output of each gauge is digitized (NCD, current receiver board) and connected to our experimental control system. The line with blue background in Figure 3.11 shows the gas flow for the case of closed-loop operation when recycling the gas from the differential-pumping system and compressing it up to the maximum pressure of 200 bar. Alternatively, the gas boosters can be skipped (V_{12} open, V_{16} closed, as shown in green in Figure 3.11), and the output of the diaphragm pump can be directly used if backing pressures
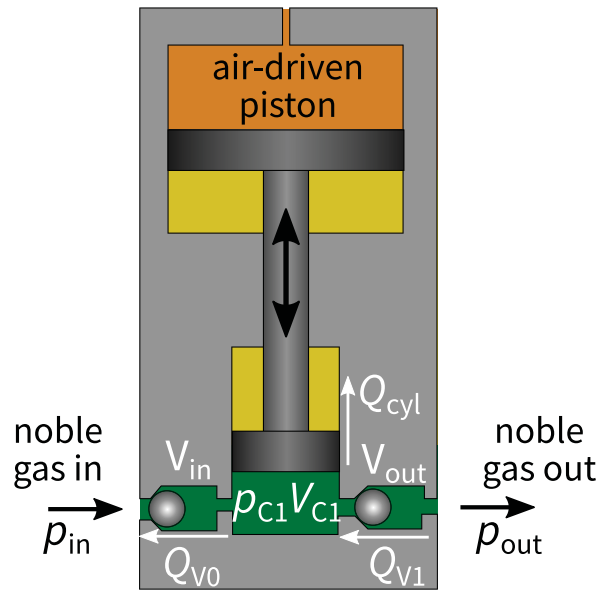
below 4 bar (abs.) are sufficient.

Figure 3.12: Schematic of the gas booster C_1 in the high-pressure compressor station. The compressed-air section is shown in orange, the exhaust-air section in yellow, and the noble gas in green. The compressed air system is drawn in a very simplified way. The noble gas pressure at the input p_{in} depends on the outlet pressure of the first stage C_0. The pressure inside the cylinder is p_{C1}, and p_{out} is the pressure after the outlet. Unidirectional valves at the inlet (V_{in}) and outlet (V_{out}) avoid backward gas flow. The compression cycle: i) noble gas enters the gas booster (V_{in} open, V_{out} closed; $p_{in} \approx p_{C1} < p_{out}$) while the piston moves upwards. ii) When the piston is at its upper limit, it reverses and moves down, compressing the noble gas within the cylinder (V_{in} closed, V_{out} closed; $p_{in} < p_{C1} < p_{out}$) until the pressure inside equals the outlet pressure $p_{C1} = p_{out}$. Then, V_{out} opens, and the pressure inside and behind the compressor increases further until the piston reaches its other limit. This cycle repeats until the product of both piston areas times their respective gas pressure becomes equal. Leakage rates are denoted as Q.

High pressure system

After compression, the gas is cleaned by a particle filter (F_2), followed by an activated carbon filter (F_3) to remove the remaining water and particles introduced by the compressor station. A 75 cm^3 tank (T_2) decouples the nozzle flow rate from the compression cycles. In total, the high-pressure system (HPS) has a volume of ~0.29 L, which at a working pressure of 100 bar results in a similar amount of gas as in the LPS at 1 bar (abs.). 1/8-inch stainless steel tubes with a total length of 4.9 m connect the HPS and the gas panel (GP). The pressure of the HPS is monitored with a digital (DG_9) and analog (AG_5) pressure gauge.

3.3.3 Gas-recycling system leakage rates

To quantify the losses in the system, the inner volumes of the sections need to be known, as summarized in Table 3.2. The stated values are either supplied by the manufacturer or obtained by measuring the length and inner diameter of the connections. Especially at high pressure, a slight change in volume results in a significant change in the stored gas amount. However, precise values are only known for some parts and need to be estimated for the remaining to the best of our knowledge [405].
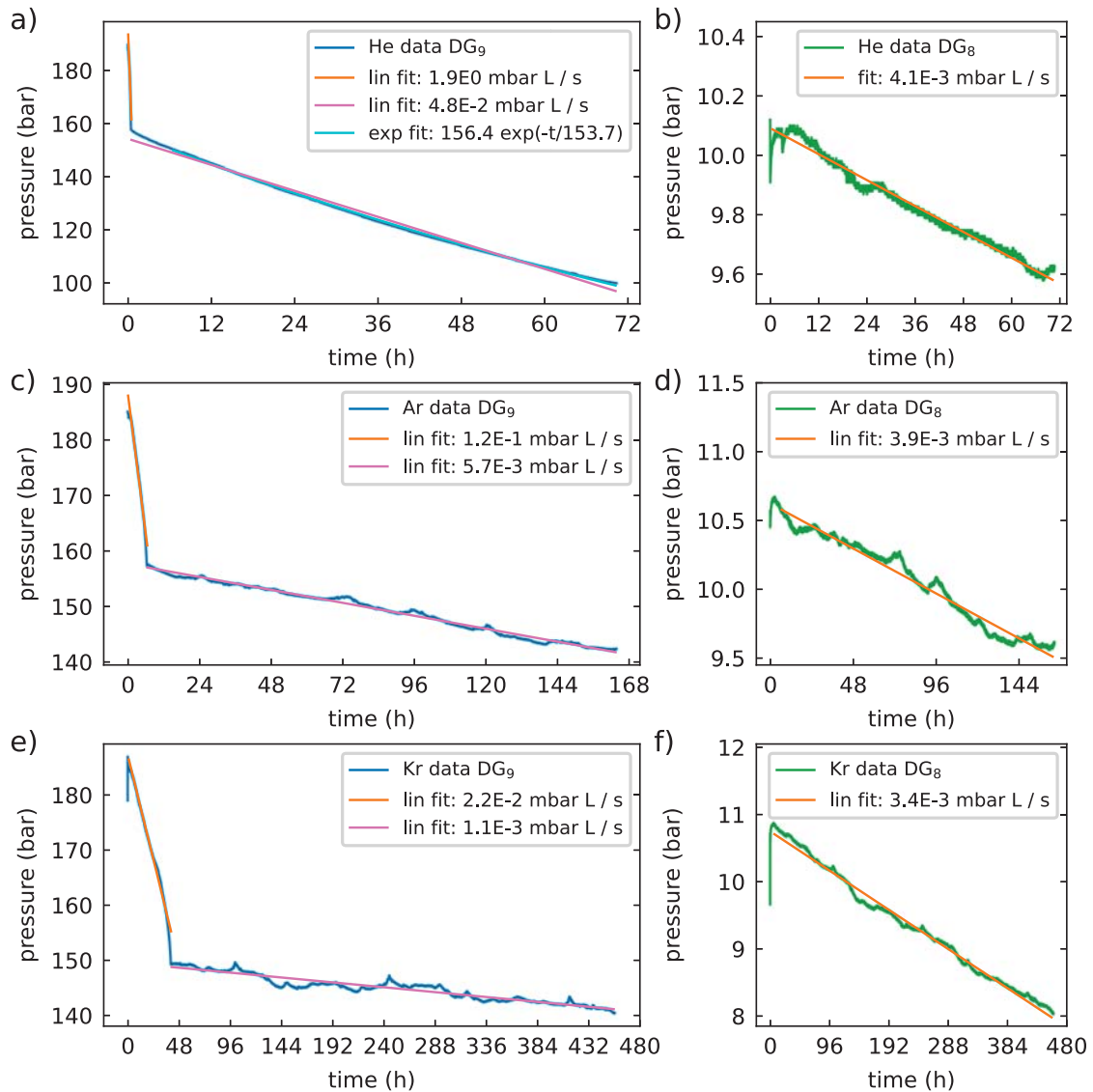
Figure 3.13: Characterization of the leakage rates of the high-pressure CS. The CS is filled with three different noble gases to estimate the leakage rates of a), b) helium, c), d) argon, and e), f) krypton. The pressure is monitored using the digital pressure gauges, as shown in Figure 3.11. a), c), e) show the output pressure of the compressor station, and b), d), f) show the pressure at the intermediate tank. The pressure drops linearly with time. However, at a certain threshold (He, Ar: 158 bar; Kr: 150 bar), the leakage rate changes drastically. Linear fits yield the leakage rates for these two regimes for each gas. Note the different time scales for the different gases. More details in the text.

For a quantitative analysis of the losses, it is useful to define the leakage rate as

$$Q_{\mathrm{L}} = V \frac{\Delta p}{\Delta t}, \tag{3.3}$$

where Δp is the difference between the internal and the external pressure, V is the volume of the closed system, and Δt is the time interval. For ideal gases, pV quantifies the amount of the gas and the mass. Furthermore, the leakage rate depends on the type of gas. Commonly, the unit of the leakage rate is $\mathrm{mbar\,L\,s^{-1}}$, which is equivalent to $10^{-3}\,\mathrm{SL\,s^{-1}}$.

Since all connections in the LPS are based on KF-flanges, the leakage rates are low and negligible compared to the components downstream. The first component of the CS is the diaphragm pump DP_0, for which we measured an air leakage rate of $\sim 4 \times 10^{-4}\,\mathrm{mbar\,L\,s^{-1}}$ after improving the sealing of the membrane [404]. The leakage rate depends on the gas pressure and if the pump is switched on or off. In a future upgrade, we will install a pump with a reduced leakage rate (for helium $6 \times 10^{-5}\,\mathrm{mbar\,L\,s^{-1}}$), which is helpful for long closed-loop operation, especially when the high-pressure gas boosters, which are currently the main loss channel, are skipped (green line in Figure 3.11).

In order to quantify the losses of the CS at high pressure, we compress helium, argon, and krypton up to $\sim 200\,\mathrm{bar}$ until a steady state is reached. Thereafter, the valves ($V_{11,\,12-15,\,17}$) are closed, and the pressure inside the station is monitored using the digital pressure gauges ($DG_{8,\,9}$), as shown in Figure 3.13. The leakage rate of helium is much higher than argon and krypton due to its smaller size; thus, the helium measurement was finished after three days, while the krypton measurement was stopped after almost three weeks. The fluctuations of the argon and krypton measurements are correlated with temperature, which is not stabilized in the experimental hall where the system is operated. At a certain pressure (He, Ar: 158 bar; Kr: 150 bar), the leakage rate changes drastically, visible as a kink in the measured pressure shown in Figure 3.13 a), c), e).

The most likely cause for this unexpected behavior is the following: When the measurement is started, the driving pressure of the compressed air is turned off, which causes the piston to move to the upper position (as shown in Figure 3.12) and results in expansion and pressure reduction of the noble gas in the cylinder ($pV_{C1} = \mathrm{const}$). The valve V_{in} is completely closed due to the (still) large pressure gradient and leak-tight ($Q_{V0} = 0$). On the contrary, the outlet valve V_{out} does not close well and is leaky. The leaking rate Q_{V1} through the outlet valve back into the cylinder depends on the gas type and varies between $\sim 8\,\mathrm{mbar\,L\,s^{-1}}$ for helium and $\sim 8 \times 10^{-3}\,\mathrm{mbar\,L\,s^{-1}}$ for krypton, as shown in Figure 3.13 a) and e). The outlet pressure of the compressor p_{out} decreases at this high rate until $p_{\mathrm{out}} \approx p_{C1}$, where the outlet valve becomes even leakier until it opens completely. This explains the increase of the leaking rate at lower pressure shortly before the kink. From this point on, the total pressure reduction rate of the system is governed by the leakage through the graphite sealing between the piston and the cylinder Q_{cyl}. Therefore, the first fast drop is not an actual leak, where gas leaves the system, but rather a backward flow of gas.

Linear fits are performed for the data after the kink and yield the leakage rates of C_1 for the different gases, as shown in Figure 3.13. A linear fit is reasonable if the pressure difference between the compressor station and the atmosphere does not change too much during the measurement, which is the case for b) to f). In the measurement shown in a), an exponential fit yields the leakage rate as a function of the pressure. At the start of the fit (at 6.5 h), a leakage rate of $2.7 \times 10^{-2}\,\mathrm{mbar\,L\,s^{-1}}$ is obtained, which reduces to $1.8 \times 10^{-2}\,\mathrm{mbar\,L\,s^{-1}}$ at the end of the measurement. The leakage rates for argon and krypton at a pressure of $\sim 150\,\mathrm{bar}$ are $5.7 \times 10^{-3}\,\mathrm{mbar\,L\,s^{-1}}$ and $1.1 \times 10^{-3}\,\mathrm{mbar\,L\,s^{-1}}$, respectively. The leakage rates of C_0 are obtained similarly. However, the rates depend much less on the gas species and are all in the range of $3.4 \times 10^{-3}\,\mathrm{mbar\,L\,s^{-1}}$ to $4.1 \times 10^{-3}\,\mathrm{mbar\,L\,s^{-1}}$.

3.3.4 Closed-loop gas recycling performance

In order to evaluate the recycling performance of the system, argon is used instead of xenon due to its availability and cost. The whole system is pumped and flushed with argon before it is filled with ~85 SL of gas until the LPS reached 1 bar (abs.), the intermediate tank T_1 reached ~10 bar, and the output pressure of the CS was set to 105 bar. The nozzle backing pressure was set to 10 bar, using PR_3. The pressures of the digital gauges and the mass spectrometer data are logged using the experimental control system. The digital gauge DG_3 (Agilent ConvecTorr thermocouple gauge) does not show reliable values. Since even replacing the sensor with a new one did not bring any improvement, it is likely the sensor type itself. However, we monitor the analog gauge AG_1 using a camera imaging the scale and convert the readings to pressure values in software.

The nozzle consumption was determined by closing the input of the gas panel and letting the gas stored in T_2 run empty, while the nozzle backing pressure is kept constant by the pressure regulator PR_3 (valve position on HPS and GP: $V_{17,19,22,24,25}$ closed, $V_{18,20,23}$ open). Linear fits of the pressure (AG_5) yield the gas consumption. At 10 bar (20 bar) of backing pressure, the nozzle consumes 1.5 mbar L s^{-1} (2.5 mbar L s^{-1}).

The presented measurement was conducted in two recycling modes: First, only the gas at the outlet of the differential-pumping system is recycled (valve settings: $V_{1-3,5,6,8,9,11,13-18,20,21,23,25}$ open, $V_{0,4,7,10,12,19,22,24,25}$ closed), as plotted in Figure 3.14 up to the dashed line. Second, the system is operated in full-recycling mode, where also the gas from the main chamber is recovered (as before, but V_0 open, V_2 closed), as shown in the same plot after the dashed line. All pumps operate continuously and keep the outlet pressure of the CS almost constant at about ~105 bar. However, the CS outlet and the nozzle backing pressure drifts slowly over time, as shown in Figure 3.14 b). The pressure of the LPS decreases over time, as shown in a). This is the expected and intended behavior, since the total gas loss of the whole system can be easily calculated from the linear decrease and can be compensated by refilling. Linear fits yield the leaking rate ~7.9×10^{-2} mbar L s^{-1}, which corresponds to a gas consumption of ~6.8 SL d^{-1}. Therefore, it is necessary to refill the system with ~15 SL argon approximately every two days, as indicated with the red letter 'R'. The gas is refilled into the LPS by opening V_{10}. The partial pressures in the main chamber are shown in c). During the measurement, the argon partial pressure decreases, which is attributed to the decrease in the nozzle backing pressure. The adsorption trap F_1 filters the water out of the system and, thus, keeps the partial pressure of water very low. No increase of nitrogen, oxygen, or hydrocarbons C_nH_{2n+2} (drawn for masses 16, 30, 56, 72, 84, 98) is observed. However, a substantial contribution of mass 20 u is detected, which correlates with the argon pressure. We attribute it to neon, which seems to be a contaminant in the argon gas bottle.

Instead of filling the entire recycling system with the target gas before starting the experiments, it is possible to use gas from a fresh bottle to start the experiments, collect the gas to fill the system, and switch to continuous operation later. In a first measurement (not shown) with compression up to 50 bar, which was conducted before the measurement presented here, we were able to operate the system without interruption on a single gas filling for ~120 h [405]. However, a leak in the LPS caused the relative contamination level in the target gas to increase from 0.2 % to 0.5 %. A paper with the results presented here and another measurement with compression up to 50 bar is in preparation [128].

In conclusion, we demonstrated closed-loop operation over more than a week and compression to above 100 bar. The leaking rates were determined. The gas consumption at 10 bar nozzle backing pressure is ~130 SL d^{-1}. In closed-loop recycling operation, the consumption is reduced to ~6.8 SL d^{-1}, which corresponds to a recycling rate of ~95 %. The tightness of the whole system is mainly limited by the high pressure in the CS. More details about the compressor leaking rates can be found in [404]. Catching gas at the pump outlet of the TMP of the main chamber does
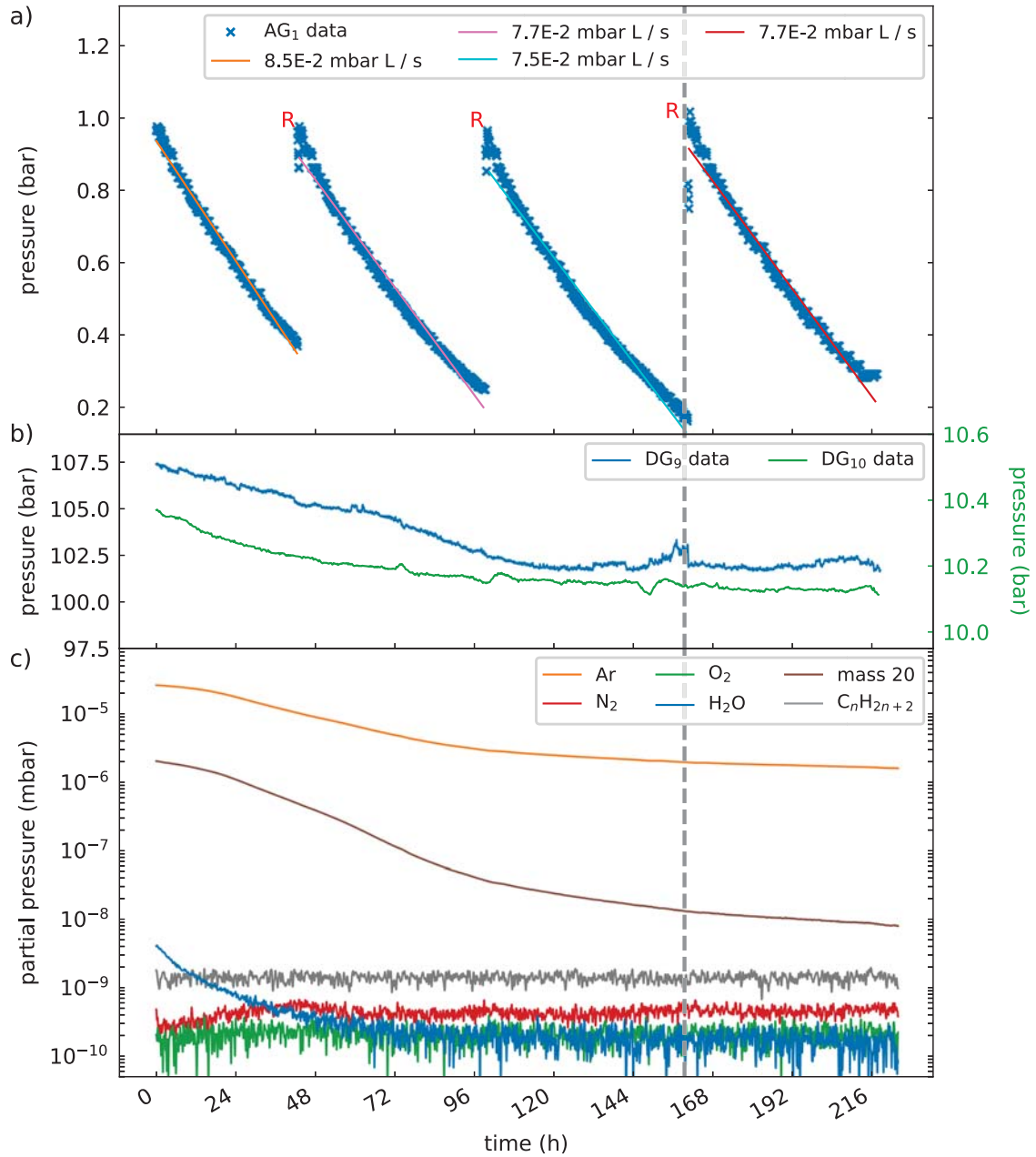
Figure 3.14: Characterization of the gas recycling system for closed-loop operation with compression to ~105 bar. The blue line indicates the gas flow in Figure 3.11. After ~160 h, the recycling mode was switched from the differential-pumping-system-recycling to full-recycling mode, as indicated by the dashed vertical line. a) The pressure of the LPS decreases over time. Linear fits yield the leaking rate ~7.9×10^{-2} mbar L s^{-1}, which corresponds to a gas consumption of ~6.8 SL d^{-1}. The system is refilled with argon approximately every two days, as indicated by the letter 'R'. b) The output pressure of the compressor station and the nozzle backing pressure decrease slowly over time. c) The decrease of the argon partial pressure in the mass spectrum is attributed to the decrease in the nozzle backing pressure. The adsorption trap filters the water out of the system. No increase of hydrocarbons C_nH_{2n+2} is observed. The strong signal at 20 u is attributed to neon.

not reduce the losses significantly and is not necessarily enabled by the differential-pumping system. The filters employed reduce the contamination, as demonstrated by the decreasing water partial pressure during the first two days of the measurement. The contamination level of non-noble gases is always approximately three orders of magnitude lower than the target gas pressure. Therefore, the gas recycling system will enable continuous XUV frequency comb generation over many days.

3.4 High-harmonic generation

In this chapter, the results of the XUV frequency comb are presented. First, it is shown that the cavity can be held on resonance, even at the highest power. After that, the results of HHG are discussed, and the performance is measured for different noble gases and gas mixtures. Then, measurements of the differential pumping system with the gas recycling system are shown, which allows for future long time measurements.

3.4.1 HHG cavity operation

For the generation of HHGs, the cavity length needs to be stabilized on resonance for the maximum enhancement, even at a large input power. This is achieved by using a small part of the light reflected from the cavity to stabilize the cavity length by the Pound-Drever-Hall (PDH) method.
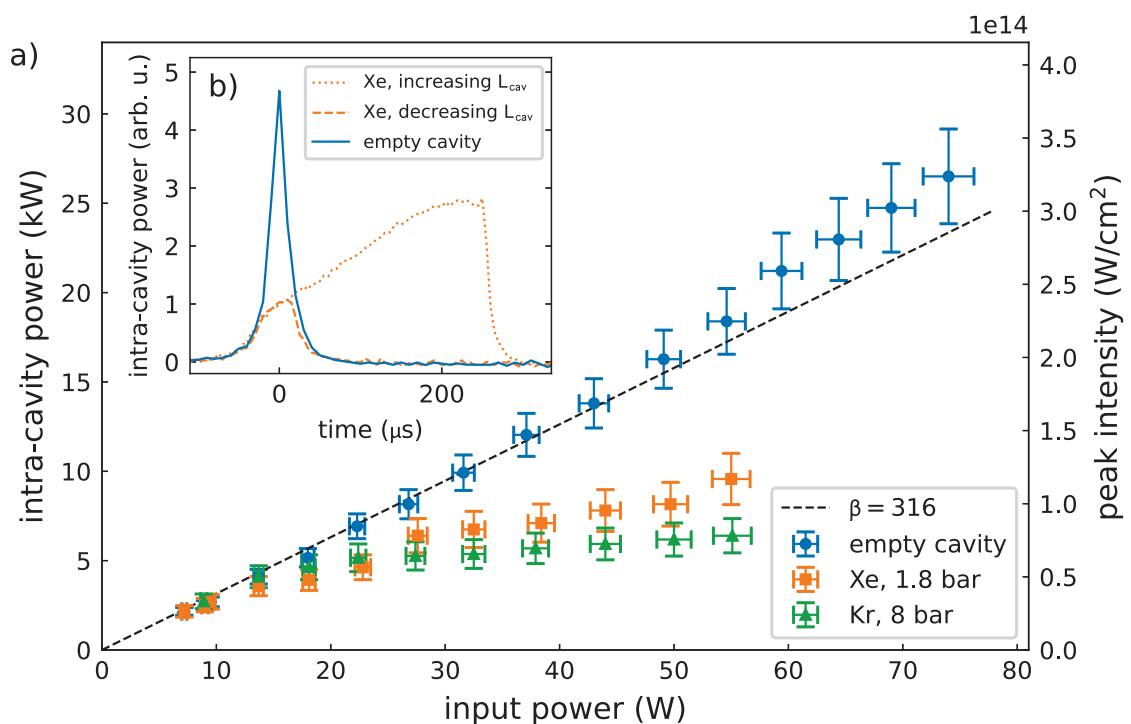

Figure 3.15: Intra-cavity enhancement of the average circulating power inside the HHG cavity. a) With an empty cavity, a multi-kW intra-cavity average power is achieved. Injecting gas into the cavity focus region, leads to intensity clamping due to plasma formation [100, 394, 406]. Inset b) shows a scan of the cavity length over the resonance. It can be seen clearly that the maximum attainable intensity is limited when gas is present in the focus. When the cavity length is increased, the resonance is broadened by the steady-state plasma phase shift, while for decreasing L_{cav}, the resonance is smaller. Figure adapted from [53].

The finesse of the cavity for the IC mirror used in all subsequent experiments ($R = 99.35\,\%$) was determined by measuring the light reflected and transmitted by the cavity to $\mathcal{F} = 805$ [53]. With a mode-matching factor $\epsilon = 0.75$, this results in an enhancement of $\beta \approx 320$. Figure 3.15 shows the measured intra-cavity power enhancement of the HHG cavity as a function of the input power. For an empty cavity, the average intra-cavity power is linear to the input power, and an average power of more than $25\,\text{kW}$ is reached at an input power of $75\,\text{W}$. With a waist

size of 14.7 µm, a pulse duration of 200 fs, and the repetition rate of 100 MHz, this corresponds to a focal peak intensity of $3.7 \times 10^{14}\,\mathrm{W\,cm^{-2}}$. When gas is injected, the maximum attainable intensity decreases, and the intra-cavity power enhancement is limited. The reason for this intensity clamping is plasma formation in the cavity focus. This effect can be seen clearly in inset b) of the same figure, where a scan of the cavity length over the resonance is shown. When increasing the cavity length, the steady-state plasma phase shift causes a broadened lineshape, while for decreasing the length, the resonance gets weaker. It is caused by the plasma induced negative phase shift that effectively shifts the cavity resonance to higher frequencies. Therefore, increasing the cavity length partially compensates the phase shift and, thus, the cavity stays on resonance much longer; a phenomenon known as plasma-induced cavity bistability [53, 88, 109, 394].
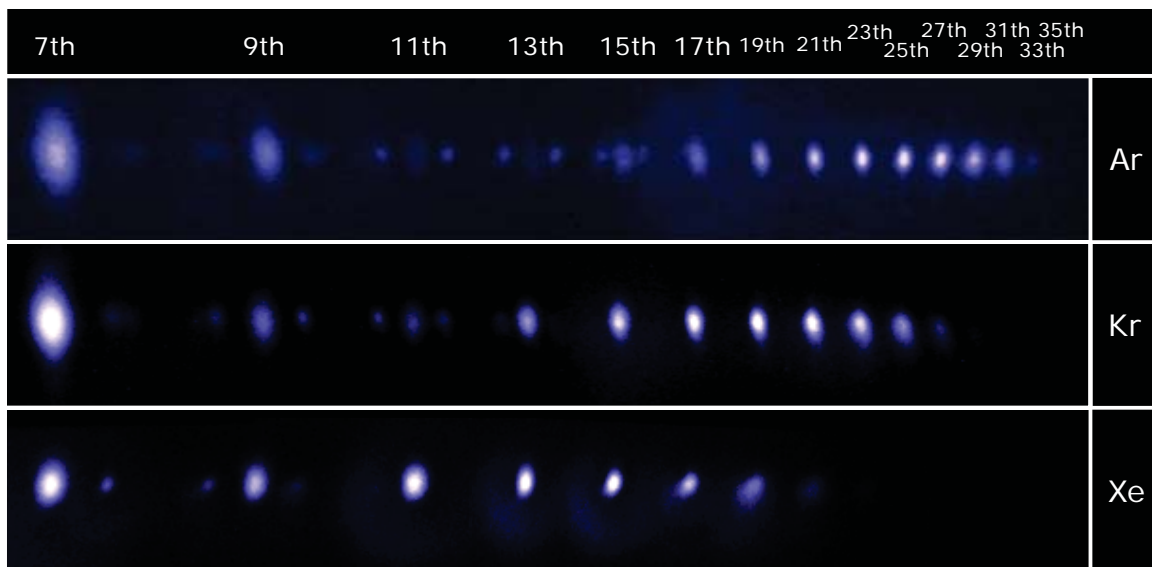
3.4.2 Generation of high-harmonics

Figure 3.16: Various harmonic orders are detected by imaging a fluorescence screen coated with sodium salicylate. The maximum harmonic order that can be achieved depends on the ionization potential of the target gas and is shown here for pure argon, krypton, and xenon. Faint dots between the odd harmonic orders originate from second-order diffraction from the grating mirror. The intensity scales are different for each gas. Reprinted with permission from [117] ©The Optical Society.

Generated XUV light is made visible by a sodium salicylate-coated fluorescent screen. This scintillating material is well-suited for comparing the yield of the harmonic orders because it has a constant quantum efficiency between 35 to 100 nm [407]. The fluorescence light around 420 nm is observed with an air-side electron-multiplying CCD camera (Luca R EMCCD, Andor). Figure 3.16 shows images of the fluorescent screen illuminated with high-harmonics generated with argon, krypton, and xenon as the target gas. The orders are identified by their position on the screen. Second-order diffraction at the grating mirror leads to faint dots between the odd harmonic orders. The bright spots come from the short trajectories, while the weaker and larger halos are generated by the long trajectories.

A GaAsP photodiode (G1127-04, Hamamatsu Photonics) in the center of a smaller second screen with a hole can be moved in front of the larger fluorescent screen to measure the power of individual harmonic orders. It is calibrated with a responsivity curve (provided by the PTB,

Germany), and the resulting photodiode current is measured with a picoampere meter (Model 152, Keithley). The sensitivity of the diode drops steeply above 680 nm, and it is therefore insensitive to residual and scattered NIR light. The sliding mechanism allows precise alignment of the photodiode with the XUV light such that the whole beam of a single harmonic is detected.

Integration of the fluorescence screen in the vertical direction yields a spectrum of the generated harmonics, as shown in Figure 3.17. The total power of the 15th harmonic (17th for argon) is measured with the photodiode which is moved in front of the screen. Integration of each harmonic (shaded areas), yields the power of each harmonic order. Above 100 nm, the spectral response of sodium salicylate is not flat anymore and was corrected for harmonic orders seven and nine.

3.4.3 HHG phase-matching by reduction of steady-state plasma

In Chapter 2 it was shown that it is possible to phase-match a large part of the harmonic spectrum by tuning the gas pressure if the overall ionization fraction is not too high. Therefore, it is advantageous to keep the ionization fraction as low as possible. From Equation 2.103 and Figure 2.22 it follows that a high pressure p_{match} is required for phase-matching in the tight focusing regime. This means that in order to achieve the required phase-matching pressure in the generation region, backing pressures in the range of several bars are necessary because the gas pressure reaching the interaction region is about ten times lower than the backing pressure.

The main disadvantage of using high repetition rates is that in the short time from one laser pulse to the next, the plasma has not completely cleared the laser focus volume, so that steady-state plasma formation occurs. To enable phase-matching also for high repetition rate systems, it is necessary to minimize the steady-state ionization fraction η_{ss} by shortening the time the atoms stay in the interaction region.

The translational gas velocity perpendicular to the laser propagation direction is given by

$$v_{gas} = \sqrt{5RT/M_{avg}}, \tag{3.4}$$

where R is the universal gas constant, T is the gas backing temperature and M_{avg} is the weighted-average molar mass of the mono-atomic gas mixture [91, 408]. Therefore, it takes the time $\tau_{atom} = \sqrt{2\ln 2}w_0 v_{gas}$ for the atom to travel through the focus region. The factor $\sqrt{2\ln 2}$ relates the laser beam FWHM to the beam radius w_0. Similarly, the time τ_{ion} is defined as the time it takes the ion to transit the ion generation volume but with the difference that in this case, the volume strongly depends on the laser intensity. Relating $\tau_{atom/ion}$ to the laser repetition rate as the relevant timescale two dimensionless parameters $\xi_{atom} = \tau_{atom} f_{rep}$ and $\xi_{ion} = \tau_{ion} f_{rep}$ are obtained [91].

Phase-matching can only be achieved if $\eta_{ss} < \eta_{crit}$, as explained in Section 2.6.3. In the few-pulse regime ($\xi_{ion} < 5$), already a significant part of the plasma clears the generation volume between consecutive pulses reducing the steady-state plasma. The ideal case is reached in the single-pulse regime, when $\xi_{ion} = 1$. To get there even at very high repetition rates, the gas velocity can be increased by increasing the temperature, which requires an intra-cavity nozzle at high temperatures [399]. It would also be possible to reduce the laser focus size, but it comes at the cost of a smaller generation volume and thus prevents a gain in total yield.

Another method is to use gas mixtures. As can be seen in Equation 3.4, the gas velocity increases when the average mass of the gas mixture becomes smaller. At room temperature, the gas velocities of the noble gases are $v_{He} \approx 1740\,\mathrm{m\,s^{-1}}$, $v_{Ne} \approx 780\,\mathrm{m\,s^{-1}}$, $v_{Ar} \approx 550\,\mathrm{m\,s^{-1}}$, $v_{Kr} \approx 380\,\mathrm{m\,s^{-1}}$, and $v_{Xe} \approx 300\,\mathrm{m\,s^{-1}}$. Xenon, argon and krypton are used as target gases in our experiments, and mixing of the latter two with helium increases their speed. Helium is well suited because it is very light and has a high ionization potential of 24.6 eV. Therefore, it does
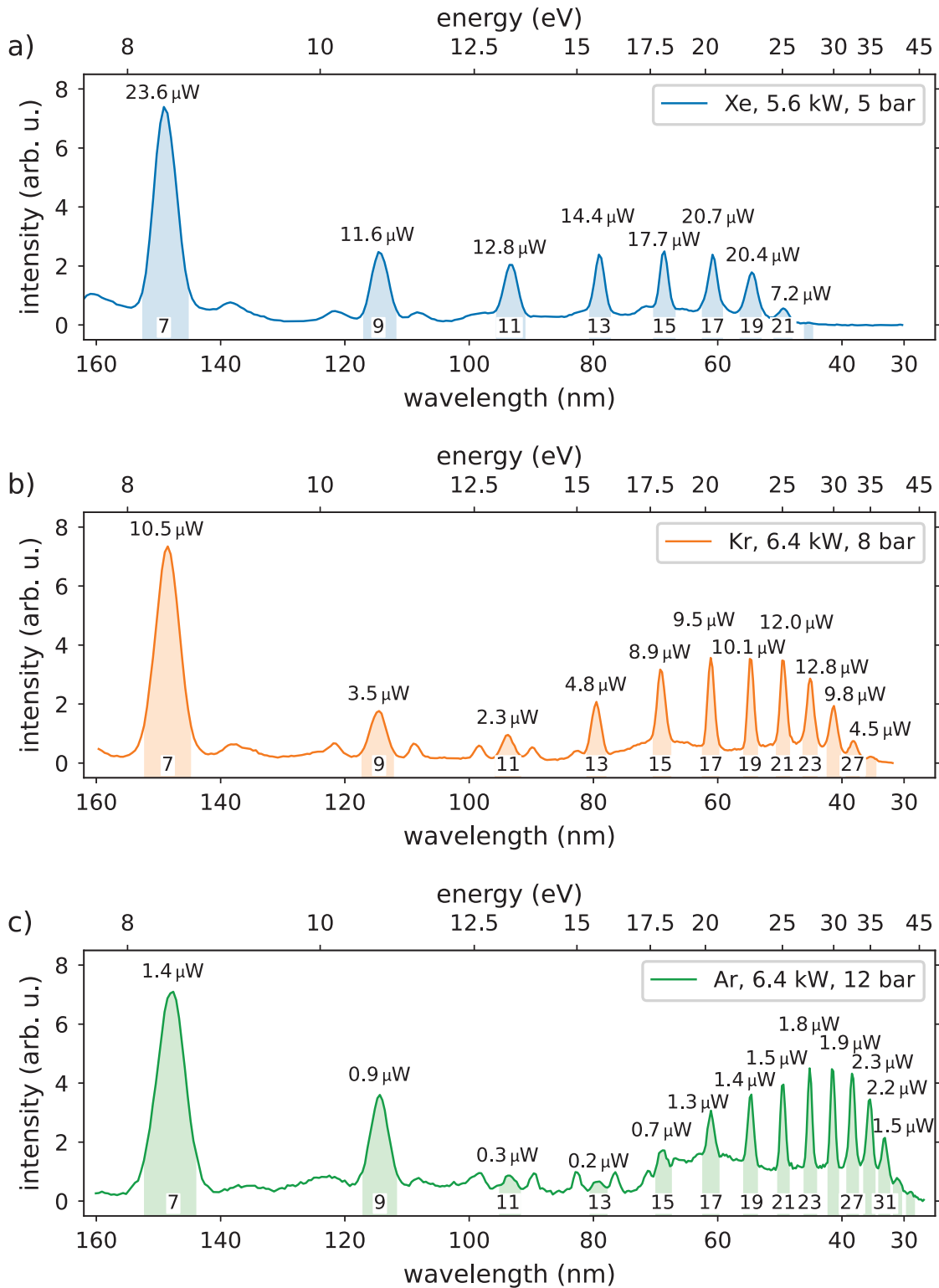
Figure 3.17: Spectra of the harmonic signal obtained by integration of the fluorescence screen. a) Harmonics from xenon gas at 5 bar backing pressure and 5.6 kW average power. b) Harmonics from 8 bar of krypton, and c) 12 bar of argon at 6.4 kW. The power of the harmonics is measured by normalizing the integrated area (drawn shaded) with the photodiode signal at the 15th, 15th and 17th harmonic, respectively. a) Adapted from [53]. b), c) Adapted with permission from [117] ©The Optical Society.

not contribute significantly to XUV emission and absorption [91]. Using a 9:1 mixture boosts the speed of krypton to $v_{9\text{He}:1\text{Kr}} = 1000\,\text{m\,s}^{-1}$, and of xenon to $v_{9\text{He}:1\text{Xe}} = 850\,\text{m\,s}^{-1}$. At a typical focal intensity of $\sim 0.75 \times 10^{14}\,\text{W\,cm}^{-2}$, the ion flight time of xenon is similar to the repetition time of 10 ns (i. e. $\xi_{\text{Xe}^+} \approx 1$). As a result, the steady state plasma is reduced.

Figure 3.18: Measured power of the 15th harmonic order as a function of partial xenon backing pressure for the cavity in a) scan mode, and b) locked state. The total gas pressure of the gas mixtures is much higher, limited only by the vacuum pumps. c) Harmonics are generated in the loc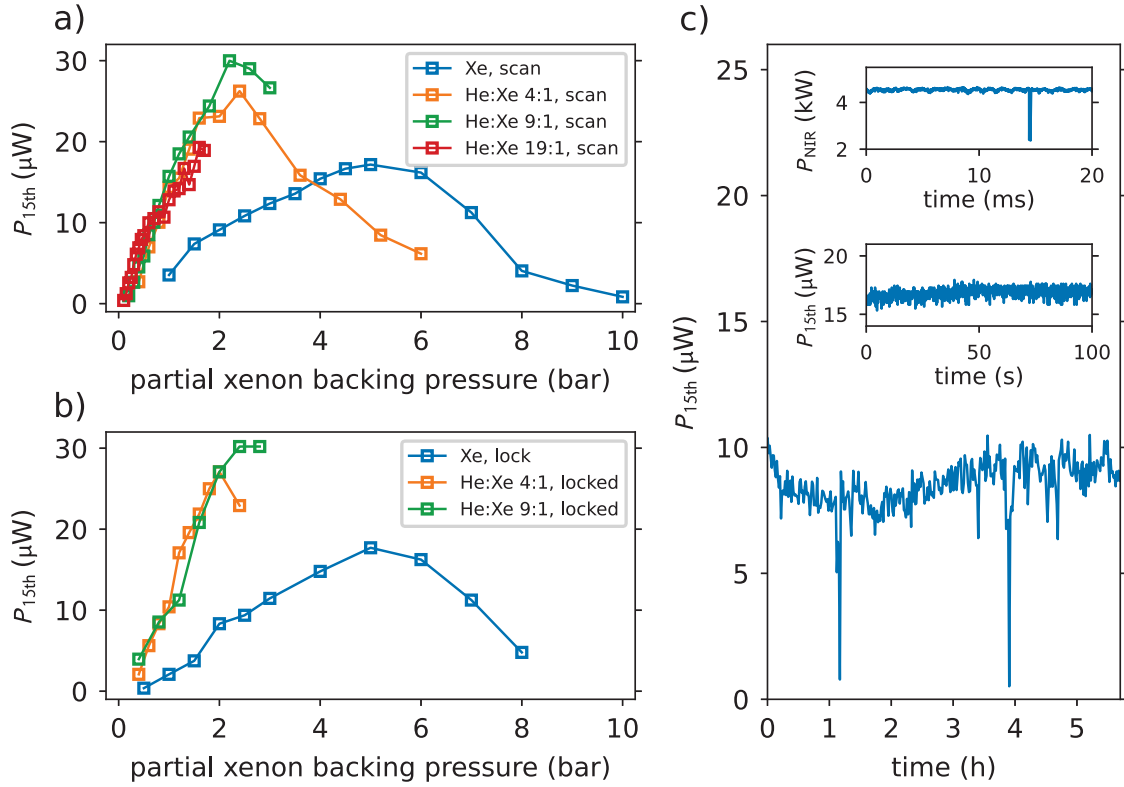ked cavity, and the power of the 15th harmonic is measured for more than 5 h of continuous operation. The two spikes are due to the cavity losing its lock. The insets show the intra-cavity power (top), and the harmonic signal is shown on a shorter time scale (bottom). Adapted from [53].

In Figure 3.18, the measured power of the 15th harmonic order is shown for a scanned a) and locked cavity b) as a function of partial xenon backing pressure for pure xenon and He:Xe gas mixtures with the ratios of 4:1, 9:1, and 19:1. In scan mode, the cavity length is scanned at a rate of 500 Hz with an asymmetric sawtooth signal, where the length was increased by $0.38\,\text{mm\,s}^{-1}$ and decreased much faster by $7.22\,\text{mm\,s}^{-1}$. Therefore, only the signal from increasing the cavity length contributes to the HHG signal, where the plasma-induced phase shift keeps the cavity on resonance longer. The stated harmonic power is obtained by extrapolation from the resonant fraction of time.

For pure xenon, the highest XUV output is achieved for $\sim 5\,\text{bar}$ of backing pressure. With xenon, the decay time of the plasma generated in the focus region is longer than the time between consecutive pulses. As a result, a steady-state ionization is induced. Mixing xenon with helium increases the gas velocity. Therefore, the partially ionized xenon gas clears the focal volume in a shorter time, thus reducing the ionization fraction η (cf. Section 2.6.3). The highest XUV yield

is obtained for the 4:1 and 9:1 mixtures. Even though the mixtures with an even larger helium fraction are expected to improve the yield further, their use is technically limited by the vacuum pumps. For example, the measurement with the 19:1 gas mixture could only be performed up to a xenon partial pressure of ~1.8 bar, which corresponds to a total backing pressure of 34 bar, which is at the limit of the pumping capability.

In addition to reducing the steady-state ionization for improving the XUV yield, using shorter pulses to generate the high harmonics is beneficial. The plasma phase shift φ_p is given by [97, 394]

$$\varphi_p = k \frac{L_p}{2N_c} (N_{pulse} - N_{ss}),\tag{3.5}$$

where k is the wavenumber, L_p is the length of the plasma, and N_c is the critical electron density, defined in Equation 2.99. The electron density at the end of the pulse is given by N_{pulse}, and the steady-state electron density by N_{ss}, with $N_c \ll N_{pulse}$, N_{ss}. If the plasma phase shift is larger than $\varphi_p > \pi/\mathcal{F}$, where $\mathcal{F}$ is the cavity finesse, the intra-cavity enhancement factor is significantly reduced [108]. A lower cavity finesse allows a larger plasma phase shift before clamping occurs but, at the same time, requires a more powerful driving laser to achieve the same intra-cavity intensity. At constant peak intensity, N_{pulse} decreases with the pulse duration, while N_{ss} decreases only with the third root because, in a weakly ionized plasma, the decay is dominated by three-body recombination [97]. Therefore, temporal pulse compression can reduce intensity clamping and further maximize the XUV yield.

Another interesting method to improve phase-matching is the use of counter-propagating pulses to achieve quasi-phase matching. So far it has only been demonstrated with conventional HHG systems at low repetition rates [180]. To demonstrate the feasibility of this, we could use the VMI cavity with counter-propagating pulses.

In order to guide the XUV light out of the cavity, the position of the harmonics needs to be determined and referenced to the rest of the optical setup. Therefore, a ruler made of titanium is fixed on the titanium mounting structure, providing a reference. Titanium is chosen to mitigate stress from unequal thermal expansion compared to the surrounding titanium structure. A sodium salicylate-coated stainless steel screen with laser-marked lines is used to determine the absolute position of the harmonics relative to the fixed ruler, as shown in Figure 3.19 a). A screen image taken with an airside camera is shown in inset c) of the figure. Thereafter, the vacuum chamber is opened, and a mirror is placed at the appropriate position to steer the harmonics towards the toroidal mirror in the focusing chamber further down the beamline. The plane gold-coated mirror is held in a Newport 8821-UHV piezo-driven mirror mount, placed upon a rotatable plate and a piezo-driven linear translation stage (Newport 9066-COM-V-M), enabling 12.5 mm of travel. This mirror positioning system is mounted on a platform since there are gaps between the bridges of the titanium mounting structure. The harmonics are reflected by the gold mirror and guided parallel to the long side of the vacuum chamber.

The focusing beamline consists of differentially-pumped stainless-steel tubes and flexible bellows to decouple the (vibrating) main vacuum system from the connected experiment, which will be mounted directly onto the optical table. The section view of the beamline is shown in Figure 3.20. Furthermore, a dedicated focusing chamber enables the kinematic mounting and adjustment of a toroidal mirror to focus the XUV light. It is crucial to have good vacuum conditions to maintain low pressures in future experiments, such as direct XUV frequency comb spectroscopy of a trapped HCI. Therefore, two-stage differential pumping is employed along the beamline. The first stage is formed by a re-entry CF250 flange, where an FKM-sealed aluminum cap in combination with skimmers is attached and pumped with a TMP. The second stage consists of the focusing chamber and the rest of the beamline and is pumped by another TMP.

A diagnostics flange allows for beam diagnosis directly before the future experiment, where
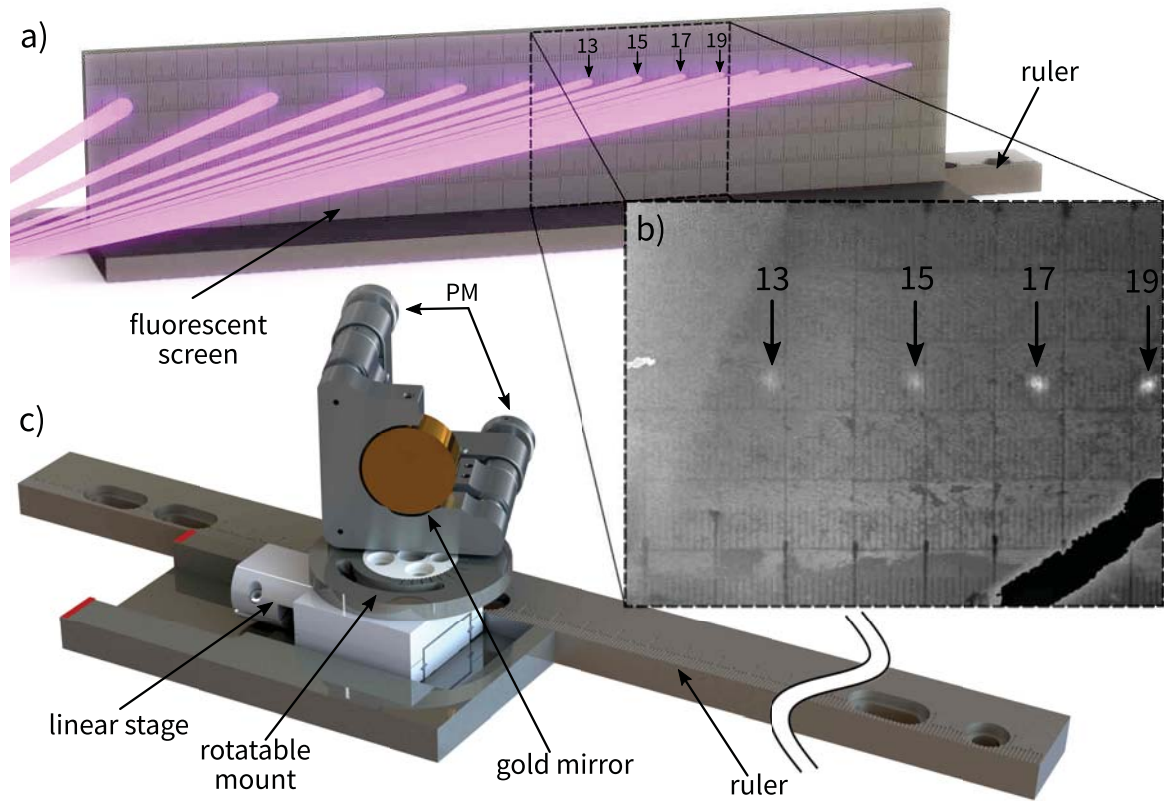
Figure 3.19: Illustration of the harmonic order selection method for guiding the light to the experiment. a) A ruler is connected to the titanium mounting structure. A stainless steel screen coated with sodium salicylate is used for detecting the position of the harmonics, shown here in the b) zoomed inset for harmonic orders 13-19. c) The screen is exchanged with a mirror assembly that can be positioned with respect to the known location of the desired harmonic order, using the ruler as the reference. A piezo-driven mirror mount (PM) on a linear translation stage can be used for fine adjustments. Adapted from [409].
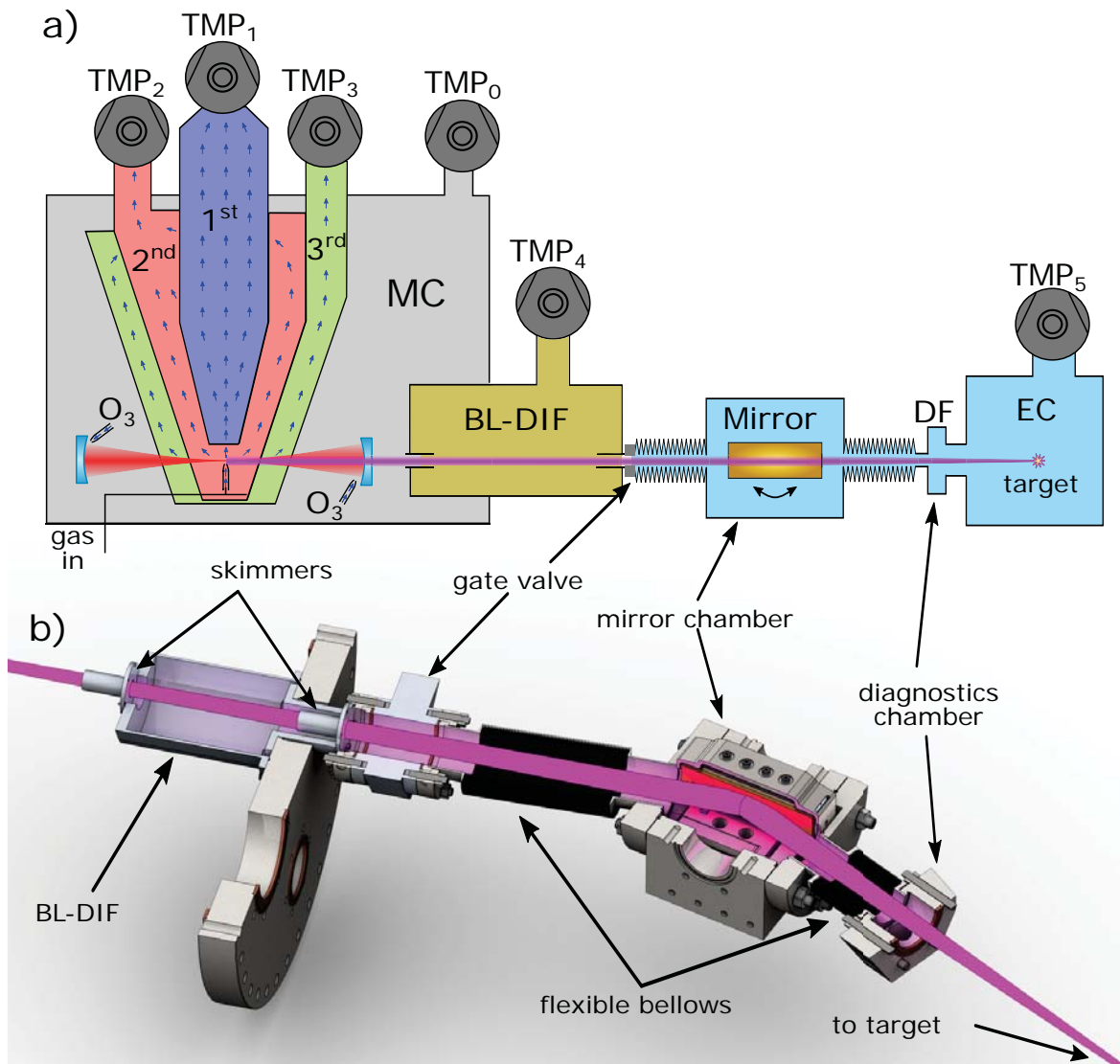
Figure 3.20: a) Schematic of the vacuum beamline that connects the main vacuum chamber (MC) with the movable mirror chamber and the experimental chamber (EC). Turbomolecular pumps (TMPs) pump a section (BL-DIF) of the beamline differentially for improving the pressure in the mirror chamber and thereafter. The gas- and ozone-injection system is described in Figure 3.10. b) Skimmers with the size of the XUV beam minimize the gas flow. The mirror chamber can be moved in four axes. The toroidal mirror focuses the XUV beam into an experimental chamber. b) Adapted from [409].

it is attached to using a CF 40 flange. The lack of space resulted in a compact hexagonal-shaped design with only 30 mm thickness. The CF 16 ports are directly machined into the flange body, and one of the edges is chamfered to make room for the coils around the CryPTEx-SC Paul trap vacuum chamber. Linear manipulators move either an angled sodium salicylate-coated glass screen or a photodiode into the XUV beam. An airside camera images the fluorescent screen from beneath the diagnostics flange through a viewport. More details about the XUV beamline can be found in [409]. At the moment, all components are installed and will be employed for first experiments soon.

4 Intra-cavity velocity-map imaging

This chapter will describe the experimental setup for intra-cavity VMI spectroscopy. It starts with a description and characterization of the VMI cavity, followed by the optical setup, including the method for input coupling counter-propagating and polarization-shaped pulses with a variable delay, which is explained in Section 4.2. For temporal pulse compression and spectral broadening, an MPC is utilized and will be described in Section 4.3. The VMI spectrometer is described in Section 4.4. Furthermore, the results of intra-cavity photoelectron tomography of xenon are shown before colliding pulse operation is demonstrated.

4.1 VMI cavity

To study multiphoton processes at megahertz repetition rates, we have developed a second cavity, the VMI cavity. In contrast to the XUV cavity, the VMI cavity provides a flexible platform with additional flat mirrors, which offers the possibility to replace them with non-standard mirrors in the future. In addition, the polarization dependence of the cavity enhancement is minimized so that pulses with arbitrary polarization can be coupled in. This allows photoelectron tomography for the reconstruction of PADs without any symmetry assumptions using the intra-cavity VMI spectrometer. Another central feature is that counter-propagating pulses with variable delay can be coupled in to produce a pulsed standing wave at the focus. As described in Chapter 1, the generation of counter-propagating pulses in fsECs does not only boost the repetition rate by orders of magnitude compared to single-pass systems, it also significantly reduces the risk of fatal damage to the laser system because the peak power is only reached at resonance inside the passive enhancement cavity and not in the laser system itself.

An essential requirement for the design of the VMI cavity is a seamless integration into the optical setup of the already existing XUV cavity, which is mounted in the titanium structure. To avoid disruptions for experiments with the XUV cavity and minimize the time the system needs to be aired up, the optical components of the VMI cavity were set up on a stand-alone titanium breadboard outside the vacuum chamber. The breadboard has the dimensions of $1050 \times 270 \times 25$ mm, with an M6 threaded hole pattern on a 25×25 mm grid, which is the same as on optical tables. After aligning the cavity optics, the breadboard was inserted into the main vacuum chamber within a single day. This approach had the additional advantage of better access to the optics, which significantly simplified the initial alignment.

The asymmetric bow-tie ring cavity is designed to have one short arm with a focus between the curved mirrors and a long arm where the beam is collimated, as shown in Figure 4.1. The IC mirror is positioned in the collimated arm. Using a traveling wave ring cavity allows manipulation of the light of both propagation directions independently, which would not be possible with a standing wave linear cavity. The length is 2997.9 mm to match the 100 MHz repetition rate of the comb laser. The long arm is folded several times with flat mirrors to fit on the breadboard, as shown in Figure 3.7. This offers the option to exchange flat cavity optics by non-standard mirrors, as will be described later in Section 4.1.5. One of these flat mirrors is piezo-actuated to change and stabilize the cavity length.

The cavity mode is simulated using the ABCD-matrix formalism that was described in Section 2.3.1. Astigmatism in the focus region is compensated with a concave cylindrical IC mirror with a curvature of $R = 25$ m. Concave mirrors (CM1/CM2), with a curvature of $R = 125$ mm at
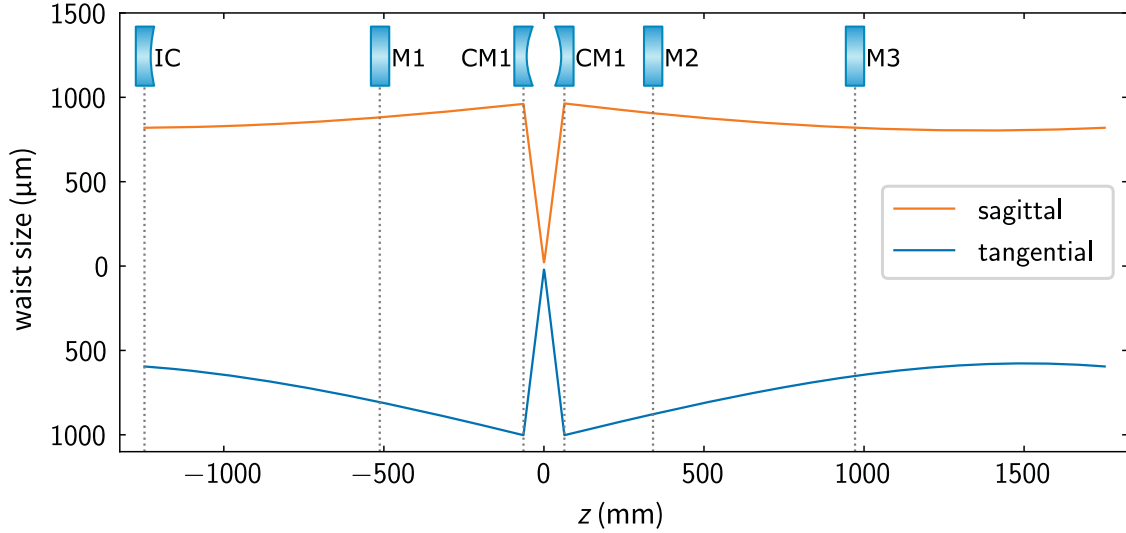
Figure 4.1: Simulated waist size of the VMI cavity mode in the sagittal (vertical) and tangential (horizontal) plane, obtained using the ABCD-matrix formalism. Astigmatism in the focus region is compensated with a cylindrical input-coupler (IC) with $R = 25\,\text{m}$. Concave mirrors (CM1/CM2) with $R = 125\,\text{mm}$ focus the beam to a waist size of $<25\,\mu\text{m}$. Flat mirrors (M1-M3) steer the beam and are used for length stabilization.

a distance of 127.4 mm, focus the beam to a round focus with a waist size of 21.3 μm, as shown in Figure 4.2, where also the stability of the cavity is plotted. Stable cavity operation ($g < 1$) is only possible for certain distances between the curved mirrors, as described by Equation 2.40.

The HR mirrors in the VMI cavity have the same ion-beam sputtering (IBS) coating of alternating SiO_2 and Ta_2O_5 quarter-wave dielectric layers as the XUV cavity. The coating is designed for minimal dispersion (GDD$< 0.5\,\text{fs}^2$) and high reflectivity ($R \approx 99.996\,\%$) between 1020 to 1060 nm with a high damage threshold. As described in Section 2.3.2, the enhancement of a low finesse cavity is maximized when the losses are dominated by the IC. Therefore we use an IC reflectivity of $R_{\text{IC}} = 99.3\,\%$.

A knife-edge scan in the horizontal (tangential) and vertical (sagittal) axes of the cavity mode between the focusing mirrors was performed by moving a razor blade into the beam and hence blocking parts of it. The blade is mounted on a three-axis micrometer-driven translation stage and is first moved horizontally and then vertically into the beam. A photodiode placed behind M1 detects the leakage of the cavity mode, which is proportional to the intra-cavity power. During this measurement, the cavity is operated in scan mode, and the average peak height of the transmitted light is recorded for each blade position. The power decrease is given by integrating across the beam profile. In the case of a Gaussian-shaped beam profile (cf. Section 2.3.1), a standard error function can be used to fit the transmitted power values

$$P = P_0 + \frac{P_{\text{max}}}{2}\left(1 - \text{erf}\left(\frac{\sqrt{2}\,(x - x_0)}{w}\right)\right), \tag{4.1}$$

with the maximum transmitted power P_{max}, the offset P_0, blade position x with offset x_0. The same procedure to obtain the beam radius w is repeated at several positions along the beam propagation axis z, ensuring that enough data points are collected in close vicinity of the focus position as well as further away.

Repeating the measurement for several curved mirror distances yields the optimal position
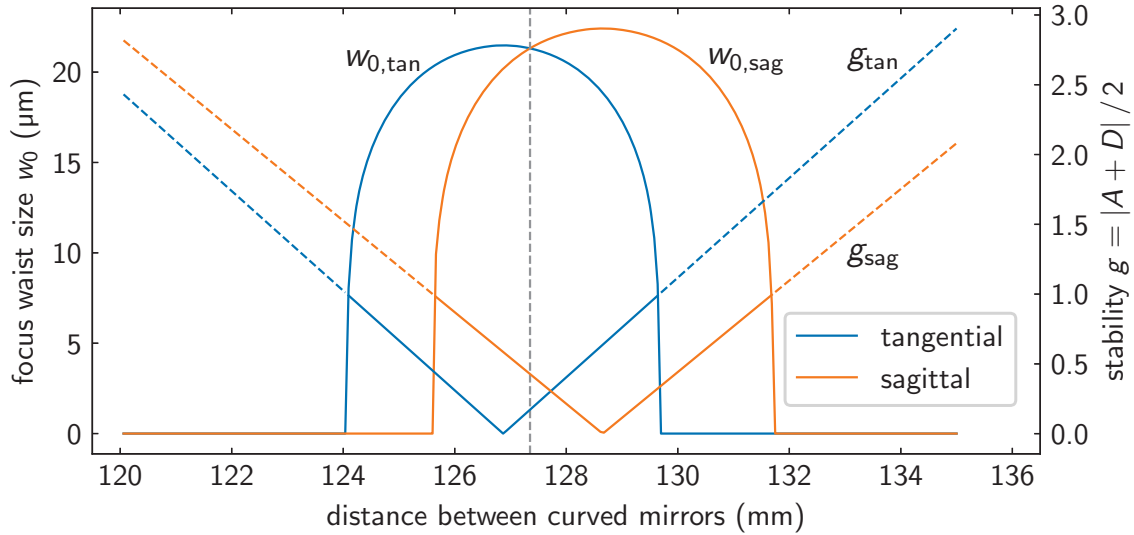
Figure 4.2: Simulated stability region and focus waist size for varying the distance between the curved focusing mirrors CM1 and CM2. A round focus with a waist size of 21.3 µm is achieved at a distance of 127.4 mm.

of both mirrors for astigmatism-compensated cavity operation. The final measurement of the cavity focus waist (beam radius) is shown in Figure 4.3. The solid lines indicate the calculated waist size obtained by ABCD-matrix simulations during the design process of the cavity. A fit of the measured cavity mode is plotted with a dashed line. The error bars indicate the combined error from the reading of the micrometer scale and the accuracy of the intra-cavity power measurement. From the fit, a waist size of 21.3 µm and 22.9 µm are obtained in the tangential and sagittal direction, respectively. It confirms that astigmatism-compensation is achieved with a residual ellipticity of 93.4 %.

4.1.1 Cavity operation

A schematic overview of the complete optical setup used for operating the VMI is shown in Figure 4.4. Pulses from the comb laser oscillator are amplified in the previously described amplifier system. Then the pulses are split in a variable ratio using a HWP and a polarizing beam splitter (PBS) to the VMI and XUV cavity. In the same way, the portion sent to the VMI is divided into the normal-propagating and counter-propagating directions of the cavity. The naming convention of the cavity circulating directions is the following: The normal-propagating direction is the one that is directly sent to the cavity. In the counter-propagating direction, the pulses pass through the SAD-box before being sent to the cavity. This setup allows shaping the pulses into a double pulse with variable delay and freely adjustable polarization, which is explained in detail in Section 4.2. Before entering the vacuum system, pulses for both directions pass through a mode-matching telescope. Compared to the mode-matching telescope for the XUV cavity, which consists of concave cylindrical lenses with long focal lengths and, thus, large dimensions, the mode-matching telescope for the VMI cavity consists of concave and convex cylindrical lenses, reducing the outer dimensions by about a factor of five. Motorized zero-order HWPs are used to rotate the polarization before the light enters the vacuum chamber through AR-coated FS windows.

Small leakages of the cavity modes of the normal-propagating and counter-propagating directions are picked up behind the flat cavity mirror M1 and guided to the outside of the vacuum
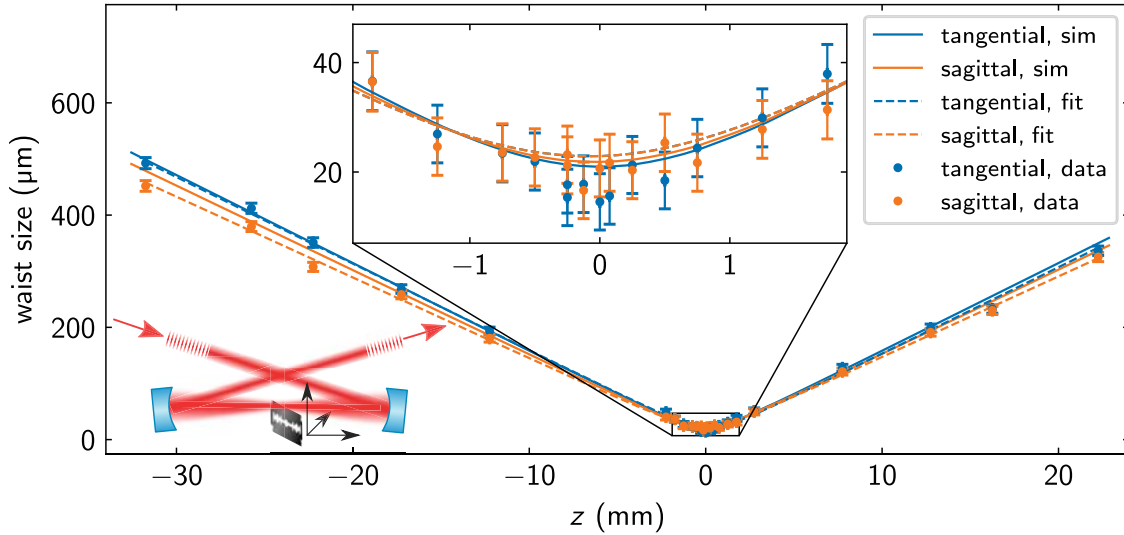
Figure 4.3: Waist size measurement at the focus. As illustrated in the bottom left, a knife-edge scan is performed at several positions along the beam propagation axis. The cavity waist size is shown in the sagittal (vertical) and tangential (horizontal) planes. The fit of the knife-edge scan data agrees well with the calculated waist size (cf. Figure 4.1). The zoomed inset shows the focus region, where many data points need to be collected to make the fit meaningful. The primary source of error is the readout inaccuracy of the translation stage micrometers.

chamber. There, polarization-independent beam splitters (BSs) split the beam. Half of each beam is sent to a camera for mode monitoring (Mako G-234B mono PoE, Allied Vision), and the other half is sent to a photodiode for power monitoring. The photodiode signal is proportional to the intra-cavity power. This signal is calibrated by removing the IC and recording the photodiode signal as a function of laser power.

The cavity length can be tuned by in total 25 mm at a stepsize of ~50 nm using a piezo-driven (N-470.22U, Physik Instrumente) translation stage (9066-COM-V-M UHV, Newport). A flat mirror (M2) is glued on a ring-shaped piezo-chip actuator for fast feedback. The pulse-to-pulse phase accumulation inside the cavity can be matched to the frequency comb CEO for maximum enhancement by tuning the comb laser CEO. The CEO of the comb drifts slowly and requires readjustment every few hours. However, maximum enhancement is reached close to $f_{\mathrm{CEO}}^{\mathrm{comb}} = 20\,\mathrm{MHz}$, the frequency at which the CEO of our comb laser can be locked, which allows many hours of continuous operation of the laser system without intervention.

4.1.2 Cavity-length stabilization

Unlike the XUV cavity, which is directly mounted to the rigid titanium rod structure, the VMI cavity is more susceptible to vibrations because the 82.5 mm beam height is larger than the 50 mm beam height of the XUV cavity. The reason is that the breadboard had to fit below the bridges and above the monolithic support structure. Its thickness was limited to 25 mm, which further reduces the stability compared to the rigid titanium structure. By connecting the breadboard to the mono-rod structure in as many places as possible, we reduced the vibration amplitude of the VMI cavity close to the XUV cavity. However, already fluctuations of the cavity length at the nanometer scale (cf. Section 3.2.3) would result in strong intensity fluctuations and thus need to be actively canceled.

To lock the cavity length to the comb laser repetition rate, we use the PDH-technique [410–
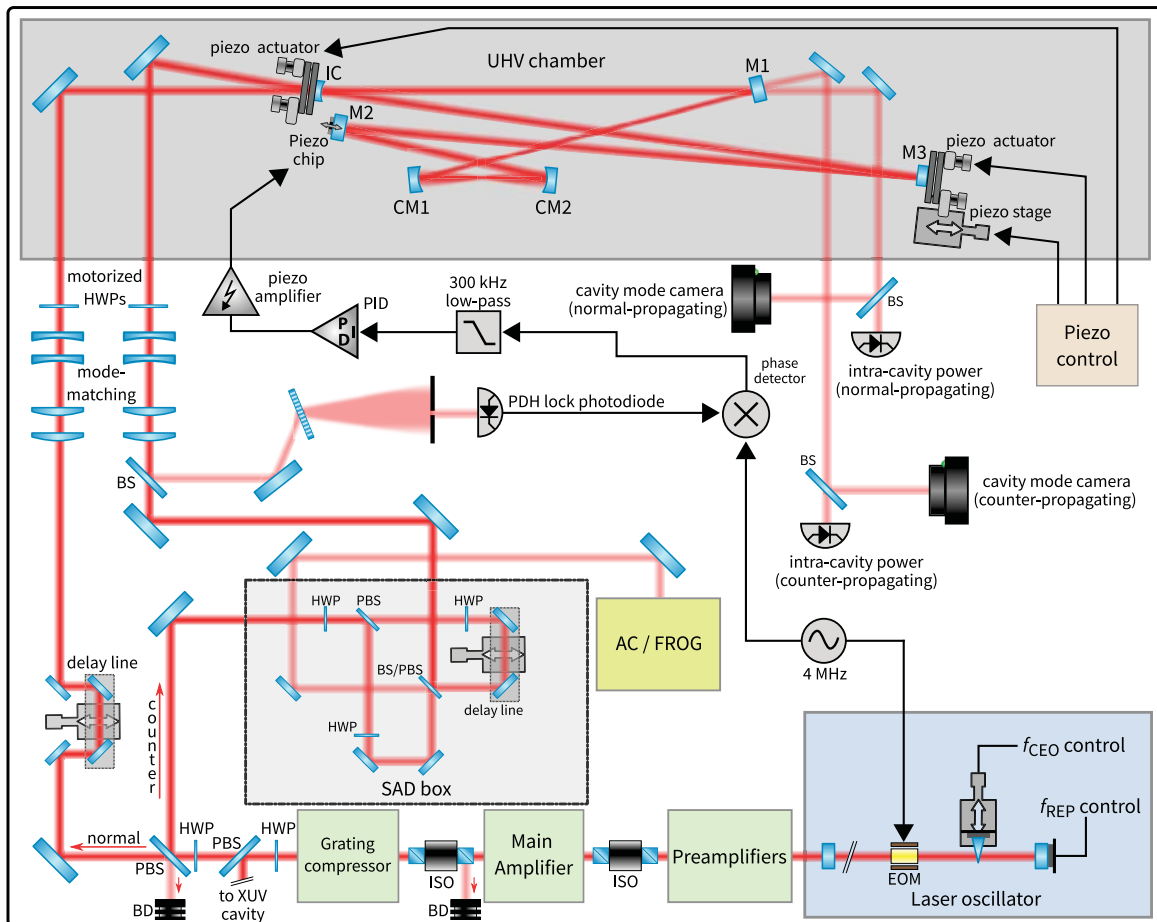
Figure 4.4: Schematic overview of the VMI cavity optical setup. Frequency comb pulses with adjustable f_{rep} and f_{CEO} are amplified in several amplifier stages separated from each other by optical isolators. A half-wave plate (HWP) after the grating compressor allows for adjustment of the power ratio of the pulses sent in the normal- and counter-propagating directions of the *in vacuo* enhancement cavity. The cavity can be aligned by four remote-controlled piezo motors behind two cavity mirrors. For PDH cavity locking, the phase of the comb pulses is modulated with an electro-optic modulator (EOM) in the laser oscillator, and a fraction of the reflected light from the IC of the cavity is spectrally dispersed and sent to a fast photodiode. The photodiode signal is sent to a phase detector to extract an error signal for the PID-controller. Fast feedback is applied to a piezo chip behind one cavity mirror to lock the cavity length to f_{rep} of the laser. Slow drifts are compensated with a motorized translation stage. In the counter-propagating direction, a split-and-delay line (SAD) box (cf. Figure 4.19) is used to split the pulse in two polarization-shaped copies with a variable time delay. A second output can be used for pulse characterization with autocorrelation (AC) or frequency-resolved optical gating (FROG). A delay line in the normal-propagating arm is used to set the pulse overlap position. The leakage of both cavity propagation directions is guided outside the vacuum chamber to measure the intra-cavity power and to monitor the cavity mode. Cylindrical lenses are used for the mode-matching of the incident light. The back-reflected light of the opposite cavity propagation directions is blocked with beam dumps (BDs).
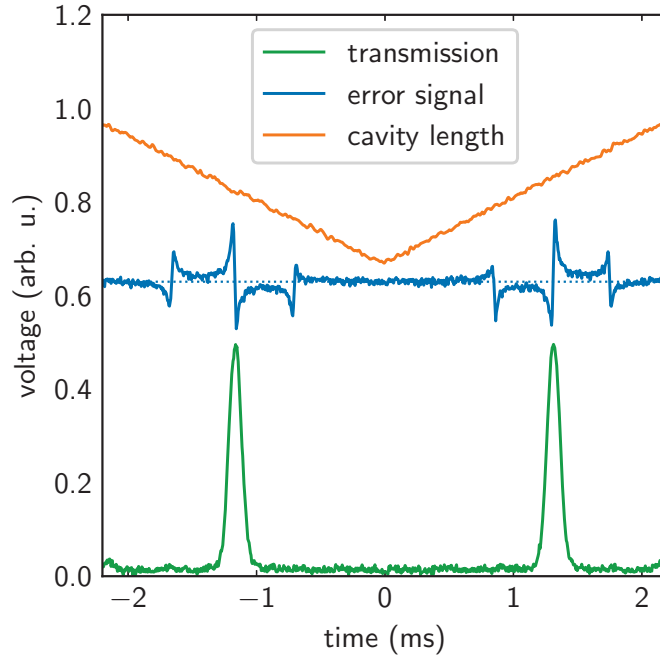
Figure 4.5: Resonance peak and error signal of the enhancement cavity. Here, the cavity length is scanned at a rate of 200 Hz by applying a symmetric sawtooth voltage to the piezo element. The PDH error signal has a zero-crossing at the transmission maximum.

412]. Compared to a side-of-fringe lock [413], it has the advantage that the cavity length can be locked to the maximum of the transmission peak. Hänsch-Couillard locking would require a polarizing element in the cavity and is thus not possible [414]. A fraction of the reflected light of the normal-propagation direction is picked up with an AR-coated beam splitter and used for the feedback loop. It is spectrally dispersed with a grating and sent through a variable slit. A variable neutral-density filter is used to adjust the power. Subsequently, the light is detected with a fast photodiode (PDA05CF2, Thorlabs) and sent to a phase detector (ZRPD-1+, Mini-Circuits). A ~4 MHz modulation signal is applied to an EOM inside the comb laser oscillator to produce sidebands. A phase detector detects the phase between the photodiode signal and a phase-shifted replica of the RF modulation signal. Amplification and low-pass filtering of the phase-signal yields the error signal, as shown in Figure 4.5. The error signal is fed to a PID controller, either a digital controller (STEMLAB 125-10 Redpitaya) [415] or an analog device (PID110, Toptica). The output voltage is amplified to 0-150 V with a piezo amplifier (PD200-V0 150, Piezodrive) that can handle the high capacitance of the piezo and then applied to the piezo chip to change the cavity length on short time scales. The piezo voltage is monitored to compensate for slow thermal drifts, and the piezo stage of M3 is moved automatically to keep the cavity length within the control range of the piezo chip. In this way, the cavity stays locked for many hours.

Typically, the feedback bandwidth of piezo mirrors is limited by strong mechanical resonances, which occur above ~10 kHz. The resonance of a piezo element is typically at least one order of magnitude higher, which depends mainly on the thickness and the piezo material. However, because the piezo is connected to the mirror and its mount, mechanical resonances are expected at much lower frequencies, making it difficult to achieve a high feedback bandwidth. To improve the locking performance, often very small mirrors ($\varnothing < 10$ mm) are used. The reason is simple when considering the mechanical model of two masses (mirror and the mirror mount)

coupled by a spring (the piezo element). A higher mirror mass will increase the motion amplitude of the mirror mount and thus introduce vibrations into the system that can excite acoustical resonances. Various mirror mount structures were demonstrated to avoid or dampen these resonances. One possibility is to decouple the piezo-mirror from its mount using soft materials such as rubber [416]. Even though this method allows using larger mirrors, we did not implement this approach because of reduced UHV-compatibility and capability to withstand high laser power. Another method is to clamp the piezo stack from the side to reduce the coupling of the acoustic wave to the mount [417]. Briles and coworkers filled a bullet-shaped copper mount with lead to dampen the mechanical resonances [418]. In a recently demonstrated setup, Nakamura and coworkers pushed the feedback bandwidth up to 500 kHz by using a wedged damping alloy [419]. The wedge is essential to avoid an acoustic resonator being formed by the damping alloy. They matched the acoustic impedance of the mirror mount and the damping alloy with an impedance-matching gel to avoid the reflection of acoustic waves from the contact area. Additionally, they used a tiny mirror ($2 \times 2 \times 0.7\,\text{mm}^3$) glued on a 0.6 mm thin piezo, which was crucial to reach the 500 kHz bandwidth.

We have incorporated these findings into our setup, even though there are some fundamental differences in the experimental conditions. For example, the minimum mirror size is determined by the size of the laser beam at the mirror position. The fraction of the power reflected by a mirror with radius r is given by

$$R_{\text{mirror}} = 1 - e^{-2r^2/w^2}, \tag{4.2}$$

where w is the $1/e^2$ intensity radius of the gaussian beam. With an intra-cavity beam radius of ~1 mm, and the requirement that the beam clipping losses should be less than the mirror losses ($< 0.004\,\%$), a minimum clear aperture of ~7.5 mm is necessary for normal incidence. The possibility of reducing the beam size is ruled out in our case since otherwise the ability to achieve high intra-cavity intensities would be limited. Another important consideration concerning the choice of piezo and mirror size is the low thermal conductivity of the piezo elements paired with a low thermal damage threshold. Already well before reaching the Curie temperature, the piezomechanical properties change irreversibly. The epoxy adhesives that are used also change their properties at temperatures in this range ($T \approx 100\,°\text{C}$). Since convective cooling by the surrounding gas does not occur in a vacuum, heat can only be dissipated by the poorly heat-conducting piezo material and thermal radiation. At the same time, several watts of optical power are transmitted through the mirrors in the locked state of the cavity. For this reason, we limit our selection to ring piezos, through which the leakage beam can pass. The lengths of both cavities fluctuate at the kilohertz level by ~30 nm, caused by vibrations from the turbomolecular pumps. Additionally, larger movements in the range of tens or even hundreds of nanometers occur when components on the optical table are bumped. Large and much slower drifts on the order of several micrometers occur when operating the system at high power. Our slow-drift compensation loop with the piezo-controlled translation stage can compensate well for the latter. The faster oscillations have to be directly counter-acted with the piezo element that needs to have a stroke of $\gtrsim 1\,\mu\text{m}$. We could use a thin and fast piezo for this, in addition to a slower and thicker piezo stack with a larger range. However, this procedure requires a crossover in the control loop, which we avoid by using a single piezo stack with medium thickness instead, simplifying the setup by sacrificing control bandwidth.

In a first attempt, we utilized a similar WC bullet mount that is also used in the XUV cavity, with a shape similar to the lead-filled copper bullet mount, which was developed by Briles *et al.* [418], as shown in Figure 4.6 a). The bullet mount is fixed inside a conventional stainless steel one-inch mirror mount with piezo-driven motors to control the tip and tilt angle. The whole assembly is mounted on a piezo-driven translation stage to change the cavity length within a large range. We have choosen WC because it is a very stiff (Young's modulus of ~600 GPa) and dense
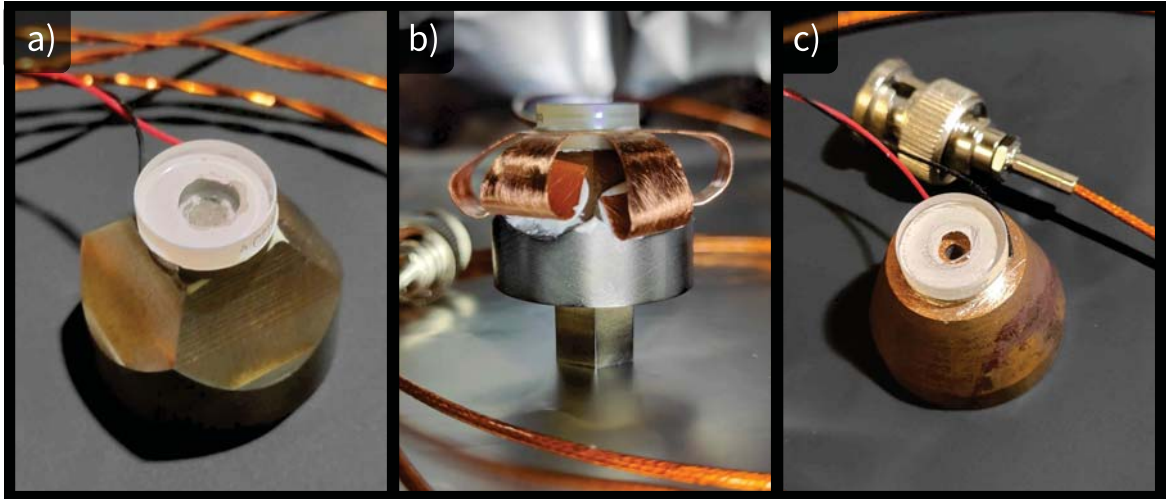
Figure 4.6: Photographs of piezo bullet mounts for cavity length stabilization: a) tungsten-carbide (WC) bullet mount, b) tungsten carbide (WC) bullet mount with copper cooling strips, and c) lead-filled copper bullet mount.

($\sim$16 g cm^{-3}) material. For the mirror, we used a 3 mm thick, $\varnothing$12.7 mm HR-coated sapphire substrate, glued with Torr Seal (Agilent) to a 2 mm thick ring-shaped piezo with an outer and inner diameter of $\varnothing$12 and $\varnothing$6 mm, respectively, and with a stroke of 2 µm (HPCh150/12-6/2, Piezomechanik). According to the simple model of spring-coupled masses, a high bandwidth was expected.

However, the first piezo mirror assembly suffered from thermally induced mirror deformation when locking the cavity at high power. As a consequence, we added cooling strips made of copper glued between the mirror and piezo to transfer the heat to the tungsten carbide, which was connected with a flexible copper link to the breadboard, as shown in Figure 4.6 b). The piezo is electrically connected to the piezo controller with a Kapton-insulated coaxial copper cable and a vacuum-compatible BNC connector and feedthrough. Unfortunately, strong mechanical resonances worsened the situation. In Figure 4.7, we estimate the frequency-dependent response of the locked cavity by observing the error signal as a function of the frequency of a small perturbation added to the feedback signal from the PID control loop, using a vector network analyzer (VNA). If the perturbation is small, the error signal changes approximately linearly with the cavity length change. Note that the recorded traces are snapshots of the locked state of the entire cavity, including the locking electronics at the time the respective measurement is taken, which differs by several months for the respective traces. Consequently, this measurement can only be a rough estimate of the actual piezo responses. The response function of the WC mount shows many resonances and severe phase fluctuations.

In an improved design, we adapted the lead-filled copper bullet mount of Briles *et al.*, which reduced the number of resonances compared to the WC mount. A photograph of this mount is shown in Figure 4.6 c). Still, the locking performance was not sufficient, and large resonances limited the locking performance. Additionally, lead should be avoided in UHV applications. We suspected that the assembly consisting of the conventional mirror mount, which fixates the bullet mount with an inset screw, and the translation stage does not provide enough stability for the dynamic piezo mirror. As a result, we separated the fast- and slow drift control and designed a dedicated piezo mount with a high-damping alloy instead of lead, which is very soft and hard to machine. In air, a wide range of high-damping materials is available [420], but UHV operation prevents the use of typical organic materials. Furthermore, mechanical stability is
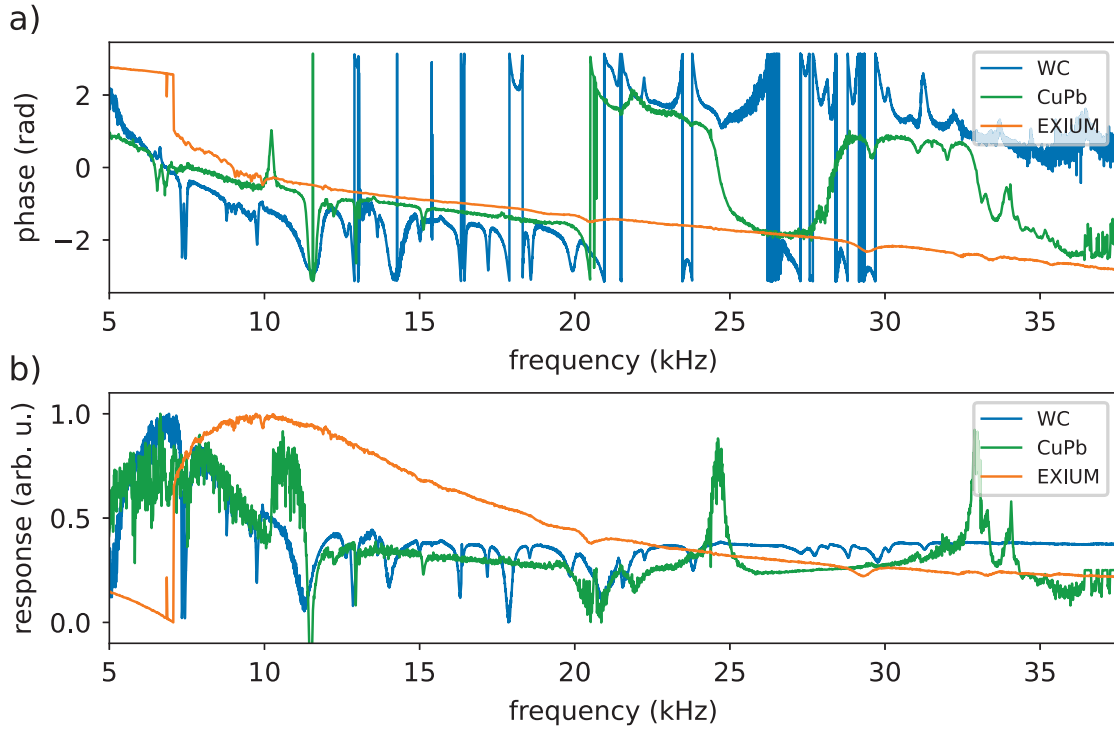
a)

b)

Figure 4.7: Determination of mechanical resonances with a vector-network analyzer to compare a tungsten carbide (WC) and a lead-filled copper (CuPb) bullet mount with a high-damping alloy piezo mount (EXIUM). The measured response is plotted in b) and its phase in a).

often a concern.

For our final design, we adapted the concept of Nakamura *et al.* [419], who employed an Al-Fe damping alloy [421, 422]. It significantly improved the locking performance of their cavity by damping the oscillation amplitude of the mirror mount. Another high-damping material class is Cu and Mn-based alloys, such as Exium AM (LBI). According to the manufacturer, it behaves about ten times better than grey cast iron, which is a well-known high-damping material, in terms of damping in the range of $-15\,°C$ to $50\,°C$.

We designed and fabricated piezo mounts from Exium and Al-Fe damping alloys, as shown in Figure 4.8. The piezo is glued with a two-component, silver-filled epoxy with a high glass transition temperature (ET-H21D-0028, EPO-TEK). Compared to an alumina-filled epoxy, such as Torr Seal, it has the advantage of approximately twice the acoustic impedance ($\sim 7\,MRayl$), which better matches the impedance of glass ($\sim 12\,MRayl$), piezo ($\sim 35\,MRayl$), and metal ($\sim 40\,MRayl$) [423]. Only a very thin layer of epoxy is applied. The damped piezo mount has the outer dimensions of $35 \times 25 \times 15\,mm$ with an angled backside to avoid standing acoustic waves and is screwed with four M3 screws on a rotatable brass plate. The brass plate sits on a solid monolithic stainless steel mount with a footprint of $64 \times 40\,mm$, clamped to the titanium breadboard. The vertical angle of the mirror is adjusted with a lockable fine-threaded screw around a 1 mm thick wire-eroded pre-stressed flexure pivot. Additional springs can be inserted to further increase the contact pressure of the hardened tip of the screw onto a hardened steel plate glued to the stainless steel mount.

A frequency analysis was performed (SolidWorks) to determine the main mechanical resonances of the high-damping piezo mount. From the lowest 50 resonances, the 12 with the largest amplitude at the piezo position were selected and shown on the right side of Digure 4.8, with i)
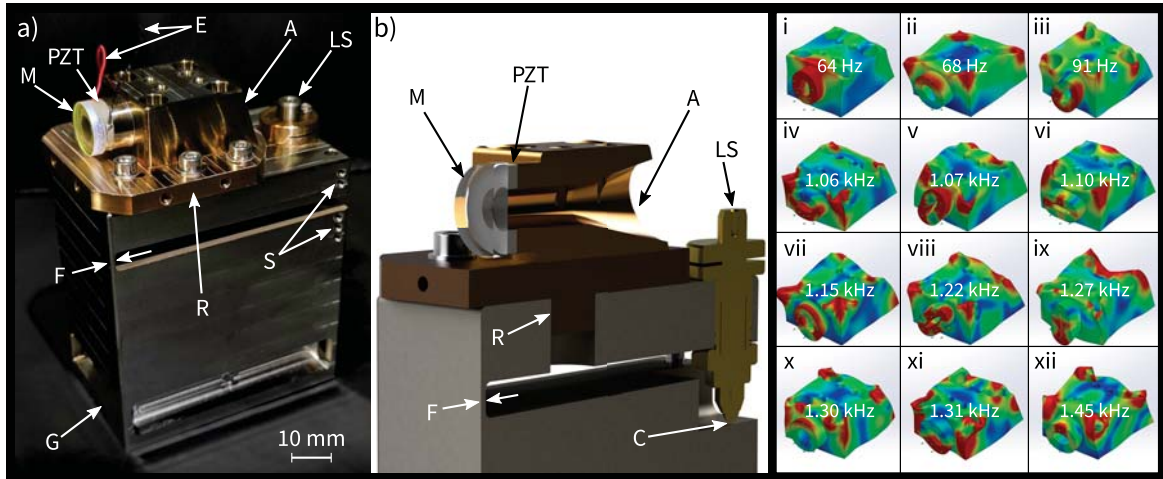
Figure 4.8: a) A photograph and b) a cross-section of the piezo mount upgrade with a flat cavity mirror (M) glued on a ring-piezo (PZT) that is glued on a mount fabricated from a damping alloy with an angled backside to avoid standing acoustic waves (A). It is placed on a rotatable brass plate (R) connected to the monolithic stainless steel mount. The vertical angle of the mirror is adjusted with a lockable screw (LS) around a flexure pivot (F). Springs (S) can be inserted to increase the contact pressure of the screw's hardened steel ball onto a hardened steel plate (C). Main mechanical resonances are determined by simulations and shown highly exaggerated on the right side in i-xii.

64 Hz, ii) 68 Hz, iii) 91 Hz, and iv-xii) 1060 Hz - 1450 Hz. Only the isolated upper part of the mount was considered, neglecting the interaction with the other components. Knowing the resonance frequencies helps to determine which component is responsible for intensity fluctuations of the locked cavity based on the noise frequency spectrum of the error signal. This procedure had proven to be helpful when we were experiencing lock instabilities, and it allowed us to trace the oscillations back to a 80 Hz vibration mode of the titanium breadboard. Cancellation of this resonance by stiffening the board at the position of maximum amplitude significantly improved the intra-cavity intensity stability. After the piezo mirror upgrade, no deterioration in the stability of the cavity was observed, indicating that the high-damping capacity of the alloy strongly reduces the vibration amplitude at the resonance frequencies.

4.1.3 Cavity ring-down measurement

The finesse of the cavity can be determined with a ring-down measurement, as explained in Section 2.3.2. Such a measurement is shown in Figure 4.9. A square waveform at a rate of 10 kHz is applied to the EOM in the frequency comb oscillator to change the phase of the incident pulses at the fastest possible rate. Simultaneously, the cavity length is scanned linearly with the piezo mirror at a much slower rate (sub-kHz). When the cavity is on resonance, the EOM rapidly changes the phase of the incident pulses resulting in an off-resonant cavity. This switching is much faster than the lifetime of the cavity. Thus, the light that was stored inside the cavity when it was resonant leaks out and is detected with a photodiode. From an exponential fit, a decay time of $\tau_{cav} = 1.274(4)\,\mu s$ is extracted. This corresponds to a finesse of 800(2).

Additionally, the light leaking out of the cavity interferes with the off-resonant incident light at the IC-mirror. A fraction of the reflected light is sent to a fast photodiode, where laser pulses are recorded at the 100 MHz repetition rate of the frequency comb, as shown in the zoomed inset of Figure 4.9. A damped-cosine with second-order chirp is fitted to the maxima of the pulses to
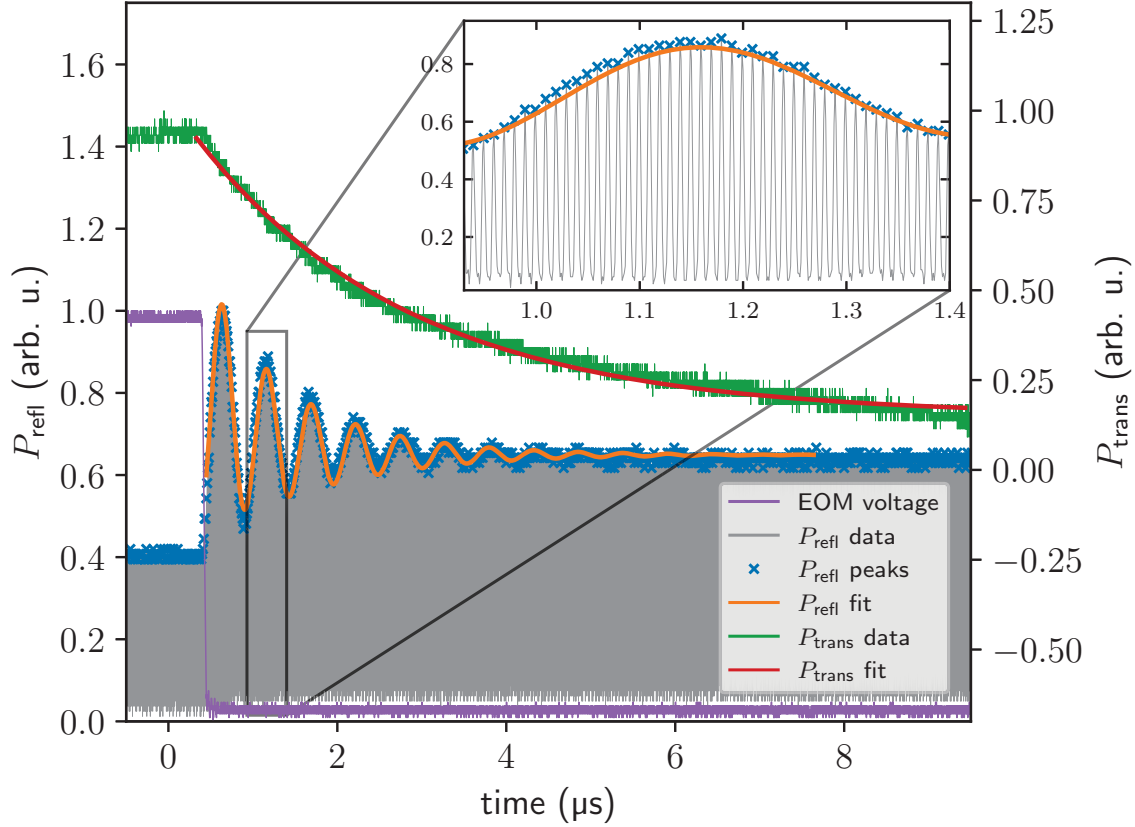
Figure 4.9: Ring-down measurement of the normal-propagating light in the VMI cavity with an IC mirror reflectivity of 99.3 %. The fit of the transmitted light yields a decay time of 1.18(2) µs, implying a finesse of 743(14). The fit of the reflected light yields a decay time of 1.274(4) µs and a finesse of 800(2) which is in broad agreement with the values obtained for the transmitted light. The stated errors are the fit standard errors.

yield the intensity decay time of 1.18(2) µs and a finesse of 743(14). For these measurements, an IC-mirror with a reflectivity of $R_{ic} = 99.35\,\%$ is used, which implies a cavity loss of $\sim\!0.14\,\%$. The intra-cavity power is enhanced by a factor of $\beta_\epsilon \approx 200$, which already includes the mode-matching losses described by Equation 2.54. These values agree with the XUV cavity, where a similar finesse of 805 is achieved with the same IC reflectivity.

4.1.4 Cavity polarization

To allow polarization dependent studies in the cavity, it is important that the light coupled into the cavity retains its polarization state while circulating. In other words, the cavity should not exhibit any birefringence and therefore be polarization-independent.

Ideally, the modes of orthogonal linear polarization are degenerate in the cavity. In reality, birefringence leads to splitting of the resonance frequencies in the cavity for the two orthogonal polarization axes [424–426]. If we consider the resonance condition in the cavity (cf. Equation 2.48), which is met when the round-trip phase accumulates to an integer multiple of $\phi_{cav} = n2\pi$, we get

$$k_s L + \phi_{pol} = k_p L,\tag{4.3}$$

where $k_{s,p} = 2\pi/\lambda_{s,p}$ is the wavevector of the orthogonally linearly polarized states of the funda-

mental TEM_{00} cavity mode of total length L. The s-polarized light acquires a phase shift of ϕ_{pol} compared to the p-polarized light within one round trip. Writing the above expression in terms of angular frequency $\omega_{s,p} = 2\pi f_{s,p} = c k_{s,p} = 2\pi/\lambda_{s,p}$, and introducing the frequency splitting $\Delta\omega = \omega_p - \omega_s$, yields $\Delta\omega = c\phi_{pol}/L$. Using Equation 2.48 and 2.49, and writing the expression in terms of the cavity finesse $\mathcal{F} = \Delta\omega_{FSR}/\Delta\omega_{FWHM}$, results in [424]

$$\frac{\Delta\omega}{\Delta\omega_{FWHM}} = \frac{\phi_{pol}}{2\pi}\mathcal{F}, \tag{4.4}$$

which is the polarization-induced frequency spliting relative to the cavity line width. As a result, phase shifts on the order of $1/\mathcal{F}$, completely alter the intra-cavity polarization state.
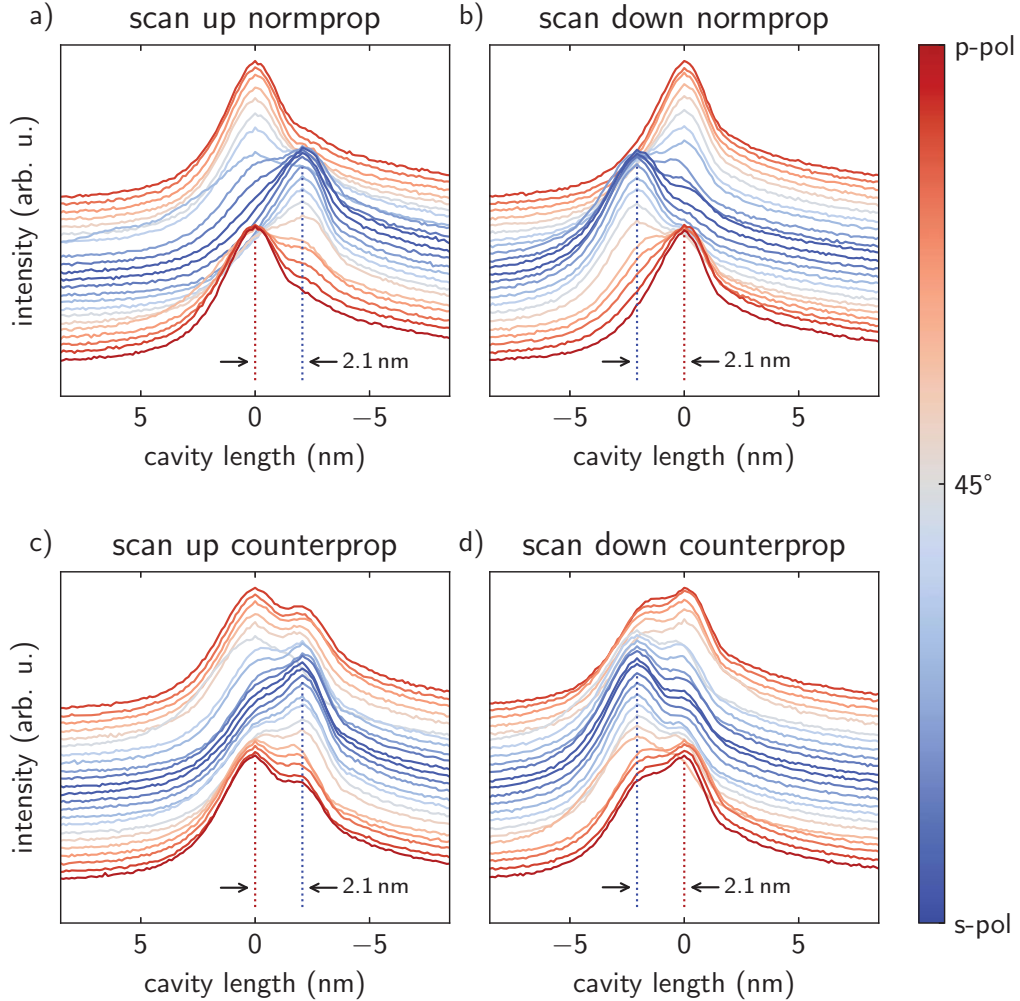
Figure 4.10: Measurement of the birefringence-induced line splitting of the VMI cavity. The cavity-transmitted light is detected with a photodiode, while the cavity length is scanned, and the input polarization is rotated with a half-wave plate (color coded). In the up-scan direction, which is shown in a) and c), the cavity length decreases, while in the down-direction, it increases, as shown in b) and d). The cavity resonance peaks for s- and p-polarized light are split by ~2.1 nm, which corresponds to a frequency shift of ~200 kHz. The frequency splitting in the normal-propagating direction is shown in a) and b). It is the same as in the counter-propagating direction of the cavity, as shown in c) and d). Note the lower total enhancement for a mixed polarization state (45°).

To measure the birefringence-induced peak splitting, we scan the cavity length with the intra-

cavity piezo element by applying a symmetric sawtooth voltage. A photodiode detects the transmitted light as a function of the angle of a motorized HWP, as shown in Figure 4.10. The cavity length is calibrated by recording the PDH error signal together with the transmission peaks (not shown). The phase modulation with a frequency of 4.5 MHz generates sidebands that serve as a length reference using the FSR of the cavity and center wavelength of the laser. The advantage of this method compared to prior length calibration is that the transmission peak is always centered between the sidebands and thus any change of the cavity piezo properties over time are taken into account. This is important because we have observed changes of the mechanical properties of the piezo after high-power cavity operation, which is most probably caused by excessive heating of the piezo itself or the glue, as described in more detail in Section 4.1.2. The birefringence-induced peak splitting is measured for the light propagating in both cavity directions, i. e. normal-propagating and counter-propagating direction. The resonance splitting of ~2.1 nm is determined from the position of the resonance maxima for pure s- and p-polarized input light and is the same for both propagation directions and cavity length scan directions. It induces a shift that corresponds to an intra-cavity $\sim\lambda/500$ waveplate. In terms of frequency, the splitting is approximately 200 kHz, which is similar to the resonance linewidth. The upwards scan direction corresponds to decreasing cavity length. Note that the line shape is not symmetric for both scan directions since the intra-cavity light leaks through mirrors once the resonance has passed.

Non-normal angles of incidence on optics can be a cause of birefringence [427]. In many thin-film designs of HR mirrors, the optical path differences between s- and p-polarization produces a phase shift that alters the polarization state of the reflected beam. Correction of the polarization aberrations of mirrors was demonstrated recently [428]. However, these techniques do not apply to dispersion-optimized HR mirrors with a high damage threshold, as it is necessary for high-power cavity operation. As pointed out by T. W. - Z. Lynn [424], the experience with high-finesse cavities for cavity QED experiments has shown that, in most cases, the dominant source of cavity birefringence is mechanical stress. Several explanations exist for the occurrence of stress: Either the mirrors are clamped too tightly in their holders, or the adhesive connection with the holder induces mechanical stress. In the latter case, it has been observed that when the glued mirror is heated, the epoxy adhesive only hardens and sets completely at the elevated temperature. After cooling, the mirror has internal mechanical stress, leading to birefringence. The author addressed the problem by only baking the mirrors at rather low temperatures and using thick mirrors with the thinnest possible adhesive layers. Alternatively, the mirror can be bonded to a holder made of the same material as the mirror.

We also apply only very thin adhesive layers. However, in our case, heating cannot be avoided due to the very high intra-cavity power and a considerable amount of light leaks through the highly reflective mirrors. We have also observed this experimentally: After the first cavity operation at high power over an extended time, the properties of the piezo have changed.

Another way to prevent birefringence is to use the thickest possible mirror substrates, which are connected to the holder as far away from the surface as possible - either by clamping or gluing. We do not use holders in the VMI cavity where the mirrors are clamped the traditional way with an inset screw. Instead, we use holders in which the mirrors are pressed gently from behind against a ring using a concentric spring ring. For some cavity mirrors, the mirrors are glued directly to the holder.

Birefringence not only results in a change of the cavity polarization state from pulse to pulse but also causes a lower intra-cavity enhancement that varies as a function of polarization angle, as shown in Figure 4.11. When the intra-cavity polarization changes each round trip but the incoming polarization stays the same, a mismatch between the two fields occurs, and less light is coupled in. For this measurement, the enhancement is recorded for the normal-propagating
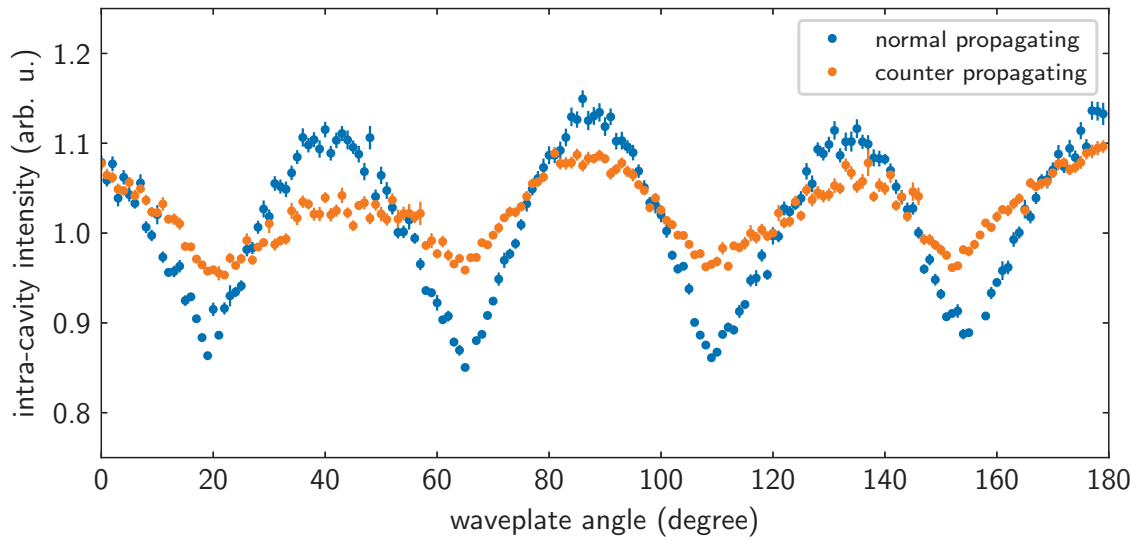
Figure 4.11: Measurement of the polarization-dependent intensity enhancement of the VMI cavity. The cavity-transmitted light is detected with a photodiode, and the input polarization is rotated with a HWP. The standard deviation of the intra-cavity intensity quantifies the polarization sensitivity. For normal-propagating light, the enhancement fluctuates by 7.5 % and for counter-propagating light by 5 %. Both are shown here normalized to their mean value. Note that the period of the fluctuation is 45° and not 90° as one would intuitively expect because 45° of waveplate rotation corresponds to a polarization rotation of 90°. It is caused by the birefringence-induced peak splitting, where maximum enhancement is achieved not only for pure s-, but also for p-polarization, and enhancement is reduced for mixed polarization.

direction and the counter-propagating direction as a function of HWP angle. Contrary to what one would intuitively expect, the enhancement changes with a periodicity of 45° and not 90° with respect to the waveplate angle. It is caused by the birefringence-induced peak splitting, where maximum enhancement is achieved not only for pure s-, but also for pure p-polarization, and enhancement is reduced for mixed polarization. We quantify the change of the enhancement with the standard deviation, which yields a change of 7.5 % for the normal-propagating direction and for the counter-propagating light by 5 %. Note that the enhancement signal is not purely sinusoidal, and fitting proved difficult, which is the reason why we state the fluctuation as the standard deviation. This is because the cavity enhancement function cannot just be regarded as a simple linear polarization-dependent loss factor, but the double-peak structure shown in Figure 4.10 needs to be considered as well.

In addition to pure birefringence, polarization-dependent losses can occur. However, as opposed to birefringence, a frequency splitting of the fundamental mode is not expected for polarization-dependent absorption or scattering of the mirrors unless the spatial mode profile of the two polarization states is different, with an additional Guoy phase that splits the resonance frequencies. If the cavity losses become polarization-dependent the intra-cavity intensity enhancement changes according to Equation 2.52 with the square of the additional polarization losses.

For highly nonlinear processes, such as MPI, the electron yield would change dramatically with I^n, where n is the order of the MPI process. A constant intensity at the target can be achieved for different polarization states by adjusting the incident power to compensate for the polarization dependence of the intra-cavity enhancement. Alternatively, polarization scan measurements can be repeated several times for different amplifier settings while recording the intra-cavity power at each step. Subsequently, the data can be classified by the recorded intensities and polarization angles. Although the cavity is slightly birefringent and has a polarization-dependent enhancement, it does not limit the investigation of polarization-dependent processes at the moment, as we demonstrate by performing intra-cavity photoelectron tomography of xenon, which is described in Section 4.5.2

4.1.5 Nonlinear cavity dynamics

The study of nonlinear optical cavity dynamics is an active field of research [429], where the Lugiato-Lefever equation is often used to model these dynamics [430, 431]. The simulations shown here utilize a similar split-step Fourier method as used for the MPC simulations described in Section 4.3. Each round trip starts in the spectral domain with a gain-loss function. The incident pulses interfere with the circulating field at the IC mirror, and transmission losses at the other HR mirrors are also included. Then, a Fourier transform is applied to transform the spectral field to the time domain, where SPM from possible nonlinearities add an intensity-dependent phase. In the last step, the temporal field is Fourier transformed back to the spectral domain, and mirror and additional dispersion contributions are added. After that, the cycle is repeated until the desired number of roundtrips is reached. Spatial effects are not considered. In Figure 4.12, the results of a cavity dynamics simulation without nonlinearities are shown for the first 800 round trips. A steady circulating field is reached after a few hundred round trips. The simulations are based on the mirror reflectivity and GDD curves from the manufacturer (Layertec), using the IC mirror with 99.35 % reflectivity, which corresponds to a finesse of ~940 at the central wavelength. Pulses with $T_{in} = 200\,\text{fs}$ are sent to the cavity with a pulse energy of 500 nJ, assuming perfect mode matching. No spectral narrowing or temporal broadening of the pulses in the cavity is observed. At the focus with a waist radius of 25 μm, a peak intensity of $3.4 \times 10^{13}\,\text{W}\,\text{cm}^{-2}$ is reached.

Figure 4.13 shows the simulation result for $T_{in} = 25\,\text{fs}$ input pulses, which are broadened by

the mirror GDD to $T_{\text{circ}} = 29$ fs inside the cavity. Compared to the 200 fs input pulses, the cavity enhancement β has decreased slightly.

Inserting a nonlinear medium and compensating the dispersion of the material and the non-linear phase by mirrors with negative GDD can lead to stable solutions of the intra-cavity field, where the pulse duration is shorter than the incident pulses. This is possible because the Kerr effect in the nonlinear medium leads to SPM, and thus, the spectrum broadens.

Dissipative solitons are stable solutions of such nonlinear systems, where not only nonlinear-ities and (anomalous) dispersion is balanced but additionally, the losses of the system are com-pensated by some sort of gain mechanism. In particular, the pulse parameters of a dissipative soliton are predetermined by the equation parameters rather than the initial conditions lead-ing to desirable properties for applications such as the generation of stable laser pulse trains by mode-locked resonators [200, 432, 433]. It has been shown that this concept can be transferred from actively pumped laser resonators to passive cavities by adding Kerr nonlinearities. By op-erating the cavity in the anomalous dispersion regime, temporal solitons can be formed, which has been first demonstrated in passive fiber resonators [434] and microresonators [435]. These dissipative intra-cavity soliton solutions were demonstrated recently in a fsEC with a spectrally tailored IC mirror [388]. It was shown that temporal self-compression of the circulating pulse is possible, and a self-stabilizing and indefinitely circulating pulse can be generated. In prin-ciple, by adding nonlinearity and compensating the dispersion it should be possible to achieve similar results with our cavity. This has already been taken into account during the planning of the VMI cavity. The cavity design allows easy replacement of the (flat) cavity-mirrors with special mirrors, such as broadband double-chirped mirror pairs [436, 437] or even mirrors with enhanced nonlinearity [438]. These mirrors have been proposed for frequency tripling [439, 440] and might provide an elegant solution to incorporate nonlinearities for spectral broadening into the passive cavity without the need to add a material plate. Inserting a Brewster plate into the cavity results in strong cavity birefringence, prohibiting the enhancement of polarization-shaped pulses.

Instead of using a spectrally tailored IC mirror, already, by using an IC mirror with flat re-flectivity and insertion of 2 mm FS into the collimated arm, spectral broadening can also be observed in the simulations shown in Figure 4.14. For that, a GDD of $-5000 \, \text{fs}^2$ is added to the cavity round-trip phase. Using a different IC with a relatively low reflectivity at the spectrum of the incident pulses and a high reflectivity everywhere else, much broader spectra with short durations are possible [388]. This is an alternative method of pulse compression, compared to a MPC, but requires a different method of cavity length locking. Additionally, the IC and other cavity optics need to be exchanged with negative-GDD mirrors to compensate for material dis-persion. Therefore, although promising, we do not further pursue this technique.
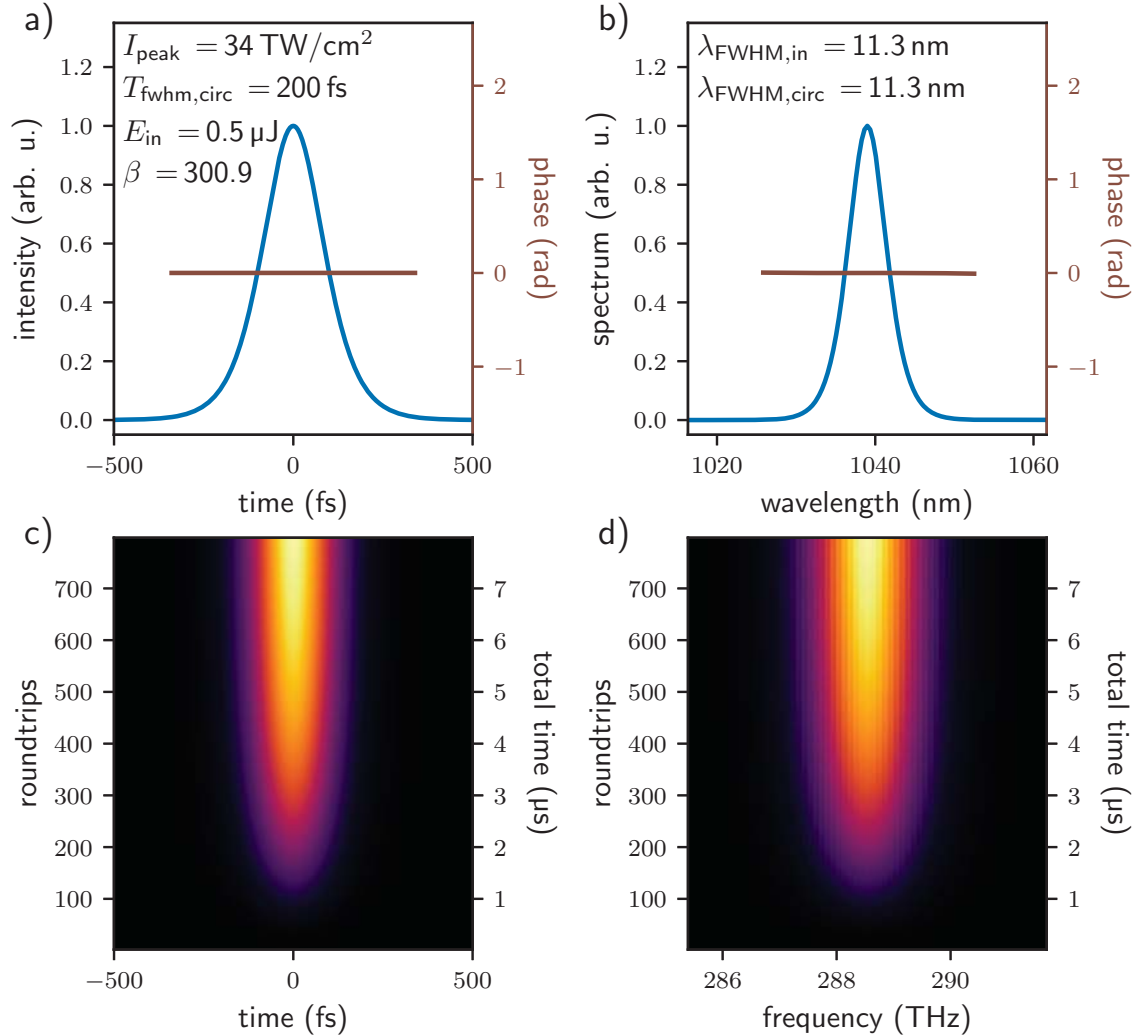
Figure 4.12: Simulated cavity dynamics of the first 800 round trips with the mirror reflectivity and GDD data from the manufacturer, using the IC mirror with 99.35 % reflectivity. Pulses with $T_{\mathrm{in}} = 200\,\mathrm{fs}$ are incident with a pulse energy of 500 nJ, assuming perfect mode matching. a) The intensity and temporal phase of the circulating field of the last round trip. A peak intensity of $3.4 \times 10^{13}\,\mathrm{W\,cm^{-2}}$ is reached in the focus with waist radius of 25 µm. b)The spectrum and spectral phase are shown. A flat phase is the result of the low-dispersion cavity, and no spectral narrowing is observed. The temporal evolution is shown in c) for the time and in d) for the spectral domain.

a)

$I_{\text{peak}} = 236\,\text{TW/cm}^2$
$T_{\text{fwhm,circ}} = 29\,\text{fs}$
$E_{\text{in}} = 0.5\,\mu\text{J}$
$\beta = 295.0$

b)

$\lambda_{\text{FWHM,in}} = 90.8\,\text{nm}$
$\lambda_{\text{FWHM,circ}} = 90.1\,\text{nm}$
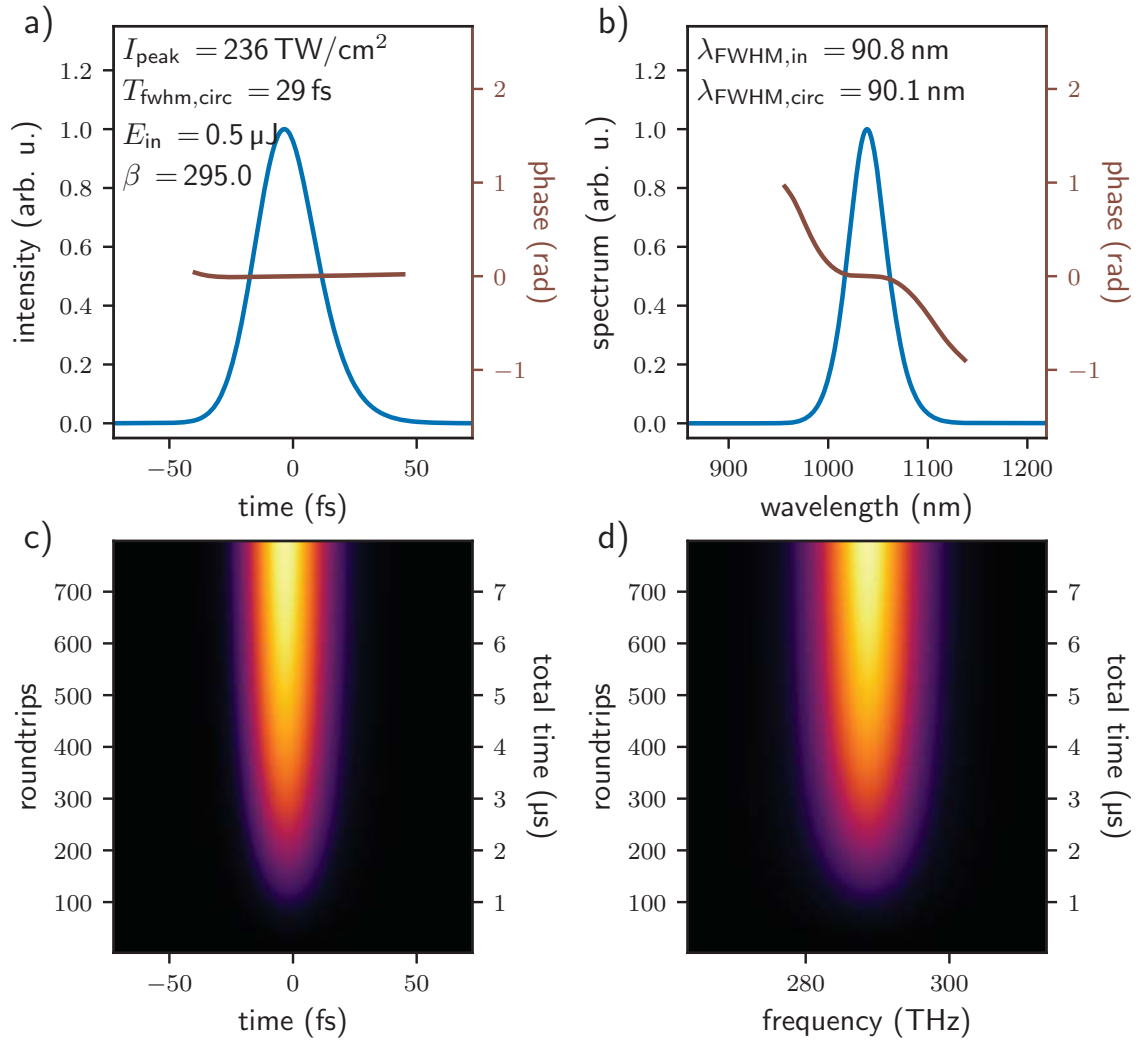
Figure 4.13: Simulated cavity dynamics with 25 fs input pulses. The broader pulse spectrum is affected by GDD, and the circulating pulse is broadened temporally to 29 fs. All other parameters are identical to Figure 4.12.
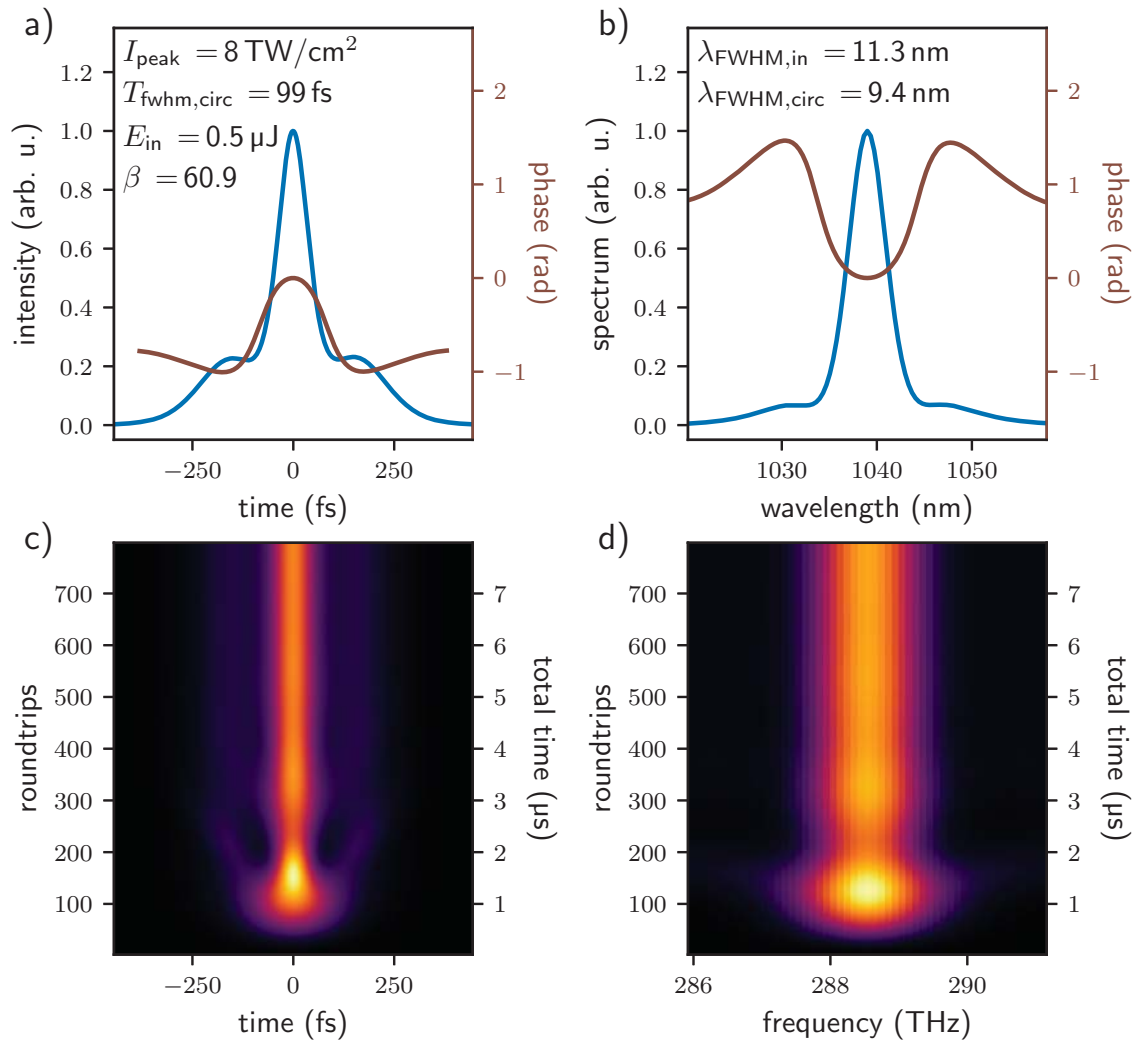
Figure 4.14: Simulated nonlinear cavity dynamics for 200 fs pulses. A 2 mm thick FS plate is inserted in the collimated arm of the cavity with a waist size of 900 μm. A negative GDD of −5000 fs² is added to the cavity, and the IC mirror with 99.35 % reflectivity is used. SPM leads to spectral broadening, and the pulse is temporally compressed by a factor of 2 with a large pedestal due to the uncompensated phase. The peak power is doubled, compared to the cavity without nonlinearities, shown in Figure 4.12.

4.1.6 Cavity dispersion

The enhancement of a frequency comb in a cavity depends on many factors, such as beam alignment, mode matching, impedance matching, and mirror reflectivity. A fundamental limit is posed by the cavity dispersion, as discussed in Section 2.3.2. To enhance the whole spectrum of the ultrashort frequency comb pulses simultaneously, the dispersion of the cavity mirrors needs to be minimized. Recalling Equation 2.44 and explicitly writing the omitted ω dependency yields [441]

$$E_{\text{cav, circ}}(\omega) = \frac{\sqrt{1 - r_{\text{ic}}(\omega)r_{\text{cav}}(\omega)}}{1 - r_{\text{ic}}(\omega)r_{\text{cav}}(\omega)\,e^{i\phi_{\text{cav}}(\omega)}}E_{\text{in}}(\omega). \tag{4.5}$$

The steady-state relative phase of the circulating pulse with respect to the incident pulses is given by the argument

$$\phi_{\text{circ}}(\omega) = \arg\left(\frac{1}{1 - r_{\text{ic}}r_{\text{cav}}\,e^{i\phi_{\text{cav}}(\omega)}}\right), \tag{4.6}$$

and the frequency-dependent power coupling efficiency can be determined from the circulating power spectrum [441]

$$\beta_{\text{coupling}}(\omega) = \frac{|E_{\text{cav, circ}}(\omega)|^2}{\beta(\omega)|E_{\text{in}}(\omega)|^2} = \left|\frac{1 - r_{\text{ic}}(\omega)r_{\text{cav}}(\omega)}{1 - r_{\text{ic}}(\omega)r_{\text{cav}}(\omega)\,e^{i\phi_{\text{cav}}(\omega)}}\right|^2, \tag{4.7}$$

where $\beta(\omega)$ is the (dispersionless) enhancement factor defined in Equation 2.52. As a result, the coupling efficiency $\beta_{\text{coupling}}(\omega)$ can take values between zero and one, with the latter reached in a perfectly dispersion-compensated cavity. It can be seen that the enhancement decreases for a nonzero intra-cavity round-trip phase that is caused by dispersion.

In Figure 4.15 a), the GDD of the VMI cavity is plotted as a function of wavelength. The GDD and mirror reflectivity curves have been provided by the manufacturer (Layertec) and are given for normal incidence. The cavity consists of an IC with a reflectivity of $R_{\text{ic}} = 99.35\,\%$ and five HR mirrors. The cavity round-trip phase $\phi_{\text{cav}}(\omega)$ is shown in b), and the resulting steady-state phase $\phi_{\text{circ}}(\omega)$ is shown in c). The power coupling efficiency is obtained from the steady-state phase and the mirror reflectivity and is shown in d). As a result, we expect that pulses can be coupled well into the cavity above 1000 nm and below 1080 nm.

Several methods have been proposed and used to measure the dispersion of enhancement cavities. They all rely on detecting a change of the resonance condition to gain insight into the circulating cavity phase, and thus, the cavity GDD [109, 221, 222]. In the method we are using, the cavity is locked at a specific wavelength, and spectra of the resonant pulses are recorded for various CEO settings of the frequency comb [442]. Recalling Equation 2.43 and 2.64, the CEO of cavity and comb can be explicitly included in the cavity round-trip phase

$$\phi_{\text{cav}}(\omega, \phi_{\text{CEO}}^{\text{comb}}) = \phi_{\text{CEO}}^{\text{comb}} - \phi_{\text{CEO}}^{\text{cav}} + T\omega + \phi(\omega), \tag{4.8}$$

where T is the round-trip time, and the higher-order phase term $\phi(\omega)$ contains the dispersion information. By locking the cavity to the comb at frequency ω_{lock}, the effective repetition rates are matched, and thus, $\phi_{\text{cav}}(\omega, \phi_{\text{CEO}}^{\text{comb}}) = 2\pi m$, with integer m. Eliminating T yields [442]

$$\phi_{\text{cav}}(\omega, \phi_{\text{CEO}}^{\text{comb}}) = \left(1 - \frac{\omega}{\omega_{\text{lock}}}\right)\left(\phi_{\text{CEO}}^{\text{comb}} - \phi_{\text{CEO}}^{\text{cav}}\right) + \frac{\omega}{\omega_{\text{lock}}}\left(2\pi m - \phi(\omega_{\text{lock}})\right) + \phi(\omega), \tag{4.9}$$

where all unknown terms are merged into a single parameter $\phi_{\text{CEO}}^{\text{res}}(\omega)$, defined as

$$\left(\frac{\omega}{\omega_{\text{lock}}} - 1\right)\phi_{\text{CEO}}^{\text{res}}(\omega) \equiv \left(\frac{\omega}{\omega_{\text{lock}}} - 1\right)\phi_{\text{CEO}}^{\text{cav}} + \frac{\omega}{\omega_{\text{lock}}}\left(2\pi m - \phi(\omega_{\text{lock}})\right) + \phi(\omega). \tag{4.10}$$
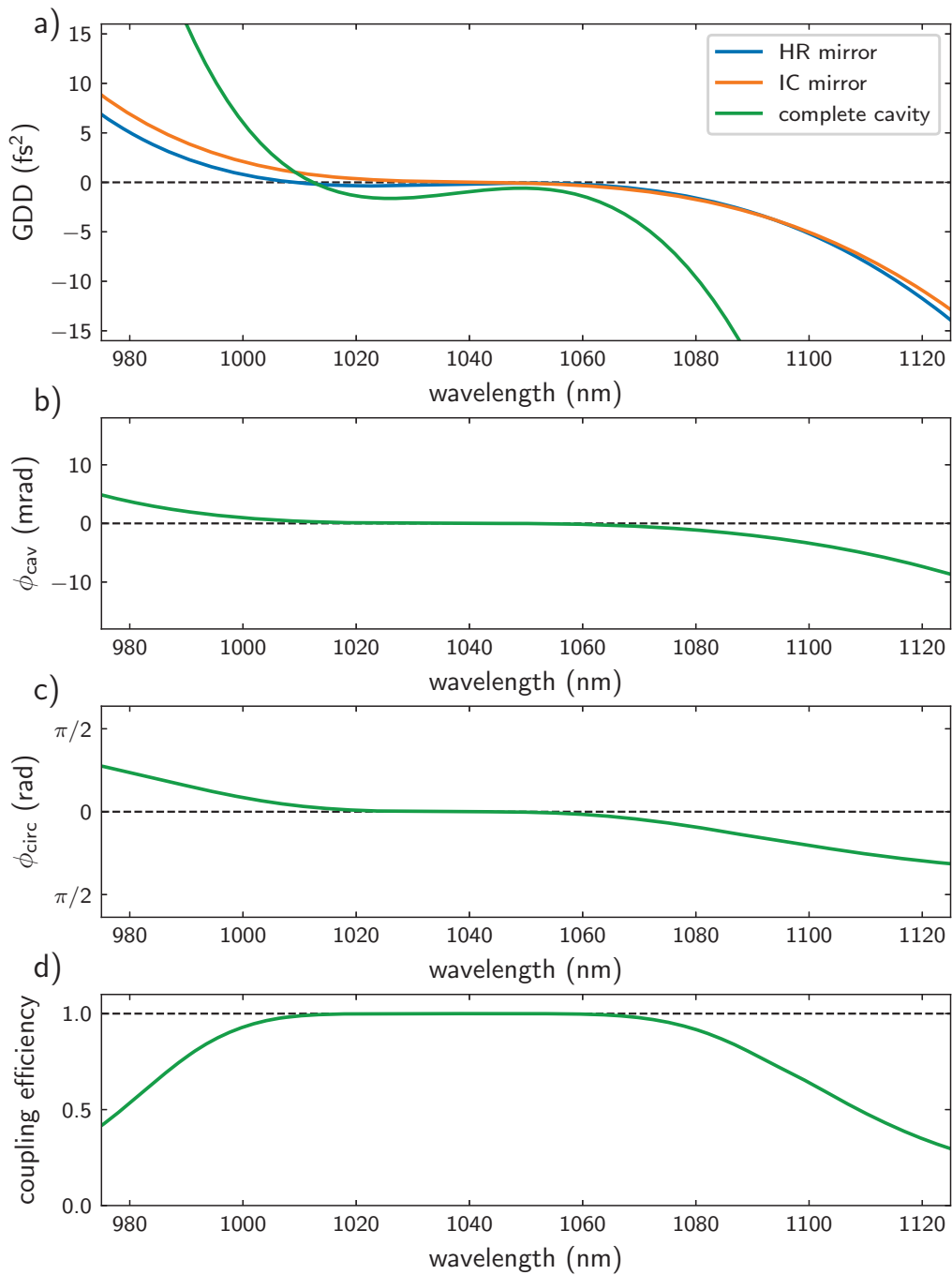
Figure 4.15: Calculated influence of mirror reflectivity and GDD cavity coupling efficiency. a) The GDD of a single HR mirror, the IC mirror, and the complete cavity is plotted as a function of wavelength. b) The total phase shift $\phi_{\text{cav}}(\omega)$ of a single cavity round trip results from the mirror dispersion. c) This phase accumulates over many roundtrips, resulting in a steady-state relative phase of the circulating pulse with respect to the incident pulses. d) The power coupling efficiency $\beta_{\text{coupling}}(\omega)$ depends on the wavelength. In a perfect dispersionless cavity $\beta_{\text{coupling}}(\omega) = 1$, but in a real cavity, the GDD limits the spectral region, where pulses are enhanced.

The recorded spectrum depends on the CEO of the comb, and is obtained from the intra-cavity circulating field (cf. Equation 4.5)

$$I_{\text{cav, circ}}(\omega, \phi_{\text{CEO}}^{\text{comb}}) = \left| E_{\text{cav, circ}}(\omega, \phi_{\text{CEO}}^{\text{comb}}) \right|^2 \quad = \left| \frac{\sqrt{1 - r_{\text{ic}} r_{\text{cav}}(\omega)}}{1 - r_{\text{ic}}(\omega) r_{\text{cav}}(\omega)\, e^{i\phi_{\text{cav}}(\omega, \phi_{\text{CEO}}^{\text{comb}})}} E_{\text{in}}(\omega) \right|^2. \quad (4.11)$$

The intra-cavity spectrum is measured at every CEO step with a fiber-coupled integration sphere that detects the cavity-transmitted light in front of the mode cameras and a spectrometer (Qmini NIR, BROADCOM).

As shown in Figure 4.4, a fraction of the reflected light of the normal-propagation direction is sampled with an AR-coated beam splitter and spectrally dispersed with a grating. A variable slit selects a part of the spectrum, and a fast photodiode is used as the feedback signal for the PDH cavity lock. It allows locking the cavity length at any frequency within the spectrum of the incident frequency comb. To verify that the cavity enhances pulses in both propagation directions and s- and p-polarization in the same way, we lock the cavity at ∼1040 nm. In Figure 4.16 a) the cavity is locked with low-power pulses in the normal-propagation direction and simultaneously injecting counter-propagating s-polarized pulses at medium power (maximum a few hundred watts of intra-cavity power). A projection of the total spectrally integrated transmitted power is shown in b). The CEO of the comb is varied, and spectra are recorded for each setting. At the lock point wavelength, the cavity is resonant for all CEO values, but enhancement of the entire spectrum is achieved only for the optimal value where it is matched with the cavity round-trip phase. Consequently, the highest intra-cavity intensity is achieved only at this value. Recently, it has been demonstrated that by detuning the CEO from its optimum value and increasing the finesse to keep the enhancement constant, it is possible to minimize the intra-cavity intensity fluctuations [443]. However, this method does not apply to our cavity since increasing the finesse would lead to narrowing of the enhanced spectrum. The measurement is repeated for p-polarized light, as shown in c) and d). For the measurements shown in e)‑f), the cavity is locked at medium power with the normal-propagating light, and this light is recorded. During these measurements, which take a few hours each, the cavity needs to stay locked, and the effective length changes induced by changing the CEO are compensated with the automatic slow-drift piezo control. The intensity jumps visible in Figure 4.16 c)‑g) are caused by the choice of the lock point at ∼1040 nm, which is directly between two local maxima of the laser spectrum. It caused the lock point to jump to the neighboring local maximum during the measurement. Overall, the traces of both polarization directions for both propagation directions agree qualitatively, showing that the dispersion is at a similar level.

It is also possible to change the lock frequency by sending a different portion of the spectrum to the locking photodiode, which is shown in Figure 4.17. There, the cavity was locked to seven different lock points between 1032.6 to 1050 nm. This measurement demonstrates that setting the CEO of the comb to specific values results in only the fraction of the comb spectrum around the lock point being enhanced. In this way, it mimics a spectral pulse shaper, allowing control of the central wavelength and spectral width of the enhanced intra-cavity laser field.

Taking the second derivative of the cavity round-trip phase $\phi_{\text{cav}}(\omega, \phi_{\text{CEO}}^{\text{comb}})$ given in Equation 4.9 yields the cavity GDD

$$\text{GDD} = \frac{\partial^2}{\partial \omega^2} \left(\frac{\omega}{\omega_{\text{lock}}} - 1 \right) \phi_{\text{CEO}}^{\text{res}}(\omega). \quad (4.12)$$

To extract $\phi_{\text{cav}}(\omega, \phi_{\text{CEO}}^{\text{comb}})$, and thus, the GDD from the measured traces, Equation 4.11 is fitted to the CEO scan for each wavelength. For most traces, the fits with the two free parameters $\phi_{\text{cav}}(\omega, \phi_{\text{CEO}}^{\text{comb}})$ and $r_{\text{ic}} r_{\text{cav}}$ agree well with the data and yield values for the cavity round-trip phase. Before differentiation, spectral filtering is applied to smooth the data because, otherwise,
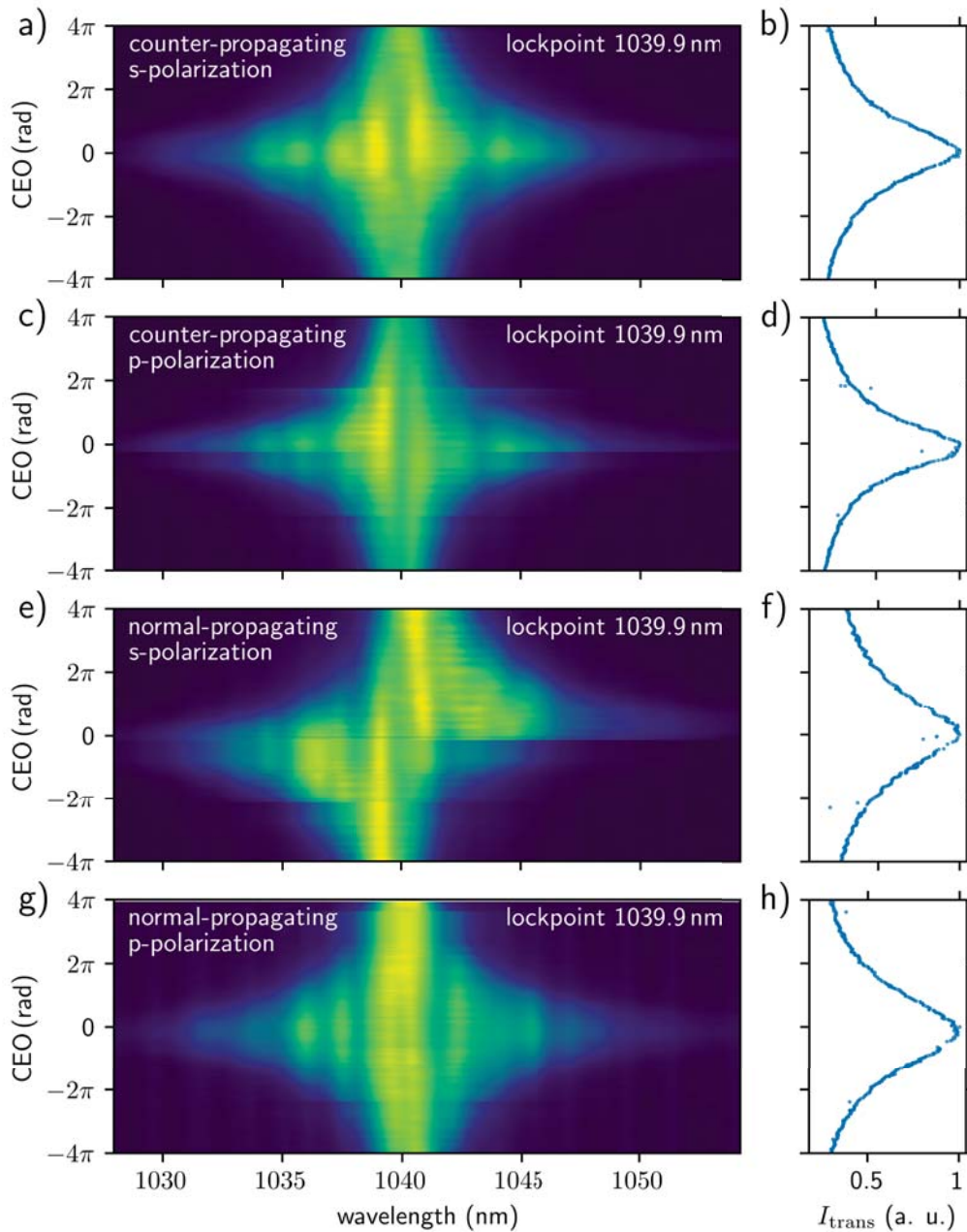
Figure 4.16: Measured transmitted spectra of the locked cavity as a function of the CEO of the comb laser. The cavity is locked at 1039.9 nm. The measurement is performed for a), b), e), f) s-polarization and c), d), g), h) p-polarization of the incident light, and for e) - g) the normal-propagation direction and a) - c) the counter-propagating direction. The right side shows projections of the total spectrally integrated transmitted power of the traces shown on the left. The traces of both polarization and propagation directions agree qualitatively, showing that the dispersion is at a similar level.
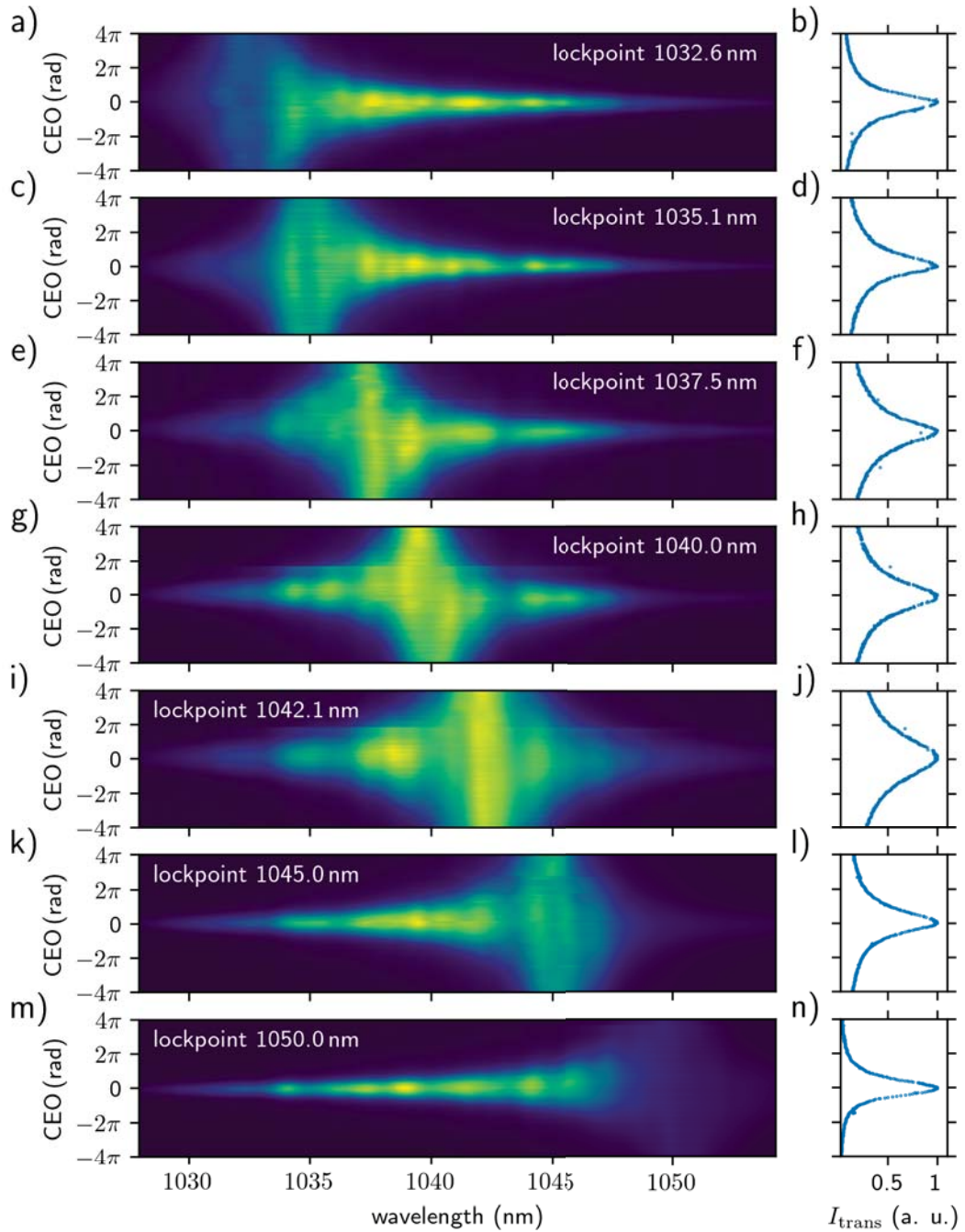
Figure 4.17: Measured transmitted spectra of the locked cavity as a function of the CEO of the comb laser are shown on the left. The cavity is locked at seven different wavelengths across the full width of the comb spectrum. The total spectrally integrated transmitted power of the traces on the left is shown on the right side. More details in the text.
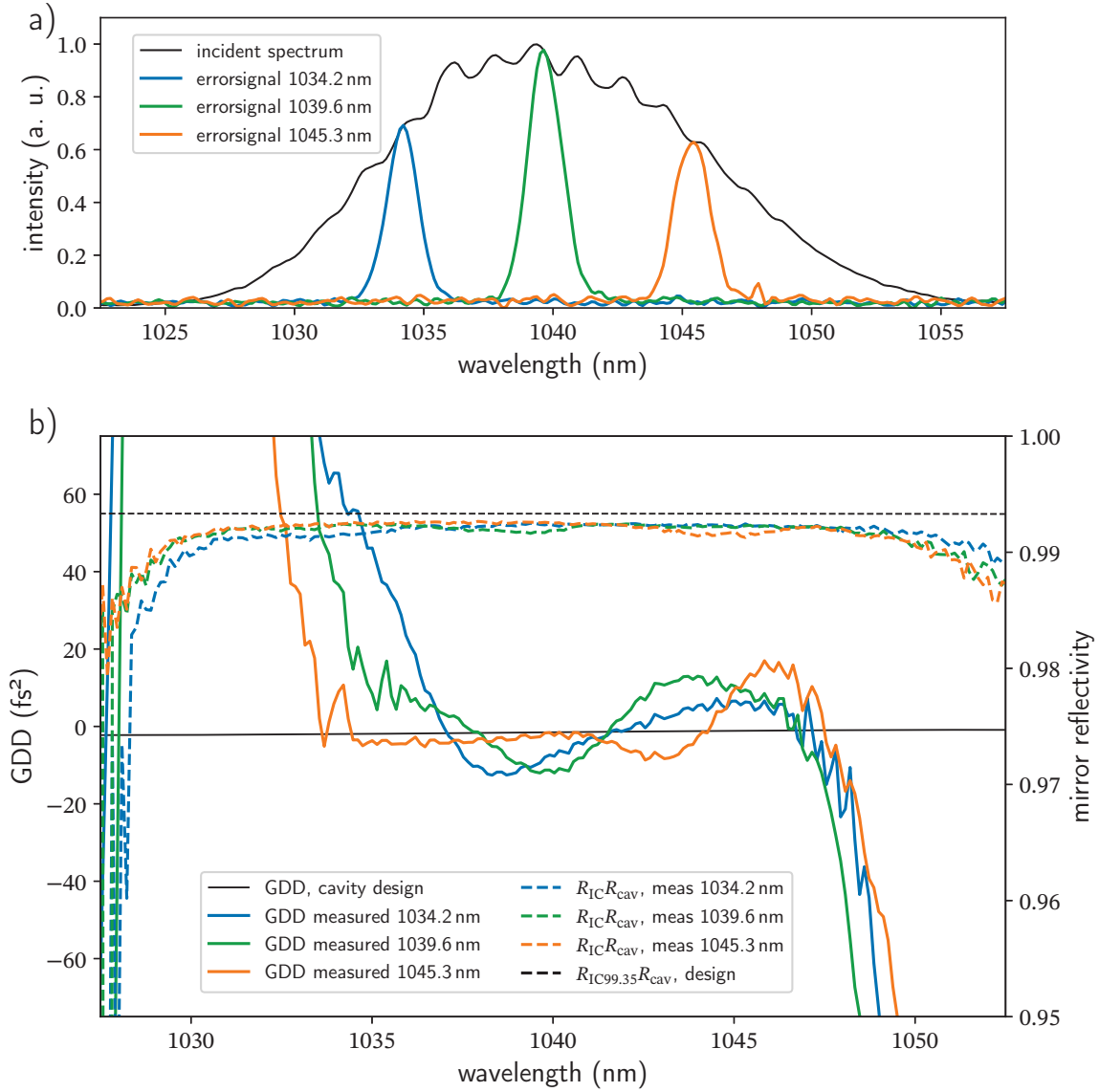
Figure 4.18: a) Incident frequency comb spectrum and error signal spectra for three lock points. b) The GDD and total cavity reflectivity $r_{ic}r_{cav}$ is measured as a function of wavelength. The measured cavity reflectivity and GDD agree with the design value within the central part of the incident spectrum. In contrast, the obtained GDD quickly diverges at the wings of the spectrum, where no meaningful results are obtained.

high-frequency fluctuations obscure the slower features in the result [442]. For that we use a Gaussian filter with $\sigma = 0.6\,\text{THz}$, which corresponds to $\sim 2\,\text{nm}$. The bandwidth of the spectral filter has a significant influence on the GDD and is selected as found in literature [117, 442]. The measurement is repeated for three locking wavelengths, as shown in Figure 4.18 a). Within the central part of the incident spectrum, the extracted GDD agrees with the design value. The remaining differences between the measured and the design values of the GDD and $r_{\text{ic}}r_{\text{cav}}$ may be attributed to the nonzero angles of incidence of the cavity mirrors. Outside the spectrum, the obtained value quickly diverges, and no meaningful results are obtained.

4.2 Split-and-delay line interferometer
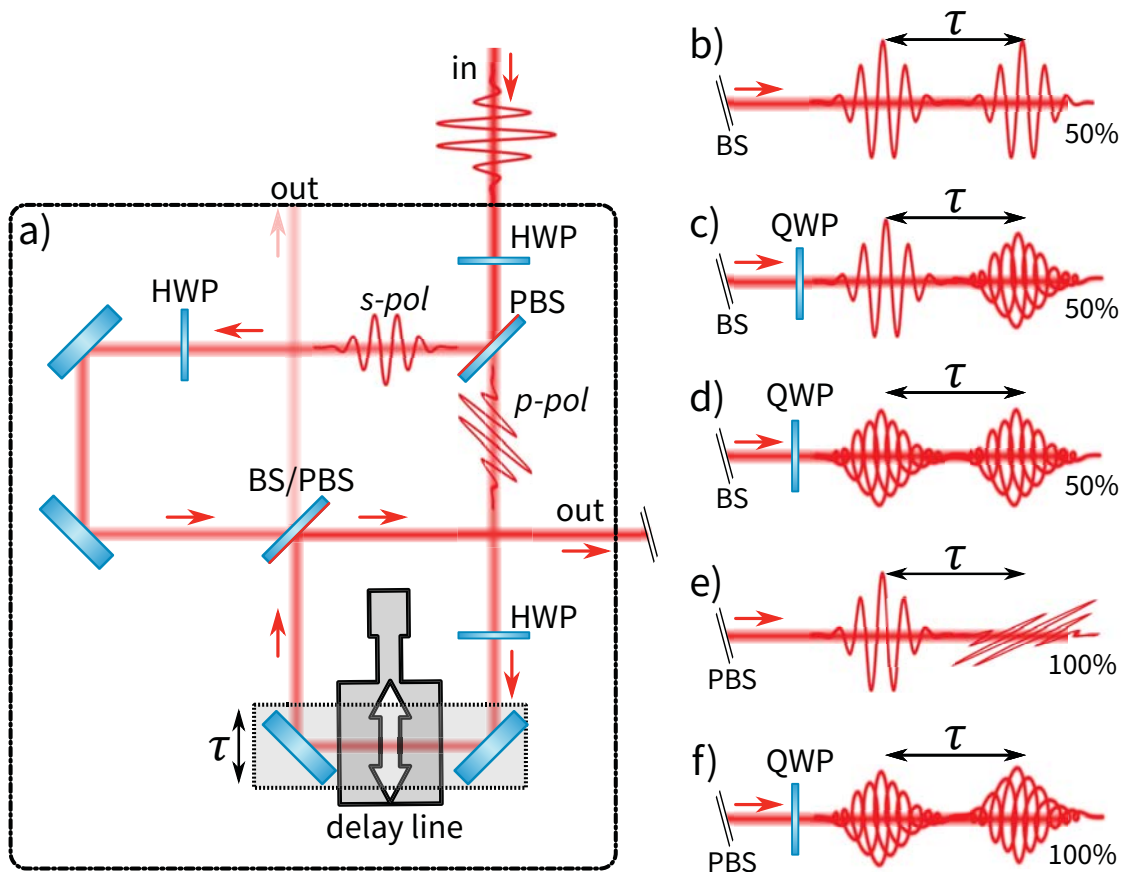
Figure 4.19: a) A dispersion-compensated Mach-Zehnder-type interferometric split-and-delay (SAD) line splits pulses, which are sent to the cavity in the counter-propagating direction, into two copies with a variable temporal delay of τ. Additionally, the polarization of the outgoing light is shaped by use of either a non-polarizing or polarizing beam splitter (BS or PBS, respectively) in combination with half-wave plates (HWPs) and a quarter-wave plate (QWP). Inserting the BS reduces the outcoming power by 50 %. Using different combinations and settings of the BS and waveplates results in vacious pulse configurations at the output: b) a linearly polarized pulse pair with identical (shown) or different (not shown) polarization axes, c) a linearly and a circularly polarized pulse, d) two co- or counter-rotating circularly polarized pulses, e) two linearly polarized pulses with orthogonal polarization, or f) two counter-rotating circularly polarized pulses.

To add the possibility of performing pump-probe experiments to our setup, we have developed a split-and-delay line based on a Mach-Zehnder interferometer [444, 445] that splits incoming

pulses into two pulse copies with variable delay. Additionally, the polarization of these double pulses can be shaped. It is helpful to recall the Jones formalism from Section 2.3.4 for the design process of this setup. The Jones matrices represent optical elements, and the Jones vector describes the polarization state of the light.

The light in the counter-propagating direction towards the VMI cavity is s-polarized, as shown in Figure 4.4. The polarization angle at the input of the SAD box is adjusted with a rotatable HWP. In this way, the power ratio of the two arms of the interferometer is determined when the light passes the PBS (PBSW-1030, Thorlabs). The optical setup of the device is shown in Figure 4.19 a). The fraction of light with s-polarization is reflected by 90° and passes through a HWP before it is combined with the beam of the other interferometer arm. The light in the latter arm is p-polarized after the PBS. A HWP rotates the polarization angle before the pulses are delayed with two mirrors on a linear translation stage. After that, the two pulse copies of both arms are recombined in either a non-polarizing BS or a PBS. We use polarizing and non-polarizing plate BSs instead of cubes because of their higher damage threshold and lower material dispersion. The BSs are installed in a dispersion-balanced configuration such that the light of each interferometer arm is reflected at the front and back surface of the BS once [446]. The reflective surface is indicated with red color in Figure 4.19 a). The other side of the BSs is AR coated.

Depending on the angle of the HWPs in the SAD box, and if the polarizing or non-polarizing BS is installed, several polarization states are obtained at the output. The splitting ratio of the non-polarizing BS is 50:50 and therefore, the output power is reduced by 50 %. The advantage of this setting is that it can produce any polarization state of each arm independently of the other. Note that for pulse delays smaller than the pulse duration $\tau < T$, the pulses start to overlap and constructive and destructive interference occurs. In this way up to 100 % of power is emitted at either port, which we utilize for *in situ* pulse characterization, as discussed in Section 4.2.3

Using the non-polarizing BS, a linearly polarized pulse pair with freely adjustable polarization axes is emitted, as shown in Figure 4.19 b). In addition, a QWP can be installed at the output port. If it is aligned at an angle of $\theta = 45°$ (fast axis with respect to the horizontal axis) it produces left-handed circularly polarized (LHCP) light out of s-polarized light. In the same way, p-polarized light is turned into right-handed circularly polarized (RHCP) light. Using the QWP at an angle of 90° and setting the polarization of the first pulse to linear polarization with the polarization axis at 45° and the second pulse to s-polarization, the scenario shown in Figure 4.19 c) is realized, where a RHCP pulse is followed by a pulse with linear polarization. It is also possible to get two circularly polarized pulses, when the non-polarizing BS is installed. On the one hand, if the polarization axis of both pulses is parallel and the fast axis of the QWP is aligned parallel to the polarization axis, co-rotating circularly polarized pulses are obtained. On the other hand, if the polarization axes of both arms are perpendicular and the QWP is at the bisecting angle, counter-rotating circularly polarized pulses are emitted.

Using the PBS instead of the non-polarizing BS has the advantage of up to 100 % power output of the SAD box. However, the polarization of the output pulses can only be orthogonal in the case of linear polarization, as shown in Figure 4.19 e). In combination with the QWP, counter-rotating circularly polarized pulses can be produced, as shown in Figure 4.19 f). The correct angle of the QWP with respect to the linearly polarized light is found with an HWP and a polarizer behind the SAD box. The HWP is aligned such that the transmission through the polarizer is minimal before the QWP is inserted and rotated until the orientation is found where the extinction is maintained. Then, the waveplate is rotated by 45° from this position so that 50 % of the light is transmitted through the PBS. The circularity of the light can be checked by rotating the polarizer or an HWP before it. When the intensity of the light passing through the polarizer remains the same for all angles, the QWP is well aligned, and circularly polarized light is produced.

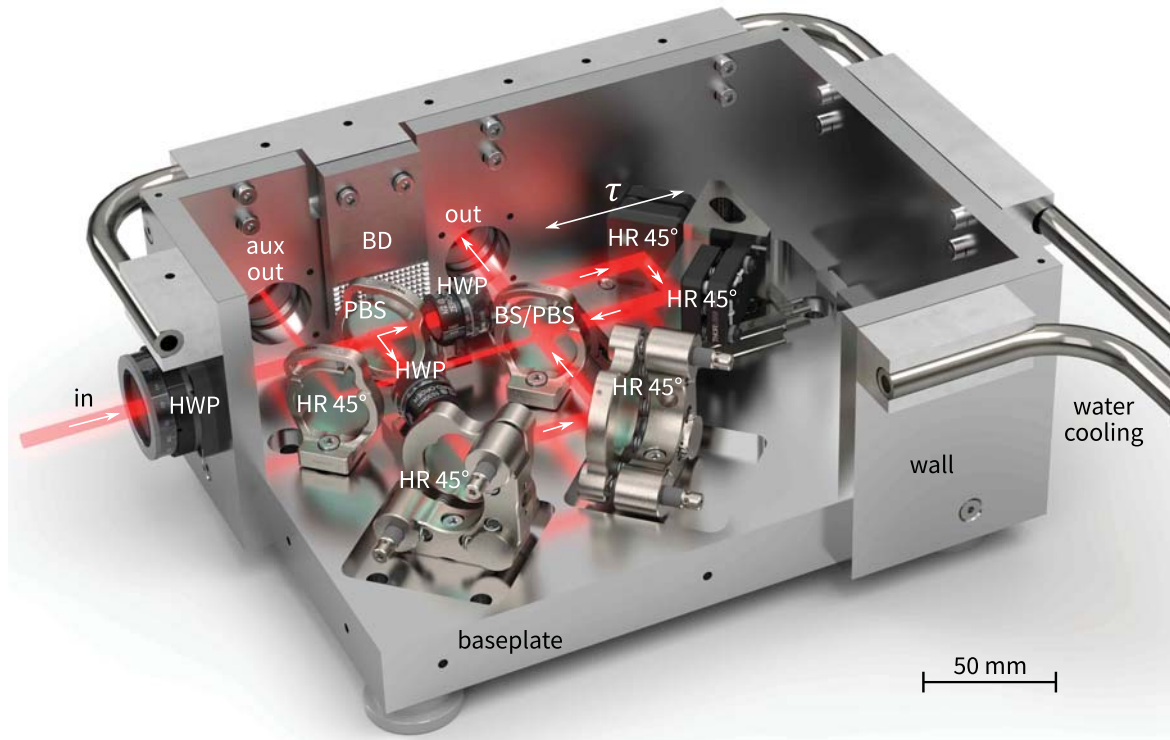## 4.2.1 Split-and-delay line mechanical design

Figure 4.20: Pulses enter the SAD box through a half-wave plate (HWP) and are split with variable power ratio into two copies with a polarizing beam splitter (PBS). In one arm, a variable temporal delay of τ is introduced with a movable retroreflector. Then, the beams are recombined using either a non-polarizing or polarizing beam splitter (BS/PBS) in combination with HWPs. An optional quarter-wave plate (QWP) at the output produces circularly polarized light. The auxiliary output is used for pulse characterization, as shown in Figure 4.23.

The SAD box is housed in a solid $245 \times 180 \times 100 \, \text{mm}^3$ stainless steel box, as shown in Figure 4.20. A 25 mm thick base plate results in high mechanical and thermal stability. The optical elements are precisely positioned on the base plate with $\varnothing \, 2 \, \text{mm}$ alignment pins. Besides easy initial optical alignment, it also allows quick removal and reinstallation of components.

The BSs are held by fixed stainless steel mounts (Polaris-B1S, Thorlabs). The $\varnothing \, 25 \, \text{mm}$, 45° steering mirrors (Layertec) in the fixed arm are adjustable with kinematic stainless steel mounts (POLARIS-K25S4/M, Thorlabs). The rectangular 45° mirrors (Layertec) of the translation stage are glued on compact kinematic mounts (KMSS/M, Thorlabs) and mounted with an adapter plate on the linear translation stage (Q545, Physik Instrumente). The referenced stage has a minimum incremental motion of 6 nm with an encoder resolution of 1 nm and a travel range of 26 mm. Thus, a maximum delay of ± 87 ps with a minimum resolved time delay step size of 7 as could principally be achieved. Note that the temporal delay τ introduced by the delay line is twice the distance traveled by the stage. Half-inch zero-order HWPs (WPHSM05-1030, Thorlabs) are placed in rotation mounts (RSP05/M, Thorlabs) and fixed to the base plate using adapter plates.

Side panels with a thickness of 10 mm are screwed from the outside to the base plate and each other, further increasing stability. SM1 threads are cut into the side panels so that one-inch shaft plates can be mounted directly with a rotatable holder (LRM1, Thorlabs). At the input, a one-inch zero-order HWP (WPH10M-1030, Thorlabs) is used to rotate the polarization, while at the output, a one-inch zero-order QWP (WPQ10M-1030, Thorlabs) is used to produce circular

polarization.

After the initial commissioning of the device, we added water cooling to the side panels. This became necessary because the SAD box heated up during high-power colliding-pulse cavity operation due to the divergent returning beam and its reflection at the first PBS hitting the wall. Therefore, aluminum adapters thermally connect a flexible stainless steel tube to the outer walls from the outside. Additionally, an aluminum beam block connected to the cooling system absorbs the light coming from the other propagation direction of the cavity.

4.2.2 Polarization shaping

To demonstrate the functioning and polarization shaping capabilities of the SAD box, we record angular-dependent optical spectra of counter-rotating circularly polarized pulse pairs. For positive pulse delays $\tau > 0$ the interferometer arm with the delay stage gets shorter, and p-polarized pulses arrive at the PBS before the s-polarized pulses from the fixed arm. Adapting the Jones formalism introduced in Section 2.3.4, the waveform of the situation described above with a p-polarized pulse before the s-polarized pulse with a delay of τ between them can be written as

$$\mathcal{A}_{\text{SAD out}}(t, \tau) = \mathcal{A}_p(t + \gamma\tau/2)\, e^{(i\omega_c(t+\gamma\tau/2))} \begin{pmatrix} 1 \\ 0 \end{pmatrix} + \mathcal{A}_s(t - \gamma\tau/2)\, e^{(i\omega_c(t-\gamma\tau/2))} \begin{pmatrix} 0 \\ 1 \end{pmatrix}, \tag{4.13}$$

with the complex pulse envelope $\mathcal{A}(t)$, and $\gamma = 1$ because the carrier wave is shifted by the same amount as the envelope. Note that by using a pulse shaper, $0 \leq \gamma \leq 1$ can be adjusted freely, enabling more control of the output waveform [447, 448]. In the above equation, the reference time frame is shifted by $\tau/2$ and the delay is applied symmetrically to the two pulse replica.

The pulse delay leads to a modulation of the combined pulse spectrum with $1/\tau$. To resolve this spectral interference, it is useful to describe Equation 4.13 in the spectral domain

$$\mathcal{A}_{\text{SAD out}}(\omega, \tau) = \mathcal{A}_p(\omega)\, e^{(-i\varphi_{\tau,p})} \begin{pmatrix} 1 \\ 0 \end{pmatrix} + \mathcal{A}_s(\omega)\, e^{(-i\varphi_{\tau,s})} \begin{pmatrix} 0 \\ 1 \end{pmatrix} \tag{4.14}$$

$$= \mathcal{A}_p(\omega)\, e^{(-i\omega\tau/2)} \begin{pmatrix} 1 \\ 0 \end{pmatrix} + \mathcal{A}_s(\omega)\, e^{(i\omega\tau/2)} \begin{pmatrix} 0 \\ 1 \end{pmatrix}, \tag{4.15}$$

with the frequency-centered complex spectral envelope $\mathcal{A}(\omega)$ that is given by the Fourier transform of the temporal envelope $\mathcal{A}(t)$, and the spectral phase $\varphi_\tau = \pm i\omega\tau/2$. The sign depends on the interferometer arm and is positive for the shorter p-polarized arm.

A QWP at an angle of 45° generates RHCP pulses from the p-polarized pulses and LHCP from s-polarization. The Jones matrix (c.f. Table 2.3) for a QWP at 45° is given by

$$\mathcal{M}_{\text{QWP, 45°}} = \frac{1}{\sqrt{2}} \begin{pmatrix} 1 & -i \\ -i & 1 \end{pmatrix}. \tag{4.16}$$

As a result, counter-rotating circularly polarized pulse pairs with the right-handed pulse before the left-handed pulse leave the instrument. The counter-rotating pulses are characterized by measuring projections of the spectrum under different angles using a motorized HWP and a PBS. The p-polarized fraction of the pulse pair is transmitted through the PBS, and the spectrum is recorded with a spectrometer as a function of HWP angle.

The spectrum is measured behind the p-polarizer varies as a function of the HWP angle, and
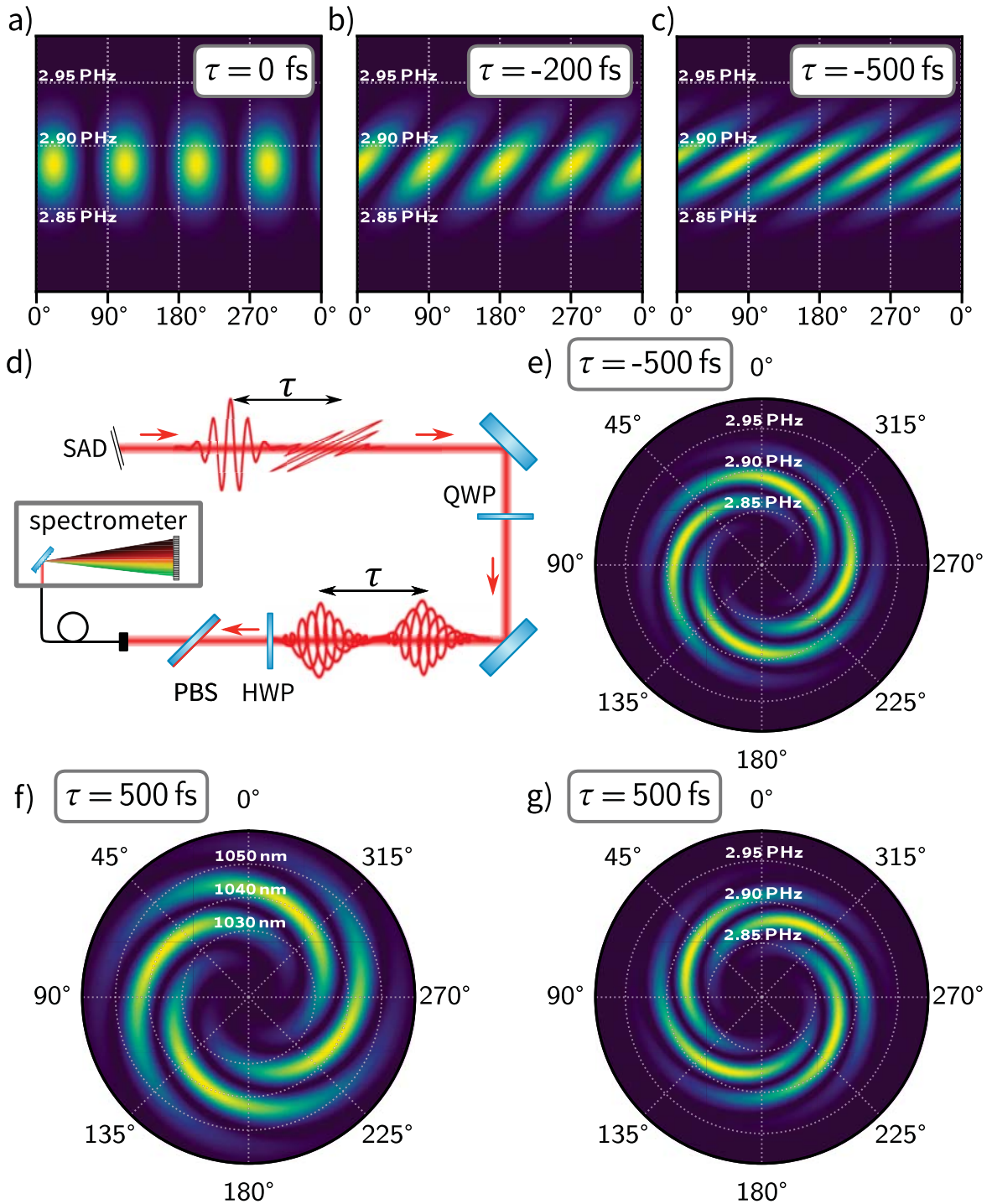
Figure 4.21: Overview of the angular-dependent spectral interference method. d) A linearly polarized pulse pair with delay τ exits the SAD box. A subsequent QWP at 45° transforms the pulses with orthogonal linear polarization in counter-rotating circularly polarized pulses. These pulses are sent through a motorized HWP and a PBS that transmits only p-polarized light. The p-polarized fraction of the pulse pair is detected with a spectrometer, and the spectrum is recorded. The simulated results are plotted as a function of HWP angle for a delay of a) $\tau = 0$ fs, b) $\tau = -200$ fs, c), e) $\tau = -500$ fs, and f), g) $\tau = 500$ fs. The spectrum is modulated with $1/\tau$. a) - c) are plotted in Cartesian coordinates, while e) - g) are shown as polar plots. The spectral interference patterns describe clockwise (counterclockwise) rotating Archimedean spirals for negative (positive) time delays with RHCP before LHCP (RHCP after LHCP) pulses. f) Plotting the spiral on a wavelength axis inverts the handedness compared to the frequency axis, shown in e) and g). Note that the polarization rotation angle is twice the waveplate rotation angle.

it is given by

$$|\mathcal{A}_{\text{out}}(\omega, \theta, \tau)|^2 \propto |\mathcal{M}_{\text{p-pol}} \times \mathcal{M}_{\text{HWP}}(\theta) \times \mathcal{M}_{\text{QWP, 45°}} \times \mathcal{A}_{\text{SAD out}}(\omega, \tau)|^2 \qquad (4.17)$$

$$= \left| \frac{e^{-\frac{i\pi}{2}}}{\sqrt{2}} \begin{pmatrix} 1 & 0 \\ 0 & 0 \end{pmatrix} \times \begin{pmatrix} \cos^2 \theta - \sin^2 \theta & 2\cos\theta\sin\theta \\ 2\cos\theta\sin\theta & \sin^2\theta - \cos^2\theta \end{pmatrix} \times \begin{pmatrix} 1 & -i \\ -i & 1 \end{pmatrix} \right.$$

$$\left. \times \mathcal{A}_{\text{SAD out}}(\omega, \tau) \right|^2$$

$$\propto \frac{1}{2} |\mathcal{A}_{\text{in}}(\omega)|^2 \left(1 + \sin(4\theta + \omega\tau) \right), \qquad (4.18)$$

under the assumption that the light is split 50:50 into both arms of the interferometer, which means $\mathcal{A}_{\text{s}}(\omega)/\sqrt{2} = \mathcal{A}_{\text{p}}(\omega)/\sqrt{2} = \mathcal{A}_{\text{in}}(\omega)$. If the fraction is not 50 %, the contrast of the spectral modulation is reduced. This angular-dependent spectral interference measurement method [449] is illustrated in Figure 4.21 d).

Simulated angular-dependent spectra are plotted in Figure 4.21 a)‑c) as a function of HWP angle and frequency for negative delays of 0, −200, and −500 fs. For zero delay, the two pulses completely overlap in time, and their superposition produces linear polarization. Since at zero delay, the spectrum is modulated entirely and the two pulses interfere constructively, a rotation of the waveplate modulates the transmitted intensity uniformly. Increasing the relative delay between the pulses increases the spectral modulation frequency, as described in Equation 4.18. In the case we are considering here with counter-rotating circularly polarized pulses, the spectral interference fringe patterns describe Archimedean spirals, when plotted as polar plots, as shown in Figure 4.21 e)‑g). The simulated spiral-shaped spectra are plotted for a negative delay of −500 fs, and a positive delay of 500 fs. The interference pattern rotates clockwise for a positive delay, and for a negative delay, the interference spectrum rotates counter-clockwise. In Figure 4.21 f), identical pulses with the same delay as in g) are plotted, but as a function of wavelength and not frequency. Note that the handedness of the Archimedean spiral is flipped in this case.

Figure 4.22 shows measured angular-dependent spectral interference patterns of the frequency comb laser pulses after polarization shaping with the SAD box. The same pulse parameters (i.e. RHCP before LHCP) as in the simulations, but for more values of the delay τ, are used, and the measurements agree well with the simulations.

In the literature [189, 449], this method used a rotatable polarizer instead of a rotatable HWP. Therefore, our spirals have a four-fold rotational symmetry (C_4 symmetry in the Schönflies notation) instead of a two-fold C_2 rotational symmetry, because rotating the HWP in front of the polarizer is equivalent to a rotating polarizer at twice the angle.

These polarization-shaped pulses will be used to generate photoelectron vortices that can be detected by photoelectron tomography with the intra-cavity VMI spectrometer. The VMI spectrometer is described in detail in Section 2.4. To observe the spectral interference pattern in the photoelectron spectrum, the following conditions need to be fulfilled [189, 450]: (1) The VMI energy resolution needs to be better than the energy separation of the interference fringes $\Delta E_{\text{fringe}} = h/\tau$. This effectively places an upper limit on the delay $\tau < h/\Delta E_{\text{VMI}}$. (2) The two pulses needs to be fully separated in time. Otherwise, linear polarization would be present in the overlap region. (3) ΔE_{fringe} needs to be below the combined spectral width ΔE_{MPI} of the n-photon spectrum of the MPI process. It means that $\Delta E_{\text{VMI}} < \Delta E_{\text{fringe}} < \Delta E_{\text{MPI}}$ needs to be fulfilled.
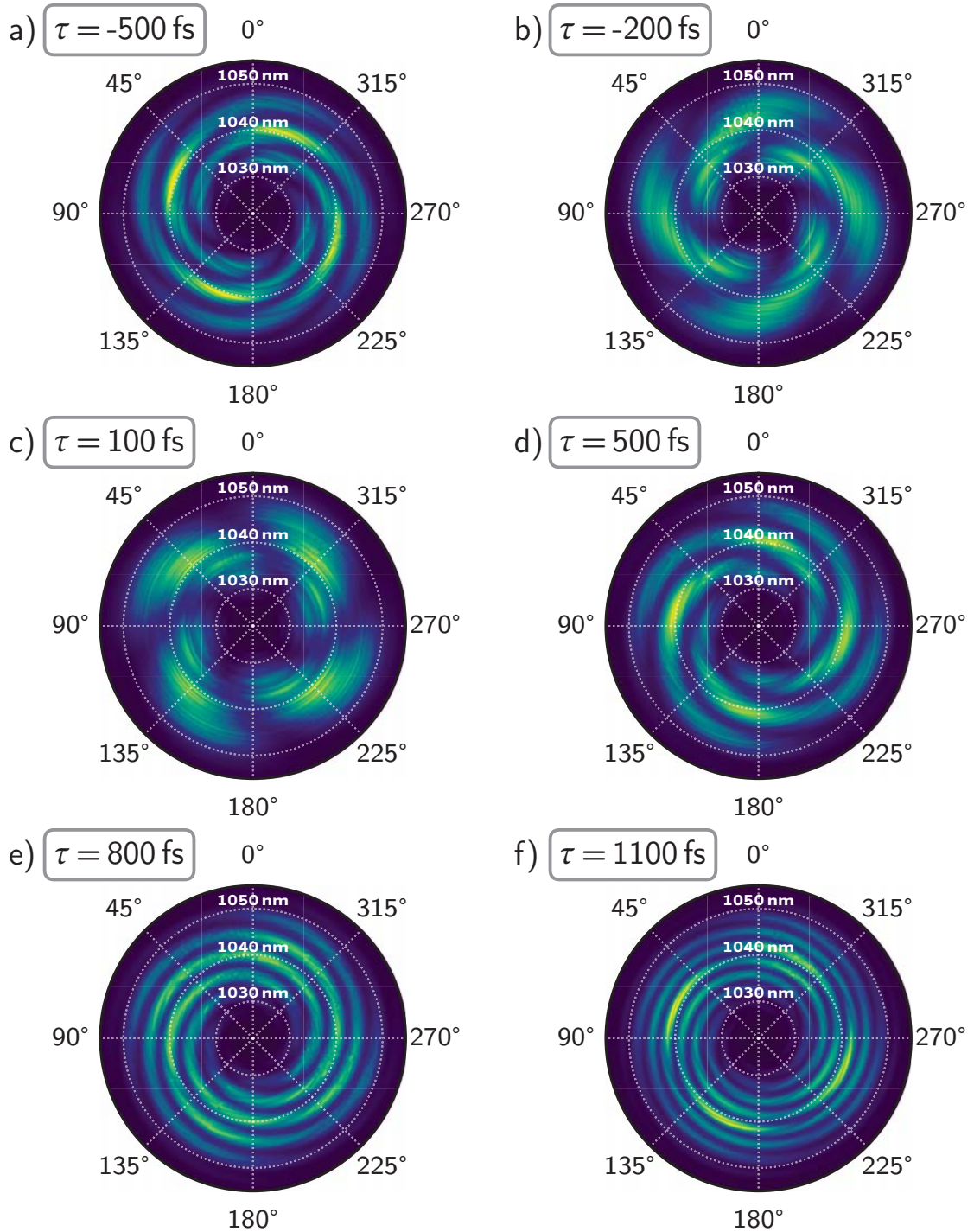
Figure 4.22: Polar plot of measured angular-dependent spectral interference traces. As described in the text and illustrated in Figure 4.21, counter-rotating circularly polarized pulses are sent through a motorized HWP and a subsequent PBS. The spectrum of the p-polarized fraction of the pulse pair is recorded as a function of HWP angle for a delay of a) $\tau = -500$ fs, b) $\tau = -200$ fs, c) $\tau = 100$ fs, d) $\tau = 500$ fs, e) $\tau = 800$ fs, and f) $\tau = 1100$ fs. The spectrum is modulated with $1/\tau$, and the spectral interference pattern describes a clockwise (counterclockwise) rotating Archimedean spiral for negative (positive) time delays with RHCP before LHCP (RHCP after LHCP) pulses. Note that the polarization rotation angle is twice the waveplate rotation angle.

Figure 4.23: Overview of the FROG setup for pulse characterization. Either the output of the SAD box can be a) directly used for an interferometric FROG measurement or b) the pulses are coupled out of the SAD box with a slight beam offset, which allows intensity FROG measurements, as shown in Figure 4.24. The SHG signal is generated inside a thin β-barium borate (BBO) crystal. A bandpass filter (BP) in the spectrometer only transmits the second-harmonic light and cuts away the fundamental light.

4.2.3 Pulse characterization by frequency-resolved optical gating
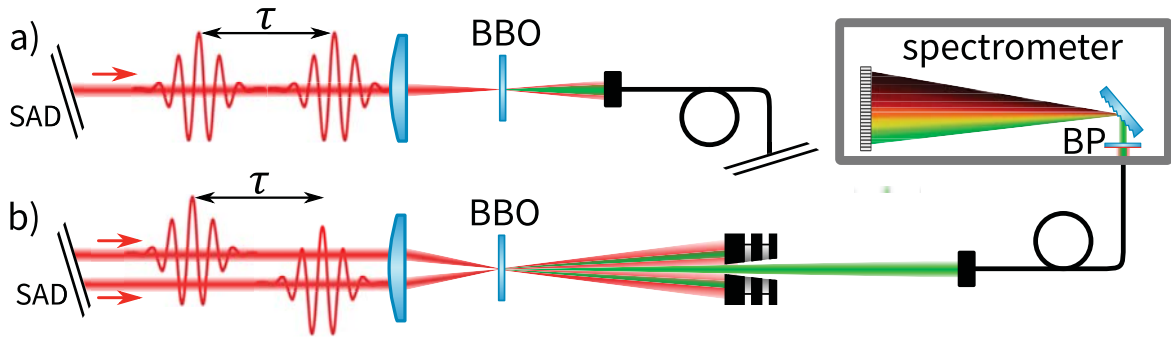
The pulse duration plays a crucial role in nonlinear optics because it affects the temporal behavior of the light pulse and determines the peak intensity for a given pulse energy. Therefore, measuring and controlling the pulse duration is essential for accurately studying nonlinear optical phenomena. Since femtosecond pulses are too short for the direct electronic measurement of the envelope of the electric field, self-referencing techniques are used [196]. The most accessible measurement is the intensity autocorrelation

$$ACF(\tau) = \int_{-\infty}^{\infty} I(t)I(t-\tau)dt, \tag{4.19}$$

where the two identical copies of the pulse with variable time delay τ interact in a nonlinear medium in a time-shifted manner. Commercial autocorrelators are readily available, as described in Section 4.3. However, it is impossible to obtain phase information from a measured autocorrelation. By extending the autocorrelator with a spectrometer and employing a phase-retrieval algorithm, it is possible to reconstruct the phase information of the pulse and, in this way, measure the complete electric field [446, 451–453].

Since the SAD box produces time-delayed pulse copies, it can be used for pulse characterization. The two pulse copies are either directly focused into a nonlinear crystal or by using a small pickup mirror to extract the pulses with a slight parallel offset, as shown in Figure 4.23 a) and b), respectively. After SHG in a BBO crystal, the spectrum of the frequency-doubled light at ~520 nm is measured at each time delay τ using a home-built spectrometer. These spectra are stacked to a so-called FROG-trace. More details about the FROG setup can be found in [304, 383, 454]. The FROG retrieval used in this work is based on freely available software [455]. The result of an intensity FROG measurement at ~8.5 W of laser power is shown in Figure 4.24. A pulse duration of 184 fs is retrieved by the algorithm, showing good agreement with the noise-filtered trace.
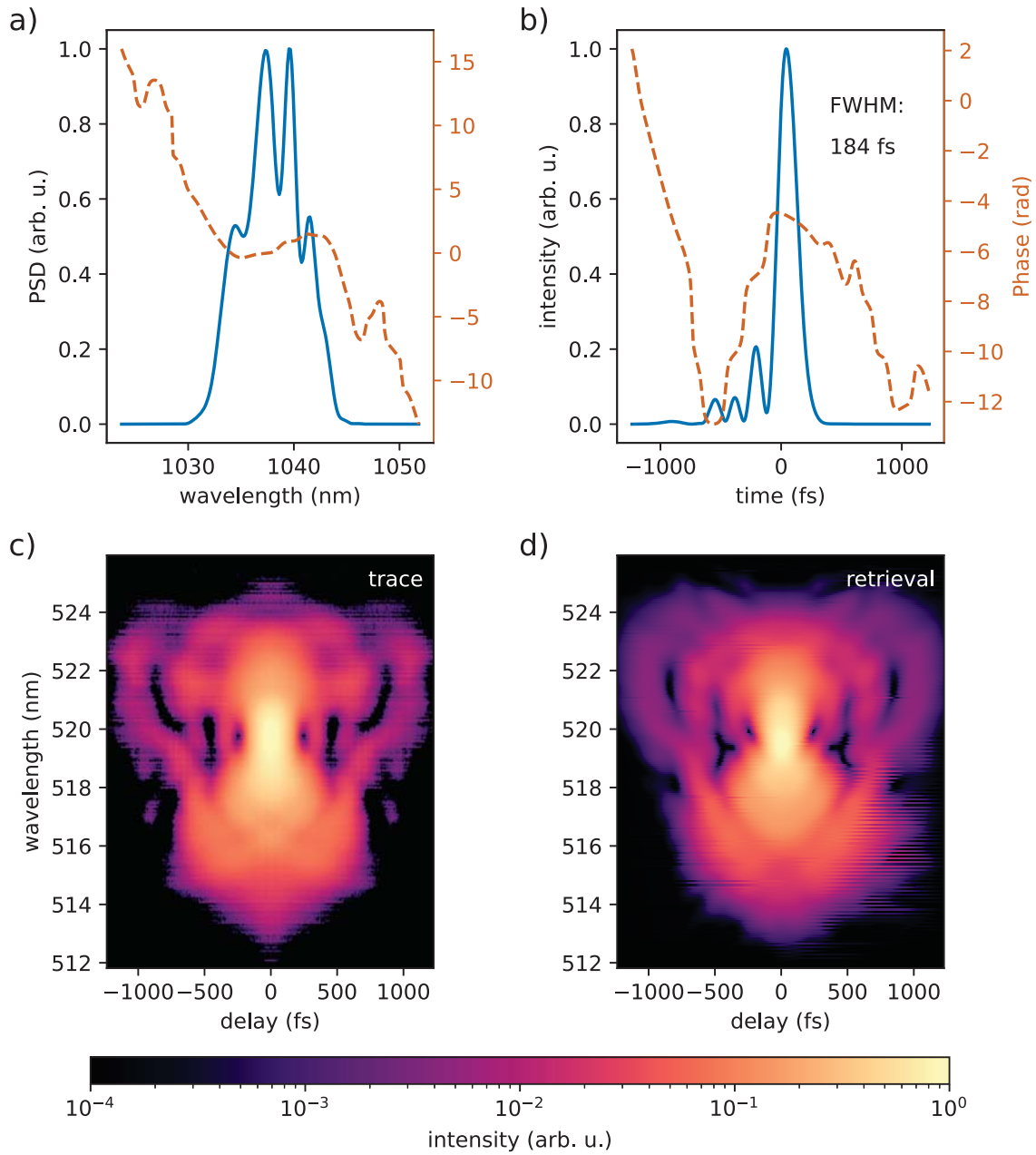
Figure 4.24: FROG measurement for pulse characterization. The iterative phase-retrieval algorithm starts with the measured FROG trace shown in c). d) The retrieved FROG trace yields the a) spectrum and spectral phase, and b) the temporal pulse shape and temporal phase. A pulse duration of 184 fs is obtained. Figure adapted from [454].

4.3 A dispersion-tunable multipass cell

As described in Section 2.7, already a slight increase in laser intensity strongly affects the yield of highly nonlinear processes, such as MPI and HHG. Furthermore, shorter pulses have broader spectra, which increases the spectral coverage for spectroscopic applications. In this section, the optical and mechanical design of a flexible, continuously dispersion-compensated MPC for spectral broadening and nonlinear temporal pulse compression is presented [304].

4.3.1 Dispersion tuning
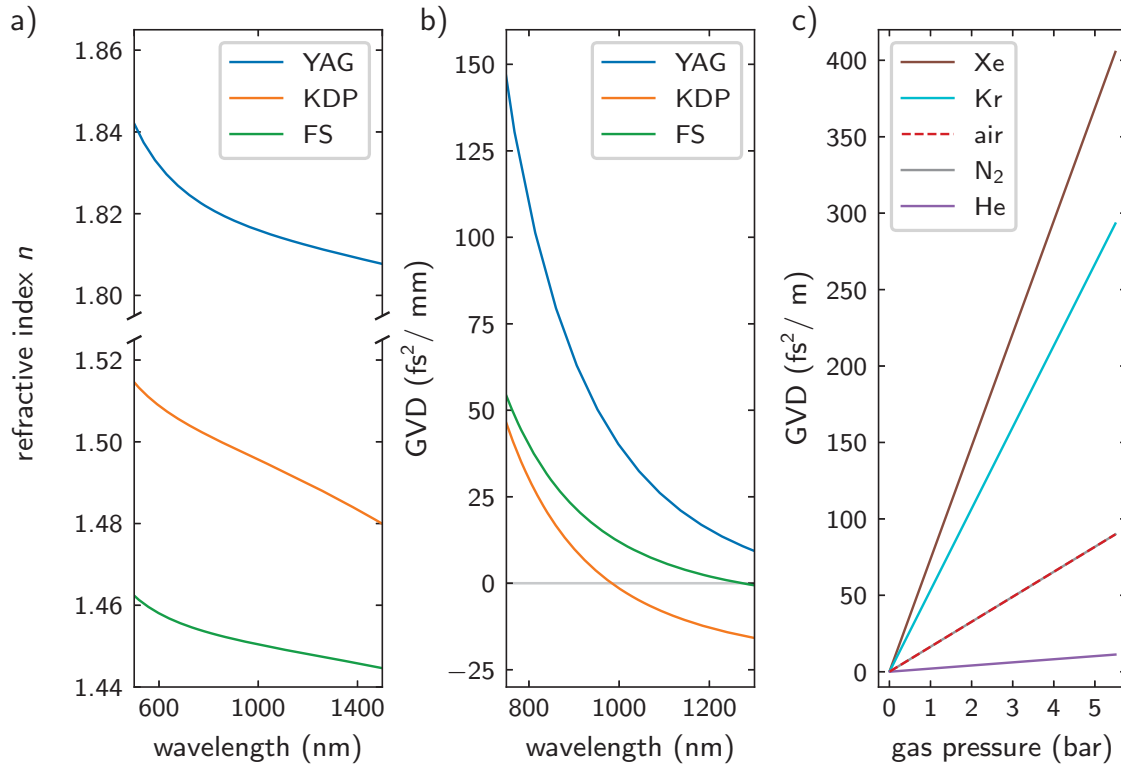
Figure 4.25: Dispersion matching by gas pressure tuning. a) Wavelength dependency of refractive indices of yttrium aluminium garnet (YAG), potassium dihydrogenphosphate (KPD) and FS. b) Dispersion values of these materials are obtained by the second derivative. c) The dispersion in the MPC can be tuned by changing the gas pressure. The GVD is plotted for selected gases. Note that the dispersion of air and nitrogen is almost identical. Adapted from [304] with data from [456–462].

The working principle of a MPC with two curved mirrors and a single material plate as the nonlinear medium is shown in Figure 2.24. The beam is coupled in with a small scraper mirror and bounces back and forth between large curved mirrors, while passing through the nonlinear medium. After the desired number of passes through the medium, the light is coupled out with a second scraper mirror on the opposite site. The nonlinear material can be chosen from a wide range of transparent media. Refractive indices of typical nonlinear materials are plotted as a function of wavelength in Figure 4.25. The second derivative of the refractive index with respect to the frequency, according to Equation 2.113, yields the GVD. From this value, the GDD value is obtained by multiplication with the propagation length. In our cell we use a single KPD crystal

with anomalous dispersion at our center wavelength. This offers the advantage that, in principle, chirped mirrors with negative GDD are not necessary to compensate the nonlinear phase. To fine-tune the dispersion, various gases can be used, while the gas pressure in the cell is tuned using the fact that the GVD is directly proportional to the gas pressure, as shown in Figure 4.25 c).

MPCs with bulk nonlinear media are usually operated in the critical self-focusing regime with non-negligible Kerr lensing. This results in a weak guiding effect within every pass that needs to be accounted for in mode-matching and in the curved mirror distance L. The critical power for self-focusing is related to the refractive index and can be estimated by $P_{crit} \approx \lambda^2/(2\pi n_0 n_2)$ [463]. Note that this value is for linearly polarized light and for circularly polarized light the Kerr effect is reduced by one third. In bulk compressors, typically fused silica is used with a critical self-focusing threshold of $P_{crit,FS} \approx 5$ MW at 1039 nm. Other materials with higher nonlinearities are for example YAG with $P_{crit,YAG} \approx 1.5$ MW and KPD with $P_{crit,KDP} \approx 1.8$ MW [294].

At full power of our amplifier system, $\sim$75 W of average power and $\sim$200 fs pulses at a repetition rate of 100 MHz can be coupled into the cell, which corresponds to a maximum peak power of the incident pulses of $\sim$3.5 MW. This means that we are operating the cell either slightly above or below the critical self-focusing threshold, depending on the choice of the nonlinear material.

It is useful to define the B-integral as the accumulated on-axis nonlinear phase of a Gaussian pulse within the MPC for a single pass through the Kerr medium [351]

$$B_{pass} = 4\pi \frac{n_2 P}{\lambda^2 z_R} \int_{d_K}^{d_K+l_K} \left(1 + z^2/z_R^2\right)^{-1} dz = 2\Phi_{max,pass}. \tag{4.20}$$

Here the Kerr medium with a thickness of l_K is located the distance d_K away from the cell center at $L/2$. The maximum nonlinear phase shift $\Phi_{max} = 2\pi/\lambda \int n_2 P/A_{eff}$, where $A_{eff} = \pi w^2$ is the effective mode area of a Gaussian beam, can be used to calculate the spectral broadening factor

$$b = \frac{\Delta\omega_{out}}{\Delta\omega_{in}} = \sqrt{1 + 4\Phi_{max}^2/(3\sqrt{3})}, \tag{4.21}$$

assuming a transform-limited Gaussian pulse shape. The spectral bandwidth $\Delta\omega$ is stated in terms of the root mean square bandwidth [361].

An MPC with 34 passes through a single 4 mm thick KPD plate in vacuum is simulated and shown in Figure 4.26. This results in a B-integral of the first pass of $B_{first\,pass} \approx 0.2\pi$, which increases to $B_{last\,pass} \approx 0.5\pi$ for the last pass. Pulses are compressed by a factor of approximately six from initially 185 fs to 31 fs. The spectral width increases by a factor of $b \approx 19.5$ to $\Delta\omega_{out}/\omega_c = 7.8\,\%$. This larger bandwidth is beneficial not only for spectroscopic applications, where it increases the number of accessible transitions, but it also greatly enhances the efficiency of nonlinear processes when the dispersion is compensated and the full spectral bandwidth is used to generate temporally compressed pulses.

4.3.2 Optical and mechanical design of the MPC

The main optical components of the MPC are placed on a rigid stainless-steel mounting structure with a U-shaped cross-section, which is held in place by a water-cooled main structure connected to the optical table. A detailed view of the optics mounting structure is shown in Figure 4.27.

The pulses enter the cell through a $\varnothing$ 25 mm AR-coated FS window and are reflected by a 45°, $\varnothing$ 12.7 mm HR mirror in a 2-axis kinematic mount (Polaris-K05, Thorlabs) towards the 0°, $\varnothing$ 6.35 mm HR scraper mirror (Layertec). The scraper is glued on a 5.5 mm wide aluminum arm that can be adjusted in length and angle. It is mounted in a kinematic holder (Polaris-K05, Thorlabs) that can be tilted in two axes and shifted along the beam propagation direction to minimize the distance to the curved mirror.
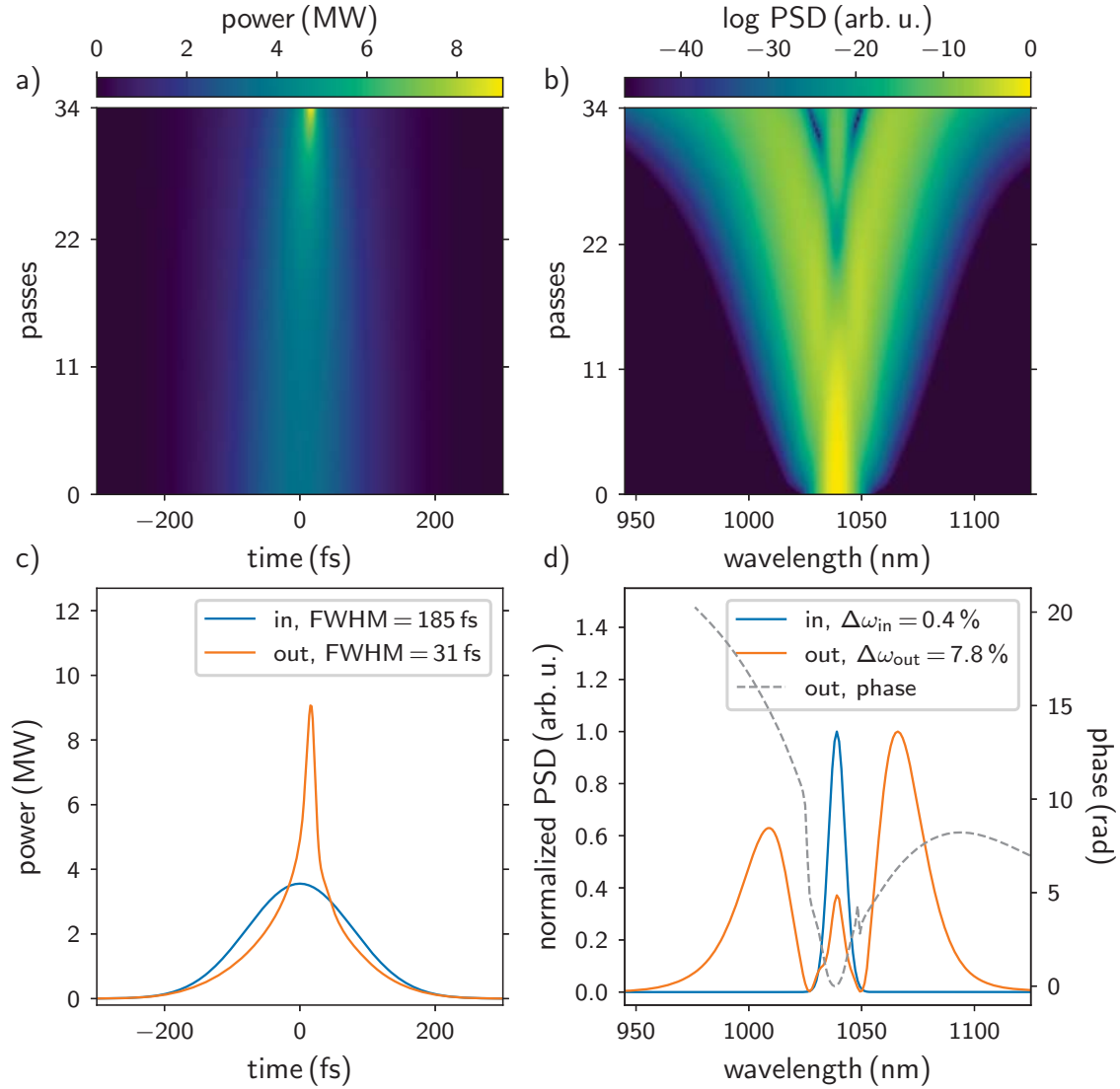
Figure 4.26: Simulation of the nonlinear dynamics inside the MPC for 185 fs pulses with an energy of 700 nJ focused to a 110 μm waist. The initial peak power of 3.6 MW increases to 9.1 MW after 34 passes through 4 mm of KPD. The evolution of the pulse is shown a) in the temporal and b) in the spectral domain. c) After propagation through the cell, the pulses are compressed to 31 fs FWHM pulse duration, and the spectrum broadens from $\Delta\omega_{in} = 0.4\,\%$ to $\Delta\omega_{out} = 7.8\,\%$, as shown in d).
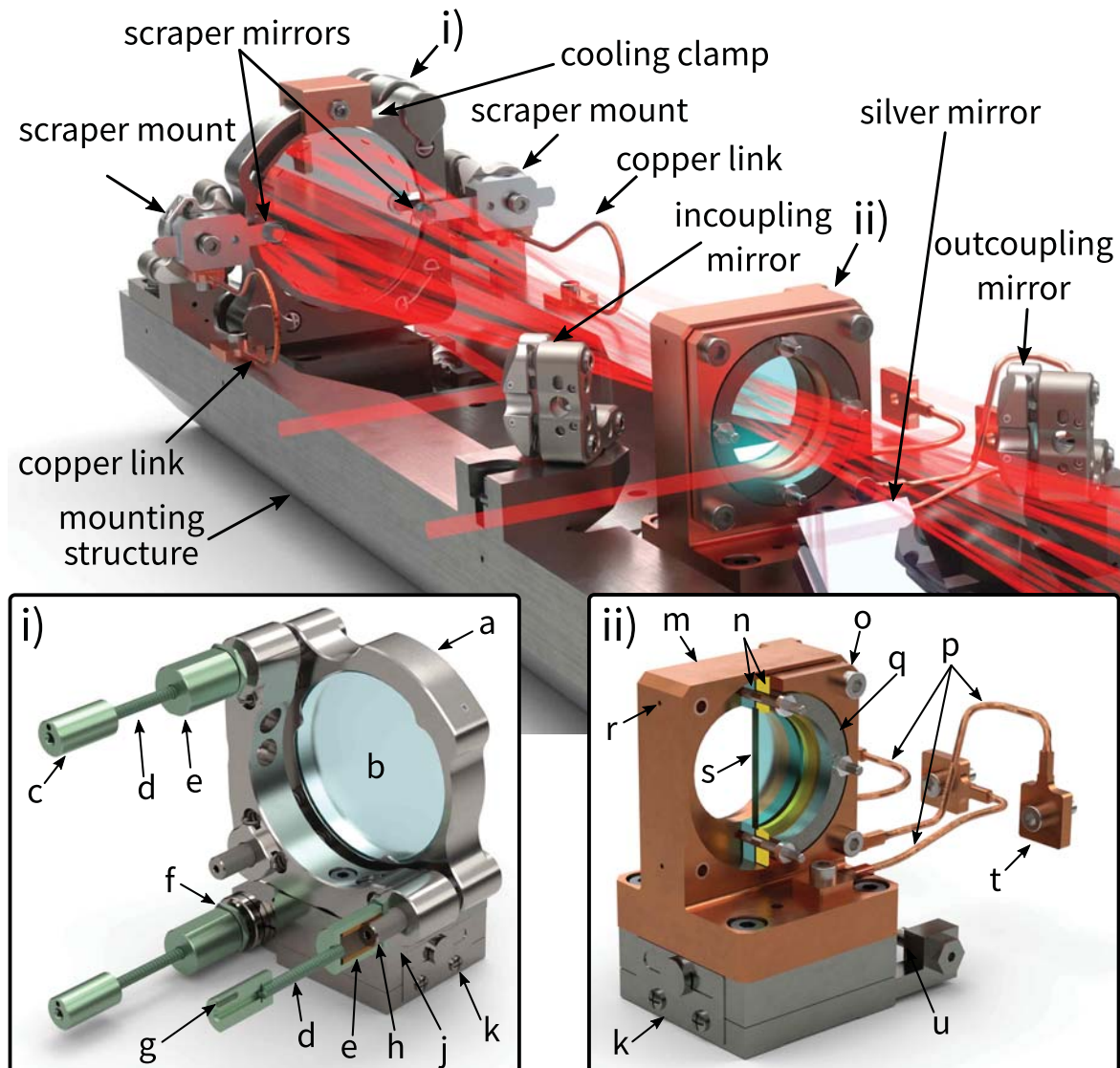
Figure 4.27: Detailed view of the optics inside the MPC. The rigid mounting structure and mirror mounts are made from stainless steel. Inset i) shows the movable mirror: a: mirror mount, b: ∅ 50 mm mirror, c: shaft coupler, d: flexible shaft, e: actuator adapter, f: locking nut, g: thread for threaded rod, h: Actuator of mirror mount, j: adapter plate, and k: translation stage. Inset ii) shows the movable crystal holder made from copper in detail: m: Mount, n: crystal holder plates, o: holding plate, p: flexible copper links, q: steel ring, r: degassing hole, s: crystal, t: copper link connection, u: micrometer screw, and k: translation stage. Two angled silver mirrors are used to image the curved mirrors with a camera (not shown) outside the chamber.

Typically, the mirror radius of curvature R is in the range of 200 to 300 mm for MPCs with solid media [348, 351, 464, 465]. This results in a good balance between the compactness of the system ($L \approx 500$ mm) and large enough focal lengths to avoid instabilities and alignment difficulties. For very high pulse energies, where only gas is used as the nonlinear medium, the cell length can be as large as 10 m [466]. Our cell is formed by two 50 mm curved mirrors with a radius of curvature of $R = 250$ mm (025-8025, EKSMA Optics) held in 2-axis kinematic mounts (POLARIS-K50S4/M, Thorlabs). Flexible links are fabricated from 2 mm^2 copper braids welded to copper end fittings to thermally connect the curved and scraper mirrors and the crystal mount to the main structure, even when the cell is evacuated. Angled silver mirrors are used to image the two curved mirrors through window flanges in the main structure with a camera outside the chamber. The mirror at the scraper mirror position sits on a translation stage (custom UHV version of 9062-COM-M, Newport), as shown in more detail in Figure 4.27. The actuators of the mirror mount and the translation stage are connected with flexible shafts (100881, Gemo) to rotary feedthroughs to enable alignment of the optics when the cell is closed and pressurized.

The heart of the cell is the nonlinear crystal that sits in a rotatable holder in the crystal mount to move the crystal with respect to the fixed laser beam pattern in case a spot is burned into the material. The crystal holder is made from annealed copper for better heat conductivity, while the other parts - screws, thread inserts, and a ring - are made from stainless steel. The ring allows for an even distribution of the clamping pressure. The same combination of translation stage and flexible shaft as for the curved mirror is used to move the crystal along the *z*-axis to optimize the crystal position relative to the cell center. In the version of the crystal holder presented here, only a single material plate is used. In a future upgrade, we will use multiple plates to achieve an even higher compression ratio [349, 350].

MPC main chamber

The complete setup with the main structure with a total height of 180 mm and a footprint of 130×175 mm^2, holding the U-shaped optics mounting structure, is shown in Figure 4.28. The water-cooled main structure is fabricated from a single piece of stainless steel. The inner part is removed by wire-cut electric discharge machining, and T-slots are machined into the contact face with the optics mounting structure in the same way. The optics mounting structure is inserted through the opening in the main structure and clamped down with M6 screws and two threaded slot nuts inserted into the T-slots, as shown in inset ii) of Figure 4.28. Tubes with a length of 255 mm (including the flanges) and an inner diameter of 130 mm are attached to the main structure from both sides. Together they form a gas-tight chamber. This mounting structure offers the advantage that a pressure-induced change in dimension does not influence the alignment of the optics since the chamber is not directly connected to the optics mounting structure. For temperature stabilization, a 20 mm deep and 6.75 mm wide serpentine-like water-cooling channel is machined into the bottom of the main body, as shown in Figure 4.28 iii). Cooling water is supplied through 1/4" NPT screw-in connections with 10 mm double ferrule tube fittings. A 14.5 mm thick and 175×225 mm^2 large base plate, which also serves as an adapter plate for mounting the whole cell on the optical table with eight M6 screws, is used to seal the water cooling channels with an O-ring.

The main structure has ten access ports with DN16CF-inspired flanges. Even though the diameter of the inner bore and the screw pattern is identical, the main difference to DN16CF flanges is that we use an O-ring made of FKM to seal the connection instead of copper gaskets. The O-ring is seated in a groove that prevents the ring from enlarging or shrinking, ensuring a tight seal under both vacuum and overpressure. We use these access ports for AR-coated laser windows, uncoated windows for monitoring the mirrors with an airside camera, gas injection, and pumping.
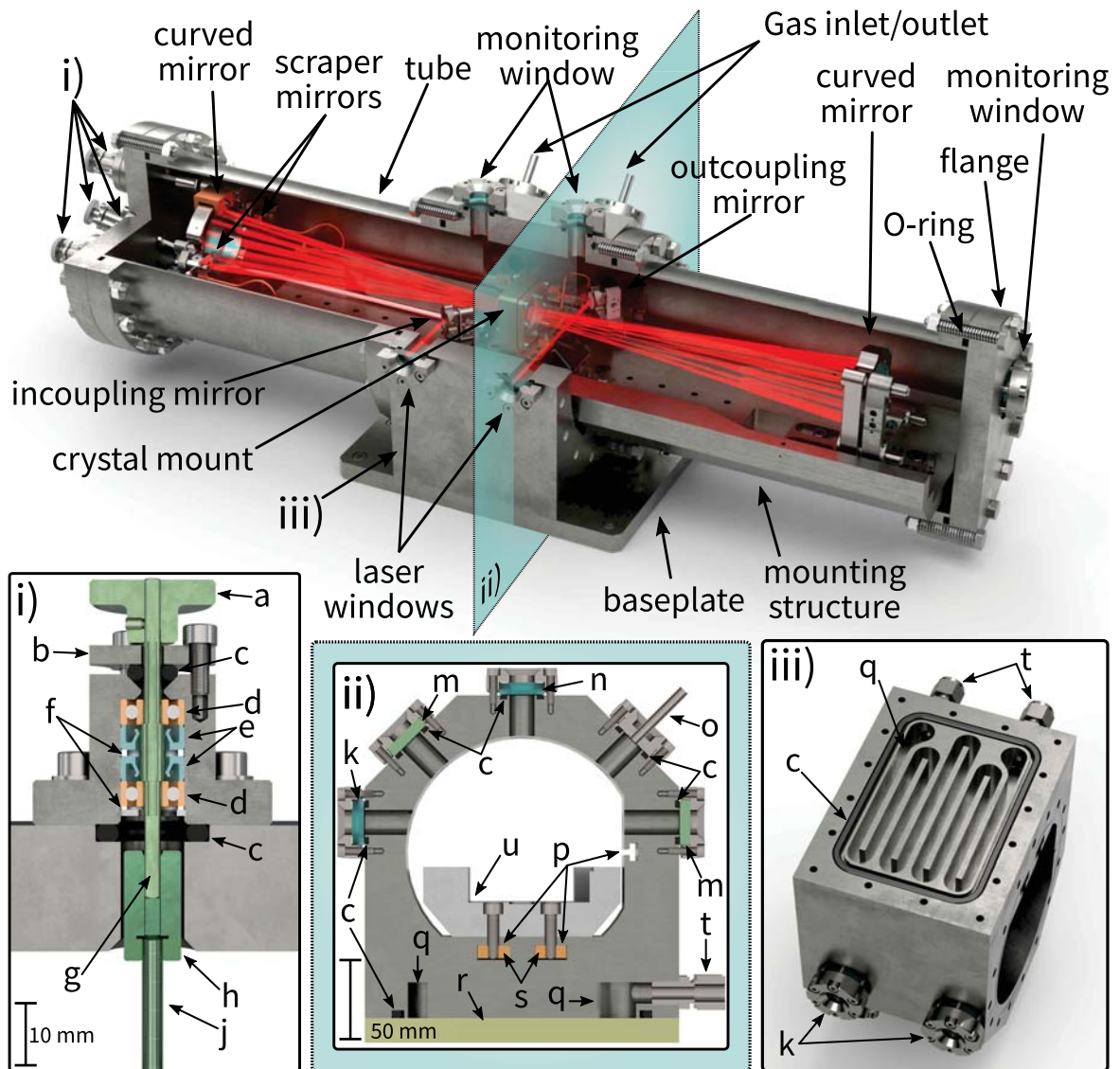
Figure 4.28: Section view of the full MPC with the optics mounting structure (cf. Figure 4.27) inside the chamber. The position of the crystal mount and the left curved mirror and the tip/tilt motion of the latter are connected with flexible links to rotary feedthroughs. Inset i) shows a cross-section of a rotary feedthrough with a: knob, b: endcap, c: O-rings, d: ball bearings, e: radial shaft seals, f: spacer, g: shaft, h: shaft coupler, and j: flexible shaft. Cross-section ii) shows how the optics mounting structure (o) is fixed in the main body with slot nuts (s) inserted into T-slots (p). The other components are: k: AR-coated laser window, m: blind flange, n: monitoring window, o: gas inlet/outlet, q: water channel, r: baseplate, t: cooling water connection, and u: optics mounting structure. Inset iii) shows the cooling channels in the bottom side of the main mounting structure with the removed baseplate.

The hole pattern and outer dimensions of the flanges for the large access ports are based on the dimensions of DN130CF flanges. Sealing is achieved in the same way as for the small flanges with an O-ring in a groove. The sealing surfaces of the main structure are machined directly into the solid stainless steel body. The chamber of the MPC is completed with two 2 mm thick tubes attached to these flanges. Large end flanges bolted to the end of these tubes have the same small access ports as the main structure for rotary feedthroughs or windows.

Rotary feedthroughs

To align the optics inside the cell during operation, vacuum-compatible piezo-motorized mirror mounts are not used due to their high cost and unknown suitability for operation at elevated pressures. As an alternative, we designed compact rotary feedthroughs with the same flange dimensions and O-rings as the other flanges. Since the system needs to withstand both over and under pressure, two polytetrafluoroethylene (PTFE) seals (Prelon, X/2-4/10x4-PTFE-8/1.4310) are used in a back-to-back arrangement for each feedthrough to allow operation between vacuum and 10 bar overpressure. All metal parts are fabricated from stainless steel, and the O-rings are made of FKM. A cross-section of the rotary feedthrough is depicted in Figure 4.28 i).

In order to transfer the rotation into the chamber, a shaft is manufactured, which has a round cross-section in the middle and a square cross-section at both ends. On the air side, a removable knurled knob is attached with an inset screw. Inside the MPC, the rotating shaft is attached to a flexible shaft using a coupler. The coupler has a square-shaped inner side that matches the outside of the shaft to minimize backlash. This axial play is needed because the flexible shaft moves forwards and backwards when the alignment screws are actuated. The coupler and the flexible shaft are electron-beam welded together to connect the feedthrough with the adjustment screws of the mirror mount and translation stages. Ball bearings are used to hold the rotary shaft in place, and to avoid tilting, they are arranged far apart. Note that the shaft has a larger diameter at the seals between the bearings. This avoids being pushed out or pulled in due to the large pressure differences. An O-ring between the main body and knob is used as an additional sealing in case the radial shaft seals are not tight enough, and it offers the advantage of locking the rotation by pushing the endcap against the body.
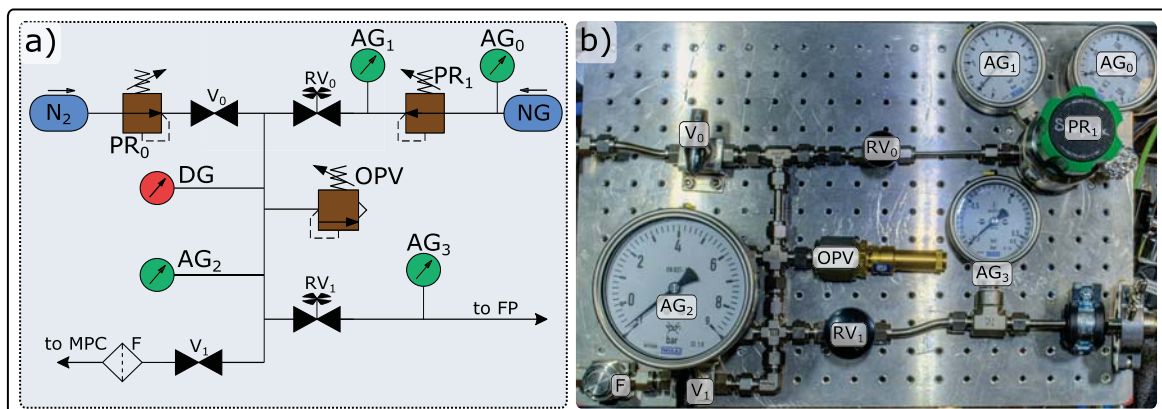
MPC gas system

Figure 4.29: Circuit diagram a) and photograph b) of the MPC gas system. The main components are labeled: valves (V), regulating and shutoff valves (RV), pressure regulator (PR) filter (F), analog/digital pressure gauges (AG/DG), and fore-vacuum pump (FP).

The MPC is designed to operate at any pressure between vacuum and a few bars of overpressure of inert gases. Therefore, the structure must withstand not only the gas pressure it is designed for but it is also necessary to follow the regulatory guidelines. Vacuum casings with a maximum allowable overpressure of less than 0.5 bar above atmospheric pressure are not considered pressure equipment but for higher overpressure, the Pressure Equipment Directive 2014/68/EU of the European Union [467] must be followed. In practice, this means that the product of pressure and volume should be below $pV \leq 25$ bar L. Otherwise, higher testing requirements would apply, and an external testing and certification procedure would have been necessary. For us this means that the maximum operating pressure of the cell is ~6 bar to stay below this threshold even though the cell is designed to withstand much higher pressure. After manufacturing, the workshop's internal quality control carefully checked the MPC assembly and conducted a hydrostatic pressure strength test at 12 bar.
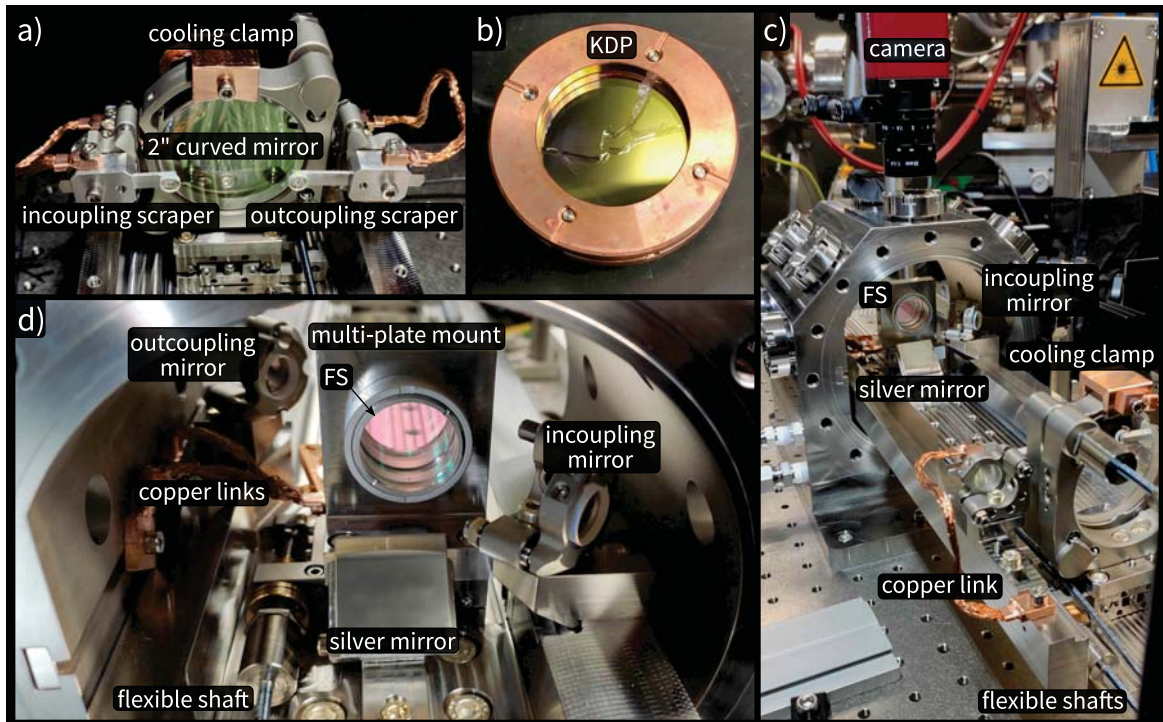
Figure 4.30: Photographs of the current MPC setup. a) The two-inch curved mirror in its kinematic mount on a linear translation stage, cooled with a copper cooling clamp. The in- and outcoupling scraper mirrors are length, angle, and tilt-adjustable and cooled by flexible copper links. b) Cracked 4 mm thick KPD crystal. c) MPC with the camera mounted above for monitoring the curved mirror and the scrapers using an angled silver mirror. Flexible shafts can be used for optical alignment when the gas cell is closed. d) Instead of the KPD mounted in the crystal holder, two 6.35 mm FS plates are inserted into a multi-plate mount. This multi-plate mount is placed on a linear translation stage connected to the outside using a flexible shaft.

Pumping of the cell and gas injection is achieved using flange-mounted inlets/outlets, as shown in Figure 4.28. The cell is connected to a gas panel by a flexible all-metal tube with an inner diameter of 6 mm. The flexible connection allows the floating optical table to move freely and reduces vibration transmission. The gas panel is shown in Figure 4.29. It allows the pumping of the cell and filling it with inert gases. The pump outlet is connected to the fore-vacuum system of the XUV comb experiment. It adds the benefit that gas used in the cell can be recycled in the gas-recycling setup, described in Section 3.3.2. With a regulating and shut-off valve,

the cell can be pumped continuously to the desired (under)pressure. It additionally offers the advantage that the cell pressure can be released smoothly without exceeding the maximum allowable pressure of the fore-vacuum line. The same valve is also installed behind the pressure regulator (Swagelock KCY1FRF412A20000). In addition, the gas panel is connected to the nitrogen supply of the institute. A pressure relief valve with a release pressure of 8.5 bar prevents the cell pressure from being dangerously exceeded. To prevent the system from contamination with dust and particles, a particle filter with a pore size of $0.5\,\mu m$ is the last element of the gas panel before the connection to the cell.

4.3.3 MPC experiments
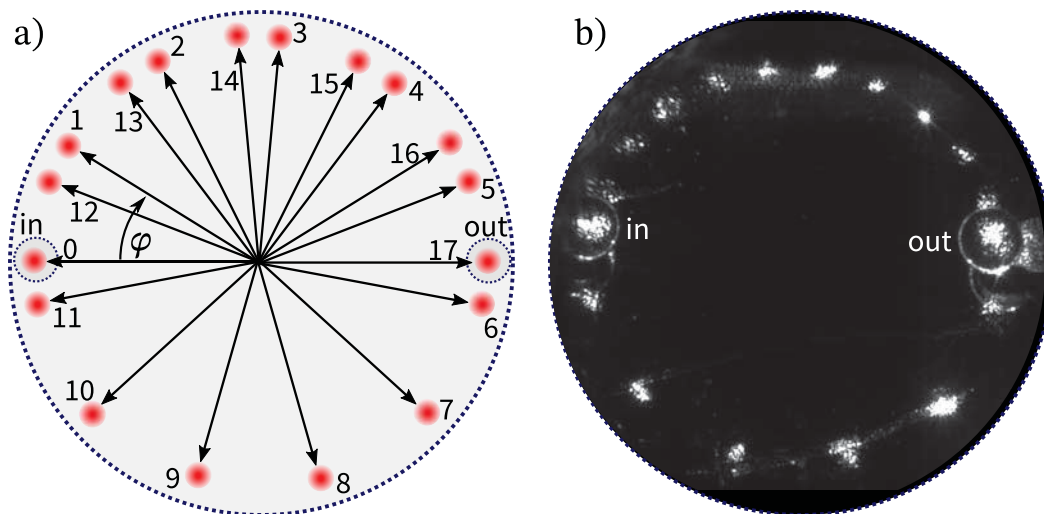
Figure 4.31: Laser spot pattern on the first curved MPC mirror. a) The spots on the mirror advance by $\varphi = \pi m/n$, as defined in Equation 2.107. The spot pattern on the end mirror is shown for 34 passes through the crystal, which corresponds to $m = 3$, $n = 17$, and an angle of $\varphi \approx 32°$. Small dotted circles indicate the position of the scaper mirrors directly in front of the curved mirror used for in- and out coupling. b) The photograph of the beam spot pattern on the end mirror is taken with the camera shown in Figure 4.30 c).

After assembly of the cell and helium-leak testing, a first test using a $25 \times 25 \times 4\,mm^3$ KPD crystal was performed. The number of passes was set to 34, as shown in Figure 4.31. According to the simulation shown in Figure 4.26, we expect spectral broadening and pulse compression to $\sim 30\,fs$ directly out of the cell at 70 W of circulating optical power, without the need for chirped cell mirrors or post compression. However, already below 2 W of laser power, the crystal cracked. Another 3 mm thick crystal from the same batch also cracked at a similar power level. Both crystals were mounted with care to avoid mechanical stress from the holder. To find out the reason for the breakdown of the crystals, we monitored a fragment of the 4 mm thick crystal with 5 passes through it with a thermal camera (FLIR E6xt). At about ~ 2 W of optical power, the crystal reached 44 °C within a very short time and broke again. In a previous experiment, a KPD crystal from another manufacturer was tested in single-pass, uncooled configuration up to ~ 73 W without damage, and we observed SPM-induced spectral broadening [304]. The most probable source is a bad crystal batch from the manufacturer. Unfortunately, such large crystals are not readily available and have long lead times.
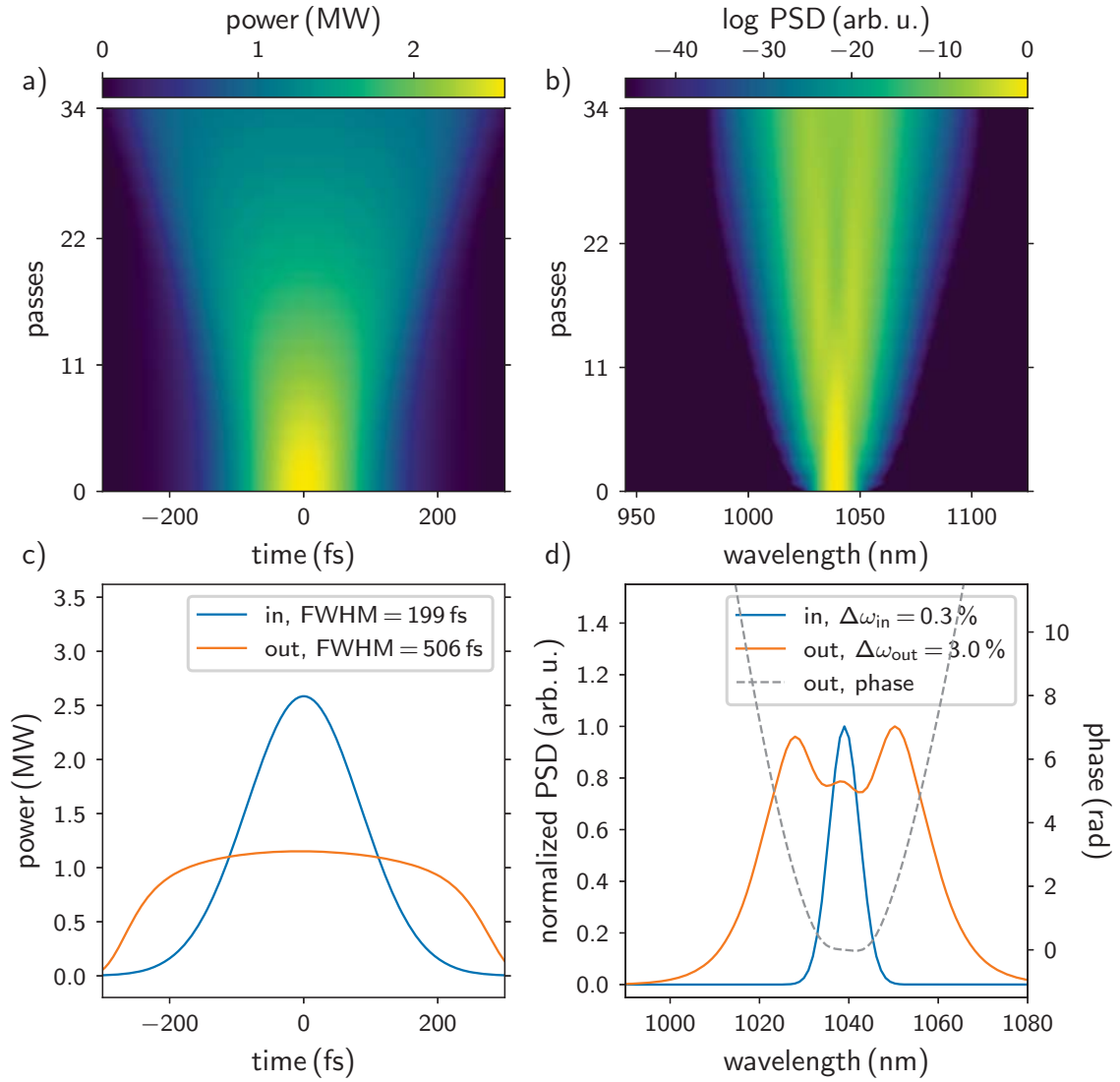
Figure 4.32: Simulation of the propagation dynamics inside a FS multi-plate MPC. Two 6.35 mm FS plates are placed in the 92 μm beam waist of a MPC with 34 passes. Spectral broadening is observed at an incident pulse energy of 550 nJ. Because the cell is operated in air and assuming zero mirror GDD, a strong quadratic spectral phase is accumulated, resulting in temporally stretched pulses at the output, which requires post-compression.
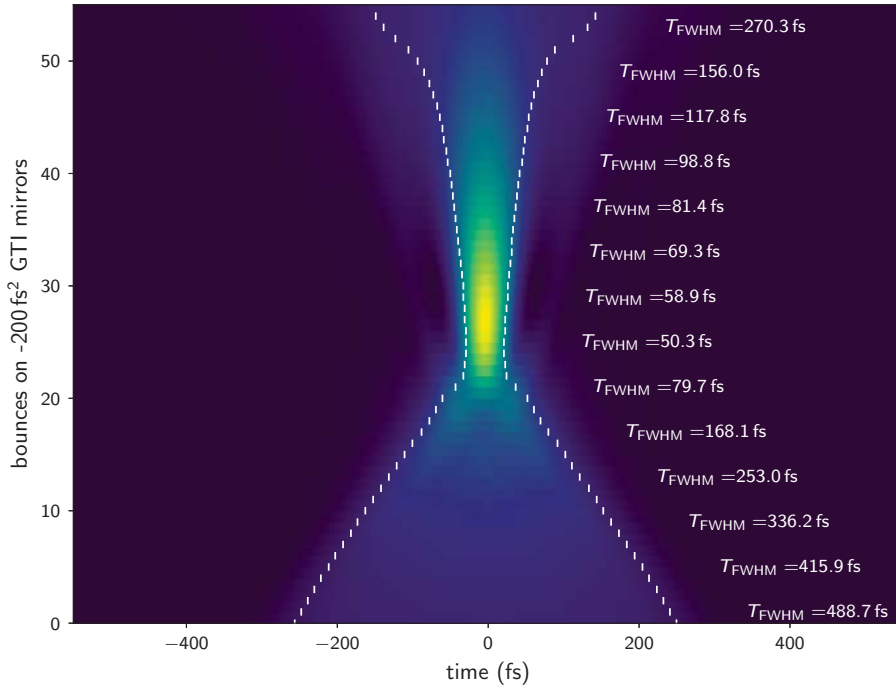
Figure 4.33: Simulation of a chirped-mirror pulse compressor behind the MPC. The output pulses of the simulation shown in Figure 4.32 are compressed using Gires-Tournois interferometer (GTI) mirrors with a GDD of each $-200\,\text{fs}^2$. After 25 to 30 bounces on such mirrors, pulses are compressed to $\sim50\,\text{fs}$, neglecting the GDD of the MPC mirrors, the outcoupling window, and collimation lenses.

A multi-plate MPC

In order to demonstrate the functioning and flexibility of the cell, we inserted an universal multi-plate mount with two AR-coated FS plates into the cell, as shown in Figure 4.30 d). The $\varnothing\,25\,\text{mm}$ FS plates have a thickness of $6.35\,\text{mm}$ and are spaced $11.6\,\text{mm}$ apart, centered between the curved mirrors. A simulation of the cell, assuming $\sim200\,\text{fs}$ input pulses at $55\,\text{W}$ of average power, which corresponds to a pulse energy of $550\,\text{nJ}$, and 34 passes through the plates, is shown in Figure 4.32.

At each pass through the cell, a positive GDD of $\sim125\,\text{fs}^2$ is added due to the dispersion of the plates and air. As a result, the pulses exiting the cell are, according to the simulations, temporally stretched to $\sim375\,\text{fs}^2$. Therefore, we implement a chirped mirror pulse compressor for the pulses exiting the cell. We use GTI mirrors with a negative GDD of $-200\,\text{fs}^2$ per bounce. GTI mirrors are based on standard thin film HR mirrors with added and precisely adjusted spacer layers in the upper section of the quarter-wave dielectric stack. These spacer layers introduce resonances that can produce high GDD values, well suited for chirped-mirror pulse compressors. A simulation of the pulse compressor using the output of the MPC simulation of Figure 4.32 is shown in Figure 4.33. According to the simulations, we could expect pulses as short as $\sim50\,\text{fs}$ after ~26 bounces on the GTI mirrors. However, the (unknown) dispersion of the HR curved mirrors of the MPC, the dispersion of the AR coating of the plates, the windows, and the mode-matching lenses was neglected. Additionally, zero power loss during cell propagation was assumed for the simulations. Therefore, we expect significantly longer pulses than the simulated best case value of $\sim50\,\text{fs}$.

Experimentally, the incoming power into the MPC is increased up to $\sim54\,\text{W}$. A lens-based telescope and focusing unit before the cell is used to match the incident beam size to the MPC

a)

b)
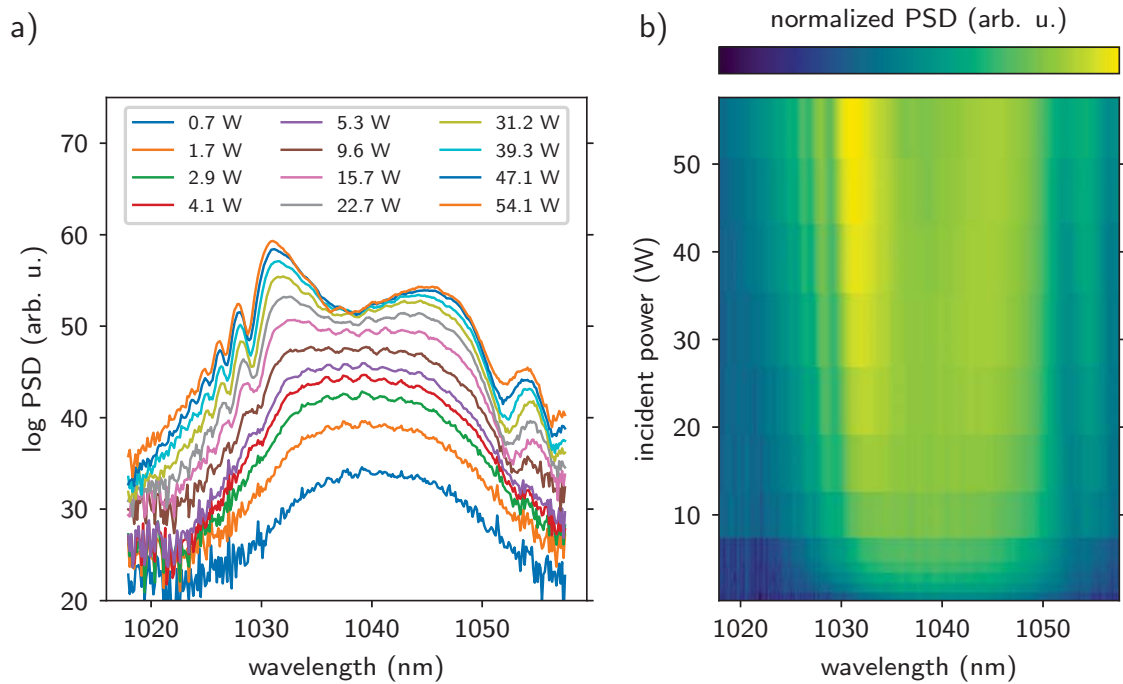
Figure 4.34: Measurement of spectral broadening in a multi-plate FS MPC. Two 6.35 mm FS plates are inserted into the multi-plate mount, as shown in Figure 4.30 d). a) MPC output spectra are plotted for several incident power levels in a logarithmic representation. b) Spectra are stacked to a 2D plot using a linear colormap. SPM-induced spectral broadening is evident from the emergence and widening of spectral wings at higher laser power.
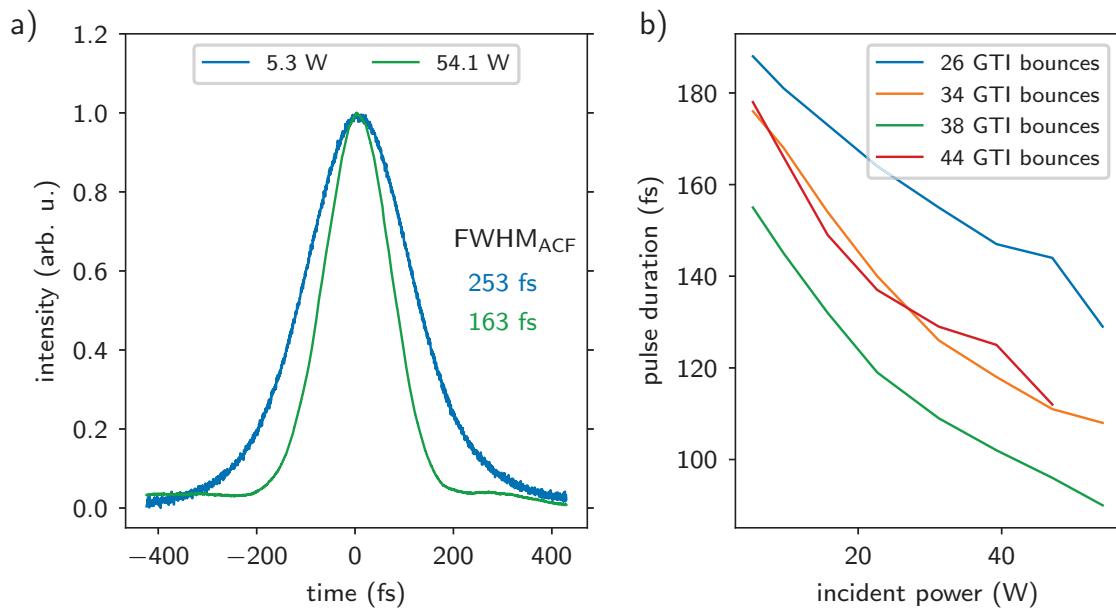
Figure 4.35: Measurement of temporal pulse compression in the FS multi-plate MPC with a subsequent chirped mirror pulse compressor. a) The autocorrelation function of the pulse after the multipass cell is measured using an autocorrelator. It is shown for 38 bounces on three pairs of GTI mirrors for low and high input power. The stated values are the FWHM of the measured autocorrelation function. b) The pulse duration changes as a function of the input power for 26, 34, 38, and 44 GTI mirror bounces. It is stated as the FWHM of a fitted sech^2 temporal pulse shape. The shortest pulse duration $T_{\text{FWHM}} \approx 90$ fs, which corresponds to a temporal pulse compression by a factor of two, is reached at maximum power and 38 GTI mirror bounces.

mode. The incident power is monitored with a reflection from a beam sampler in front of the cell. The transmission of the empty MPC after 34 passes is ~85 %, mainly limited by the standard HR coating of the curved mirrors. It reduces to ~75 % when the two 6.35 mm thick FS plates are inserted. The output beam of the cell is collimated and sent to a power meter, a spectrometer, and an autocorrelator (APE plseCheck). SPM leads to spectral broadening, indicated by the emergence and widening of spectral wings at higher laser power, as shown in Figure 4.34.

Figure 4.35 a) shows the measured autocorrelation function using the autocorrelator. As expected, the pulse duration decreases when increasing the input power because the spectrum is broadened stronger at higher intensity. We tried four different chirped-mirror pulse compressor settings with 26, 34, 38, and 44 bounces on two to three GTI mirror pairs [468]. The shortest pulses are reached at the highest input power employing 38 bounces with a GDD of in total $-7600\,\text{fs}^2$, as shown in Figure 4.35 b).

A minimum pulse duration of ~90 fs is reached, which corresponds to a temporal compression of the incident pulses by a factor of approximately two. The pulse duration is stated as the FWHM of the intensity envelope of the pulse (not to be confused with the plotted autocorrelation function), assuming a sech^2 temporal pulse shape, and it is obtained from the commercial device. With the achieved transmission of 75 %, this corresponds to an increase of the peak intensity by a factor of ~1.5, which already will be advantageous for the study of highly nonlinear processes.

In the future, we will replace the curved mirrors, which currently have a medium-quality coating, with an improved coating for higher cell transmission. Soon, we will test higher-quality KPD crystals to exploit the high nonlinearities and dispersion self-compensating properties of this material, which, in principle, allows for omitting chirped mirrors. However, since the first test was unsuccessful, we will also test chirped-curved mirrors, operating the cell in multi-plate configuration using FS or YAG as the nonlinear material. In contrast to our current setup, this will enable short pulses directly from the MPC without needing post-compression. For fine-tuning the dispersion, the gas pressure can be varied in a wide range from vacuum to 6 bar above atmospheric pressure. Using xenon and 34 passes through the cell, this corresponds to a GDD tuning range of $8200\,\text{fs}^2$. In summary, due to its versatile design, the MPC offers a wide range of pulse compression options.

4.4 VMI spectrometer

In this section, we present the design and construction of a new dedicated VMI spectrometer which is compact enough for intra-cavity use. The description closely follows our recent publication [469]. The new VMI spectrometer incorporates many crucial improvements over our earlier proof-of-principle version [129]. First, image deformations are avoided by shielding all non-conducting surfaces, and magnetic shielding is added around the flight path. Without loss of compactness, the number of electrodes is greatly increased to allow for more versatile experiments. Space-charge effects, which limit the maximum achievable resolution, are mitigated by recording less than a single ionization event per pulse due to the high repetition rate of the pulses inside the polarization-insensitive cavity. Therefore, it enables the first tomographic reconstruction of 3D PADs at 100 MHz.
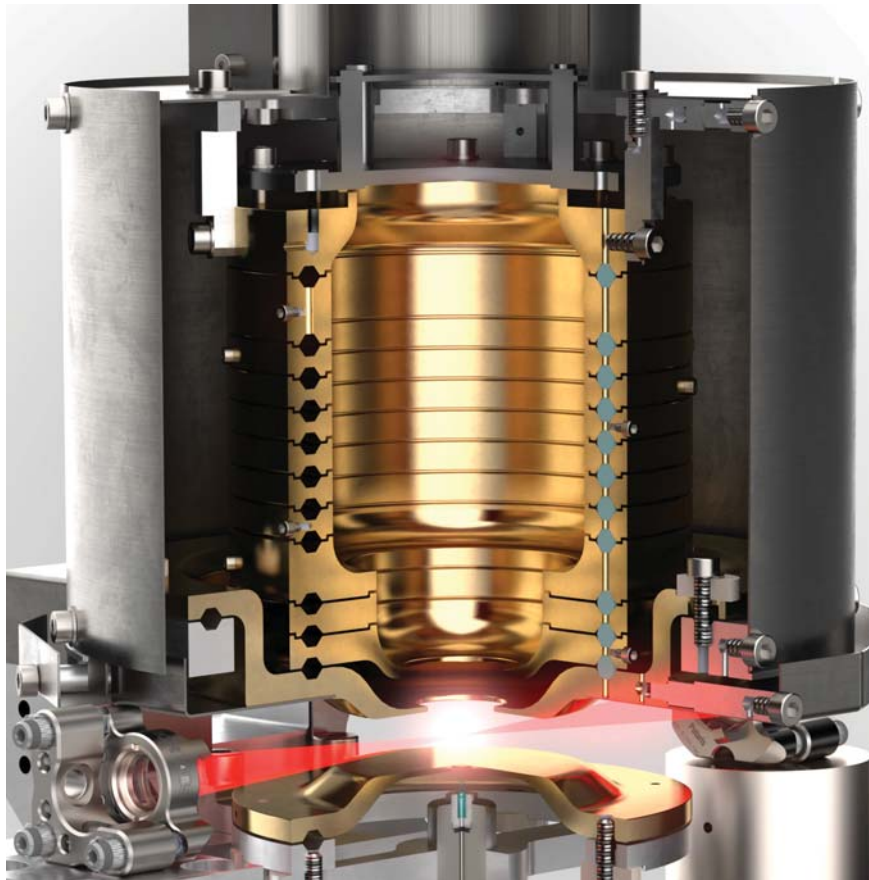
Figure 4.36: Section through the VMI spectrometer showing two concave cavity mirrors and the laser beam (red). A μ-metal (dark grey) shield surrounds the electrode stack (gold), shielding it from external electromagnetic fields. Reproduced from [469], with the permission of AIP Publishing.

4.4.1 VMI design considerations

In a recently reported VMI spectrometer design, a photoelectron kinetic energy resolution of $\Delta E/E \approx 0.53\,\%$ has been demonstrated experimentally [470]. In that work, conventional plate electrodes held by spacers were used to focus the electrons through a 500 mm long double μ-metal shielded flight tube onto the MCP detector. Even though this design is desirable for VMI

applications, the small vertical dimension of our vacuum chamber and the fixed horizontal distance of the curved mirrors of the fsEC dictated strict space limitations. Thus, the development of a novel compact and shielded VMI setup for intra-cavity use was required, as shown in Figure 4.36.

Electrostatic shielding is essential because we aim to study low-energy electrons, which are strongly influenced by electric potentials. Furthermore, electromagnetic waves are a concern if no shielding is applied. A central goal for the VMI design is a versatile spectrometer platform, which can be extended in the future. Therefore, we use a stack of thirteen electrodes instead of only three and a flight tube, which enables a large control over the imaging capabilities of the setup by shaping the potential landscape inside the spectrometer. This method has been shown to improve the spectrometer resolution and increase the maximum attainable energy [470–475].

For future upgrades and modifications, the platform should provide the option to exchange the standard electrodes with other components, such as an electrode with integrated gas injection [476] or a compact einzel-lens deflector [477]. Furthermore, the setup is designed to accommodate a probe holder for specimens, such as nano-tips. These can be utilized as a probe for the standing light field of counter-propagating pulses in the cavity focus, as shown in Section 4.6.2. The whole system needs to be motorized in three translational degrees of freedom to align the gas jet, or any other target, to the fixed cavity focus.

4.4.2 Electron optics

For intra-cavity VMI operation, the distance between the curved focusing mirrors limits the spectrometer dimensions, which in our case is 125 mm. Additionally, compact XYZ-manipulators for UHV conditions are limited to low loads. To achieve a low-weight setup, we designed a self-supporting electrode stack made from aluminum that is compact enough to fit between the cavity focusing mirrors.

The weight of the upper electrode stack, without connections, shielding and detector is 0.65 kg; the weight of all moving parts is 2 kg, and the weight of the whole assembly amounts to 3.5 kg. The maximum weight of the moving parts is limited by the 22 N load capacity of the vertical alignment actuator (Newport, 8301-UHV Picomotor). Linear translation stages (custom UHV-compatible version of Newport 9062-COM-M) equipped with these actuators are integrated in the setup. Aluminum offers the advantage of being a non-ferromagnetic, lightweight, and strong material, which is well-machinable. The major disadvantage of aluminum is the formation of a non-conductive Al_2O_3 oxide layer, which leads to surface potentials [478], which can be mitigated by gold plating the electrodes. For this, all electrodes are completely copper-electroplated with a thickness of 3 μm. Because of the high material price of gold, the electrodes are only silver- and gold-electroplated on the inside of the spectrometer with a layer thickness of 10 μm and 3.5 μm, respectively.

The inner diameter and height of the electrodes vary along the TOF axis, as shown in Figure 4.36 and 4.37. The electrode dimensions of the spectrometer are optimized with electron trajectory simulations. The repeller and extractor (E0 and E1) electrodes are spaced 10 mm apart to allow access for the focused laser beam. Furthermore, collimated laser beams of the VMI and HHG cavity pass closely, as shown in Figure 3.7. The inner diameter of E1 is 16 mm, with a thickness of 1 mm and a distance of 6.5 mm to the ground electrode E2, which has an inner diameter of 20 mm, gradually increasing to 40 mm to match the size of E3 and E4. The inner diameter of E4 increases to 60 mm, the same as E5 to E11. At E12, the inner diameter tapers to 48 mm, which is slightly larger than the 44 mm diameter of the active area of the MCP. The distance between E0 and the front plate of the MCP is 101 mm, and the outer diameter of the electrode stack is 80 mm.

Ceramic spheres (Al_2O_3) are used to align and stack the electrodes, as visualized in Figure 4.37
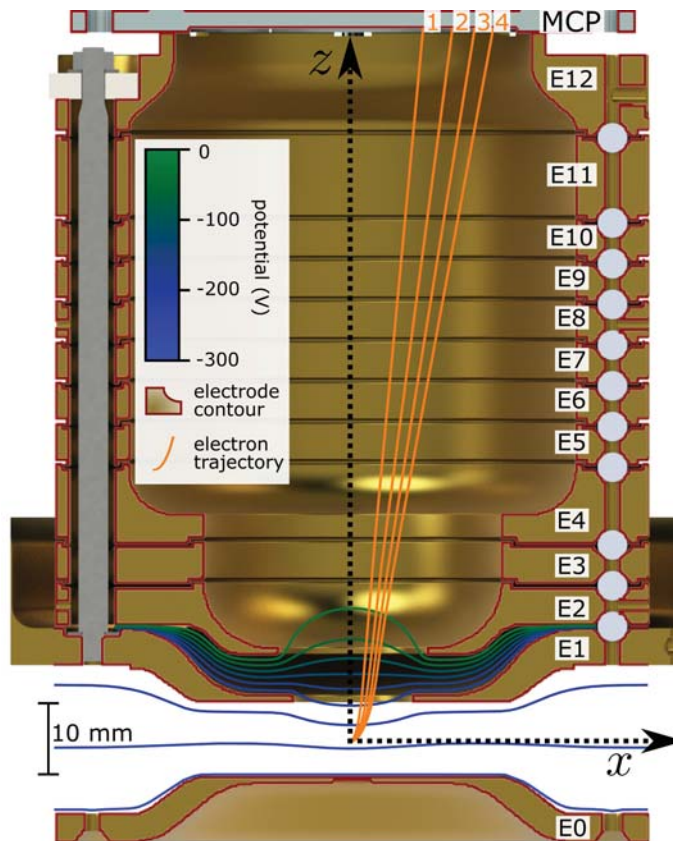
Figure 4.37: Section view of the VMI electrode stack with overlaid exemplary electron trajectories. The electrode contours used in the simulations are drawn in dark red and trajectories of four electrons ionized in x direction with energies of 1, 2, 3 and 4 photon energies ($\hbar\omega \approx 1.2\,\text{eV}$) are drawn in orange and labeled accordingly. Equipotential lines resulting from the applied voltages are indicated in green and blue color. The electrode number (E0 at −300 V, E1 at −221 V and E2 to E12 at ground potential) and the MCP-detector are labeled in black. The coordinate axes are drawn as dashed arrows with the interaction region as the origin. Reproduced from [469], with the permission of AIP Publishing.

and Figure 4.39 ii). V-shaped grooves are machined into the upper and lower surfaces of the electrodes on a lathe with high precision and reproducibility. Three spheres are inserted between two adjacent electrodes, touching on a point on both surfaces of the V-shaped grooves, thus defining the distance and orientation between the electrode pair. A hole drilled at each ball position ensures angular alignment. However, the holes are slightly oversized to allow for some play of the spheres in angular direction to avoid over-defining the assembly. The electrodes are within RZ 16 surface roughness tolerances. After electroplating (Drollinger Metallveredelungswerke), the electrodes are cleaned in a heated ultrasonic bath in citric acid to remove the oxidation layer from the copper.

The electrode stack is held together by three titanium rods, which are screwed into the lower electrode (extractor electrode E1, as shown in Figure 4.37). At the top, a ceramic insulator ensures no electrical contact is made between the rod and the upper electrode (E12). At the same time, it is tensioned with a nut to press the whole electrode stack together. A creepage distance of 2.8 mm on the ball surface ensures a sufficient path length to allow for inter-electrode voltages of ∼5 kV. Electrodes are shaped such that they overlap for shielding against stray electric fields. The nested structure of the cylindrical electrodes, with a minimum electrode-electrode

distance of 0.5 mm, ensures that the line of sight from the inside of the spectrometer is shielded from the outside, the insulating balls, the tensioning rods, and the electrical connections. Simulations confirmed voltages outside the electrodes in the range of tens of kV do not influence the trajectories of low energy ($\approx$ 1 eV) electrons significantly. All electrodes are connected by 1 mm diameter Kapton insulated copper wires, specified up to 10 kV, which are bundled and guided from the top of the assembly to SHV vacuum feedthroughs.

4.4.3 Electron-trajectory simulations

The total experimentally realizable resolution of the system depends, besides the MCP pitch and pore size and the resolution of the data acquisition camera, on the geometry of the VMI setup itself. Non-ideal parallel projections inside the VMI spectrometer lead to larger spot sizes on the detector. We used SIMION (Version 8.1.3.9) to simulate electron trajectories during the design process of the VMI. The ionization region is set to be a sphere with a variable radius. This sphere is centered on the spectrometer axis at half the distance between the two lowest electrodes. The electrode contours used in the simulations, as well as equipotential lines and exemplary electron trajectories, are shown in Figure 4.37. For these trajectories, we assume a maximum electron kinetic energy of four near-infrared photon energies (i.e. $E_{e,max} = 4.73$ eV; $v_{max} = 1290$ mm μs^{-1}) and a repeller voltage of $U_R = -300$ V. These are typical values for our MPI experiments.

For ideal parallel projections, all electrons with the same initial perpendicular velocity vector components v_x and v_y, shall arrive at the same detector position irrespective of their parallel components v_z along the spectrometer axis. Therefore, the initial velocity distribution consists of 15 different groups with each $N = 2000$ electrons and discretely spaced v_x. We limit v_z to the maximum of $|v_x|$. It is sufficient to test the setup for a single value of $v_y = 0$, as the setup is rotationally symmetric around the spectrometer axis (i.e. $x = 0$, $y = 0$). This is a more realistic initial electron momentum distribution, shown in Figure 4.38 b) in blue, compared to what was used in the early days of VMI [136], marked with red dots. It leads to a better estimate of the actual energy and momentum resolution of the VMI. At perfect focusing, we expect 15 discrete spots for each group of v_x. However, imperfections lead to scattering around the mean detector position $\langle x \rangle$, which is quantified by the standard deviation of the electron detector hit positions σ_x.

The repeller voltage U_R is selected such that the total detector size is utilized for imaging. The optimal repeller to extractor voltage ratio is found to be $U_E/U_R = -221$ V/-300 V $= 0.738$, while variations of the voltage ratio of 1 % result in a change of σ_x of only 1.5 μm. We plot the detector image after propagation of the initial electron momentum distribution through the spectrometer in Figure 4.38 a). The focus sizes in radial and azimuthal directions are quantified as σ_x and σ_y, respectively. The time of flight of the electron bunches from ionization until they hit the detector is 12.5 ns with a standard deviation of 0.4 ns. Figure 4.38 c) shows the resolution of the VMI as a function of the radial detector position. The radial spot size (in this case: σ_x) first increases for a larger initial v_x and then slowly decreases again. At the same time, the azimuthal spread (quantified by σ_y) is always better than the MCP resolution (12 μm channel pitch). For the outermost bunch with maximum $|v_x|$, the spread of parallel components $|v_z|$ is minimal, and thus, all particles arrive at the detector within a small spot.

To study the influence of the size of the interaction region on the VMI resolution, electron bunches starting with equal momentum, but varying sizes of the spherical source are propagated. A source diameter of 50 μm is assumed for the results shown in Figure 4.38 a) - c), which corresponds to twice the laser beam waist radius at the focus. Even though this is a reasonable estimate for the source size perpendicular to the laser beam propagation axis, it can be significantly larger along the axis. The energy resolution does not only depend on the source size but
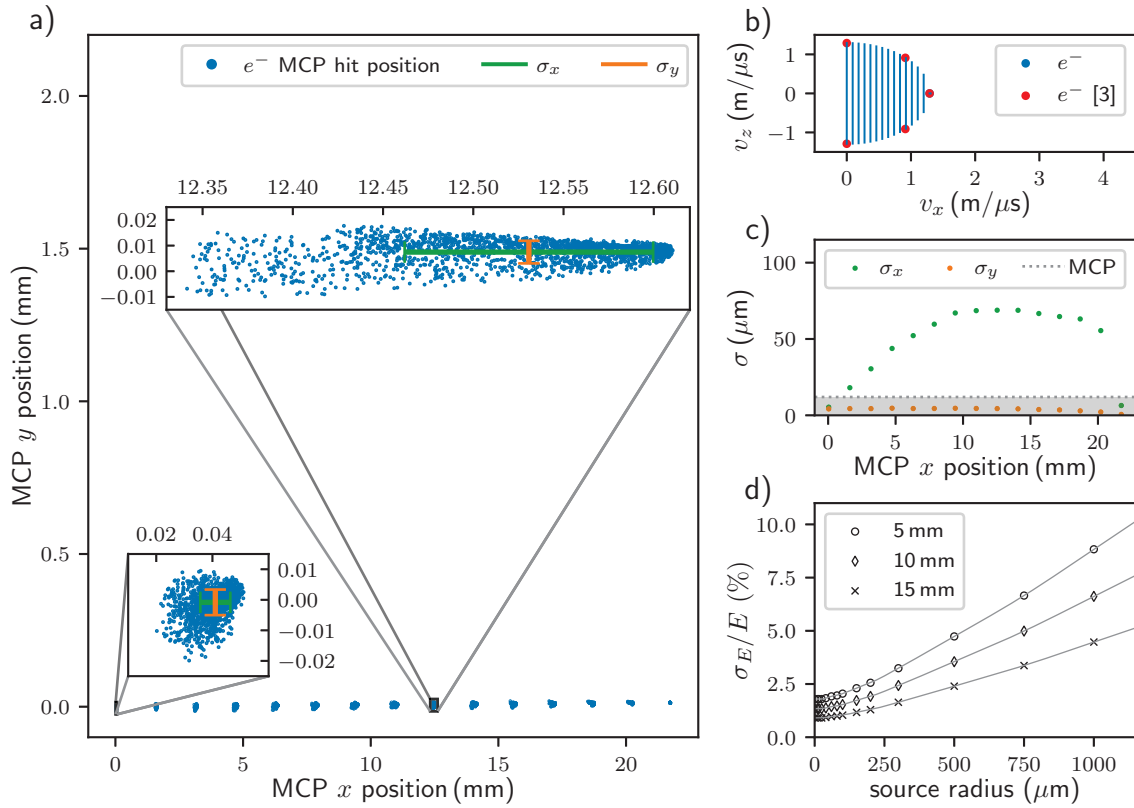
Figure 4.38: SIMION performance simulations for the optimal voltage ratio of $U_E/U_R = 0.738$ of repeller and extractor electrode voltages to demonstrate the focusing capabilities of the VMI spectrometer. a) We characterize the focused size of the electrons on the MCP after propagation through the VMI by the standard deviations σ_x and σ_y. b) The initial electron momentum distribution used for the simulations is shown in blue. In contrast to the first VMI design by Eppink and Parker [136], where discrete vertical velocities were used to determine the resolution (red dots), we utilized 15 groups with $v_y = 0$ and discretely spaced v_x, which are quasi-continuous in v_z. c) The imaging quality of the VMI spectrometer is mainly determined by σ_x of the photoelectrons. In contrast, σ_y is always better than the MCP resolution, which is indicated by the grey shaded area. d) The relative electron energy resolution σ_E/E of the VMI spectrometer depends on the source size and is shown for three radial detector positions. It is optimal for the outer parts of the detector and typically better than 2 % for source radii below 100 µm. Reproduced from [469], with the permission of AIP Publishing.

also on the radial detector position for a given U_R and U_E/U_R. This is taken into account for the determination of the relative energy resolution, shown in Figure 4.38 d) for radial detector positions $r = 5$, 10 and 15 mm. For fixed electrode voltages, these positions correspond to energies of 1, 4 and 9 eV at a maximum detectable electron energy at the outer edge of the detector of ~20 eV, following the relation $r \propto \sqrt{E_e/U_R}$. We use the standard deviation σ_E to define the relative energy resolution σ_E/E, which is twice the value of the momentum resolution.

For our current laser parameters and assuming eleventh-order nonlinearities (I^{11}), the interaction volume can reach a length of up to ~1 mm. Under these conditions and without any assumptions for the extent of the gas target, we expect an energy resolution of about $\sigma_E/E = 3\,\%$, limited mainly by the size along the laser beam propagation axis. The resolution could be significantly improved by shrinking the width of the gas jet (as discussed in Section 4.4.6) or by using counter-propagating pulses that collide at the focal point, which would reduce the interaction volume to a sphere with a diameter of about 50 μm and improve the resolution to below 2 %. A lower limit for the achievable resolution is the spectral bandwidth of the laser, which in our case is ~1 %. By increasing the repeller voltage to −5 kV at constant U_E/U_R, it is possible to image electrons with kinetic energies up to 105 eV without any noticeable change in (relative) energy resolution.

4.4.4 Magnetic shielding

For both providing magnetic and improving electrostatic shielding, a μ-metal (Aaronia MagnoShield DUR panel) shield with a thickness of 0.5 mm encloses the whole upper electrode stack. At the top, a cable guide and a tube surrounding the MCP detector, both made of μ-metal, protrude into the vacuum chamber to keep magnetic fields away from the VMI interior. To restore the high permeability of the μ-metal shielding after machining and welding, all parts were annealed in vacuum at 1050 °C for three hours and then slowly cooled down to room temperature over the course of ten hours. The magnetic shielding performance is experimentally evaluated by placing a strong permanent magnet in close vicinity to the setup and measuring the magnetic field at the center point of the assembly with and without the μ-metal enclosure. The annealed μ-metal shield reduced the magnetic field inside the VMI by a factor of ~270. The annealing process improved the shielding by a factor of 15 compared to the shielding performance directly after machining.

4.4.5 Imaging electron and ion detector

An MCP detector in Chevron configuration (TOPAG, MCPD-50-C-P), equipped with a P43 phosphor screen, is used for electron/ion detection. The active area has a diameter of 44 mm with a channel diameter and pitch of 10 μm and 12 μm, respectively. The front plate of the metallic detector frame is conductively mounted directly on the uppermost electrode. This avoids non-conducting or high voltage parts in line of sight to the inside of the VMI setup causing image distortions. The fluorescent phosphor screen is imaged through a vacuum window with an air-side camera (Allied Vision, Mako G-234B mono), and the raw images are stored on a computer for further analysis. A photograph of the assembled VMI spectrometer, before installing the electrical connections, the MCP detector, and the shielding, is depicted in Figure 4.39.

4.4.6 Gas target for VMI studies

The VMI spectrometer is mounted together with the cavity optics inside the main vacuum chamber, as described in Section 4.1 and shown in Figure 3.7. A pressure of up to 7×10^{-6} mbar is reached during gas injection, which corresponds to the maximum pressure the MCP detector
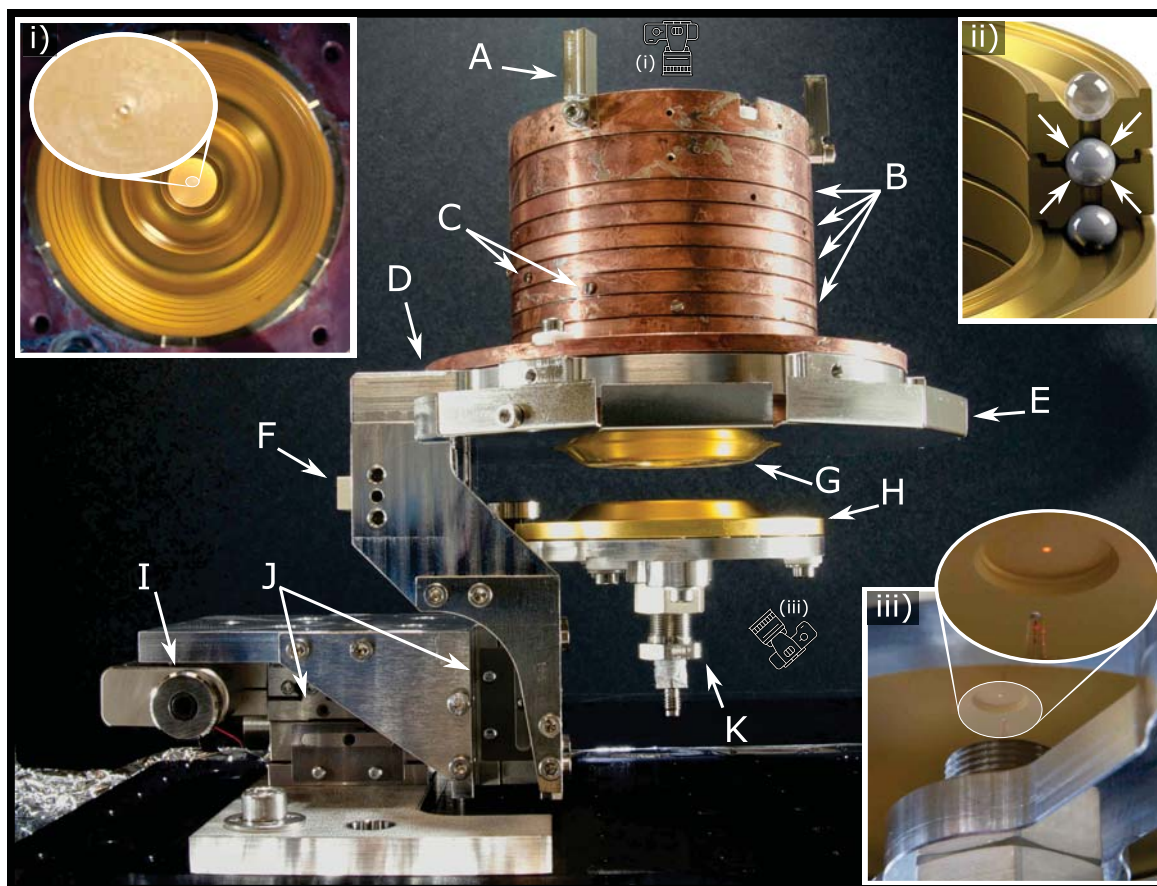
Figure 4.39: Photograph of the VMI setup stripped of MCP, gas supply, electrical connections, and the upper part of the μ-metal shielding, viewed in the direction of laser propagation. A: holder for the μ-metal shielding, B: electrode stack, C: screws for electrical connection, D: mounting brace of the electrode stack and upper part of extractor electrode E1, E: lower part of μ-metal shielding attached to the extractor electrode, F: PEEK mounting adapter for the nano-tip holder (not shown here, cf. Figure 4.46), G: lower part of the extractor electrode, H: repeller electrode E0, I: piezo motor, J: translation stages for XYZ-movement and K: nozzle holder with gas connector. i) Top view with zoomed inset of the lowest electrode (repeller) with a 100 μm diameter hole, from where the gas, injected by a 50 μm diameter nozzle 4 mm below the electrode, enters the target region. ii) Detail view of the electrodes and ceramic spheres used as spacers. They rest on V-shaped grooves on the electrodes, as marked by the white arrows. Vertical bores restrain the motion of each of the three balls between each electrode pair but do not over-define the assembly. Overlapping of the electrodes enhances electrostatic shielding. The upper sphere is shown translucently for clarity. iii) View from below the lowest electrode (repeller E0) with the gas nozzle pointing upwards. A red laser pointer pointing downwards along the spectrometer axis from above the electrode stack illuminates the nozzle tip during the alignment procedure. A zoomed inset shows the nozzle and the hole in more detail. For drilling the 100 μm hole, material was removed from the bottom side such that the residual electrode material was thin enough for the drill bit. Reproduced from [469], with the permission of AIP Publishing.

can be operated at without damage. The pressure is measured with a vacuum gauge located 0.5 m away from the pump inlet.

The repeller electrode (E0) has a hole with a diameter of $b = 100\,\mu m$ drilled through in the center, as shown in Figure 4.39 i). A gas nozzle with an opening diameter of $50\,\mu m$ is placed $d = 4\,mm$ below the electrode. Axial alignment of the nozzle is ensured upon assembly by a red laser pointing downwards, illuminating the nozzle tip through the hole in the electrode, as shown in Figure 4.39 iii). This procedure ensures that as much gas as possible from the vertical gas jet passes through the hole in the electrode. The pressure in the chamber assures operation in the free molecular flow regime, implying that the small hole effectively serves as a skimmer to collimate the expanding gas cloud. The terminal velocity of the gas injected by the gas nozzle into the chamber can be calculated by [408]

$$v_\infty = \sqrt{\frac{2R}{W}\left(\frac{\gamma}{\gamma - 1}\right)(T_0 - T)}, \tag{4.22}$$

with the molar gas constant R, the atomic weight W, and $\gamma = (f + 2)/f$, where f is the number of degrees of freedom of the molecular motion (i.e. $\gamma = 5/3$ for monoatomic gases). T_0 is the initial temperature before expansion, and T is the temperature after expansion, approximated by $T \approx 0$. For xenon gas expanding from room temperature, this corresponds to a maximum terminal velocity of $\sim 305\,\mathrm{m\,s^{-1}}$. The Doppler width of a transition in a gas jet atom moving with velocity v is given by

$$\Delta\nu_\mathrm{D}(\mathrm{FWHM}) = 2\nu_0(v/c)\sqrt{\ln 2}, \tag{4.23}$$

for a transition center frequency ν_0 and the speed of light c. The collimation of the gas jet by the electrode hole leads to a reduction of Doppler broadening at our central wavelength of 1039 nm from approximately 500 MHz to 6 MHz for xenon because the Doppler width scales according to the collimation factor [479] $b/(2d) = 0.0125$. Provided that our laser spectrum covers a sufficiently narrow transition of a gas jet atom, we could resolve it by direct frequency-comb spectroscopy [39] with a 100 MHz comb tooth spacing. However, we have yet to measure the target gas velocity and collimation experimentally. Even though we operate the whole system in the free molecular flow regime, a higher local pressure below the repeller electrode might lead to backscattering. To investigate if this is the case, we plan to assess the quality of the gas sample using ion spatial imaging.

It is possible to increase the target density at the cost of sacrificing the reduction in Doppler width by exchanging the repeller electrode with an electrode with an integrated gas nozzle [476].

4.5 Intra-cavity xenon multiphoton ionization

In a first experiment, we use our compact VMI system for intra-cavity photoionization of xenon to demonstrate the performance under real experimental conditions. The description of the experiments follows our recent publication [469]. For technical reasons, we had to operate the enhancement cavity in scan mode, which means the cavity length is scanned over the resonance, where maximum enhancement is achieved. Compared to continuous resonant operation, this reduces the time the cavity is actually resonant and photoelectrons are emitted. The cavity was scanned at a frequency of 460 Hz across the resonance, resulting in an effective duty cycle of 2.3 %. This fraction of time corresponds to 99.6 % of the total photoelectron yield. The maximum intra-cavity peak intensity in the focus region is calculated from the measured temporal pulse shape, the focus size and the photodiode signal of the leakage through one of the cavity mirrors. At cavity resonance, xenon atoms are ionized above threshold in the cavity focus.

When xenon is ionized from the outer orbital, the generated Xe^+ can be either in the ground state $Xe^+(^2P_{3/2})$ with $I_p = 12.13$ eV or in the first excited state $Xe^+(^2P_{1/2})$ with $I_p = 13.44$ eV. However, ionization to the latter is very unlikely for our laser wavelength [260].

4.5.1 Angularly integrated photoelectron spectra

To record xenon PADs with subsequent Abel inversion, the laser polarization is set parallel to the detector. Photoelectrons are imaged onto the MCP detector and recorded with the camera. 74 raw images with an exposure time of 5 s are dark-frame corrected and hot pixels are removed. Then, the images are overlaid with a vertically mirrored copy of themselves since the sensitivity of the MCP detector, unfortunately, changes from the upper to the lower half of the image, causing one half of the raw images to appear darker. From the raw images, we estimate that the circularity differs from perfect circles only on the sub-percent level, and no circularization or other more advanced image processing steps are needed. The sum of the dark-frame corrected original images and the central slice after Abel inversion are depicted in Figure 4.41 for various laser intensities.

As described in Section 2.5.2, the energy of the photoelectrons at a given laser intensity after absorption of n photons is given by $E_e = n\hbar\omega - (I_p + U_p)$, where I_p is the ionization potential of the atom and U_p is the ponderomotive energy shift induced by the laser field. Not only does the ionization threshold shift ponderomotively but also Rydberg states shift and can become resonant, which results in Freeman resonances in the photoelectron energy spectrum [256].

Starting at relatively low intensities, the simultaneous absorption of eleven near-infrared photons is sufficient to overcome the ionization potential of xenon. When increasing the intensity above 1×10^{13} W cm^{-2}, the combined energy of eleven photons is not sufficient anymore, and twelve photons become necessary (cf. Section 2.5.2).

MPI of xenon at a laser peak intensity of approximately 1.6×10^{13} W cm^{-2} is shown in Figure 4.40 d). At this intensity, sharp features originating from Freeman resonances are visible in the detector and Abel inverted images. Eleven photons of the NIR frequency comb are resonant with the xenon $5p^5(^2P_{3/2})5g$ state, and absorption of an additional photon leads to the first ATI ring. More details on the method of determining resonances are presented in Section 4.5.2, where tomographic reconstruction is carried out at low intensity.

Angular integration of the Abel images, such as the ones shown in Figure 4.40 a) - d), yields the photoelectron momentum distribution for each intensity. The detector is calibrated by fitting the ATI peak positions to a quadratic function assuming zero momentum in the center and an $\hbar\omega$ energy spacing of the rings, yielding the momentum and energy scale as a function of radial detector position.
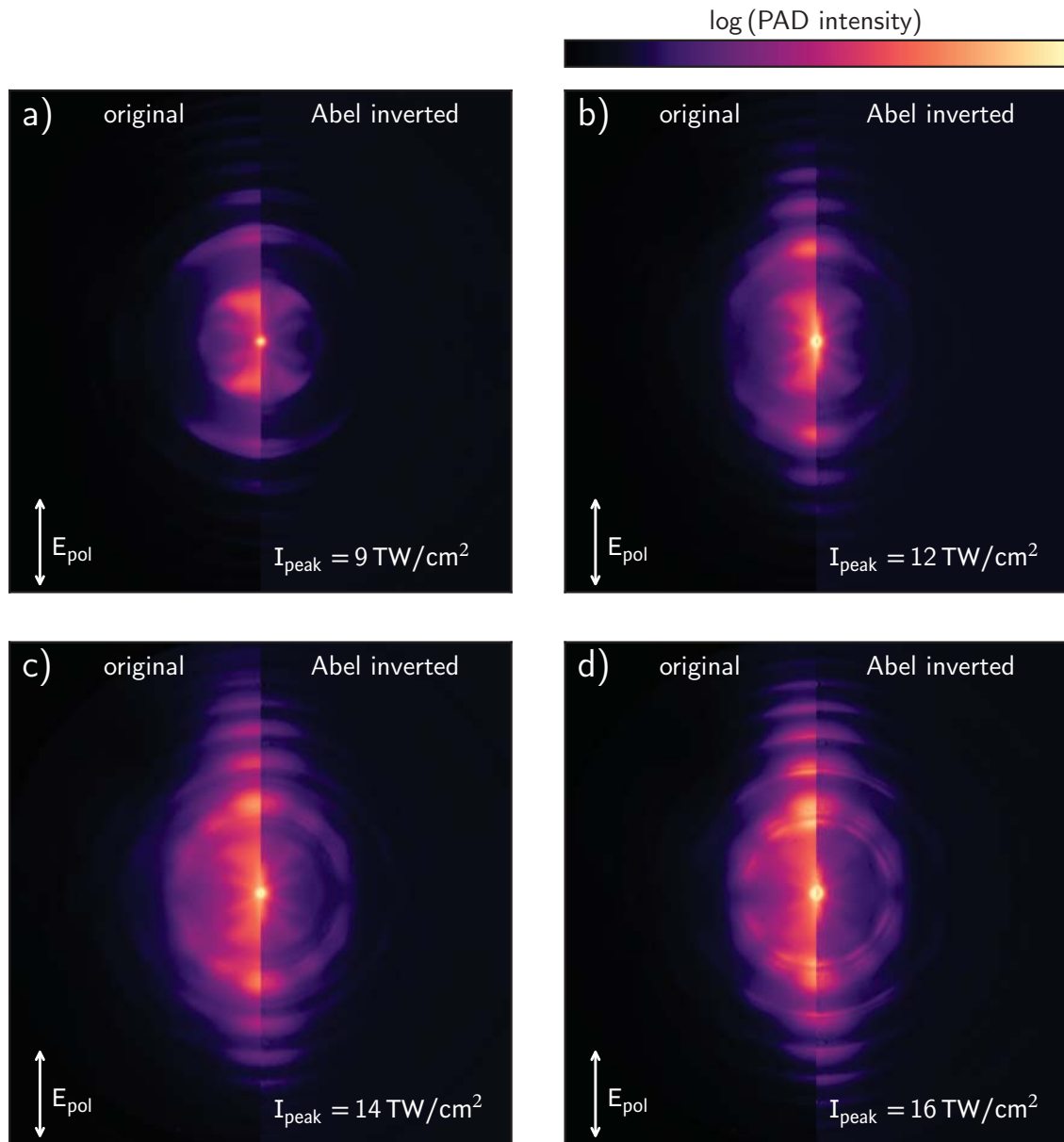
Figure 4.40: Detector images of the VMI spectrometer show 2D projections of photoelectrons from xenon MPI before (left half) and after (right half) Abel inversion for various laser intensities between 9×10^{12} W cm^{-2} and 16×10^{12} W cm^{-2}. While in a) - c) no distinct resonances are visible, sharp features originating from Freeman resonances are imprinted on the detector image shown in d). More details in Figure 4.41 and the main text.
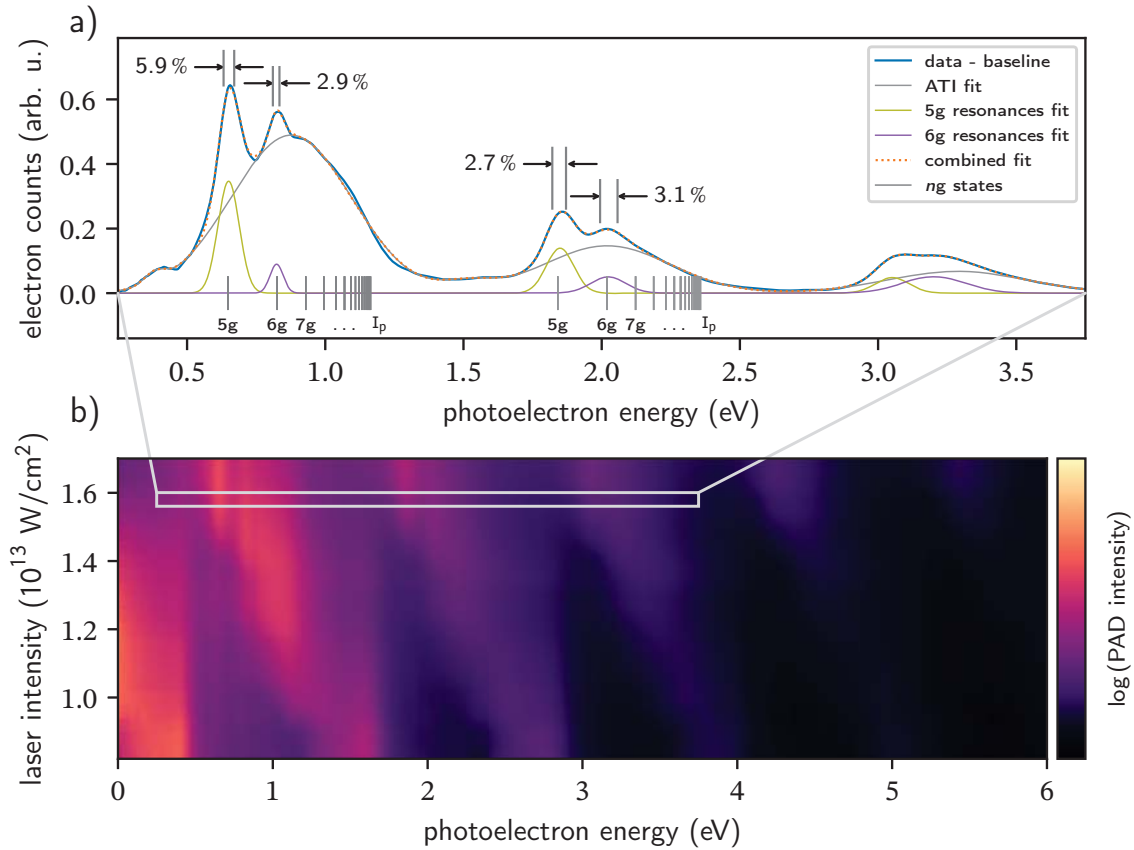
Figure 4.41: a) Section of the photoelectron energy spectrum retrieved from the Abel-inverted image shown in Figure 4.40 d) by angular integration. Resonances are fitted as described in the text. The most prominent features originating from the 5*g* and 6*g* resonances are drawn separately for illustration and their relative energy widths are given. b) The photoelectron energy spectrum is modified due to the ponderomotive shift of the xenon ionization potential, appearing as an angled pattern. At $\sim 1 \times 10^{13}$ W cm^{-2}, the ionization channel with eleven photons closes, and twelve photons become necessary for ionization. However, this ionization channel does not close abruptly because intensities below the peak intensity are still present in the focus region. Narrow vertical features originate from Freeman resonances. At a laser intensity of $\sim 1.5 \times 10^{13}$ W cm^{-2}, the $5p^5(^2P_{3/2})5g$ resonance can be reached by eleven photons and absorption of an additional photon leads to the first ATI ring.

Figure 4.41 b) shows the photoelectron spectrum as a function of laser intensity. The xenon ionization potential is shifted ponderomotively, appearing as angled features. At $\sim 1 \times 10^{13}\,\mathrm{W\,cm^{-2}}$, the ionization channel with eleven photons closes, and twelve photons become necessary for ionization. However, this closing of the eleven-photon and opening of the twelve-photon ionization channel is gradual. Due to the spatial laser beam profile, the temporal pulse shape, and the scan-mode operation of the cavity, all intensities up to the peak intensity are still present in the focus region and contribute to ionization. Therefore, at positions or times with lower intensity than the peak intensity, ionization via the eleven-photon channel still occurs and contributes to the signal. Vertical, narrow features originate from photoelectrons that are ionized from resonant states. Their position does not shift in the photoelectron spectrum because resonances are reached only at fixed laser intensities; thus, the electron energy is always constant. The width of these features depends on the linewidth of the transition and the spectral width of the laser.

Figure 4.41 a) shows the photoelectron energy spectrum obtained from the detector image of Figure 4.40 d), after correction by an exponential baseline, as well as the expected $5p^5(^2P_{3/2})ng$ level positions for the first and second ATI peak. The electron spectrum is fitted with a model composed of Gaussians accounting for the well-resolved resonances added on top of larger Gaussians. It takes the overall structure of the ATI peaks into account, which consists of poorly separated narrow features and non-resonant contributions. The fits of the most prominent features originating from the $5g$ and $6g$ resonances are drawn separately for illustration. Faint peaks at approximately 0.4 eV and 1.6 eV are expected to come from the nine-photon resonant $5p^5(^2P_{3/2})5d$-state at lower intensity levels and are included in the fit model. Standard deviations of the $5g$ and $6g$ resonances are extracted, and their relative values σ_E/E are stated. These values are considered a reasonable estimate of the actual energy resolution reached in the experiment. It means that the relative energy resolution of the VMI spectrometer is in the range of about 3 %. This value is in good agreement with the simulations presented in Section 4.4.3 and represents a significant improvement in comparison to our previous setup [129] for which we estimate an energy resolution of not better than 10 %.

Note that in some other works, the relative energy resolution is given as the ratio of total energy and FWHM, while we use the standard deviation of the Gaussian distribution fit instead [136, 470–472, 475]. Currently, the resolution of our compact spectrometer is about ten times lower than that of larger, established instruments [470, 475]. However, we can implement a well-collimated supersonic gas jet in the horizontal plane to shorten the length of the interaction region to improve it. Operating the cavity with counter-propagating pulses will reduce the effective target length in the propagation direction to a value similar to the beam waist, given the 184 fs pulse duration and the nonlinearity of the multiphoton processes.

4.5.2 Intra-cavity tomography of xenon PADs at low laser intensity

In order to perform photoelectron tomography, the experimental method that was used to produce Abel inverted photoelectron images had to be modified since many projections of the 3D PADs are to be recorded from various angles. As a result, the laser polarization is rotated around the beam propagation axis. Figure 4.42 schematically shows the experimental setup and the data acquisition and tomographic reconstruction method. The Nyquist-Shannon sampling theorem and simulations suggest that the number of recorded angles should be similar to the number of x and y pixels of the detector [244]. Experimentally, we rotate the polarization using an AR-coated zero-order half-wave plate (B. Halle Nachfl. GmbH) mounted in a motorized rotation mount (Thorlabs, PRM1/MZ8) in steps of 1° between 0° to 89°, which corresponds to a polarization rotation step size of $\theta = 2°$. This is sufficient because after a polarization change of 180°, the initial polarization is restored, and the electric field is essentially the same. This may not necessarily be the case for few-cycle pulses with stabilized CEP. In the case of electron photoemission
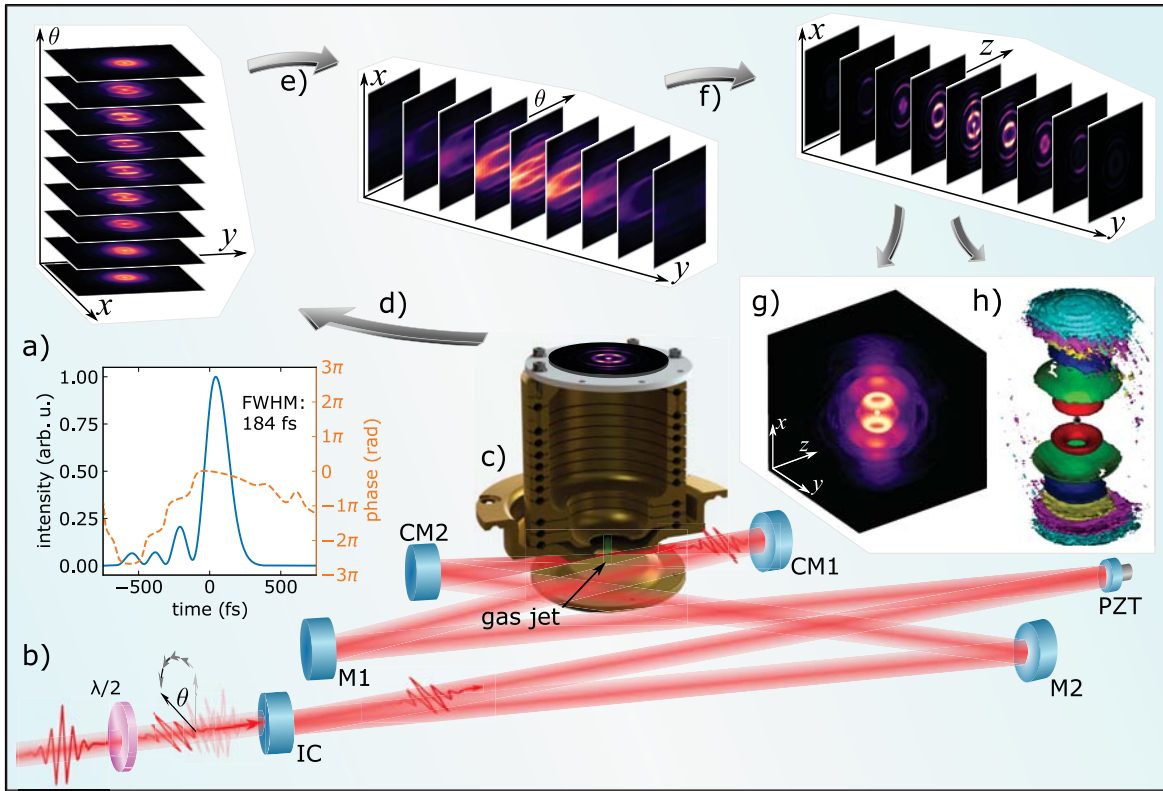
Figure 4.42: Schematic overview of the experimental setup and the tomographic method. a) Femtosecond pulses with a pulse duration of 184 fs, determined by a FROG measurement, b) are fed into the VMI cavity at a repetition rate of 100 MHz. To perform tomography, the polarization is rotated by θ between each acquisition step with a motorized half-wave plate ($\lambda/2$) before the input coupler mirror (IC). The light is focused by two curved mirrors (CM1, CM2), and a piezo-actuated mirror (PZT) is used to adjust the cavity length. Two additional flat mirrors (M1, M2) are used to fold the cavity to reduce the outer dimensions. c) Atoms from the gas jet are ionized by the laser pulses in the cavity focus and PADs are mapped on the MCP detector by the VMI spectrometer. d) Detector images are recorded for each polarization angle θ and stacked together into a single array. e) Slices of this array (the sinograms) are extracted for each y-pixel, f) reconstructed by filtered back-projection (FBP) one by one, and stacked to a 3D array, yielding the reconstructed 3D PAD, as described in Section 2.4.2. The 3D PAD are visualized either as a g) maximum intensity projection plot or an h) isosurface plot. The individual ATI-shells are identified and highlighted in different colors (in rising order: gray, red, green, blue, yellow, purple, cyan). Note that, compared to g), some details are lost due to the restriction of one iso-value per shell. Reproduced from [469], with the permission of AIP Publishing.

from metallic nanostructures, CEP effects become important [480, 481] and require a 360° polarization rotation to restore the initial electric field. Even though we typically lock the CEO of our frequency comb to 20 MHz, these CEO effects are not a concern for the 50-cycle pulses of our laser.

To demonstrate the feasibility of performing photoelectron tomography even at relatively low intensities, photoelectrons are detected at an intra-cavity peak intensity of $\sim 7.7 \times 10^{12}\,\mathrm{W\,cm^{-2}}$. Photoelectrons are imaged on the MCP detector for each polarization angle θ, as described earlier and schematically shown in Figure 4.42. Camera images are taken with an exposure time of 10 s and corrected as described before. These images are averaged for each angle and reduced in size to 128×128 pixels, the next higher power of two compared to the number of recorded polarization angles. Then, they are stacked together into a single array, and slices of this array (the sinograms) are extracted for each y-pixel.

Tomographic reconstruction of each sinogram is performed using the FBP method that was introduced in Section 2.4.2. After reconstruction, the images are combined to a 3D array and the 3D PAD can be visualized in different ways, either as a maximum intensity projection plot, as shown in Figure 4.42 g), or as an isosurface plot, as shown in Figure 4.42 h). In both representations, ATI rings (i.e. 3D shells) are clearly visible and in the latter, an isosurface for each shell is identified and drawn in a different color (in rising order: gray, red, green, blue, yellow, purple, cyan). Note that some details of the angular structure are lost due to the isosurface representation, but the overall structure with the shells spaced by the photon energy is clearly visualized.

Azimuthal integration of the reconstructed PAD around the polarization symmetry axis (vertical axis in Figure 4.43 a)) yields a single half-image. This half-image is mirrored horizontally, which gives a result similar to the central slice after Abel inversion but retrieved by tomography instead. To indicate the ranges used for radial integration, colored semi-circles are drawn on top of the left side of the image in Figure 4.43 a), with the same color code of the ATI rings as before. These angular distributions of the inner rings are plotted with a vertical offset for clarity as a function of the polar angle φ in Figure 4.43 b), disregarding the outer 10° due to the vertical artifact in the center of the retrieved image.

A clear angular structure is visible in the angular distribution and the signal is not mainly oriented in the laser polarization direction which hints towards resonant ionization [167]. From the maxima and minima of the PADs it is noticeable that the total angular momentum change Δl switches between odd and even values for consecutive rings. The first ATI ring (red) shows four nodes, indicating contributions of partial waves of $l = 4$, suggesting that the electrons originate from an f state, most likely from $5p^5(^2P_{3/2})4f$, from where absorption of a single photon (indicated by the red arrow in Figure 4.43 c)) is sufficient to overcome the ionization potential of $\mathrm{Xe}^+(^2P_{3/2})$. This resonance can be reached by absorbing ten photons from the $5p^6$ ground state at an intensity of $6.8 \times 10^{12}\,\mathrm{W\,cm^{-2}}$ with a total angular momentum change of ($\Delta l = 2$). Even though the $5p^5(^2P_{3/2})8s$ state would be resonant at the same intensity, the required $\Delta l = 1$ cannot be reached by an even number of photons. At lower intensities (approximately $4.5 \times 10^{12}\,\mathrm{W\,cm^{-2}}$), the resonances $5p^5(^2P_{3/2})7d$ and $8p$ are excluded due to a mismatch of the measured photoelectron energy of $0.32\,\hbar\omega$. It is obtained by angular integration of all Abel inverted raw images, where the polarization is parallel to the detector and shown in Figure 4.43 d). The nine-photon resonance $5p^5(^2P_{3/2})5d$ could also be excited at slightly higher or lower intensity levels. The second ring (green) exhibits five nodes ($l = 5$) pointing towards ionization with two photons from the same state. As the first ring, the third ATI ring (blue) shows four nodes, indicating ionization with three photons from the same $5p^5(^2P_{3/2})4f$ state, but with the Δl of the two additional photons canceling each other. The fourth ring (orange) has an additional node compared to the third ring, as expected. The resonant $4f$ state mentioned in the discussion above is marked by a dotted ellipse in Figure 4.43 c). Since xenon exhibits many
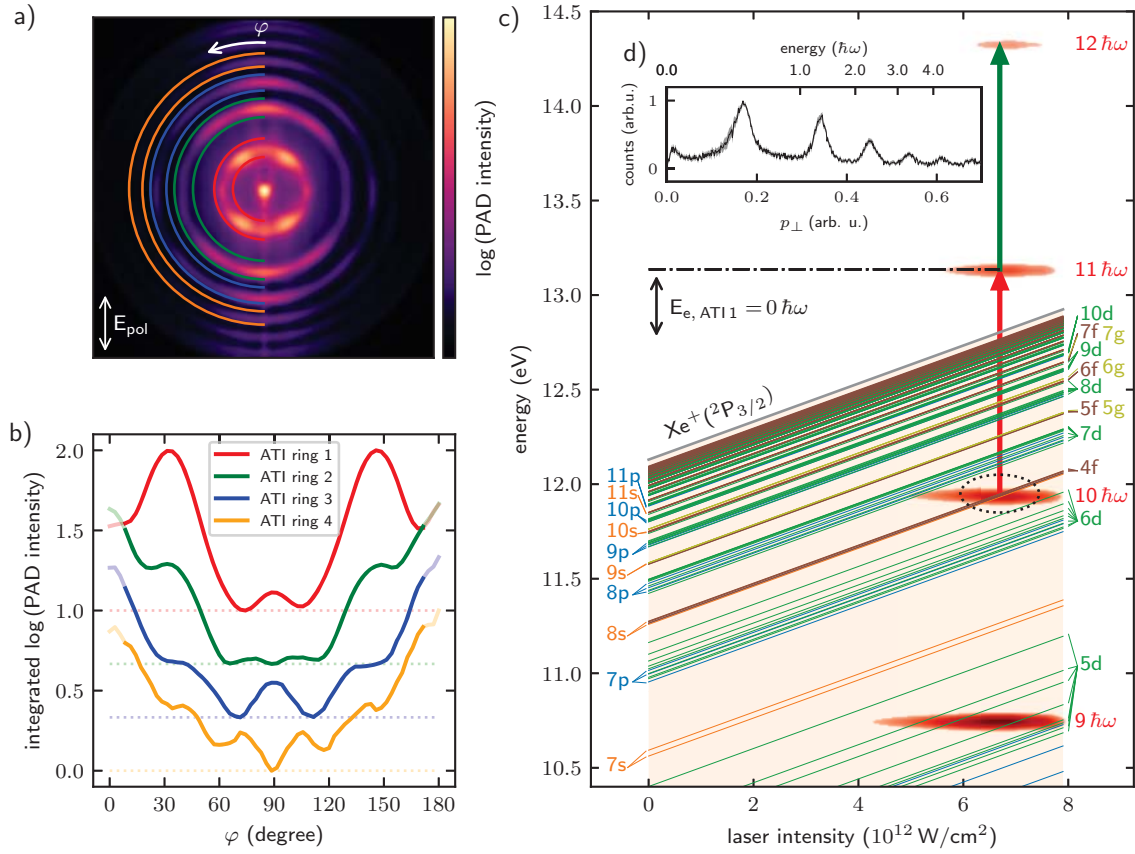
Figure 4.43: a) 2D projection of tomographically reconstructed 3D PADs from MPI of xenon, by azimuthal integration around the polarization symmetry axis (vertical). Integrated photoelectron yields of the first four of total six ATI rings found within the color-coded semi-circles are shown in b) as a function of the polar angle φ with an offset for clarity. c) Rydberg states of xenon shift ponderomotively in the laser field and can become resonant by simultaneous absorption of n photons. Red features labeled with $n\,\hbar\omega$ illustrate the likelihood of an n-photon absorption process in a logarithmic colormap, using the laser intensity distribution and photon multiples of the fundamental spectrum, weighted by the photon number. The most likely resonant $5p^5(^2P_{3/2})4f$ state can be reached by ten photons and is marked by a dotted ellipse. From this state, photoionization by absorption of a photon (red arrow) leads to the first ATI ring and an additional photon (green arrow) causes the second ring and so on. From the photoelectron momentum distribution, shown in inset d), the mean kinetic electron energy $E_{e,\,\mathrm{ATI1}}$ of the first ATI ring is extracted and marked by dashdotted lines. Adapted from [469], with the permission of AIP Publishing.

resonances at the 10th harmonic of our laser frequency, contributions of other (non) resonant ionization pathways cannot be fully excluded.

Due to the operation in scan mode, intensities from zero up to the maximum intensity contribute to the ionization process and the recorded images average over all of these electrons. Therefore, it can be indeed possible to record photoelectrons on the inner rings that also come from ionization at rather low intensities. For the outer rings, these low-intensity pathways are more strongly suppressed because of the higher photon number. At lower laser intensities, also higher-lying Rydberg states shift into resonance, but ionization is much less probable, because the ionization rate scales with I^n, with n being the number of required photons. This highly nonlinear intensity scaling is accounted for in the graphic representation of Figure 4.43 c) by weighting the laser spectrum of each photon multiple with the measured laser intensity distribution to the power of the respective photon number. For better clarity it is drawn in a logarithmic colormap.

Even with the limitation of operating the cavity in scan mode, the electron count rate is in the range of a few kHz and the recording of the complete dataset for tomography took about 12 h. In the future, we will lock the cavity length to the repetition rate of the driving frequency comb for continuous high intensity operation.

Additionally, a repeller electrode with an integrated gas nozzle would increase the target density, and thus the count rate, by orders of magnitude, as described before in Section 4.4.6. As already demonstrated in our previous work [129], we would then expect count rates in the range of a few MHz and exposure times of single images well below one second.

4.6 Counter-propagating pulses

The pulses coupled in both propagation directions of the ring cavity collide at the focus if the propagation distance from the focus to the beam splitter is the same for both paths. This distance of a few meters must be matched to within a few micrometers. By carefully positioning the optics and measuring the length by hand, it is possible to match the propagation distances to within a few millimeters. In principle, it is possible to start from this point by detecting photoelectrons with the VMI spectrometer. Because the underlying processes are (highly) nonlinear, we expect an enormously increased count rate if the pulses meet at the focus. However, this method was not very helpful in finding the initial pulse overlap because even though the electron count rate is relatively high at our repetition rate, the signal fluctuates over time due to the strong intensity dependence of the process, and long measurement times are necessary to probe several millimeters of delay at micrometer resolution.

4.6.1 Determination of the overlap position of counter-propagating pulses

A more practical technique is to exploit the spectral modulation of two time-delayed short pulses. The same idea was already used within the angularly resolved spectral interference technique to characterize the SAD-box in Section 4.2. If two pulses have a time delay of τ, the spectrum is modulated with the frequency $f_{mod} = 1/\tau$. To measure the spectrum of the two interfering pulses at the focus position, a tool is inserted into the VMI spectrometer, as shown in Figure 4.44. A 3 mm right angle prism (PS905, Thorlabs) at the end of the 3D-printed holder reflects a small portion of the incident light from each propagation direction by 90°. The parallel propagating beams are re-focused by a $\varnothing$3 mm, $f = 9$ mm lens into a multi-mode fiber (M53L01, Thorlabs) connected to a spectrometer (Qmini NIR, BROADCOM). The delay τ between the pulses is varied with the air-side translation stage in the SAD-box, and spectra are recorded at each step.
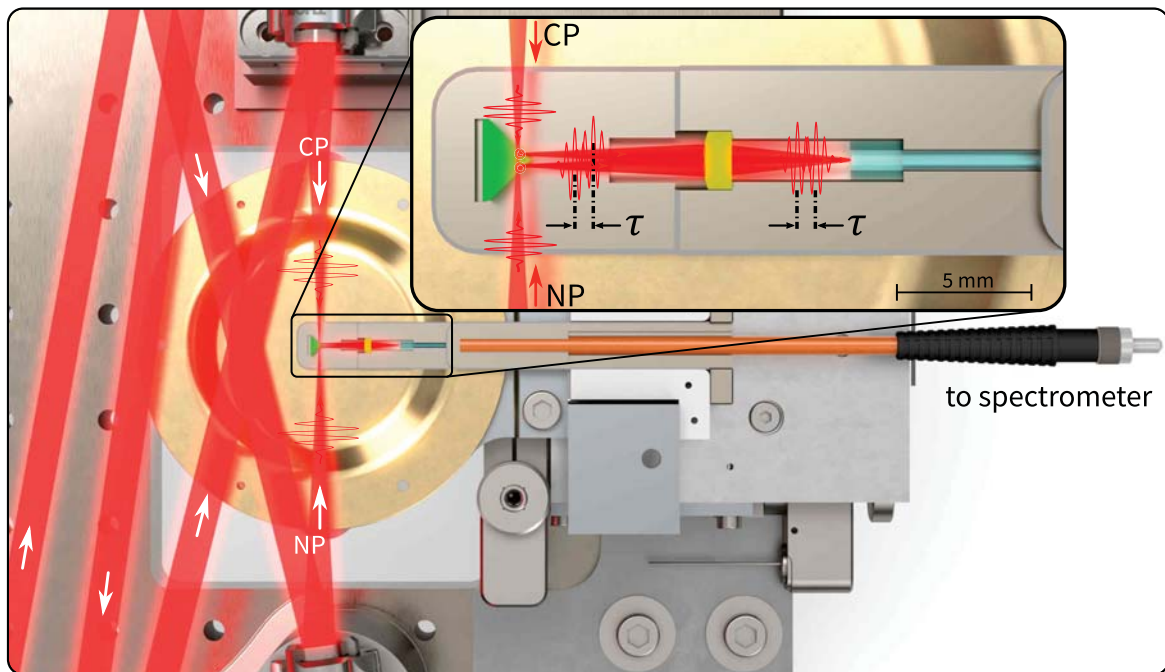
Figure 4.44: Illustration of the method to find the pulse overlap of colliding pulses in the cavity focus. A small prism (green) at the end of a 3D-printed holder is inserted into the VMI spectrometer and redirects a small portion of the incident light from each propagation direction by 90°. A lens (yellow) re-focuses the divergent beams into an optical fiber (blue) connected to an optical spectrometer (not shown). The delay τ between the counter-propagating pulses is scanned with an air-side translation stage, and spectra are recorded at each step.
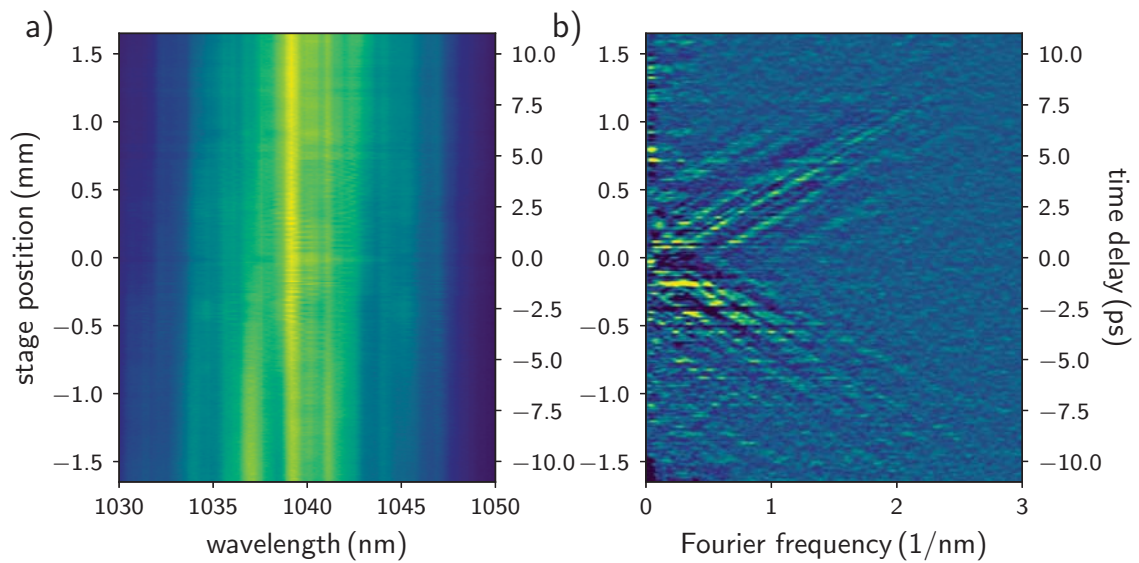
Figure 4.45: The cavity overlap of counter-propagating pulses is found by varying the delay τ between the pulses with a translation stage. As the two delayed pulses reach the spectrometer one after the other, the spectrum is modulated with $1/\tau$. a) A spectrum is recorded at each delay stage position, but no clear sign of the pulse overlap can be seen from the trace itself. b) At every delay stage position, a Fourier transform of a) yields the 'spectrum of the spectrum'. It shows that the modulation in the spectrum changes with the delay stage position, which manifests as the triangular structure that points towards the pulse overlap. At the overlap position, the entire spectrum is modulated as a whole, and either constructive or destructive interference occurs.

The cavity overlap of counter-propagating pulses is found by varying the delay τ and recording spectra at each delay stage position, as shown in Figure 4.45 a), but no clear sign of the pulse overlap can be seen in the trace itself. Note that the absolute zero of the stage position, i.e. the time delay between the pulses, is only known after the overlap has been found. However, by Fourier transforming the spectrum, the 'spectrum of the spectrum' is obtained, as shown in b). It shows the change of spectral modulation as a function of the delay stage position, which manifests as a triangular structure that points towards the pulse overlap. The smaller the time delay of the pulses gets with respect to each other, the larger gets the fraction of the spectrum that is modulated. At the overlap position, the entire spectrum is modulated as a whole, and either constructive or destructive interference occurs. After the overlap had been found, the tool was removed to allow for a first MPI experiment with counter-propagating pulses.

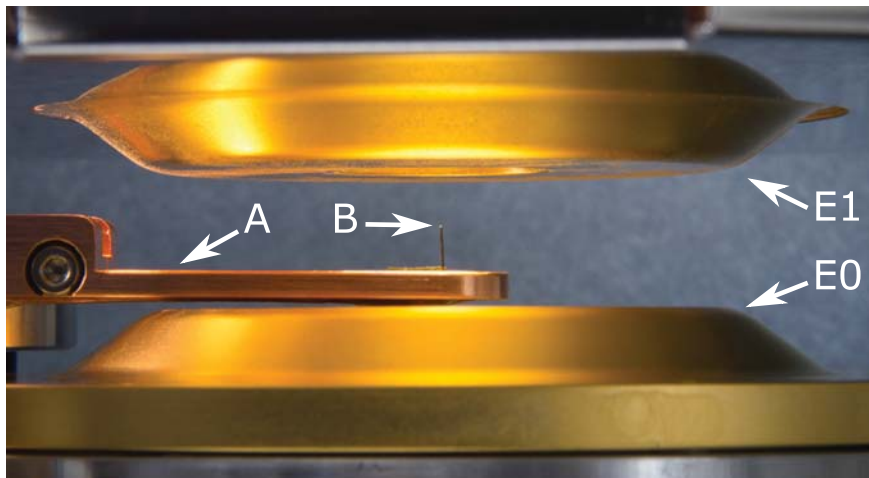### 4.6.2 Probing counter-propagating pulses with a nano-tip

Figure 4.46: Photograph of the VMI setup with a nano-tip inserted between the repeller (E0) and extractor (E1) electrode. Both the copper tip holder (A) and the tungsten nano-tip (B) can be biased independently. Reproduced from [469], with the permission of AIP Publishing.

The modular design of the VMI spectrometer allows the insertion of a sample holder that can be moved into the focus of the cavity. It acts as a second independent lower electrode and is electrically isolated from the individually biasable target. In a first test a nano-tip is inserted into the holder, as shown in Figure 4.46. It allows us to utilize the local field enhancement at the sharp tip [482]. The tip points upwards along the VMI spectrometer axis, making it difficult to fulfill the VMI condition. However, biasing the tip, the tip-mount, and other electrodes of the VMI spectrometer makes it possible to detect photoelectrons in a confined space on the MCP detector. We successfully detected photoemission from the nano-tip during extended intra-cavity operation over many hours without damaging the tip.

In order to probe the intense standing waves in the cavity focus, either the tip can be moved together with the VMI spectrometer using the piezo-driven motors, or the standing wave can be moved with respect to the stationary tip. In a first experiment, we move the standing wave using the same delay stage used in the previous subsection, which has the advantage of a referenced absolute position. The polarization of both propagation directions is set to s-polarization using the motorized HWPs after the mode-matching telescope. Detector images are recorded for each delay stage position. Figure 4.47 shows the zoomed-in accumulated detector images of such a measurement. The non-circular shape of the electron distribution on the detector is attributed
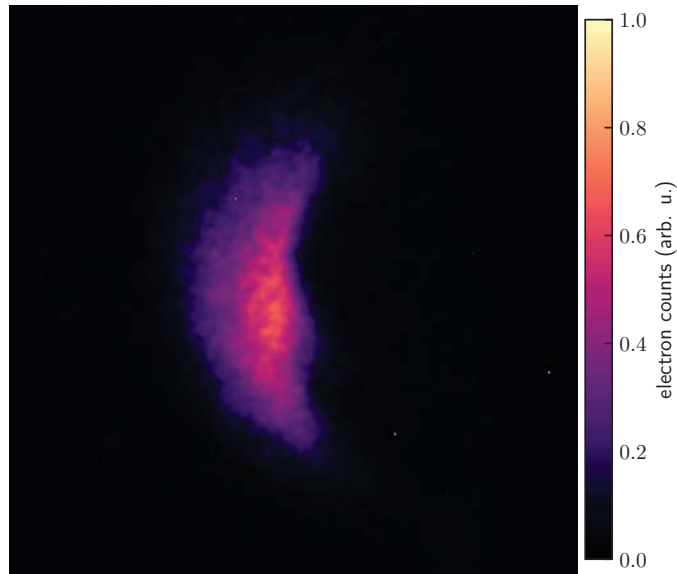
Figure 4.47: Accumulated detector images from nano-tip photoemission. Detector images are collected at several positions of the tip with respect to the light field. Here, a cropped image of all these detector images is shown. The shape of the electron distribution on the detector is attributed to the emission at the edge of the tip. Furthermore, image distortions are caused by electric field inhomogeneities originating from the sharp tip.

to the emission at the edge of the tip [483] and electric field inhomogeneities originating from the sharp tip.

Integration of the detector images at each delay step yields the photoelectron yield, as shown in Figure 4.48. For this measurement, the delay was scanned three times within two minutes. The data is fitted with a sine taken to the fourth power, yielding a period of ∼1070 nm, which is close to the expected value of 1039 nm. We attribute this difference to drifts of the interferometer arms of the two propagation directions, each several meters long. These drifts are estimated to be ∼25 nm min^{-1}, which corresponds to <100 as, at several watts of incident laser power. In a future upgrade, we will install a drift compensation control loop to achieve long-term temporal stability of a few attoseconds [484, 485]. Furthermore, we are currently upgrading the design of the nano-tip mount to fulfill the VMI conditions [486].

Figure 4.48: Probing the intense standing light field produced by counter-propagating pulses using the photoemission from a nano-tip target. For this measurement, the standing wave is moved with respect to the stationary tip using the delay stage in the SAD box. A sine taken to the fourth power is fitted to the data, yielding a period of ∼1070 nm.
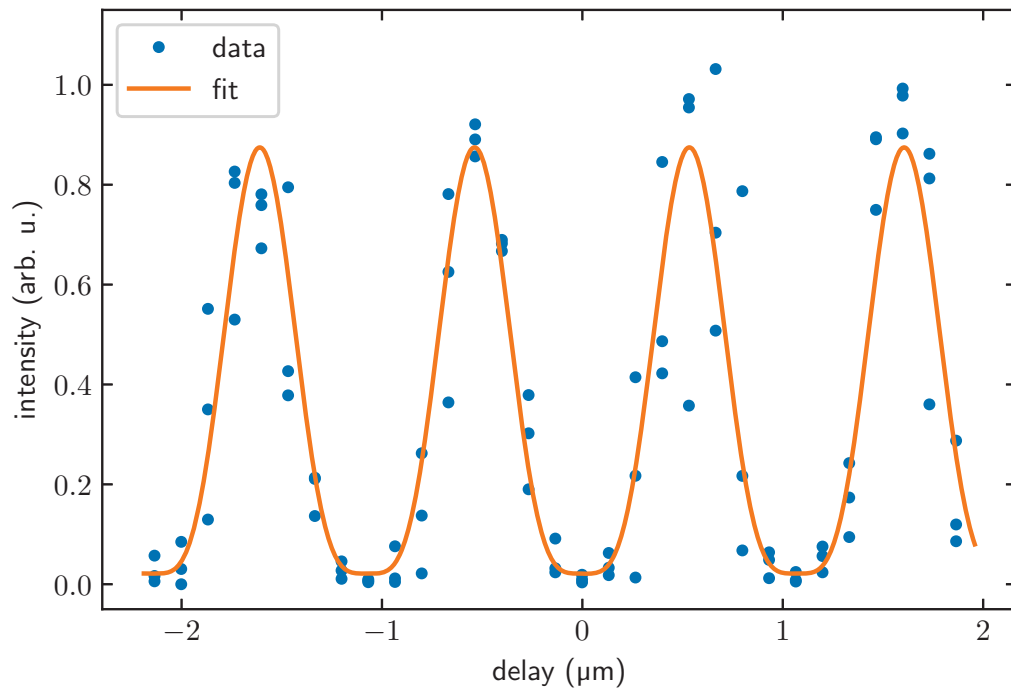
5 Conclusion and Outlook

The heart of this thesis is to bridge the technological gap between the areas of high-precision laser spectroscopy and strong-field physics. Up to now, the two fields of frequency metrology and highly nonlinear optics were mostly separated, but recent experiments have shown that it is possible to transfer the coherence from the infrared to the XUV spectral region using cavity-enhanced frequency combs. In that manner, the motivation for the research presented in this thesis is twofold. First, to advance these methods to enable long-term high-precision frequency spectroscopy of HCIs in the XUV spectral region, and second, directly use the intense coherent light to study highly nonlinear light-matter interaction.

In order to initiate highly nonlinear processes such as MPI and HHG, high intensities well above 10^{12} W cm^{-2} are required. Typically, these intensities are achieved by amplifying ultra-short laser pulses to high energy at kilohertz repetition rates. The transition to multi-megahertz repetition rates, retaining a similar pulse energy, would result in very high average powers in the range of tens of kilowatts, which is not yet technically feasible. To overcome this limitation, the frequency comb laser pulses are passively amplified in optical enhancement cavities to reach the required average powers. Using the technique of intra-cavity enhancement, peak intensities up to 10^{14} W cm^{-2} are readily achieved at 100 MHz repetition rate. This thesis has advanced the synergy between highly nonlinear processes and precision experiments in three main ways.

First, a rod-type Yb:fiber-based amplifier system, providing sub-200 fs pulses at over 80 W of average power was developed to serve as the source of high-power ultrashort laser pulses. The grating-based pulse compressor has a very high power-transmission efficiency of 95 %, and the system runs reliably in a turnkey operation. In addition, a dispersion-tunable MPC for nonlinear spectral broadening and temporal pulse compression was designed and built. The design allows for fine-tuning the dispersion by changing the gas pressure in a wide range from vacuum to 6 bar above atmosphere. Misalignment of the optics by a change in pressure is avoided by design since the chamber walls are mechanically isolated from the optics mounting structure. Filling the cell with xenon, a GDD tuning range of 8200 fs^2 can be reached with 34 passes through the nonlinear material. A first successful operation with a subsequent chirped-mirror-based compressor demonstrated pulse compression by a factor of two, which can be further improved using chirped-focusing mirrors inside the cell.

Second, an XUV frequency comb source based on intra-cavity HHG was developed together with J. Nauta, and its continuous operation for several hours was demonstrated. Using He:Xe gas mixtures, the yield of the 15th harmonic was up to 32 µW, which is sufficient to drive transitions in HCIs. Recently, the XUV frequency comb excitation of the $^3P_1$ - $^1S_0$ transition of Ar^{6+} at 88 nm (14.1 eV) was studied theoretically [126]. For this transition, which has a natural linewidth of 122 kHz, a population inversion of 0.14, was calculated at 40 µW comb power.

A closed-loop gas-recycling and compression system was designed, implemented, and tested within this thesis. It enables future precision measurements in the XUV spectral region that will require long data acquisition times by recycling the target gas with an efficiency of ~95 % and recompressing it up to more than 100 bar. Using a $\varnothing$40 µm gas nozzle at a backing pressure of 10 bar, more than 120 SL of gas are saved per day. Using xenon gas, this translates to cost savings of several thousand euro per day. For this measurement, the nozzle backing pressure was limited by the maximum background pressure of the mass spectrometer, which was used to monitor the contamination level during the nine-day measurement. Contaminants did not accumulate

inside the system during closed-loop operation and were kept below 2×10^{-9} mbar partial pressure due to the employed filters. Without the mass spectrometer, the nozzle can be operated well above 10 bar of backing pressure, enabling continuous phase-matched XUV frequency comb operation using gas mixtures. The novel gas-recycling and compression system could also find applications in other high repetition rate HHG laser sources or other instruments, for instance, in semiconductor manufacturing, where contamination-free recycling of noble gases is beneficial.

Third, a novel polarization-insensitive fsEC was developed, which allows photoelectron tomography at 100 MHz repetition rate, using the VMI technique. Imaging and reconstruction of 3D photoelectron distributions are enabled by a compact intra-cavity VMI spectrometer, which was developed and tested within the scope of this work. The VMI spectrometer uses a lightweight, self-supporting structure of thirteen nested, individually addressable gold-coated aluminum electrodes isolated and aligned by ceramic balls. This allows meeting the VMI conditions using the three lowest electrodes while making it possible to improve focusing and modifying the trajectories of charged particles inside the apparatus by applying voltages to the other electrodes. Using this apparatus, 3D PADs from gas-phase xenon MPI were tomographically reconstructed, revealing resonant Rydberg states during the ionization process. A relative energy resolution of ~3 % was obtained by resolving these sharp resonance features from Abel-inverted images. This value agrees well with electron trajectory simulations of the apparatus. Adjusting the intra-cavity intensity allowed to ponderomotively shift Rydberg states into resonance. The tomographic measurements are analyzed using an algorithm that does not require an inverse Abel transformation, which allows the reconstruction of non-cylindrically symmetric distributions. Additionally, the VMI spectrometer can accommodate a holder for nano-tip targets to study strong-field nano-optics.

Furthermore, the optical setup feeding the VMI cavity delivers counter-propagating pulses, which are simultaneously enhanced in the cavity. They collide at the focus producing a pulsed and intense standing light field to study highly nonlinear light-matter interaction. The overlap position of the colliding pulses was found by sampling a fraction of the light of each propagation direction at the focus position and detecting their spectral interference. The intense light field produced by the counter-propagating pulses was probed using multiphoton-induced electron emission from a nano-tip. The field of the standing wave was sampled at the nanometer scale. In addition, a Mach-Zehnder-interferometer-based SAD-line device enables pump-probe experiments using polarization-shaped pulse pairs.

The counter-propagating pulses can be immediately used to calibrate the position of zero momentum on the detector of the VMI spectrometer. The cavity ensures that the two propagation directions follow the same beam path, just in opposite directions, thus excluding laser misalignment as a potential error source. With this calibrated zero-momentum position, it should be possible to study the forward-backward symmetry of electron emission in strong-field ionization, which has recently been shown to be broken by magnetic- [175], and electric-nondipole effects [177]. The very high repetition rate of our system will be advantageous for these kinds of experiments. However, the resolution of the VMI spectrometer needs to be improved for such measurements, which can be done by extending the flight tube [470, 474]. In addition, a well-collimated supersonic gas jet in the horizontal plane could be implemented to shorten the length of the interaction region and thereby improve the resolution. The counter-propagating light can also be employed for Doppler-free spectroscopy of multiphoton transitions [21, 187].

Another exciting application is the production and manipulation of matter waves, such as free-electron wavepackets, by the standing wave of counter-propagating light. The ponderomotive potential of the standing wave can deflect these matter waves just like a grating refracts light waves, but with switched wave and matter roles. This Kapitza-Dirac effect [182] was demonstrated in 2001 [184], and since then, the theory of shaping electron wave packets by light has

advanced [487]. Indeed, further studies using phase-stable pulses will be helpful for benchmarking the underlying theory.

Within the last decade, ultrafast transmission electron microscopy has matured [488–491]. Utilizing the localized laser-driven electron emission from nanometric tips has resulted in many recent advances in the field, such as significantly enhanced beam coherence [483], quantum-coherent manipulation of free-electron wavefunctions by their interaction with nano-confined light fields [492], coherent interaction between free electrons and photonic cavities [493], and attosecond structuring of free-electron beams [494, 495].

These experiments indicate that the phase stability of the frequency comb is transferred to the free-electron wavefunctions emitted from the nano-tip inside our cavity. Thus, the frequency comb structure with its fine $100\,\mathrm{MHz}$ ($\approx 4 \times 10^{-7}\,\mathrm{eV}$) frequency spacing is most likely also imprinted on the photoelectron energy spectrum. However, these are much narrower features than what can be directly resolved with the VMI spectrometer, even when studying low-energy photoelectrons at an energy of $<0.1\,\mathrm{eV}$. Finding ways to detect and utilize these finely resolved peaks will allow unprecedented control of the coherence properties of these free-electron wavepackets. One method would be to launch these wavepackets with a first pulse and then probe them shortly afterwards using the standing light field or vice versa. Such pulse sequences are enabled by the SAD-box developed in this work. These new experiments will undoubtedly be linked to ultrafast electron microscopy, attosecond spectroscopy, and quantum optics and contribute to their advancement.

A recent quantum mechanical theory of extreme nonlinear optics showed that each frequency component of HHG can be bunched and squeezed and that each emitted photon is a superposition of all frequencies in the spectrum, which has not yet been measured experimentally. A proposed autocorrelation experiment, where the HHG light is attenuated to leave, on average, less than one photon per laser pulse, and detecting the autocorrelation signal as a function of the attenuator strength, could show the quantum optical nature of HHG when the transmitted intensity is reduced from that of a classical field towards the single-photon limit [496]. For such measurements, a high repetition rate is advantageous since, at most, one event can be detected per laser shot. XUV frequency combs provide such an experimental platform and will enable further investigation in the field of quantum optics towards the XUV region.

This work has resulted in a novel high-intensity laser source that provides ultrashort pulses for nonlinear optics experiments at a high repetition rate. It enables nonlinear multiphoton excitation and ionization experiments with unprecedented control using counter-propagating and polarization-shaped laser pulses. Doppler-free spectroscopy and time-resolved pump-probe experiments utilizing the coherence and absolute frequency reference of the comb laser are within reach. Furthermore, the metrology-capable XUV frequency comb that was co-developed within this work provides sufficient flux in the XUV to drive transitions in HCIs for future precision measurements for fundamental physics and frequency standards running at frequencies beyond the optical. A closed-loop high-pressure gas-recycling system enables long data acquisition times, which are needed for such high-precision measurements. Consequently, the future for investigating nonlinear light-matter interactions at a high repetition rate shines brighter than ever.

List of publications

Parts of this work have been published or prepared in the following articles:

- **J.-H. Oelmann**, T. Heldt, L. Guth, J. Nauta, N. Lackmann, V. Wössner, S. Kokh, T. Pfeifer, and J. R. Crespo López-Urrutia. "Photoelectron tomography with an intra-cavity velocity-map imaging spectrometer at 100 MHz repetition rate." In: *Review of Scientific Instruments* 93.12 (2022), p.123303. DOI: 10.1063/5.0104679.

- **J.-H. Oelmann**, J. Nauta, A. Ackermann, P. Knauer, R. Pappenberger, S. Kühn, J. Stark, J. R. Crespo López-Urrutia, and T. Pfeifer. "Development of an XUV Frequency Comb for Precision Spectroscopy of Highly Charged Ions." In: *2019 Conference on Lasers and Electro-Optics Europe and European Quantum Electronics Conference* (2019). DOI: 10.1109/CLEOE-EQEC.2019.8872682.

- **J.-H. Oelmann**, L. Guth, T. Heldt, N. Griesbach, R. Hector, N. Lackmann, J. Nauta, T. Pfeifer, and J. R. Crespo López-Urrutia. "Closed-cycle noble gas recycling system for high-repetition rate high-harmonic generation." *In preparation.*

- **J.-H. Oelmann**, T. Heldt, L. Guth, N. Lackmann, V. Wössner, S. Kokh, J. Nauta, T. Pfeifer, and J. R. Crespo López-Urrutia. "A Polarization Insensitive Femtosecond Enhancement Cavity for Photoelectron Tomography at 100 MHz Repetition Rate." In: *2023 Conference on Lasers and Electro-Optics Europe and European Quantum Electronics Conference* (2023). *Submitted.*

Additional publications with own contributions:

- J. Nauta, **J.-H. Oelmann**, A. Ackermann, P. Knauer, R. Pappenberger, A. Borodin, I. S. Muhammad, H. Ledwa, T. Pfeifer, and J. R. Crespo López-Urrutia. "100 MHz frequency comb for low-intensity multi-photon studies: intra-cavity velocity-map imaging of xenon." In: *Optics Letters* 45.8 (2020), p. 2156. DOI: 10.1364/OL.389327.

- J. Nauta, **J.-H. Oelmann**, A. Borodin, A. Ackermann, P. Knauer, I. S. Muhammad, R. Pappenberger, T. Pfeifer, and J. R. Crespo López-Urrutia. "XUV frequency comb production with an astigmatism-compensated enhancement cavity." In: *Optics Express* 29.2 (2021), p. 2624. DOI: 10.1364/oe.414987.

- J. Stark, C. Warnecke, S. Bogen, S. Chen, E. A. Dijck, S. Kühn, M. K. Rosner, A. Graf, J. Nauta, **J.-H. Oelmann**, *et al.* "An ultralow-noise superconducting radio-frequency ion trap for frequency metrology with highly charged ions." In: *Review of Scientific Instruments* 92.8 (2021), p. 083203. DOI: 10.1063/5.0046569.

- J. Nauta, **J.-H. Oelmann**, R. Pappenberger, P. Knauer, J. Krummeich, J. Stark, T. Heldt, L. Guth, N. Lackmann, T. Pfeifer, and J. R. Crespo López-Urrutia. "A differentially pumped and mechanically decoupled vacuum system for phase-matched intra-cavity high-harmonic generation." *In preparation.*

- I. Babushkin, A. Tajalli, H. Sayinc, **J.-H. Oelmann**, U. Morgner, G. Steinmeyer, and A. Demircan. "Higher order soliton breakup via implosion." In: *2016 Conference on Lasers and Electro-Optics Europe and European Quantum Electronics Conference* (2016). DOI: 10.1364/cleo_si.2016.stu1i.2.

Bibliography

[1] T. H. Maiman. "Stimulated Optical Radiation in Ruby." In: *Nature* 187.4736 (1960), pp. 493–494. DOI: 10.1038/187493a0.

[2] P. A. Franken, A. E. Hill, C. W. Peters, and G. Weinreich. "Generation of Optical Harmonics." In: *Physical Review Letters* 7.4 (1961), pp. 118–119. DOI: 10.1103/physrevlett.7.118.

[3] N. Colthup. *Introduction to Infrared and Raman Spectroscopy*. Elsevier Science and Technology Books, 2012.

[4] R. J. Glauber. "Coherent and Incoherent States of the Radiation Field." In: *Physical Review* 131.6 (1963), pp. 2766–2788. DOI: 10.1103/physrev.131.2766.

[5] D. F. Walls. "Squeezed states of light." In: *Nature* 306.5939 (1983), pp. 141–146. DOI: 10.1038/306141a0.

[6] L. S. Madsen, F. Laudenbach, M. F. Askarani, F. Rortais, T. Vincent, J. F. F. Bulmer, F. M. Miatto, L. Neuhaus, L. G. Helt, M. J. Collins, et al. "Quantum computational advantage with a programmable photonic processor." In: *Nature* 606.7912 (2022), pp. 75–81. DOI: 10.1038/s41586-022-04725-x.

[7] N. Gisin and R. Thew. "Quantum communication." In: *Nature Photonics* 1.3 (2007), pp. 165–171. DOI: 10.1038/nphoton.2007.22.

[8] R. Schnabel, N. Mavalvala, D. E. McClelland, and P. K. Lam. "Quantum metrology for gravitational wave astronomy." In: *Nature Communications* 1.1 (2010). DOI: 10.1038/ncomms1122.

[9] F. Riehle. *Frequency standards: basics and applications*. Wiley-VCH, 2004.

[10] A. D. Ludlow, M. M. Boyd, J. Ye, E. Peik, and P. O. Schmidt. "Optical atomic clocks." In: *Reviews of Modern Physics* 87.2 (2015), pp. 637–701. DOI: 10.1103/revmodphys.87.637.

[11] C. Zimmermann. *Cold Atoms And Molecules A Testground For Fundamental Many Particle Physics*. Wiley-VCH, 2009.

[12] F. Serwane, G. Zürn, T. Lompe, T. B. Ottenstein, A. N. Wenz, and S. Jochim. "Deterministic Preparation of a Tunable Few-Fermion System." In: *Science* 332.6027 (2011), pp. 336–338. DOI: 10.1126/science.1201351.

[13] S. Murmann, A. Bergschneider, V. M. Klinkhamer, G. Zürn, T. Lompe, and S. Jochim. "Two Fermions in a Double Well: Exploring a Fundamental Building Block of the Hubbard Model." In: *Physical Review Letters* 114.8 (2015), p. 080402. DOI: 10.1103/physrevlett.114.080402.

[14] L. Bayha, M. Holten, R. Klemt, K. Subramanian, J. Bjerlin, S. M. Reimann, G. M. Bruun, P. M. Preiss, and S. Jochim. "Observing the emergence of a quantum phase transition shell by shell." In: *Nature* 587.7835 (2020), pp. 583–587. DOI: 10.1038/s41586-020-2936-y.

[15] C. Y. Chen, Y. M. Li, K. Bailey, T. P. O'Connor, L. Young, and Z.-T. Lu. "Ultrasensitive Isotope Trace Analyses with a Magneto-Optical Trap." In: *Science* 286.5442 (1999), pp. 1139–1141. DOI: 10.1126/science.286.5442.1139.

[16] F. Ritterbusch, S. Ebser, J. Welte, T. Reichel, A. Kersting, R. Purtschert, W. Aeschbach-Hertig, and M. K. Oberthaler. "Groundwater dating with Atom Trap Trace Analysis of 39Ar." In: *Geophysical Research Letters* 41.19 (2014), pp. 6758–6764. DOI: 10.1002/2014g l061120.

[17] S. Ebser, A. Kersting, T. Stöven, Z. Feng, L. Ringena, M. Schmidt, T. Tanhua, W. Aeschbach, and M. K. Oberthaler. "39Ar dating with small samples provides new key constraints on ocean ventilation." In: *Nature Communications* 9.1 (2018). DOI: 10.1038/ s41467-018-07465-7.

[18] D. L. Mills. *Computer Network Time Synchronization*. CRC Press, 2006. DOI: 10.1201/ 9781420006155.

[19] T. Schuldt, M. Gohlke, M. Oswald, J. Wüst, T. Blomberg, K. Döringshoff, A. Bawamia, A. Wicht, M. Lezius, K. Voss, et al. "Optical clock technologies for global navigation satellite systems." In: *GPS Solutions* 25.3 (2021). DOI: 10.1007/s10291-021-01113-2.

[20] T. W. Hänsch. "Repetitively Pulsed Tunable Dye Laser for High Resolution Spectroscopy." In: *Applied Optics* 11.4 (1972), p. 895. DOI: 10.1364/ao.11.000895.

[21] T. W. Hänsch, S. A. Lee, R. Wallenstein, and C. Wieman. "Doppler-Free Two-Photon Spectroscopy of Hydrogen 1S-2S." In: *Physical Review Letters* 34.6 (1975), pp. 307–309. DOI: 10.1103/physrevlett.34.307.

[22] N. Bloembergen. "Nonlinear optics and spectroscopy." In: *Reviews of Modern Physics* 54.3 (1982), pp. 685–695. DOI: 10.1103/revmodphys.54.685.

[23] N. Huntemann, C. Sanner, B. Lipphardt, C. Tamm, and E. Peik. "Single-Ion Atomic Clock with 3x10^{-18} Systematic Uncertainty." In: *Physical Review Letters* 116.6 (2016), p. 063001. DOI: 10.1103/physrevlett.116.063001.

[24] E. Oelker, R. B. Hutson, C. J. Kennedy, L. Sonderhouse, T. Bothwell, A. Goban, D. Kedar, C. Sanner, J. M. Robinson, G. E. Marti, et al. "Demonstration of 4.8×10-17 stability at 1 s for two independent optical clocks." In: *Nature Photonics* 13.10 (2019), pp. 714–719. DOI: 10.1038/s41566-019-0493-4.

[25] T. Bothwell, D. Kedar, E. Oelker, J. M. Robinson, S. L. Bromley, W. L. Tew, J. Ye, and C. J. Kennedy. "JILA SrI optical lattice clock with uncertainty of 2.0x10^{-18}." In: *Metrologia* 56.6 (2019), p. 065004. DOI: 10.1088/1681-7575/ab4089.

[26] S. M. Brewer, J.-S. Chen, A. M. Hankin, E. R. Clements, C. W. Chou, D. J. Wineland, D. B. Hume, and D. R. Leibrandt. "^{27}Al^{+} Quantum-Logic Clock with a Systematic Uncertainty below 10^{-18}." In: *Physical Review Letters* 123.3 (2019), p. 033201. DOI: 10.1103/physre vlett.123.033201.

[27] K. Beloy, M. I. Bodine, T. Bothwell, S. M. Brewer, S. L. Bromley, J.-S. Chen, J.-D. Deschênes, S. A. Diddams, R. J. Fasano, T. M. Fortier, et al. "Frequency ratio measurements at 18-digit accuracy using an optical clock network." In: *Nature* 591.7851 (2021), pp. 564–569. DOI: 10.1038/s41586-021-03253-4.

[28] T. Bothwell, C. J. Kennedy, A. Aeppli, D. Kedar, J. M. Robinson, E. Oelker, A. Staron, and J. Ye. "Resolving the gravitational redshift across a millimetre-scale atomic sample." In: *Nature* 602.7897 (2022), pp. 420–424. DOI: 10.1038/s41586-021-04349-7.

[29] T. W. Hänsch. "Nobel lecture: passion for precision." In: *Reviews of Modern Physics* 78.4 (2006), pp. 1297–1309. DOI: 10.1103/revmodphys.78.1297.

[30] J. L. Hall. "Nobel Lecture: Defining and measuring optical frequencies." In: *Reviews of Modern Physics* 78.4 (2006), pp. 1279–1295. DOI: 10.1103/revmodphys.78.1279.

[31] J. N. Eckstein, A. I. Ferguson, and T. W. Hänsch. "High-Resolution Two-Photon Spectroscopy with Picosecond Light Pulses." In: *Physical Review Letters* 40.13 (1978), pp. 847–850. DOI: 10.1103/physrevlett.40.847.

[32] D. J. Jones, S. A. Diddams, J. K. Ranka, A. Stentz, R. S. Windeler, J. L. Hall, and S. T. Cundiff. "Carrier-Envelope Phase Control of Femtosecond Mode-Locked Lasers and Direct Optical Frequency Synthesis." In: *Science* 288.5466 (2000), pp. 635–639. DOI: 10.1126/science.288.5466.635.

[33] S. A. Diddams, D. J. Jones, J. Ye, S. T. Cundiff, J. L. Hall, J. K. Ranka, R. S. Windeler, R. Holzwarth, T. Udem, and T. W. Hänsch. "Direct Link between Microwave and Optical Frequencies with a 300 THz Femtosecond Laser Comb." In: *Physical Review Letters* 84.22 (2000), pp. 5102–5105. DOI: 10.1103/physrevlett.84.5102.

[34] R. Holzwarth, T. Udem, T. W. Hänsch, J. C. Knight, W. J. Wadsworth, and P. S. J. Russell. "Optical Frequency Synthesizer for Precision Spectroscopy." In: *Physical Review Letters* 85.11 (2000), pp. 2264–2267. DOI: 10.1103/physrevlett.85.2264.

[35] H. Telle, G. Steinmeyer, A. Dunlop, J. Stenger, D. Sutter, and U. Keller. "Carrier-envelope offset phase control: A novel concept for absolute optical frequency measurement and ultrashort pulse generation." In: *Applied Physics B* 69.4 (1999), pp. 327–332. DOI: 10.1007/s003400050813.

[36] J. Reichert, R. Holzwarth, T. Udem, and T. Hänsch. "Measuring the frequency of light with mode-locked lasers." In: *Optics Communications* 172.1-6 (1999), pp. 59–68. DOI: 10.1016/s0030-4018(99)00491-5.

[37] T. Udem, R. Holzwarth, and T. W. Hänsch. "Optical frequency metrology." In: *Nature* 416.6877 (2002), p. 233. DOI: 10.1038/416233a.

[38] S. T. Cundiff and J. Ye. "Colloquium: Femtosecond optical frequency combs." In: *Reviews of Modern Physics* 75.1 (2003), pp. 325–342. DOI: 10.1103/revmodphys.75.325.

[39] N. Picqué and T. W. Hänsch. "Frequency comb spectroscopy." In: *Nature Photonics* 13.3 (2019), pp. 146–157. DOI: 10.1038/s41566-018-0347-5.

[40] T. Ideguchi, A. Poisson, G. Guelachvili, N. Picqué, and T. W. Hänsch. "Adaptive real-time dual-comb spectroscopy." In: *Nature Communications* 5.1 (2014). DOI: 10.1038/ncomms4375.

[41] J. Riemensberger, A. Lukashchuk, M. Karpov, W. Weng, E. Lucas, J. Liu, and T. J. Kippenberg. "Massively parallel coherent laser ranging using a soliton microcomb." In: *Nature* 581.7807 (2020), pp. 164–170. DOI: 10.1038/s41586-020-2239-3.

[42] T. Wilken, G. L. Curto, R. A. Probst, T. Steinmetz, A. Manescau, L. Pasquini, J. I. G. Hernández, R. Rebolo, T. W. Hänsch, T. Udem, and R. Holzwarth. "A spectrograph for exoplanet observations calibrated at the centimetre-per-second level." In: *Nature* 485.7400 (2012), pp. 611–614. DOI: 10.1038/nature11092.

[43] A. Baltuška, T. Udem, M. Uiberacker, M. Hentschel, E. Goulielmakis, C. Gohle, R. Holzwarth, V. S. Yakovlev, A. Scrinzi, T. W. Hänsch, and F. Krausz. "Attosecond control of electronic processes by intense light fields." In: *Nature* 421.6923 (2003), pp. 611–615. DOI: 10.1038/nature01414.

[44] V. Torres-Company and A. M. Weiner. "Optical frequency comb technology for ultra-broadband radio-frequency photonics." In: *Laser Photon. Rev.* 8.3 (2013), pp. 368–393. DOI: 10.1002/lpor.201300126.

[45] D. Allan. "Statistics of atomic frequency standards." In: *Proceedings of the IEEE* 54.2 (1966), pp. 221–230. DOI: 10.1109/proc.1966.4634.

[46] W. M. Itano, J. C. Bergquist, J. J. Bollinger, J. M. Gilligan, D. J. Heinzen, F. L. Moore, M. G. Raizen, and D. J. Wineland. "Quantum projection noise: Population fluctuations in two-level systems." In: *Physical Review A* 47.5 (1993), pp. 3554–3570. DOI: `10.1103/physreva.47.3554`.

[47] A. Bauch. "Caesium atomic clocks: function, performance and applications." In: *Measurement Science and Technology* 14.8 (2003), pp. 1159–1173. DOI: `10.1088/0957-0233/14/8/301`.

[48] X. Zheng, J. Dolde, V. Lochab, B. N. Merriman, H. Li, and S. Kolkowitz. "Differential clock comparisons with a multiplexed optical lattice clock." In: *Nature* 602.7897 (2022), pp. 425–430. DOI: `10.1038/s41586-021-04344-y`.

[49] R. X. Schüssler, H. Bekker, M. Braß, H. Cakir, J. R. Crespo López-Urrutia, M. Door, P. Filianin, Z. Harman, M. W. Haverkort, W. J. Huang, et al. "Detection of metastable electronic states by Penning trap mass spectrometry." In: *Nature* 581.7806 (2020), pp. 42–46. DOI: `10.1038/s41586-020-2221-0`.

[50] M. S. Safronova, V. A. Dzuba, V. V. Flambaum, U. I. Safronova, S. G. Porsev, and M. G. Kozlov. "Highly Charged Ions for Atomic Clocks, Quantum Information, and Search for α variation." In: *Physical Review Letters* 113.3 (2014), p. 030801. DOI: `10.1103/PhysRevLett.113.030801`.

[51] M. G. Kozlov, M. S. Safronova, J. R. Crespo López-Urrutia, and P. O. Schmidt. "Highly charged ions: Optical clocks and applications in fundamental physics." In: *Reviews of Modern Physics* 90 (2018), p. 045005. DOI: `10.1103/RevModPhys.90.045005`.

[52] S. M. Cavaletto, Z. Harman, C. Ott, C. Buth, T. Pfeifer, and C. H. Keitel. "Broadband high-resolution X-ray frequency combs." In: *Nature Photonics* 8.7 (2014), pp. 520–523. DOI: `10.1038/nphoton.2014.113`.

[53] J. Nauta. "An extreme-ultraviolet frequency comb enabling frequency metrology with highly charged ions." PhD thesis. Ruprecht-Karls-Universität, Heidelberg, 2020. DOI: `10.11588/heidok.00028798`.

[54] L. Schmöger, O. O. Versolato, M. Schwarz, M. Kohnen, A. Windberger, B. Piest, S. Feuchtenbeiner, J. Pedregosa-Gutierrez, T. Leopold, P. Micke, et al. "Coulomb crystallization of highly charged ions." In: *Science* 347.6227 (2015), pp. 1233–1236. DOI: `10.1126/science.aaa2960`.

[55] T. Baumann. "Spektroskopische Untersuchungen resonanter Rekombinationsprozesse an hochgeladenem Silizium in einer Elektronenstrahl-Ionenfalle." PhD thesis. Ruprecht-Karls-Universität, Heidelberg, 2012. DOI: `10.11588/HEIDOK.00013380`.

[56] M. Schwarz, O. O. Versolato, A. Windberger, F. R. Brunner, T. Ballance, S. N. Eberle, J. Ullrich, P. O. Schmidt, A. K. Hansen, A. D. Gingell, et al. "Cryogenic linear Paul trap for cold highly charged ion experiments." In: *Review of Scientific Instruments* 83.8 (2012), p. 083115. DOI: `10.1063/1.4742770`.

[57] L. Schmöger, M. Schwarz, T. M. Baumann, O. O. Versolato, B. Piest, T. Pfeifer, J. Ullrich, P. O. Schmidt, and J. R. Crespo López-Urrutia. "Deceleration, precooling, and multi-pass stopping of highly charged ions in Be+ Coulomb crystals." In: *Review of Scientific Instruments* 86.10 (2015), p. 103111. DOI: `10.1063/1.4934245`.

[58] P. Micke, S. Kühn, L. Buchauer, J. R. Harries, T. M. Bücking, K. Blaum, A. Cieluch, A. Egl, D. Hollain, S. Kraemer, et al. "The Heidelberg compact electron beam ion traps." In: *Review of Scientific Instruments* 89.6 (2018), p. 063109. DOI: `10.1063/1.5026961`.

[59] P. Micke, J. Stark, S. A. King, T. Leopold, T. Pfeifer, L. Schmöger, M. Schwarz, L. J. Spieß, P. O. Schmidt, and J. R. Crespo López-Urrutia. "Closed-cycle, low-vibration 4 K cryostat for ion traps and other applications." In: *Review of Scientific Instruments* 90.6 (2019), p. 065104. DOI: 10.1063/1.5088593.

[60] T. Leopold, S. A. King, P. Micke, A. Bautista-Salvador, J. C. Heip, C. Ospelkaus, J. R. Crespo López-Urrutia, and P. O. Schmidt. "A cryogenic radio-frequency ion trap for quantum logic spectroscopy of highly charged ions." In: *Review of Scientific Instruments* 90.7 (2019), p. 073201. DOI: 10.1063/1.5100594.

[61] J. Stark, C. Warnecke, S. Bogen, S. Chen, E. A. Dijck, S. Kühn, M. K. Rosner, A. Graf, J. Nauta, J.-H. Oelmann, et al. "An ultralow-noise superconducting radio-frequency ion trap for frequency metrology with highly charged ions." In: *Review of Scientific Instruments* 92.8 (2021), p. 083203. DOI: 10.1063/5.0046569.

[62] E. A. Dijck, C. Warnecke, M. Wehrheim, T. Pfeifer, J. R. Crespo López-Urrutia, et al. *Cold highly charged ions in a radio-frequency trap with superconducting magnetic shielding*. In preparation. 2023.

[63] P. Micke, T. Leopold, S. A. King, E. Benkler, L. J. Spieß, L. Schmöger, M. Schwarz, J. R. Crespo López-Urrutia, and P. O. Schmidt. "Coherent laser spectroscopy of highly charged ions using quantum logic." In: *Nature* 578.7793 (2020), pp. 60–65. DOI: 10.1038/s41586-020-1959-8.

[64] P. O. Schmidt, T. Rosenband, C. Langer, W. M. Itano, J. C. Bergquist, and D. J. Wineland. "Spectroscopy Using Quantum Logic." In: *Science* 309.5735 (2005), pp. 749–752. DOI: 10.1126/science.1114375.

[65] S. A. King, L. J. Spieß, P. Micke, A. Wilzewski, T. Leopold, J. R. Crespo López-Urrutia, and P. O. Schmidt. "Algorithmic Ground-State Cooling of Weakly Coupled Oscillators Using Quantum Logic." In: *Physical Review X* 11.4 (2021), p. 041049. DOI: 10.1103/physrevx.11.041049.

[66] S. A. King, L. J. Spieß, P. Micke, A. Wilzewski, T. Leopold, E. Benkler, R. Lange, N. Huntemann, A. Surzhykov, V. A. Yerokhin, et al. "An optical atomic clock based on a highly charged ion." In: *Nature* 611.7934 (2022), pp. 43–47. DOI: 10.1038/s41586-022-05245-4.

[67] A. Ong, J. C. Berengut, and V. V. Flambaum. "Optical Transitions in Highly Charged Ions for Detection of Variations in the Fine-Structure Constant." In: *Springer Tracts in Modern Physics*. Springer Berlin Heidelberg, 2014, pp. 293–314. DOI: 10.1007/978-3-642-45201-7_9.

[68] J. C. Berengut, V. A. Dzuba, and V. V. Flambaum. "Enhanced Laboratory Sensitivity to Variation of the Fine-Structure Constant using Highly Charged Ions." In: *Physical Review Letters* 105.12 (2010), p. 120801. DOI: 10.1103/physrevlett.105.120801.

[69] J. C. Berengut, V. A. Dzuba, V. V. Flambaum, and A. Ong. "Electron-Hole Transitions in Multiply Charged Ions for Precision Laser Spectroscopy and Searching for Variations in α." In: *Physical Review Letters* 106.21 (2011), p. 210802. DOI: 10.1103/physrevlett.106.210802.

[70] D. Antypas, A. Banerjee, C. Bartram, M. Baryakhtar, J. Betz, J. J. Bollinger, C. Boutan, D. Bowring, D. Budker, D. Carney, et al. *New Horizons: Scalar and Vector Ultralight Dark Matter*. 2022. DOI: 10.48550/ARXIV.2203.14915.

[71] A. D. Sakharov. "Violation of CP-invariance, C-asymmetry, and baryon asymmetry of the Universe." In: *In The Intermissions... Collected Works on Research into the Essentials of Theoretical Physics in Russian Federal Nuclear Center, Arzamas* (1998), pp. 84–87. DOI: 10.1142/9789812815941_0013.

[72] J. C. Berengut, D. Budker, C. Delaunay, V. V. Flambaum, C. Frugiuele, E. Fuchs, C. Grojean, R. Harnik, R. Ozeri, G. Perez, and Y. Soreq. "Probing New Long-Range Interactions by Isotope Shift Spectroscopy." In: *Physical Review Letters* 120.9 (2018), p. 091801. DOI: 10.1103/physrevlett.120.091801.

[73] W. H. King. "Comments on the Article "Peculiarities of the Isotope Shift in the Samarium Spectrum"." In: *Journal of the Optical Society of America* 53.5 (1963), p. 638. DOI: 10.1364/josa.53.000638.

[74] C. Delaunay, R. Ozeri, G. Perez, and Y. Soreq. "Probing atomic Higgs-like forces at the precision frontier." In: *Physical Review D* 96.9 (2017), p. 093001. DOI: 10.1103/physrevd.96.093001.

[75] K. Mikami, M. Tanaka, and Y. Yamamoto. "Probing new intra-atomic force with isotope shifts." In: *The European Physical Journal C* 77.12 (2017). DOI: 10.1140/epjc/s10052-017-5467-4.

[76] J. C. Berengut, C. Delaunay, A. Geddes, and Y. Soreq. "Generalized King linearity and new physics searches with isotope shifts." In: *Physical Review Research* 2.4 (2020), p. 043444. DOI: 10.1103/physrevresearch.2.043444.

[77] N.-H. Rehbehn, M. K. Rosner, H. Bekker, J. C. Berengut, P. O. Schmidt, S. A. King, P. Micke, M. F. Gu, R. Müller, A. Surzhykov, and J. R. Crespo López-Urrutia. "Sensitivity to new physics of isotope-shift studies using the coronal lines of highly charged calcium ions." In: *Physical Review A* 103.4 (2021), p. l040801. DOI: 10.1103/physreva.103.l040801.

[78] V. Debierre, N. S. Oreshkina, I. A. Valuev, Z. Harman, and C. H. Keitel. "Testing standard-model extensions with isotope shifts in few-electron ions." In: *Physical Review A* 106.6 (2022), p. 062801. DOI: 10.1103/physreva.106.062801.

[79] A. L'Huillier, K. J. Schafer, and K. C. Kulander. "Higher-order harmonic generation in xenon at 1064 nm: The role of phase matching." In: *Physical Review Letters* 66.17 (1991), pp. 2200–2203. DOI: 10.1103/physrevlett.66.2200.

[80] J. J. Macklin, J. D. Kmetec, and C. L. Gordon. "High-order harmonic generation using intense femtosecond pulses." In: *Physical Review Letters* 70.6 (1993), pp. 766–769. DOI: 10.1103/physrevlett.70.766.

[81] T. Brabec and F. Krausz. "Intense few-cycle laser fields: Frontiers of nonlinear optics." In: *Reviews of Modern Physics* 72.2 (2000), pp. 545–591. DOI: 10.1103/revmodphys.72.545.

[82] M. Hentschel, R. Kienberger, C. Spielmann, G. A. Reider, N. Milosevic, T. Brabec, P. Corkum, U. Heinzmann, M. Drescher, and F. Krausz. "Attosecond metrology." In: *Nature* 414.6863 (2001), pp. 509–513. DOI: 10.1038/35107000.

[83] R. J. Jones, K. D. Moll, M. J. Thorpe, and J. Ye. "Phase-Coherent Frequency Combs in the Vacuum Ultraviolet via High-Harmonic Generation inside a Femtosecond Enhancement Cavity." In: *Physical Review Letters* 94 (2005), p. 193201. DOI: 10.1103/PhysRevLett.94.193201.

[84] C. Gohle, T. Udem, M. Herrmann, J. Rauschenberger, R. Holzwarth, H. A. Schuessler, F. Krausz, and T. W. Hänsch. "A frequency comb in the extreme ultraviolet." In: *Nature* 436.7048 (2005), pp. 234–237. DOI: 10.1038/nature03851.

[85] A. Ozawa and Y. Kobayashi. "VUV frequency-comb spectroscopy of atomic xenon." In: *Physical Review A* 87 (2013), p. 022507. DOI: 10.1103/PhysRevA.87.022507.

[86] D. C. Yost, T. R. Schibli, and J. Ye. "Efficient output coupling of intracavity high-harmonic generation." In: *Optics Letters* 33.10 (2008), pp. 1099–1101. DOI: 10.1364/OL.33.001099.

[87] D. C. Yost, T. R. Schibli, J. Ye, J. L. Tate, J. Hostetter, M. B. Gaarde, and K. J. Schafer. "Vacuum-ultraviolet frequency combs from below-threshold harmonics." In: *Nature Physics* 5.11 (2009), pp. 815–820. DOI: 10.1038/nphys1398.

[88] D. C. Yost, A. Cingöz, T. K. Allison, A. Ruehl, M. E. Fermann, I. Hartl, and J. Ye. "Power optimization of XUV frequency combs for spectroscopy applications." In: *Optics Express* 19.23 (2011), pp. 23483–23493. DOI: 10.1364/OE.19.023483.

[89] A. Cingöz, D. C. Yost, T. K. Allison, A. Ruehl, M. E. Fermann, I. Hartl, and J. Ye. "Direct frequency comb spectroscopy in the extreme ultraviolet." In: *Nature* 482.7383 (2012), pp. 68–71. DOI: 10.1038/nature10711.

[90] C. Benko, T. K. Allison, A. Cingöz, L. Hua, F. Labaye, D. C. Yost, and J. Ye. "Extreme ultraviolet radiation with coherence time greater than 1 s." In: *Nature Photonics* 8.7 (2014), pp. 530–536. DOI: 10.1038/nphoton.2014.132.

[91] G. Porat, C. M. Heyl, S. B. Schoun, C. Benko, N. Dörre, K. L. Corwin, and J. Ye. "Phase-matched extreme-ultraviolet frequency-comb generation." In: *Nature Photonics* 12.7 (2018), pp. 387–391. DOI: 10.1038/s41566-018-0199-z.

[92] C. Zhang, S. B. Schoun, C. M. Heyl, G. Porat, M. B. Gaarde, and J. Ye. "Noncollinear Enhancement Cavity for Record-High Out-coupling Efficiency of an Extreme-UV Frequency Comb." In: *Physical Review Letters* 125.9 (2020), p. 093902. DOI: 10.1103/physrevlett.125.093902.

[93] I. Pupeza, C. Zhang, M. Högner, and J. Ye. "Extreme-ultraviolet frequency combs for precision metrology and attosecond science." In: *Nature Photonics* 15.3 (2021), pp. 175–186. DOI: 10.1038/s41566-020-00741-3.

[94] C. Zhang, P. Li, J. Jiang, L. von der Wense, J. F. Doyle, M. E. Fermann, and J. Ye. "Tunable VUV frequency comb for ^{229m}Th nuclear spectroscopy." In: *Optics Letters* 47.21 (2022), p. 5591. DOI: 10.1364/ol.473006.

[95] A. Ozawa, A. Vernaleken, W. Schneider, I. Gotlibovych, T. Udem, and T. W. Hänsch. "Non-collinear high harmonic generation: a promising outcoupling method for cavity-assisted XUV generation." In: *Optics Express* 16.9 (2008), pp. 6233–6239. DOI: 10.1364/OE.16.006233.

[96] A. Ozawa, J. Rauschenberger, C. Gohle, M. Herrmann, D. R. Walker, V. Pervak, A. Fernandez, R. Graf, A. Apolonski, R. Holzwarth, et al. "High Harmonic Frequency Combs for High Resolution Spectroscopy." In: *Physical Review Letters* 100 (2008), p. 253901. DOI: 10.1103/PhysRevLett.100.253901.

[97] I. Pupeza, S. Holzberger, T. Eidam, H. Carstens, D. Esser, J. Weitenberg, P. Rußbüldt, J. Rauschenberger, J. Limpert, T. Udem, et al. "Compact high-repetition-rate source of coherent 100 eV radiation." In: *Nat. Photon.* 7.8 (2013), pp. 608–612. DOI: 10.1038/nphoton.2013.156.

[98] I. Pupeza, M. Högner, J. Weitenberg, S. Holzberger, D. Esser, T. Eidam, J. Limpert, A. Tünnermann, E. Fill, and V. S. Yakovlev. "Cavity-Enhanced High-Harmonic Generation with Spatially Tailored Driving Fields." In: *Physical Review Letters* 112 (2014), p. 103902. DOI: 10.1103/PhysRevLett.112.103902.

[99] H. Carstens, M. Högner, T. Saule, S. Holzberger, N. Lilienfein, A. Guggenmos, C. Jocher, T. Eidam, D. Esser, V. Tosa, et al. "High-harmonic generation at 250 MHz with photon energies exceeding 100 eV." In: *Optica* 3.4 (2016), p. 366. DOI: 10.1364/optica.3.000366.

[100] T. Saule, M. Högner, N. Lilienfein, O. de Vries, M. Plötner, V. S. Yakovlev, N. Karpowicz, J. Limpert, and I. Pupeza. "Cumulative plasma effects in cavity-enhanced high-order harmonic generation in gases." In: *APL Photonics* 3.10 (2018), p. 101301. DOI: 10.1063/1.5037196.

[101] T. Saule, S. Heinrich, J. Schötz, N. Lilienfein, M. Högner, O. deVries, M. Plötner, J. Weitenberg, D. Esser, J. Schulte, et al. "High-flux ultrafast extreme-ultraviolet photoemission spectroscopy at 18.4 MHz pulse repetition rate." In: *Nature Communications* 10.1 (2019), p. 458. DOI: 10.1038/s41467-019-08367-y.

[102] M. Högner, T. Saule, S. Heinrich, N. Lilienfein, D. Esser, M. Trubetskov, V. Pervak, and I. Pupeza. "Cavity-enhanced noncollinear high-harmonic generation." In: *Optics Express* 27.14 (2019), p. 19675. DOI: 10.1364/oe.27.019675.

[103] X. Li, M. A. R. Reber, C. Corder, Y. Chen, P. Zhao, and T. K. Allison. "High-power ultrafast Yb:fiber laser frequency combs using commercially available components and basic fiber tools." In: *Review of Scientific Instruments* 87.9 (2016), p. 093114. DOI: 10.1063/1.4962867.

[104] C. Corder, P. Zhao, J. Bakalis, X. Li, M. D. Kershis, A. R. Muraca, M. G. White, and T. K. Allison. "Ultrafast extreme ultraviolet photoemission without space charge." In: *Structural Dynamics* 5.5 (2018), p. 054301. DOI: 10.1063/1.5045578.

[105] A. Ozawa, Z. Zhao, M. Kuwata-Gonokami, and Y. Kobayashi. "High average power coherent VUV generation at 10 MHz repetition frequency by intracavity high harmonic generation." In: *Optics Express* 23.12 (2015), pp. 15107–15118. DOI: 10.1364/OE.23.015107.

[106] Z. Zhao, A. Ozawa, M. Kuwata-Gonokami, and Y. Kobayashi. "Efficient high harmonics generation by enhancement cavity driven with a post-compressed FCPA laser at 10 MHz." In: *High Power Laser Science and Engineering* 6 (2018). DOI: 10.1017/hpl.2018.19.

[107] T. J. Hammond, A. K. Mills, and D. J. Jones. "Near-threshold harmonics from a femtosecond enhancement cavity-based EUV source: effects of multiple quantum pathways on spatial profile and yield." In: *Optics Express* 19.25 (2011), pp. 24871–24883. DOI: 10.1364/OE.19.024871.

[108] J. Lee, D. R. Carlson, and R. J. Jones. "Optimizing intracavity high harmonic generation for XUV fs frequency combs." In: *Optics Express* 19.23 (2011), pp. 23315–23326. DOI: 10.1364/OE.19.023315.

[109] A. K. Mills, T. J. Hammond, M. H. C. Lam, and D. J. Jones. "XUV frequency combs via femtosecond enhancement cavities." In: *Journal of Physics B: Atomic, Molecular and Optical Physics* 45.14 (2012), p. 142001. DOI: 10.1088/0953-4075/45/14/142001.

[110] A. K. Mills, S. Zhdanovich, A. Sheyerman, G. Levy, A. Damascelli, and D. J. Jones. "An XUV source using a femtosecond enhancement cavity for photoemission spectroscopy." In: *Advances in X-ray Free-Electron Lasers Instrumentation III*. Ed. by S. G. Biedron. SPIE, 2015. DOI: 10.1117/12.2184547.

[111] A. K. Mills, S. Zhdanovich, M. X. Na, F. Boschini, E. Razzoli, M. Michiardi, A. Sheyerman, M. Schneider, T. J. Hammond, V. Süss, et al. "Cavity-enhanced high harmonic generation for XUV time-resolved ARPES." In: *Review of Scientific Instruments* 90.8 (2019), p. 083001. DOI: 10.1063/1.5090507.

[112] G. Winkler, J. Fellinger, J. Seres, E. Seres, and T. Schumm. "Non-planar femtosecond enhancement cavity for VUV frequency comb applications." In: *Optics Express* 24.5 (2016), pp. 5253–5262. DOI: 10.1364/OE.24.005253.

[113] J. Seres, E. Seres, C. Serrat, E. C. Young, J. S. Speck, and T. Schumm. "All-solid-state VUV frequency comb at 160 nm using multi-harmonic generation in a non-linear femtosecond enhancement cavity." In: *Optics Express* 27.5 (2019), p. 6618. DOI: 10.1364/oe.27.006618.

[114] M. Zhu, J. Zhang, L. Hua, Z. Xiao, S. Xu, X. Lai, and X. Liu. "Molecular structural effects in below- and near-threshold harmonics in XUV-comb generation." In: *Physical Review A* 104.4 (2021), p. 043111. DOI: 10.1103/physreva.104.043111.

[115] J. Nauta, A. Borodin, H. B. Ledwa, J. Stark, M. Schwarz, L. Schmöger, P. Micke, J. R. Crespo López-Urrutia, and T. Pfeifer. "Towards precision measurements on highly charged ions using a high harmonic generation frequency comb." In: *Nuclear Instruments and Methods in Physics Research Section B: Beam Interactions with Materials and Atoms* 408 (2017), pp. 285–288. DOI: 10.1016/j.nimb.2017.04.077.

[116] J.-H. Oelmann, J. Nauta, A. Ackermann, P. Knauer, R. Pappenberger, S. Kühn, J. Stark, J. R. Crespo López-Urrutia, and T. Pfeifer. "Development of an XUV frequency comb for precision spectroscopy of highly charged ions." In: *2019 Conference on Lasers and Electro-Optics Europe and European Quantum Electronics Conference* (2019). DOI: 10.1109/CLEOE-EQEC.2019.8872682.

[117] J. Nauta, J.-H. Oelmann, A. Borodin, A. Ackermann, P. Knauer, I. S. Muhammad, R. Pappenberger, T. Pfeifer, and J. R. Crespo López-Urrutia. "XUV frequency comb production with an astigmatism-compensated enhancement cavity." In: *Optics Express* 29.2 (2021), p. 2624. DOI: 10.1364/oe.414987.

[118] A. Ozawa, J. Davila-Rodriguez, J. R. Bounds, H. A. Schuessler, T. W. Hänsch, and T. Udem. "Single ion fluorescence excited with a single mode of an UV frequency comb." In: *Nature Communications* 8.1 (2017), p. 44. DOI: 10.1038/s41467-017-00067-9.

[119] M. Herrmann, M. Haas, U. D. Jentschura, F. Kottmann, D. Leibfried, G. Saathoff, C. Gohle, A. Ozawa, V. Batteiger, S. Knünz, et al. "Feasibility of coherent xuv spectroscopy on the 1S-2S transition in singly ionized helium." In: *Physical Review A* 79.5 (2009), p. 52505. DOI: 10.1103/physreva.79.052505.

[120] F. Schmid, J. Weitenberg, J. Moreno, T. W. Hänsch, T. Udem, and A. Ozawa. "Number-resolved detection of dark ions in Coulomb crystals." In: *Physical Review A* 106.4 (2022), p. l041101. DOI: 10.1103/physreva.106.l041101.

[121] K. Beeks, T. Sikorsky, T. Schumm, J. Thielking, M. V. Okhapkin, and E. Peik. "The thorium-229 low-energy isomer and the nuclear clock." In: *Nature Reviews Physics* 3.4 (2021), pp. 238–248. DOI: 10.1038/s42254-021-00286-6.

[122] D. Z. Kandula, C. Gohle, T. J. Pinkert, W. Ubachs, and K. S. E. Eikema. "Extreme Ultraviolet Frequency Comb Metrology." In: *Physical Review Letters* 105.6 (2010). DOI: 10.1103/physrevlett.105.063001.

[123] L. Dreissen, C. Roth, E. Gründeman, J. Krauth, M. Favier, and K. Eikema. "High-Precision Ramsey-Comb Spectroscopy Based on High-Harmonic Generation." In: *Physical Review Letters* 123.14 (2019), p. 143001. DOI: 10.1103/physrevlett.123.143001.

[124] J. J. Krauth, L. S. Dreissen, C. Roth, E. L. Gründeman, M. Collombon, M. Favier, and K. S. Eikema. "Paving the way for fundamental physics tests with singly-ionized helium." In: *Proceedings of International Conference on Precision Physics and Fundamental Physical Constants*. Sissa Medialab, 2019. DOI: 10.22323/1.353.0049.

[125] N. F. Ramsey. "A Molecular Beam Resonance Method with Separated Oscillating Fields." In: *Physical Review* 78.6 (1950), pp. 695–699. DOI: 10.1103/physrev.78.695.

[126] C. Lyu, S. M. Cavaletto, C. H. Keitel, and Z. Harman. "Interrogating the Temporal Coherence of EUV Frequency Combs with Highly Charged Ions." In: *Physical Review Letters* 125.9 (2020), p. 093201. DOI: 10.1103/physrevlett.125.093201.

[127] J. Nauta, J.-H. Oelmann, R. Pappenberger, P. Knauer, J. Krummeich, J. Stark, T. Heldt, L. Guth, N. Lackmann, T. Pfeifer, and J. R. Crespo López-Urrutia. *A differentially pumped and mechanically decoupled vacuum system for phase-matched intra-cavity high-harmonic generation*. In preparation. 2023.

[128] J.-H. Oelmann, L. Guth, T. Heldt, N. Griesbach, R. Hector, N. Lackmann, J. Nauta, T. Pfeifer, and J. R. Crespo López-Urrutia. *Closed-cycle noble gas recycling system for high-repetition rate high-harmonic generation*. In preparation. 2023.

[129] J. Nauta, J.-H. Oelmann, A. Ackermann, P. Knauer, R. Pappenberger, A. Borodin, I. S. Muhammad, H. Ledwa, T. Pfeifer, and J. R. Crespo López-Urrutia. "100 MHz frequency comb for low-intensity multi-photon studies: intra-cavity velocity-map imaging of xenon." In: *Optics Letters* 45.8 (2020), p. 2156. DOI: 10.1364/OL.389327.

[130] F. Lindner, W. Stremme, M. G. Schätzel, F. Grasbon, G. G. Paulus, H. Walther, R. Hartmann, and L. Strüder. "High-order harmonic generation at a repetition rate of 100 kHz." In: *Physical Review A* 68.1 (2003), p. 013814. DOI: 10.1103/physreva.68.013814.

[131] S. Hädrich, J. Rothhardt, M. Krebs, S. Demmler, A. Klenke, A. Tünnermann, and J. Limpert. "Single-pass high harmonic generation at high repetition rate and photon flux." In: *Journal of Physics B: Atomic, Molecular and Optical Physics* 49.17 (2016), p. 172002. DOI: 10.1088/0953-4075/49/17/172002.

[132] A. Harth, C. Guo, Y.-C. Cheng, A. Losquin, M. Miranda, S. Mikaelsson, C. M. Heyl, O. Prochnow, J. Ahrens, U. Morgner, et al. "Compact 200 kHz HHG source driven by a few-cycle OPCPA." In: *Journal of Optics* 20.1 (2017), p. 014007. DOI: 10.1088/2040-8986/aa9b04.

[133] P. Salières, B. Carré, L. L. Déroff, F. Grasbon, G. G. Paulus, H. Walther, R. Kopold, W. Becker, D. B. Milošević, A. Sanpera, and M. Lewenstein. "Feynman's Path-Integral Approach for Intense-Laser-Atom Interactions." In: *Science* 292.5518 (2001), pp. 902–905. DOI: 10.1126/science.108836.

[134] P. Agostini, F. Fabre, G. Mainfray, G. Petite, and N. K. Rahman. "Free-Free Transitions Following Six-Photon Ionization of Xenon Atoms." In: *Physical Review Letters* 42.17 (1979), pp. 1127–1130. DOI: 10.1103/physrevlett.42.1127.

[135] B. J. Whitaker. *Imaging in molecular dynamics: technology and applications*. Cambridge university press, 2003.

[136] A. T. J. B. Eppink and D. H. Parker. "Velocity map imaging of ions and electrons using electrostatic lenses: Application in photoelectron and photofragment ion imaging of molecular oxygen." In: *Review of Scientific Instruments* 68.9 (1997), pp. 3477–3484. DOI: 10.1063/1.1148310.

[137] D. W. Chandler and P. L. Houston. "Two-dimensional imaging of state-selected photodissociation products detected by multiphoton ionization." In: *The Journal of Chemical Physics* 87.2 (1987), pp. 1445–1447. DOI: 10.1063/1.453276.

[138] D. H. Parker and A. T. J. B. Eppink. "Photoelectron and photofragment velocity map imaging of state-selected molecular oxygen dissociation/ionization dynamics." In: *The Journal of Chemical Physics* 107.7 (1997), pp. 2357–2362. DOI: 10.1063/1.474624.

[139] M. N. R. Ashfold, N. H. Nahler, A. J. Orr-Ewing, O. P. J. Vieuxmaire, R. L. Toomes, T. N. Kitsopoulos, I. A. Garcia, D. A. Chestakov, S.-M. Wu, and D. H. Parker. "Imaging the dynamics of gas phase reactions." In: *Phys. Chem. Chem. Phys.* 8.1 (2006), pp. 26–53. DOI: 10.1039/B509304J.

[140] K. T. Lorenz, D. W. Chandler, J. W. Barr, W. Chen, G. L. Barnes, and J. I. Cline. "Direct Measurement of the Preferred Sense of NO Rotation After Collision with Argon." In: *Science* 293.5537 (2001), pp. 2063–2066. DOI: 10.1126/science.1062754.

[141] D. M. Neumark. "Slow Electron Velocity-Map Imaging of Negative Ions: Applications to Spectroscopy and Dynamics." In: *The Journal of Physical Chemistry A* 112.51 (2008), pp. 13287–13301. DOI: 10.1021/jp807182q.

[142] M. Nisoli, P. Decleva, F. Calegari, A. Palacios, and F. Martín. "Attosecond Electron Dynamics in Molecules." In: *Chemical Reviews* 117.16 (2017), pp. 10760–10825. DOI: 10.1021/acs.chemrev.6b00453.

[143] D. Townsend, M. P. Minitti, and A. G. Suits. "Direct current slice imaging." In: *Review of Scientific Instruments* 74.4 (2003), pp. 2530–2539. DOI: 10.1063/1.1544053.

[144] D. A. Horke, G. M. Roberts, J. Lecointre, and J. R. R. Verlet. "Velocity-map imaging at low extraction fields." In: *Review of Scientific Instruments* 83.6 (2012), p. 063101. DOI: 10.1063/1.4724311.

[145] Y. Huismans, A. Rouzee, A. Gijsbertsen, J. H. Jungmann, A. S. Smolkowska, P. S. W. M. Logman, F. Lepine, C. Cauchy, S. Zamith, T. Marchenko, et al. "Time-Resolved Holography with Photoelectrons." In: *Science* 331.6013 (2010), pp. 61–64. DOI: 10.1126/science.1198450.

[146] S. Zherebtsov, T. Fennel, J. Plenge, E. Antonsson, I. Znakovskaya, A. Wirth, O. Herrwerth, F. Süßmann, C. Peltz, I. Ahmad, et al. "Controlled near-field enhanced electron acceleration from dielectric nanospheres with intense few-cycle laser fields." In: *Nature Physics* 7.8 (2011), pp. 656–662. DOI: 10.1038/nphys1983.

[147] T. Remetter, P. Johnsson, J. Mauritsson, K. Varjú, Y. Ni, F. Lépine, E. Gustafsson, M. Kling, J. Khan, R. López-Martens, et al. "Attosecond electron wave packet interferometry." In: *Nature Physics* 2.5 (2006), pp. 323–326. DOI: 10.1038/nphys290.

[148] J. Mauritsson, P. Johnsson, E. Mansten, M. Swoboda, T. Ruchon, A. L'Huillier, and K. J. Schafer. "Coherent Electron Scattering Captured by an Attosecond Quantum Stroboscope." In: *Physical Review Letters* 100.7 (2008), p. 073003. DOI: 10.1103/physrevlett.100.073003.

[149] G. Sansone, F. Kelkensberg, J. F. Pérez-Torres, F. Morales, M. F. Kling, W. Siu, O. Ghafur, P. Johnsson, M. Swoboda, E. Benedetti, et al. "Electron localization following attosecond molecular photoionization." In: *Nature* 465.7299 (2010), pp. 763–766. DOI: 10.1038/nature09084.

[150] D. M. Villeneuve, P. Peng, and H. Niikura. "Complete characterization of attosecond photoelectron wave packets." In: *Physical Review A* 104.5 (2021), p. 053526. DOI: 10.1103/physreva.104.053526.

[151] M. Weger, J. Maurer, A. Ludwig, L. Gallmann, and U. Keller. "Transferring the attoclock technique to velocity map imaging." In: *Optics Express* 21.19 (2013), p. 21981. DOI: 10.1364/oe.21.021981.

[152] R. Dörner, V. Mergel, O. Jagutzki, L. Spielberger, J. Ullrich, R. Moshammer, and H. Schmidt-Böcking. "Cold Target Recoil Ion Momentum Spectroscopy: a 'momentum microscope' to view atomic collision dynamics." In: *Physics Reports* 330.2-3 (2000), pp. 95–192. DOI: 10.1016/s0370-1573(99)00109-x.

[153] J. Ullrich, R. Moshammer, A. Dorn, R. Dörner, L. P. H. Schmidt, and H. Schmidt-Böcking. "Recoil-ion and electron momentum spectroscopy: reaction-microscopes." In: *Reports on Progress in Physics* 66.9 (2003), pp. 1463–1545. DOI: 10.1088/0034-4885/66/9/203.

[154] D. Rolles, Z. D. Pešić, M. Perri, R. C. Bilodeau, G. D. Ackerman, B. S. Rude, A. L. D. Kilcoyne, J. D. Bozek, and N. Berrah. "A velocity map imaging spectrometer for electron–ion and ion–ion coincidence experiments with synchrotron radiation." In: *Nuclear Instruments and Methods in Physics Research Section B: Beam Interactions with Materials and Atoms* 261.1-2 (2007), pp. 170–174. DOI: 10.1016/j.nimb.2007.04.186.

[155] A. Vredenborg, W. G. Roeterdink, and M. H. M. Janssen. "A photoelectron-photoion coincidence imaging apparatus for femtosecond time-resolved molecular dynamics with electron time-of-flight resolution of 18ps and energy resolution 3.5 percent." In: *Review of Scientific Instruments* 79.6 (2008), p. 063108. DOI: 10.1063/1.2949142.

[156] C. S. Lehmann, N. B. Ram, and M. H. M. Janssen. "Velocity map photoelectron-photoion coincidence imaging on a single detector." In: *Review of Scientific Instruments* 83.9 (2012), p. 093103. DOI: 10.1063/1.4749843.

[157] A. Zhao, M. van Beuzekom, B. Bouwens, D. Byelov, I. Chakaberia, C. Cheng, E. Maddox, A. Nomerotski, P. Svihra, J. Visser, et al. "Coincidence velocity map imaging using Tpx3Cam, a time stamping optical camera with 1.5 ns timing resolution." In: *Review of Scientific Instruments* 88.11 (2017), p. 113104. DOI: 10.1063/1.4996888.

[158] A. Zhao, P. Sándor, and T. Weinacht. "Coincidence velocity map imaging using a single detector." In: *The Journal of Chemical Physics* 147.1 (2017), p. 013922. DOI: 10.1063/1.4981917.

[159] Y. Liu, D. Ye, J. Liu, A. Rudenko, S. Tschuch, M. Dürr, M. Siegel, U. Morgner, Q. Gong, R. Moshammer, and J. Ullrich. "Multiphoton Double Ionization of Ar and Ne Close to Threshold." In: *Physical Review Letters* 104.17 (2010). DOI: 10.1103/physrevlett.104.173002.

[160] F. J. Furch, S. Birkner, F. Kelkensberg, A. Giree, A. Anderson, C. P. Schulz, and M. J. J. Vrakking. "Carrier-envelope phase stable few-cycle pulses at 400 kHz for electron-ion coincidence experiments." In: *Optics Express* 21.19 (2013), p. 22671. DOI: 10.1364/oe.21.022671.

[161] M. Baudisch, B. Wolter, M. Pullen, M. Hemmer, and J. Biegert. "High power multi-color OPCPA source with simultaneous femtosecond deep-UV to mid-IR outputs." In: *Optics Letters* 41.15 (2016), p. 3583. DOI: 10.1364/ol.41.003583.

[162] B. Wolter, M. G. Pullen, M. Baudisch, M. Sclafani, M. Hemmer, A. Senftleben, C. D. Schröter, J. Ullrich, R. Moshammer, and J. Biegert. "Strong-Field Physics with Mid-IR Fields." In: *Physical Review X* 5.2 (2015). DOI: 10.1103/physrevx.5.021034.

[163] G. G. Paulus, F. Grasbon, A. Dreischuh, H. Walther, R. Kopold, and W. Becker. "Above-Threshold Ionization by an Elliptically Polarized Field: Interplay between Electronic Quantum Trajectories." In: *Physical Review Letters* 84.17 (2000), pp. 3791–3794. DOI: 10.1103/physrevlett.84.3791.

[164] E. Eremina, X. Liu, H. Rottke, W. Sandner, A. Dreischuh, F. Lindner, F. Grasbon, G. G. Paulus, H. Walther, R. Moshammer, et al. "Laser-induced non-sequential double ionization investigated at and below the threshold for electron impact ionization." In: *Journal of Physics B: Atomic, Molecular and Optical Physics* 36.15 (2003), pp. 3269–3280. DOI: 10.1088/0953-4075/36/15/308.

[165] M. Kübel, M. Arbeiter, C. Burger, N. G. Kling, T. Pischke, R. Moshammer, T. Fennel, M. F. Kling, and B. Bergues. "Phase- and intensity-resolved measurements of above threshold ionization by few-cycle pulses." In: *Journal of Physics B: Atomic, Molecular and Optical Physics* 51.13 (2018), p. 134007. DOI: 10.1088/1361-6455/aac584.

[166] M. Li, Y. Liu, H. Liu, Y. Yang, J. Yuan, X. Liu, Y. Deng, C. Wu, and Q. Gong. "Photoelectron angular distributions of low-order above-threshold ionization of Xe in the multiphoton regime." In: *Physical Review A* 85.1 (2012), p. 013414. DOI: 10.1103/physreva.85.013414.

[167] M. Goto and K. Hansen. "Branching ratio between resonant and non-resonant ionization of xenon evaluated from photoelectron angular distributions." In: *Physica Scripta* 86.3 (2012), p. 035303. DOI: 10.1088/0031-8949/86/03/035303.

[168] P. Kaminski, R. Wiehle, V. Renard, A. Kazmierczak, B. Lavorel, O. Faucher, and B. Witzel. "Wavelength dependence of multiphoton ionization of xenon." In: *Physical Review A* 70.5 (2004), p. 053413. DOI: 10.1103/physreva.70.053413.

[169] B. Bergues, S. Zherebtsov, Y. Deng, X. Gu, I. Znakovskaya, R. Kienberger, F. Krausz, G. Marcus, and M. F. Kling. "Sub-cycle electron control in the photoionization of xenon using a few-cycle laser pulse in the mid-infrared." In: *New Journal of Physics* 13.6 (2011), p. 063010. DOI: 10.1088/1367-2630/13/6/063010.

[170] H. Helm, N. Bjerre, M. J. Dyer, D. L. Huestis, and M. Saeed. "Images of photoelectrons formed in intense laser fields." In: *Physical Review Letters* 70 (1993), pp. 3221–3224. DOI: 10.1103/PhysRevLett.70.3221.

[171] C. Marceau, G. Gingras, and B. Witzel. "Excitation with Effective Subcycle Laser Pulses." In: *Physical Review Letters* 111.20 (2013), p. 203005. DOI: 10.1103/physrevlett.111.203005.

[172] C. I. Blaga, F. Catoire, P. Colosimo, G. G. Paulus, H. G. Muller, P. Agostini, and L. F. DiMauro. "Strong-field photoionization revisited." In: *Nature Physics* 5.5 (2009), pp. 335–338. DOI: 10.1038/nphys1228.

[173] D. D. Hickstein, P. Ranitovic, S. Witte, X.-M. Tong, Y. Huismans, P. Arpin, X. Zhou, K. E. Keister, C. W. Hogle, B. Zhang, et al. "Direct Visualization of Laser-Driven Electron Multiple Scattering and Tunneling Distance in Strong-Field Ionization." In: *Physical Review Letters* 109.7 (2012), p. 073004. DOI: 10.1103/physrevlett.109.073004.

[174] C. T. L. Smeenk, L. Arissian, B. Zhou, A. Mysyrowicz, D. M. Villeneuve, A. Staudte, and P. B. Corkum. "Partitioning of the Linear Photon Momentum in Multiphoton Ionization." In: *Physical Review Letters* 106.19 (2011), p. 193002. DOI: 10.1103/physrevlett. 106.193002.

[175] A. Hartung, S. Eckart, S. Brennecke, J. Rist, D. Trabert, K. Fehre, M. Richter, H. Sann, S. Zeller, K. Henrichs, et al. "Magnetic fields alter strong-field ionization." In: *Nature Physics* (2019). DOI: 10.1038/s41567-019-0653-y.

[176] K. Lin, S. Brennecke, H. Ni, X. Chen, A. Hartung, D. Trabert, K. Fehre, J. Rist, X.-M. Tong, J. Burgdörfer, et al. "Magnetic-Field Effect in High-Order Above-Threshold Ionization." In: *Physical Review Letters* 128.2 (2022), p. 023201. DOI: 10.1103/physrevlett.128. 023201.

[177] A. Hartung, S. Brennecke, K. Lin, D. Trabert, K. Fehre, J. Rist, M. Schöffler, T. Jahnke, L. P. H. Schmidt, M. Kunitski, et al. "Electric Nondipole Effect in Strong-Field Ionization." In: *Physical Review Letters* 126.5 (2021), p. 053202. DOI: 10.1103/physrevlett. 126.053202.

[178] J. Peatross, S. Voronov, and I. Prokopovich. "Selective zoning of high harmonic emission using counter-propagating light." In: *Optics Express* 1.5 (1997), p. 114. DOI: 10.1364/oe. 1.000114.

[179] S. L. Voronov, I. Kohl, J. B. Madsen, J. Simmons, N. Terry, J. Titensor, Q. Wang, and J. Peatross. "Control of Laser High-Harmonic Generation with Counterpropagating Light." In: *Physical Review Letters* 87.13 (2001). DOI: 10.1103/physrevlett.87.133902.

[180] X. Zhang, A. L. Lytle, T. Popmintchev, X. Zhou, H. C. Kapteyn, M. M. Murnane, and O. Cohen. "Quasi-phase-matching and quantum-path control of high-harmonic generation using counterpropagating light." In: *Nature Physics* 3.4 (2007), pp. 270–275. DOI: 10. 1038/nphys541.

[181] O. Cohen, A. L. Lytle, X. Zhang, M. M. Murnane, and H. C. Kapteyn. "Optimizing quasi-phase matching of high harmonic generation using counterpropagating pulse trains." In: *Optics Letters* 32.20 (2007), p. 2975. DOI: 10.1364/ol.32.002975.

[182] P. L. Kapitza and P. A. M. Dirac. "The reflection of electrons from standing light waves." In: *Mathematical Proceedings of the Cambridge Philosophical Society* 29.2 (1933), pp. 297– 300. DOI: 10.1017/s0305004100011105.

[183] P. H. Bucksbaum, D. W. Schumacher, and M. Bashkansky. "High-Intensity Kapitza-Dirac Effect." In: *Physical Review Letters* 61.10 (1988), pp. 1182–1185. DOI: 10.1103/physrevl ett.61.1182.

[184] D. L. Freimund, K. Aflatooni, and H. Batelaan. "Observation of the Kapitza-Dirac effect." In: *Nature* 413.6852 (2001), pp. 142–143. DOI: 10.1038/35093065.

[185] C. Solaro, C. Debavelaere, P. Cladé, and S. Guellati-Khelifa. "Atom Interferometer Driven by a Picosecond Frequency Comb." In: *Physical Review Letters* 129.17 (2022), p. 173204. DOI: 10.1103/physrevlett.129.173204.

[186] C. Wieman and T. W. Hänsch. "Doppler-Free Laser Polarization Spectroscopy." In: *Physical Review Letters* 36.20 (1976), pp. 1170–1173. DOI: 10.1103/physrevlett.36.1170.

[187] G. Grynberg and B. Cagnac. "Doppler-free multiphotonic spectroscopy." In: *Reports on Progress in Physics* 40.7 (1977), pp. 791–841. DOI: 10.1088/0034-4885/40/7/002.

[188] D. Pengel, S. Kerbstadt, L. Englert, T. Bayer, and M. Wollenhaupt. "Control of three-dimensional electron vortices from femtosecond multiphoton ionization." In: *Physical Review A* 96.4 (2017), p. 043426. DOI: 10.1103/physreva.96.043426.

[189] D. Pengel, S. Kerbstadt, D. Johannmeyer, L. Englert, T. Bayer, and M. Wollenhaupt. "Electron Vortices in Femtosecond Multiphoton Ionization." In: *Physical Review Letters* 118.5 (2017), p. 053003. DOI: 10.1103/physrevlett.118.053003.

[190] S. Kerbstadt, K. Eickhoff, T. Bayer, and M. Wollenhaupt. "Odd electron wave packets from cycloidal ultrashort laser fields." In: *Nature Communications* 10.1 (2019), p. 658. DOI: 10.1038/s41467-019-08601-7.

[191] H. Stapelfeldt and T. Seideman. "Colloquium: Aligning molecules with strong laser pulses." In: *Reviews of Modern Physics* 75.2 (2003), pp. 543–557. DOI: 10.1103/revmodphys.75.543.

[192] S. Fleischer, Y. Khodorkovsky, E. Gershnabel, Y. Prior, and I. S. Averbukh. "Molecular Alignment Induced by Ultrashort Laser Pulses and Its Impact on Molecular Motion." In: *Israel Journal of Chemistry* 52.5 (2012), pp. 414–437. DOI: 10.1002/ijch.201100161.

[193] E. Gershnabel and I. Averbukh. "Orienting Asymmetric Molecules by Laser Fields with Twisted Polarization." In: *Physical Review Letters* 120.8 (2018), p. 083204. DOI: 10.1103/physrevlett.120.083204.

[194] C. P. Koch, M. Lemeshko, and D. Sugny. "Quantum control of molecular rotation." In: *Reviews of Modern Physics* 91.3 (2019), p. 035005. DOI: 10.1103/revmodphys.91.035005.

[195] J.-C. Diels and W. Rudolph. *Ultrashort Laser Pulse Phenomena*. Elsevier, 2006. DOI: 10.1016/b978-0-12-215493-5.x5000-9.

[196] R. Trebino. *Lecture notes: Ultrafast Optics Course*. https://frog.gatech.edu/talks.html. [Online; accessed 20-December-2022]. 2022.

[197] U. Morgner. *Lecture notes: Optik und Photonik*. 2009.

[198] D. Strickland. "Nobel Lecture: Generating high-intensity ultrashort optical pulses." In: *Reviews of Modern Physics* 91.3 (2019), p. 030502. DOI: 10.1103/revmodphys.91.030502.

[199] D. Kuizenga and A. Siegman. "FM and AM mode locking of the homogeneous laser - Part I: Theory." In: *IEEE Journal of Quantum Electronics* 6.11 (1970), pp. 694–708. DOI: 10.1109/jqe.1970.1076343.

[200] H. A. Haus. "Mode-locking of lasers." In: *IEEE Journal of Selected Topics in Quantum Electronics* 6.6 (2000), pp. 1173–1185. DOI: 10.1109/2944.902165.

[201] U. Keller, K. Weingarten, F. Kartner, D. Kopf, B. Braun, I. Jung, R. Fluck, C. Honninger, N. Matuschek, and J. A. der Au. "Semiconductor saturable absorber mirrors (SESAM's) for femtosecond to nanosecond pulse generation in solid-state lasers." In: *IEEE Journal of Selected Topics in Quantum Electronics* 2.3 (1996), pp. 435–453. DOI: 10.1109/2944.571743.

[202] H. Haus, E. Ippen, and K. Tamura. "Additive-pulse modelocking in fiber lasers." In: *IEEE Journal of Quantum Electronics* 30.1 (1994), pp. 200–208. DOI: 10.1109/3.272081.

[203] U. Morgner, F. X. Kätner, S. H. Cho, Y. Chen, H. A. Haus, J. G. Fujimoto, E. P. Ippen, V. Scheuer, G. Angelow, and T. Tschudi. "Sub-two-cycle pulses from a Kerr-lens mode-locked Ti:sapphire laser." In: *Optics Letters* 24.6 (1999), p. 411. DOI: 10.1364/ol.24.000411.

[204] S. T. Cundiff. "Phase stabilization of ultrashort optical pulses." In: *Journal of Physics D: Applied Physics* 35.8 (2002), pp. 43–59. DOI: 10.1088/0022-3727/35/8/201.

[205] T. Fortier and E. Baumann. "20 years of developments in optical frequency comb technology and applications." In: *Communications Physics* 2.1 (2019). DOI: 10.1038/s42005-019-0249-y.

[206] R. Ell, U. Morgner, F. X. Kärtner, J. G. Fujimoto, E. P. Ippen, V. Scheuer, G. Angelow, T. Tschudi, M. J. Lederer, A. Boiko, and B. Luther-Davies. "Generation of 5-fs pulses and octave-spanning spectra directly from a Ti:sapphire laser." In: *Optics Letters* 26.6 (2001), pp. 373–375. DOI: 10.1364/OL.26.000373.

[207] T. M. Fortier, D. J. Jones, and S. T. Cundiff. "Phase stabilization of an octave-spanning Ti:sapphire laser." In: *Optics Letters* 28.22 (2003), p. 2198. DOI: 10.1364/ol.28.002198.

[208] L. Matos, D. Kleppner, O. Kuzucu, T. R. Schibli, J. Kim, E. P. Ippen, and F. X. Kaertner. "Direct frequency comb generation from an octave-spanning, prismless Ti:sapphire laser." In: *Optics Letters* 29.14 (2004), p. 1683. DOI: 10.1364/ol.29.001683.

[209] N. Hodgson. *Laser resonators and beam propagation. fundamentals, advanced concepts and applications*. Springer, 2005.

[210] O. Svelto. *Principles of Lasers*. Springer US, 2010. DOI: 10.1007/978-1-4419-1302-9.

[211] H. Kogelnik and T. Li. "Laser Beams and Resonators." In: *Applied Optics* 5.10 (1966), p. 1550. DOI: 10.1109/proc.1966.5119.

[212] O. Martinez. "Matrix formalism for dispersive laser cavities." In: *IEEE Journal of Quantum Electronics* 25.3 (1989), pp. 296–300. DOI: 10.1109/3.18543.

[213] L. G. Gouy. *Sur une propriété nouvelle des ondes lumineuses*. Gauthier-Villars, 1890.

[214] D. Meschede. *Optik, Licht und Laser*. 3rd ed. Springer, 2008.

[215] A. E. Siegman. *Lasers*. University science books, 1986.

[216] H. Abitan and T. Skettrup. "Laser resonators with several mirrors and lenses with the bow-tie laser resonator with compensation for astigmatism and thermal lens effects as an example." In: *Journal of Optics A: Pure and Applied Optics* 7.1 (2005), p. 7. DOI: 10.1088/1464-4258/7/1/002.

[217] D. C. Yost. "Development of an Extreme Ultraviolet Frequency Comb for Precision Spectroscopy." PhD thesis. University of Colorado, 2011.

[218] W. Nagourney. *Quantum Electronics for Atomic Physics and Telecommunication*. Oxford University Press, 2014. DOI: 10.1093/acprof:oso/9780199665488.001.0001.

[219] C. Benko. "Extreme ultraviolet frequency combs for precision measurement and strong-field physics." PhD thesis. University of Colorado, 2016.

[220] J. Ye, H. Schnatz, and L. Hollberg. "Optical frequency combs: From frequency metrology to optical phase control." In: *IEEE Journal of Selected Topics in Quantum Electronics* 9.4 (2003), pp. 1041–1058. DOI: 10.1109/jstqe.2003.819109.

[221] M. J. Thorpe, R. J. Jones, K. D. Moll, J. Ye, and R. Lalezari. "Precise measurements of optical cavity dispersion and mirror coating properties via femtosecond combs." In: *Optics Express* 13.3 (2005), pp. 882–888. DOI: 10.1364/OPEX.13.000882.

[222] T. Hammond, A. K. Mills, and D. J. Jones. "Simple method to determine dispersion of high-finesse optical cavities." In: *Optics Express* 17.11 (2009), pp. 8998–9005. DOI: 10.1364/OE.17.008998.

[223] T. J. Hammond. "Intracavity generation of high order harmonics." PhD thesis. University of British Columbia, 2011.

[224] A. Gerrard and J. M. Burch. *Introduction to matrix methods in optics*. Courier Corporation, 1994.

[225] E. Hecht. *Optics*. Pearson Education India, 2012.

[226] W. A. Shurcliff. *Polarized light*. Harvard University Press, 2013.

[227] C. Sparling and D. Townsend. "Tomographic reconstruction techniques optimized for velocity-map imaging applications." In: *The Journal of Chemical Physics* 157.11 (2022), p. 114201. DOI: 10.1063/5.0101789.

[228] N. H. Abel. "Auflösung einer mechanischen Aufgabe." In: *Journal für die reine und angewandte Mathematik (Crelles Journal)* 1826.1 (1826), pp. 153–157. DOI: 10.1515/crll.1826.1.153.

[229] C. R. Gebhardt, T. P. Rakitzis, P. C. Samartzis, V. Ladopoulos, and T. N. Kitsopoulos. "Slice imaging: A new approach to ion imaging and velocity mapping." In: *Review of Scientific Instruments* 72.10 (2001), pp. 3848–3853. DOI: 10.1063/1.1403010.

[230] S. K. Lee, Y. F. Lin, S. Lingenfelter, L. Fan, A. H. Winney, and W. Li. "Communication: Time- and space-sliced velocity map electron imaging." In: *The Journal of Chemical Physics* 141.22 (2014), p. 221101. DOI: 10.1063/1.4903744.

[231] C. Cheng, G. Moğol, T. Weinacht, A. Nomerotski, and C. Trallero-Herrero. "3D velocity map imaging of electrons with TPX3CAM." In: *Review of Scientific Instruments* 93.1 (2022), p. 013003. DOI: 10.1063/5.0071804.

[232] M. Wollenhaupt, M. Krug, J. Köhler, T. Bayer, C. Sarpe-Tudoran, and T. Baumert. "Three-dimensional tomographic reconstruction of ultrashort free electron wave packets." In: *Applied Physics B* 95.4 (2009), pp. 647–651. DOI: 10.1007/s00340-009-3513-0.

[233] C. Smeenk, L. Arissian, A. Staudte, D. M. Villeneuve, and P. B. Corkum. "Momentum space tomographic imaging of photoelectrons." In: *Journal of Physics B: Atomic, Molecular and Optical Physics* 42.18 (2009), p. 185402. DOI: 10.1088/0953-4075/42/18/185402.

[234] P. Hockett, M. Staniforth, and K. L. Reid. "Photoelectron angular distributions from rotationally state-selected $NH_3(B^1E'')$: dependence on ion rotational state and polarization geometry." In: *Molecular Physics* 108.7-9 (2010), pp. 1045–1054. DOI: 10.1080/00268971003639266.

[235] J. Maurer, D. Dimitrovski, L. Christensen, L. B. Madsen, and H. Stapelfeldt. "Molecular-Frame 3D Photoelectron Momentum Distributions by Tomographic Reconstruction." In: *Physical Review Letters* 109.12 (2012), p. 123001. DOI: 10.1103/physrevlett.109.123001.

[236] M. J. J. Vrakking. "An iterative procedure for the inversion of two-dimensional ion/photoelectron imaging experiments." In: *Review of Scientific Instruments* 72.11 (2001), pp. 4084–4089. DOI: 10.1063/1.1406923.

[237] V. Dribinski, A. Ossadtchi, V. A. Mandelshtam, and H. Reisler. "Reconstruction of Abel-transformable images: The Gaussian basis-set expansion Abel transform method." In: *Review of Scientific Instruments* 73.7 (2002), pp. 2634–2642. DOI: 10.1063/1.1482156.

[238] D. D. Hickstein, S. T. Gibson, R. Yurchak, D. D. Das, and M. Ryazanov. "A direct comparison of high-speed methods for the numerical Abel transform." In: *Review of Scientific Instruments* 90.6 (2019), p. 065115. DOI: 10.1063/1.5092635.

[239] C. Sparling, A. Ruget, J. Leach, and D. Townsend. "Arbitrary image reinflation: A deep learning technique for recovering 3D photoproduct distributions from a single 2D projection." In: *Review of Scientific Instruments* 93.2 (2022), p. 023303. DOI: 10.1063/5.0082744.

[240] E. Seeram. *Computed Tomography - E-Book*. Elsevier HealthScience, 2015.

[241] A. C. Kak. *Principles of computerized tomographic imaging*. IEEE Press, 1988.

[242] J. Radon. "Über die Bestimmung von Funktionen durch ihre Integralwerte längs gewisser Mannigfaltigkeiten." In: *Berichte über die Verhandlungen der Königlich-Sächsischen Akademie der Wissenschaften zu Leipzig, Mathematisch-Physische Klasse 69* (1917), pp. 262–277.

[243] S. van der Walt, J. L. Schönberger, J. Nunez-Iglesias, F. Boulogne, J. D. Warner, N. Yager, E. Gouillart, and T. Yu. "scikit-image: image processing in Python." In: *PeerJ* 2 (2014). DOI: 10.7717/peerj.453.

[244] V. Wössner. "Tomographische Rekonstruktion dreidimensionaler Photoelektronen-verteilungen mittels intra-cavity Velocity Map Imaging." Bachelor thesis. Ruprecht-Karls-Universität, Heidelberg, 2020.

[245] A. Einstein. "Über einen die Erzeugung und Verwandlung des Lichtes betreffenden heuristischen Gesichtspunkt." In: *Annalen der Physik* 322.6 (1905), pp. 132–148. DOI: 10.1002/andp.19053220607.

[246] M. Göppert-Mayer. "Über Elementarakte mit zwei Quantensprüngen." In: *Annalen der Physik* 401.3 (1931), pp. 273–294. DOI: 10.1002/andp.19314010303.

[247] W. Kaiser and C. G. B. Garrett. "Two-Photon Excitation in CaF_2:Eu^{2+}." In: *Physical Review Letters* 7.6 (1961), pp. 229–231. DOI: 10.1103/physrevlett.7.229.

[248] A. L. Schawlow and C. H. Townes. "Infrared and Optical Masers." In: *Physical Review* 112.6 (1958), pp. 1940–1949. DOI: 10.1103/physrev.112.1940.

[249] A. M. Zheltikov. "Keldysh photoionization theory: through the barriers." In: *Physics-Uspekhi* 60.11 (2017), pp. 1087–1120. DOI: 10.3367/ufne.2017.08.038198.

[250] L. Keldysh. "Ionization in the field of a strong electromagnetic wave." In: *Sov. Phys. JETP* 20.5 (1965), pp. 1307–1314.

[251] G. G. Paulus. *Multiphotonenionisation mit intensiven, ultrakurzen Laserpulsen*. Herbert Utz Verlag, 1996.

[252] W. Becker, F. Grasbon, R. Kopold, D. Milošević, G. Paulus, and H. Walther. "Above-Threshold Ionization: From Classical Features to Quantum Effects." In: *Advances In Atomic, Molecular, and Optical Physics*. Vol. 48. Elsevier, 2002, pp. 35–98. DOI: 10.1016/s1049-250x(02)80006-4.

[253] J. E. Hansen and W. Persson. "Revised analysis of singly ionized xenon, Xe II." In: *Physica Scripta* 36.4 (1987), pp. 602–643. DOI: 10.1088/0031-8949/36/4/005.

[254] Z. Chang. *Fundamentals of attosecond optics*. CRC press, 2016.

[255] R. R. Freeman and P. H. Bucksbaum. "Investigations of above-threshold ionization using subpicosecond laser pulses." In: *Journal of Physics B: Atomic, Molecular and Optical Physics* 24.2 (1991), pp. 325–347. DOI: 10.1088/0953-4075/24/2/004.

[256] R. R. Freeman, P. H. Bucksbaum, H. Milchberg, S. Darack, D. Schumacher, and M. E. Geusic. "Above-threshold ionization with subpicosecond laser pulses." In: *Phys. Rev. Lett.* 59 (1987), pp. 1092–1095. DOI: 10.1103/PhysRevLett.59.1092.

[257] P. Hansch, M. A. Walker, and L. D. Van Woerkom. "Eight- and nine-photon resonances in multiphoton ionization of xenon." In: *Physical Review A* 57.2 (1998), pp. 709–712. DOI: 10.1103/PhysRevA.57.R709.

[258] V. Schyja, T. Lang, and H. Helm. "Channel switching in above-threshold ionization of xenon." In: *Physical Review A* 57.5 (1998), pp. 3692–3697. DOI: 10.1103/PhysRevA.57.3692.

[259] Y. Huismans, A. Rouzée, A. Gijsbertsen, P. S. W. M. Logman, F. Lépine, C. Cauchy, S. Zamith, A. S. Stodolna, J. H. Jungmann, J. M. Bakker, et al. "Photoelectron angular distributions from the ionization of xenon Rydberg states by midinfrared radiation." In: *Physical Review A* 87.3 (2013). DOI: 10.1103/physreva.87.033413.

[260] L. Zhang, Z. Miao, W. Zheng, X. Zhong, and C. Wu. "Nonresonant multiphoton ionization of xenon atoms by femtosecond laser pulses." In: *Chemical Physics* 523 (2019), pp. 52–56. DOI: 10.1016/j.chemphys.2019.04.005.

[261] A. Kramida and Y. Ralchenko. *NIST Atomic Spectra Database, NIST Standard Reference Database 78*. 1999. DOI: 10.18434/T4W30F.

[262] P. Kruit, J. Kimman, H. G. Muller, and M. J. van der Wiel. "Electron spectra from multiphoton ionization of xenon at 1064, 532, and 355 nm." In: *Physical Review A* 28.1 (1983), pp. 248–255. DOI: 10.1103/physreva.28.248.

[263] H. G. Muller, A. Tip, and M. J. van der Wiel. "Ponderomotive force and AC Stark shift in multiphoton ionisation." In: *Journal of Physics B: Atomic and Molecular Physics* 16.22 (1983), pp. 679–685. DOI: 10.1088/0022-3700/16/22/001.

[264] C. J. Joachain. "Atoms in intense laser fields." In: *AIP Conference Proceedings*. AIP, 1998. DOI: 10.1063/1.55247.

[265] N. B. Delone and V. P. Krainov. "Tunneling and barrier-suppression ionization of atoms and ions in a laser radiation field." In: *Physics-Uspekhi* 41.5 (1998), pp. 469–485. DOI: 10.1070/pu1998v041n05abeh000393.

[266] G. G. Paulus, W. Nicklich, H. Xu, P. Lambropoulos, and H. Walther. "Plateau in above threshold ionization spectra." In: *Physical Review Letters* 72.18 (1994), pp. 2851–2854. DOI: 10.1103/physrevlett.72.2851.

[267] D. N. Fittinghoff, P. R. Bolton, B. Chang, and K. C. Kulander. "Observation of nonsequential double ionization of helium with optical tunneling." In: *Physical Review Letters* 69.18 (1992), pp. 2642–2645. DOI: 10.1103/physrevlett.69.2642.

[268] R. Moshammer, B. Feuerstein, W. Schmitt, A. Dorn, C. D. Schröter, J. Ullrich, H. Rottke, C. Trump, M. Wittmann, G. Korn, et al. "Momentum Distributions of Ne^{n+} Ions Created by an Intense Ultrashort Laser Pulse." In: *Physical Review Letters* 84.3 (2000), pp. 447–450. DOI: 10.1103/physrevlett.84.447.

[269] M. V. Ammosov, N. B. Delone, and V. P. Krainov. "Tunnel ionization of complex atoms and of atomic ions in an alternating electromagnetic field." In: *Soviet Journal of Experimental and Theoretical Physics* 64.6 (1986), p. 1191.

[270] X. M. Tong and C. D. Lin. "Empirical formula for static field ionization rates of atoms and molecules by lasers in the barrier-suppression regime." In: *Journal of Physics B: Atomic, Molecular and Optical Physics* 38.15 (2005), pp. 2593–2600. DOI: 10.1088/0953-4075/38/15/001.

[271] C. Benko. *HHG phase-matching code repository*. [Online: https://github.com/c-benko/HHG_Phasematching; accessed 1-February-2023]. 2016.

[272]   F. H. M. Faisal. "Collision of electrons with laser photons in a background potential." In: *Journal of Physics B: Atomic and Molecular Physics* 6.11 (1973), pp. 312–315. DOI: 10. 1088/0022-3700/6/11/003.

[273]   H. R. Reiss. "Effect of an intense electromagnetic field on a weakly bound system." In: *Physical Review A* 22.5 (1980), pp. 1786–1813. DOI: 10.1103/physreva.22.1786.

[274]   P. B. Corkum. "Plasma perspective on strong field multiphoton ionization." In: *Physical Review Letters* 71.13 (1993), pp. 1994–1997. DOI: 10.1103/physrevlett.71.1994.

[275]   P. B. Corkum and F. Krausz. "Attosecond science." In: *Nature Physics* 3.6 (2007), pp. 381–387. DOI: 10.1038/nphys620.

[276]   P. M. Paul. "Observation of a Train of Attosecond Pulses from High Harmonic Generation." In: *Science* 292.5522 (2001), pp. 1689–1692. DOI: 10.1126/science.1059413.

[277]   K. L. Ishikawa. "High-Harmonic Generation." In: *Advances in Solid State Lasers Development and Applications*. Ed. by M. Grishin. IntechOpen, 2010. DOI: 10.5772/7961.

[278]   M. Lewenstein, P. Balcou, M. Y. Ivanov, A. L'Huillier, and P. B. Corkum. "Theory of high-harmonic generation by low-frequency laser fields." In: *Physical Review A* 49.3 (1994), pp. 2117–2132. DOI: 10.1103/physreva.49.2117.

[279]   M. B. Gaarde, F. Salin, E. Constant, P. Balcou, K. J. Schafer, K. C. Kulander, and A. L'Huillier. "Spatiotemporal separation of high harmonic radiation into two quantum path components." In: *Physical Review A* 59.2 (1999), pp. 1367–1373. DOI: 10.1103/physreva.59.1367.

[280]   C. Heyl. "Scaling and Gating Attosecond Pulse Generation." PhD thesis. Lund University, 2014.

[281]   P. D. Maker, R. W. Terhune, M. Nisenoff, and C. M. Savage. "Effects of Dispersion and Focusing on the Production of Optical Harmonics." In: *Physical Review Letters* 8.1 (1962), pp. 21–22. DOI: 10.1103/physrevlett.8.21.

[282]   A. Rundquist, C. G. Durfee, Z. Chang, C. Herne, S. Backus, M. M. Murnane, and H. C. Kapteyn. "Phase-Matched Generation of Coherent Soft X-rays." In: *Science* 280.5368 (1998), pp. 1412–1415. DOI: 10.1126/science.280.5368.1412.

[283]   T. Popmintchev, M.-C. Chen, A. Bahabad, M. Gerrity, P. Sidorenko, O. Cohen, I. P. Christov, M. M. Murnane, and H. C. Kapteyn. "Phase matching of high harmonic generation in the soft and hard X-ray regions of the spectrum." In: *Proceedings of the National Academy of Sciences* 106.26 (2009), pp. 10516–10521. DOI: 10.1073/pnas.0903748106.

[284]   C. M. Heyl, C. L. Arnold, A. Couairon, and A. L'Huillier. "Introduction to macroscopic power scaling principles for high-order harmonic generation." In: *Journal of Physics B: Atomic, Molecular and Optical Physics* 50.1 (2016), p. 013001. DOI: 10.1088/1361-6455/50/1/013001.

[285]   C. Hernández-García, T. Popmintchev, M. M. Murnane, H. C. Kapteyn, L. Plaja, A. Becker, and A. Jaron-Becker. "Group velocity matching in high-order harmonic generation driven by mid-infrared lasers." In: *New Journal of Physics* 18.7 (2016), p. 073031. DOI: 10.1088/1367-2630/18/7/073031.

[286]   E. Constant, D. Garzella, P. Breger, E. Mével, C. Dorrer, C. L. Blanc, F. Salin, and P. Agostini. "Optimizing High Harmonic Generation in Absorbing Gases: Model and Experiment." In: *Physical Review Letters* 82.8 (1999), pp. 1668–1671. DOI: 10.1103/physrevlett.82.1668.

[287] W. F. Chan, G. Cooper, X. Guo, G. R. Burton, and C. E. Brion. "Absolute optical oscillator strengths for the electronic excitation of atoms at high resolution. III. The photoabsorption of argon, krypton, and xenon." In: *Physical Review A* 46.1 (1992), pp. 149–171. DOI: `10.1103/physreva.46.149`.

[288] R. Weissenbilder, S. Carlström, L. Rego, C. Guo, C. M. Heyl, P. Smorenburg, E. Constant, C. L. Arnold, and A. L'Huillier. "How to optimize high-order harmonic generation in gases." In: *Nature Reviews Physics* (2022). DOI: `10.1038/s42254-022-00522-7`.

[289] R. W. Boyd. *Nonlinear optics*. Academic Press, 2008.

[290] M. Lewenstein, P. Salières, and A. L'Huillier. "Phase of the atomic polarization in high-order harmonic generation." In: *Physical Review A* 52.6 (1995), pp. 4747–4754. DOI: `10.1103/physreva.52.4747`.

[291] C. M. Heyl, J. Güdde, A. L'Huillier, and U. Höfer. "High-order harmonic generation with μJ laser pulses at high repetition rates." In: *Journal of Physics B: Atomic, Molecular and Optical Physics* 45.7 (2012), p. 074020. DOI: `10.1088/0953-4075/45/7/074020`.

[292] C. G. Durfee, A. R. Rundquist, S. Backus, C. Herne, M. M. Murnane, and H. C. Kapteyn. "Phase Matching of High-Order Harmonics in Hollow Waveguides." In: *Physical Review Letters* 83.11 (1999), pp. 2187–2190. DOI: `10.1103/physrevlett.83.2187`.

[293] Á. Börzsönyi, Z. Heiner, A. Kovács, M. P. Kalashnikov, and K. Osvay. "Measurement of pressure dependent nonlinear refractive index of inert gases." In: *Optics Express* 18.25 (2010), p. 25847. DOI: `10.1364/oe.18.025847`.

[294] P. Kabaciński, T. M. Kardaś, Y. Stepanenko, and C. Radzewicz. "Nonlinear refractive index measurement by SPM-induced phase regression." In: *Optics Express* 27.8 (2019), p. 11018. DOI: `10.1364/oe.27.011018`.

[295] M. N. Polyanskiy. *Refractive index database*. [Online: `https://refractiveindex.info`; accessed 23-October-2022].

[296] B. Henke, E. Gullikson, and J. Davis. "X-Ray Interactions: Photoabsorption, Scattering, Transmission, and Reflection at E = 50-30,000 eV, Z = 1-92." In: *Atomic Data and Nuclear Data Tables* 54.2 (1993), pp. 181–342. DOI: `10.1006/adnd.1993.1013`.

[297] L. Tonks and I. Langmuir. "Oscillations in Ionized Gases." In: *Physical Review* 33.2 (1929), pp. 195–210. DOI: `10.1103/physrev.33.195`.

[298] D. Popmintchev, C. Hernández-García, F. Dollar, C. Mancuso, J. A. Pérez-Hernández, M.-C. Chen, A. Hankla, X. Gao, B. Shim, A. L. Gaeta, et al. "Ultraviolet surprise: Efficient soft x-ray high-harmonic generation in multiply ionized plasmas." In: *Science* 350.6265 (2015), pp. 1225–1231. DOI: `10.1126/science.aac9755`.

[299] A. Paul, E. Gibson, X. Zhang, A. Lytle, T. Popmintchev, X. Zhou, M. Murnane, I. Christov, and H. Kapteyn. "Phase-Matching Techniques for Coherent Soft X-Ray Generation." In: *IEEE Journal of Quantum Electronics* 42.1 (2006), pp. 14–26. DOI: `10.1109/jqe.2005.859914`.

[300] J. Rothhardt, M. Krebs, S. Hädrich, S. Demmler, J. Limpert, and A. Tünnermann. "Absorption-limited and phase-matched high harmonic generation in the tight focusing regime." In: *New Journal of Physics* 16.3 (2014), p. 033022. DOI: `10.1088/1367-2630/16/3/033022`.

[301] S. Kraemer, J. Moens, M. Athanasakis-Kaklamanakis, S. Bara, K. Beeks, P. Chhetri, K. Chrysalidis, A. Claessens, T. E. Cocolios, J. M. Correia, et al. *Observation of the radiative decay of the ^{229}Th nuclear clock isomer*. 2022. DOI: `10.48550/ARXIV.2209.10276`.

[302] L. von der Wense, B. Seiferle, S. Stellmer, J. Weitenberg, G. Kazakov, A. Pálffy, and P. G. Thirolf. "A Laser Excitation Scheme for Th229m." In: *Physical Review Letters* 119.13 (2017), p. 132503. DOI: 10.1103/PhysRevLett.119.132503.

[303] B. Seiferle, L. von der Wense, P. V. Bilous, I. Amersdorffer, C. Lemell, F. Libisch, S. Stellmer, T. Schumm, C. E. Düllmann, A. Pálffy, and P. G. Thirolf. "Energy of the 229Th nuclear clock transition." In: *Nature* 573.7773 (2019), pp. 243–246. DOI: 10.1038/s41586-019-1533-4.

[304] S. Angstenberger. "Design of a setup for flexible, dispersion-compensated nonlinear femtosecond laser pulse compression adapted to an extreme ultraviolet frequency comb." Master's thesis. Ruprecht-Karls-Universität, Heidelberg, 2021.

[305] M. Nisoli, S. D. Silvestri, and O. Svelto. "Generation of high energy 10 fs pulses by a new pulse compression technique." In: *Applied Physics Letters* 68.20 (1996), pp. 2793–2795. DOI: 10.1063/1.116609.

[306] A. Suda, M. Hatayama, K. Nagasaka, and K. Midorikawa. "Generation of sub-10-fs, 5-mJ-optical pulses using a hollow fiber with a pressure gradient." In: *Applied Physics Letters* 86.11 (2005), p. 111116. DOI: 10.1063/1.1883706.

[307] F. Böhle, M. Kretschmar, A. Jullien, M. Kovacs, M. Miranda, R. Romero, H. Crespo, U. Morgner, P. Simon, R. Lopez-Martens, and T. Nagy. "Compression of CEP-stable multi-mJ laser pulses down to 4 fs in long hollow fibers." In: *Laser Physics Letters* 11.9 (2014), p. 095401. DOI: 10.1088/1612-2011/11/9/095401.

[308] T. Nagy, L. von Grafenstein, D. Ueberschaer, and U. Griebner. "Femtosecond multi-10-mJ pulses at 2 μm wavelength by compression in a hollow-core fiber." In: *Optics Letters* 46.13 (2021), p. 3033. DOI: 10.1364/ol.426340.

[309] P. Russell. "Photonic crystal fibres." In: *Optical Fiber Communication Conference*. Optical Society of America. 2009.

[310] F. Benabid and P. Roberts. "Linear and nonlinear optical properties of hollow core photonic crystal fiber." In: *Journal of Modern Optics* 58.2 (2011), pp. 87–124. DOI: 10.1080/09500340.2010.543706.

[311] P. S. J. Russell, P. Hölzer, W. Chang, A. Abdolvand, and J. C. Travers. "Hollow-core photonic crystal fibres for gas-based nonlinear optics." In: *Nature Photonics* 8.4 (2014), pp. 278–286. DOI: 10.1038/nphoton.2013.312.

[312] O. H. Heckl, C. J. Saraceno, C. R. E. Baer, T. Südmeyer, Y. Y. Wang, Y. Cheng, F. Benabid, and U. Keller. "Temporal pulse compression in a xenon-filled Kagome-type hollow-core photonic crystal fiber at high average power." In: *Optics Express* 19.20 (2011), p. 19142. DOI: 10.1364/oe.19.019142.

[313] K. F. Mak, J. C. Travers, N. Y. Joly, A. Abdolvand, and P. S. J. Russell. "Two techniques for temporal pulse compression in gas-filled hollow-core kagomé photonic crystal fiber." In: *Optics Letters* 38.18 (2013), p. 3592. DOI: 10.1364/ol.38.003592.

[314] F. Emaury, C. F. Dutin, C. J. Saraceno, M. Trant, O. H. Heckl, Y. Y. Wang, C. Schriber, F. Gerome, T. Südmeyer, F. Benabid, and U. Keller. "Beam delivery and pulse compression to sub-50 fs of a modelocked thin-disk laser in a gas-filled Kagome-type HC-PCF fiber." In: *Optics Express* 21.4 (2013), p. 4986. DOI: 10.1364/oe.21.004986.

[315] K. F. Mak, M. Seidel, O. Pronin, M. H. Frosz, A. Abdolvand, V. Pervak, A. Apolonski, F. Krausz, J. C. Travers, and P. S. J. Russell. "Compressing μJ-level pulses from 250 fs to sub-10 fs at 38-MHz repetition rate using two gas-filled hollow-core photonic crystal fiber stages." In: *Optics Letters* 40.7 (2015), p. 1238. DOI: 10.1364/ol.40.001238.

[316] E. Haddad, R. Safaei, A. Leblanc, R. Piccoli, Y.-G. Jeong, H. Ibrahim, B. E. Schmidt, R. Morandotti, L. Razzari, F. Légaré, and P. Lassonde. "Molecular gases for pulse compression in hollow core fibers." In: *Optics Express* 26.19 (2018), p. 25426. DOI: 10.1364/oe.26.025426.

[317] F. Couny, F. Benabid, P. J. Roberts, P. S. Light, and M. G. Raymer. "Generation and Photonic Guidance of Multi-Octave Optical-Frequency Combs." In: *Science* 318.5853 (2007), pp. 1118–1121. DOI: 10.1126/science.1149091.

[318] S. Février, B. Beaudou, and P. Viale. "Understanding origin of loss in large pitch hollow-core photonic crystal fibers and their design simplification." In: *Optics Express* 18.5 (2010), p. 5142. DOI: 10.1364/oe.18.005142.

[319] F. Emaury, C. J. Saraceno, B. Debord, D. Ghosh, A. Diebold, F. Gèrôme, T. Südmeyer, F. Benabid, and U. Keller. "Efficient spectral broadening in the 100-W average power regime using gas-filled kagome HC-PCF and pulse compression." In: *Optics Letters* 39.24 (2014), p. 6843. DOI: 10.1364/ol.39.006843.

[320] J. K. Ranka, R. S. Windeler, and a. J. Stentz. "Visible continuum generation in air-silica microstructure optical fibers with anomalous dispersion at 800 nm." In: *Optics Letters* 25.1 (2000), pp. 25–27. DOI: 10.1109/CLEO.1999.834609.

[321] J. M. Dudley, S. Coen, and G. Genty. "Supercontinuum generation in photonic crystal fiber." In: *Reviews of Modern Physics* 78.4 (2006), pp. 1135–1184. DOI: 10.1103/RevModPhys.78.1135.

[322] W. H. Reeves, J. C. Knight, P. S. J. Russell, and P. J. Roberts. "Demonstration of ultra-flattened dispersion in photonic crystal fibers." In: *Optics express* 10.14 (2002), pp. 609–613. DOI: 10.1364/OE.10.000609.

[323] A. V. Husakou and J. Herrmann. "Supercontinuum generation, four-wave mixing, and fission of higher-order solitons in photonic-crystal fibers." In: *Journal of the Optical Society of America B* 19.9 (2002), p. 2171. DOI: 10.1364/josab.19.002171.

[324] G. P. Agrawal. *Nonlinear fiber optics*. Academic press, 2007.

[325] A. Demircan, S. Amiranashvili, and G. Steinmeyer. "Controlling light by light with an optical event horizon." In: *Physical Review Letters* 106.16 (2011), p. 163901. DOI: 10.1103/PhysRevLett.106.163901.

[326] I. Babushkin, A. Tajalli, H. Sayinc, J.-H. Oelmann, U. Morgner, G. Steinmeyer, and A. Demircan. "Higher order soliton breakup via implosion." In: *Conference on Lasers and Electro-Optics* (2016). DOI: 10.1364/cleo_si.2016.stu1i.2.

[327] I. Babushkin, A. Tajalli, H. Sayinc, U. Morgner, G. Steinmeyer, and A. Demircan. "Simple route toward efficient frequency conversion for generation of fully coherent supercontinua in the mid-IR and UV range." In: *Light: Science and Applications* 6.2 (2016), pp. 16218–16218. DOI: 10.1038/lsa.2016.218.

[328] G. Genty, T. Ritari, and H. Ludvigsen. "Supercontinuum generation in large mode-area microstructured fibers." In: *Optics Express* 13.21 (2005), p. 8625. DOI: 10.1364/opex.13.008625.

[329] J. R. C. Andrade, N. Modsching, A. Tajalli, C. M. Dietrich, S. Kleinert, F. Placzek, B. Kreipe, S. Schilt, V. J. Wittwer, T. Südmeyer, and U. Morgner. "Carrier-Envelope Offset Frequency Stabilization of a Thin-Disk Laser Oscillator via Depletion Modulation." In: *IEEE Photonics Journal* 12.2 (2020), pp. 1–9. DOI: 10.1109/jphot.2020.2970858.

[330] C.-H. Lu, Y.-J. Tsou, H.-Y. Chen, B.-H. Chen, Y.-C. Cheng, S.-D. Yang, M.-C. Chen, C.-C. Hsu, and A. H. Kung. "Generation of intense supercontinuum in condensed media." In: *Optica* 1.6 (2014), p. 400. DOI: 10.1364/optica.1.000400.

[331] Y.-C. Cheng, C.-H. Lu, Y.-Y. Lin, and A. H. Kung. "Supercontinuum generation in a multi-plate medium." In: *Optics Express* 24.7 (2016), p. 7224. DOI: 10.1364/oe.24.007224.

[332] J. E. Beetar, S. Gholam-Mirzaei, and M. Chini. "Spectral broadening and pulse compression of a $400\mu J$, 20 W Yb:KGW laser using a multi-plate medium." In: *Applied Physics Letters* 112.5 (2018), p. 051102. DOI: 10.1063/1.5018758.

[333] C.-H. Lu, T. Witting, A. Husakou, M. J. Vrakking, A. H. Kung, and F. J. Furch. "Sub-4 fs laser pulses at high average power and high repetition rate from an all-solid-state setup." In: *Optics Express* 26.7 (2018), p. 8941. DOI: 10.1364/oe.26.008941.

[334] D. Herriott, H. Kogelnik, and R. Kompfner. "Off-Axis Paths in Spherical Mirror Interferometers." In: *Applied Optics* 3.4 (1964), p. 523. DOI: 10.1364/ao.3.000523.

[335] D. R. Herriott and H. J. Schulte. "Folded Optical Delay Lines." In: *Applied Optics* 4.8 (1965), p. 883. DOI: 10.1364/ao.4.000883.

[336] A. Javan, W. R. Bennett, and D. R. Herriott. "Population Inversion and Continuous Optical Maser Oscillation in a Gas Discharge Containing a He-Ne Mixture." In: *Physical Review Letters* 6.3 (1961), pp. 106–110. DOI: 10.1103/physrevlett.6.106.

[337] J. Altmann, R. Baumgart, and C. Weitkamp. "Two-mirror multipass absorption cell." In: *Applied Optics* 20.6 (1981), p. 995. DOI: 10.1364/ao.20.000995.

[338] J. B. McManus, P. L. Kebabian, and M. S. Zahniser. "Astigmatic mirror multipass absorption cells for long-path-length spectroscopy." In: *Applied Optics* 34.18 (1995), p. 3336. DOI: 10.1364/ao.34.003336.

[339] F. Adler, P. Masłowski, A. Foltynowicz, K. C. Cossel, T. C. Briles, I. Hartl, and J. Ye. "Mid-infrared Fourier transform spectroscopy with a broadband frequency comb." In: *Optics Express* 18.21 (2010), p. 21861. DOI: 10.1364/oe.18.021861.

[340] A. Sennaroglu and J. Fujimoto. "Design criteria for Herriott-type multi-pass cavities for ultrashort pulse lasers." In: *Optics Express* 11.9 (2003), p. 1106. DOI: 10.1364/oe.11.001106.

[341] G. Palmer, M. Schultze, M. Emons, A. L. Lindemann, M. Pospiech, D. Steingrube, M. Lederer, and U. Morgner. "12 MW peak power from a two-crystal Yb:KYW chirped-pulse oscillator with cavity-dumping." In: *Optics Express* 18.18 (2010), p. 19095. DOI: 10.1364/oe.18.019095.

[342] L. Lavenu, M. Natile, F. Guichard, Y. Zaouter, X. Delen, M. Hanna, E. Mottay, and P. Georges. "Nonlinear pulse compression based on a gas-filled multipass cell." In: *Optics Letters* 43.10 (2018), p. 2252. DOI: 10.1364/ol.43.002252.

[343] M. Ueffing, S. Reiger, M. Kaumanns, V. Pervak, M. Trubetskov, T. Nubbemeyer, and F. Krausz. "Nonlinear pulse compression in a gas-filled multipass cell." In: *Optics Letters* 43.9 (2018), p. 2070. DOI: 10.1364/ol.43.002070.

[344] C. Grebing, M. Müller, J. Buldt, H. Stark, and J. Limpert. "Kilowatt-average-power compression of millijoule pulses in a gas-filled multi-pass cell." In: *Optics Letters* 45.22 (2020), p. 6250. DOI: 10.1364/ol.408998.

[345] J. Schulte, T. Sartorius, J. Weitenberg, A. Vernaleken, and P. Russbueldt. "Nonlinear pulse compression in a multi-pass cell." In: *Optics Letters* 41.19 (2016), p. 4511. DOI: 10.1364/ol.41.004511.

[346]   P. Russbueldt, J. Weitenberg, A. Vernaleken, T. Sartorius, and J. Schulte. *Method and arrangement for spectral broadening of laser pulses for non-linear pulse compression.* US Patent [9,847,615]. 2017.

[347]   M. Hanna, X. Délen, L. Lavenu, F. Guichard, Y. Zaouter, F. Druon, and P. Georges. "Non-linear temporal compression in multipass cells: theory." In: *Journal of the Optical Society of America B* 34.7 (2017), p. 1340. DOI: `10.1364/josab.34.001340`.

[348]   M. Hanna, F. Guichard, N. Daher, Q. Bournet, X. Délen, and P. Georges. "Nonlinear Optics in Multipass Cells." In: *Laser & Photonics Reviews* 15.12 (2021), p. 2100220. DOI: `10.1002/lpor.202100220`.

[349]   M. Seidel, P. Balla, T. Binhammer, M. Frede, G. Arisholm, L. Winkelmann, I. Hartl, and C. M. Heyl. "Hybridizing Multi-pass and Multi-plate Bulk Compression." In: *9th EPS-QEOD Europhoton Conference on Solid-State, Fibre, and Waveguide Coherent Light Sources.* EDP Sciences, 2020. DOI: `10.1051/epjconf/202024321001`.

[350]   M. Seidel, P. Balla, C. Li, G. Arisholm, L. Winkelmann, I. Hartl, and C. M. Heyl. "Factor 30 Pulse Compression by Hybrid Multipass Multiplate Spectral Broadening." In: *Ultrafast Science* 2022 (2022), pp. 1–10. DOI: `10.34133/2022/9754919`.

[351]   A.-L. Viotti, M. Seidel, E. Escoto, S. Rajhans, W. P. Leemans, I. Hartl, and C. M. Heyl. "Multi-pass cells for post-compression of ultrashort laser pulses." In: *Optica* 9.2 (2022), p. 197. DOI: `10.1364/optica.449225`.

[352]   N. Daher, F. Guichard, S. W. Jolly, X. Délen, F. Quéré, M. Hanna, and P. Georges. "Multipass cells: 1D numerical model and investigation of spatio-spectral couplings at high nonlinearity." In: *Journal of the Optical Society of America B* 37.4 (2020), p. 993. DOI: `10.1364/josab.386049`.

[353]   P. Redman, M. Zatorska, A. Pawłowski, D. Szulc, S. Majchrowska, and K. Tarnowski. *gnlse-python: Open Source Software to Simulate Nonlinear Light Propagation In Optical Fibers.* 2021. DOI: `10.48550/arXiv.2110.00298`.

[354]   J. M. Dudley and J. R. Taylor, eds. *Supercontinuum Generation in Optical Fibers.* Cambridge University Press, 2010. DOI: `10.1017/cbo9780511750465`.

[355]   M. Sheik-bahae, A. A. Said, and E. W. V. Stryland. "High-sensitivity, single-beam n_2 measurements." In: *Optics Letters* 14.17 (1989), p. 955. DOI: `10.1364/ol.14.000955`.

[356]   F. DeMartini, C. H. Townes, T. K. Gustafson, and P. L. Kelley. "Self-steepening of light pulses." In: *Physical Review* 164.2 (1967), p. 312. DOI: `10.1103/PhysRev.164.312`.

[357]   G. Yang and Y. R. Shen. "Spectral broadening of ultrashort pulses in a nonlinear medium." In: *Optics Letters* 9.11 (1984), pp. 510–512. DOI: `10.1364/OL.9.000510`.

[358]   R. R. Alfano et al. *The supercontinuum laser source.* Springer, 1989.

[359]   G. Genty, P. Kinsler, B. Kibler, and J. M. Dudley. "Nonlinear envelope equation modeling of sub-cycle dynamics and harmonic generation in nonlinear waveguides." In: *Optics Express* 15.9 (2007), pp. 5382–5387. DOI: `10.1364/OE.15.005382`.

[360]   K. J. Blow and D. Wood. "Theoretical description of transient stimulated Raman scattering in optical fibers." In: *IEEE Journal of Quantum Electronics* 25.12 (1989), pp. 2665–2673. DOI: `10.1109/3.40655`.

[361]   S. C. Pinault and M. J. Potasek. "Frequency broadening by self-phase modulation in optical fibers." In: *Journal of the Optical Society of America B* 2.8 (1985), p. 1318. DOI: `10.1364/josab.2.001318`.

[362] P. F. Moulton. "Spectroscopic and laser characteristics of Ti:Al$_2$O$_3$." In: *Journal of the Optical Society of America B* 3.1 (1986), p. 125. DOI: 10.1364/josab.3.000125.

[363] D. E. Spence, P. N. Kean, and W. Sibbett. "60-fsec pulse generation from a self-mode-locked Ti:sapphire laser." In: *Optics Letters* 16.1 (1991), p. 42. DOI: 10.1364/ol.16.000042.

[364] M. T. Asaki, C.-P. Huang, D. Garvey, J. Zhou, H. C. Kapteyn, and M. M. Murnane. "Generation of 11-fs pulses from a self-mode-locked Ti:sapphire laser." In: *Optics Letters* 18.12 (1993), p. 977. DOI: 10.1364/ol.18.000977.

[365] D. Strickland and G. Mourou. "Compression of amplified chirped optical pulses." In: *Optics Communications* 56.3 (1985), pp. 219–221. DOI: 10.1016/0030-4018(85)90120-8.

[366] A. Egl, I. Arapoglou, M. Höcker, K. König, T. Ratajczyk, T. Sailer, B. Tu, A. Weigel, K. Blaum, W. Nörtershäuser, and S. Sturm. "Application of the Continuous Stern-Gerlach Effect for Laser Spectroscopy of the ^{40}Ar^{13+} Fine Structure in a Penning Trap." In: *Physical Review Letters* 123.12 (2019), p. 123001. DOI: 10.1103/physrevlett.123.123001.

[367] Y. Zaouter, D. N. Papadopoulos, M. Hanna, J. Boullet, L. Huang, C. Aguergaray, F. Druon, E. Mottay, P. Georges, and E. Cormier. "Stretcher-free high energy nonlinear amplification of femtosecond pulses in rod-type fibers." In: *Optics Letters* 33.2 (2008), p. 107. DOI: 10.1364/ol.33.000107.

[368] J. Zhao, W. Li, C. Wang, Y. Liu, and H. Zeng. "Pre-chirping management of a self-similar Yb-fiber amplifier towards 80 W average power with sub-40 fs pulse generation." In: *Optics Express* 22.26 (2014), p. 32214. DOI: 10.1364/oe.22.032214.

[369] W. Liu, D. N. Schimpf, T. Eidam, J. Limpert, A. Tünnermann, F. X. Kärtner, and G. Chang. "Pre-chirp managed nonlinear amplification in fibers delivering 100 W, 60 fs pulses." In: *Optics Letters* 40.2 (2015), p. 151. DOI: 10.1364/ol.40.000151.

[370] C. V. Raman. "A new radiation." In: *Indian Journal of physics* 2 (1928), pp. 387–398.

[371] A. Kobyakov, M. Sauer, and D. Chowdhury. "Stimulated Brillouin scattering in optical fibers." In: *Advances in Optics and Photonics* 2.1 (2009), p. 1. DOI: 10.1364/aop.2.000001.

[372] J. Limpert, F. Roser, T. Schreiber, and A. Tunnermann. "High-power ultrafast fiber laser systems." In: *IEEE Journal of Selected Topics in Quantum Electronics* 12.2 (2006), pp. 233–244. DOI: 10.1109/jstqe.2006.872729.

[373] J. Limpert, A. Liem, M. Reich, T. Schreiber, S. Nolte, H. Zellmer, A. Tünnermann, J. Broeng, A. Petersson, and C. Jakobsen. "Low-nonlinearity single-transverse-mode ytterbium-doped photonic crystal fiber amplifier." In: *Optics Express* 12.7 (2004), p. 1313. DOI: 10.1364/opex.12.001313.

[374] J. Limpert, N. Deguil-Robin, I. Manek-Hönninger, F. Salin, F. Röser, A. Liem, T. Schreiber, S. Nolte, H. Zellmer, A. Tünnermann, et al. "High-power rod-type photonic crystal fiber laser." In: *Optics Express* 13.4 (2005), p. 1055. DOI: 10.1364/opex.13.001055.

[375] F. Stutzki, F. Jansen, T. Eidam, A. Steinmetz, C. Jauregui, J. Limpert, and A. Tünnermann. "High average power large-pitch fiber amplifier with robust single-mode operation." In: *Optics Letters* 36.5 (2011), p. 689. DOI: 10.1364/ol.36.000689.

[376] C. Jauregui, J. Limpert, and A. Tünnermann. "High-power fibre lasers." In: *Nature Photonics* 7.11 (2013), pp. 861–867. DOI: 10.1038/nphoton.2013.273.

[377] Y. Wang. "Optimization of pulse amplification in ytterbium-doped double-clad fiber amplifiers." In: *Journal of lightwave technology* 23.6 (2005), p. 2139.

[378] R. Paschotta, J. Nilsson, A. Tropper, and D. Hanna. "Ytterbium-doped fiber amplifiers." In: *IEEE Journal of Quantum Electronics* 33.7 (1997), pp. 1049–1056. DOI: 10.1109/3.594865.

[379] M. Loeser, F. Röser, A. Reichelt, M. Siebold, S. Grimm, D. Litzkendorf, A. Schwuchow, J. Kirchhof, and U. Schramm. "Broadband, diode pumped Yb:SiO$_2$multicomponent glass laser." In: *Optics Letters* 37.19 (2012), p. 4029. DOI: 10.1364/ol.37.004029.

[380] A. Ruehl, A. Marcinkevicius, M. E. Fermann, and I. Hartl. "80 W, 120 fs Yb-fiber frequency comb." In: *Optics Letters* 35.18 (2010), p. 3015. DOI: 10.1364/ol.35.003015.

[381] W. Zhang, S. Fu, W. Kong, G. Wang, F. Xing, F. Zhang, and H. Zhang. "Review of pulse compression gratings for chirped pulse amplification system." In: *Optical Engineering* 60.02 (2021). DOI: 10.1117/1.oe.60.2.020902.

[382] A. Ackermann. "Modellierung und Charakterisierung eines Kompressors für ultrakurze Laserpulse durch Strahlenverfolgung." Bachelor thesis. Ruprecht-Karls-Universität, Heidelberg, 2017.

[383] A. Ackermann. "Development and characterization of a femtosecond-pulse compressor." Master's thesis. Ruprecht-Karls-Universität, Heidelberg, 2019.

[384] R. L. Fork, C. H. B. Cruz, P. C. Becker, and C. V. Shank. "Compression of optical pulses to six femtoseconds by using cubic phase compensation." In: *Optics Letters* 12.7 (1987), p. 483. DOI: 10.1364/ol.12.000483.

[385] S. Kane and J. Squier. "Grism-pair stretcher–compressor system for simultaneous second- and third-order dispersion compensation in chirped-pulse amplification." In: *Journal of the Optical Society of America B* 14.3 (1997), p. 661. DOI: 10.1364/josab.14.000661.

[386] A. Zeytunyan, G. Yesayan, and L. Mouradian. "Pulse compression to 14 fs by third-order dispersion control in a hybrid grating-prism compressor." In: *Applied Optics* 52.32 (2013), p. 7755. DOI: 10.1364/ao.52.007755.

[387] H. Kogelnik, E. Ippen, A. Dienes, and C. Shank. "Astigmatically compensated cavities for CW dye lasers." In: *IEEE Journal of Quantum Electronics* 8.3 (1972), pp. 373–379. DOI: 10.1109/jqe.1972.1076964.

[388] N. Lilienfein, C. Hofer, M. Högner, T. Saule, M. Trubetskov, V. Pervak, E. Fill, C. Riek, A. Leitenstorfer, J. Limpert, et al. "Temporal solitons in free-space femtosecond enhancement cavities." In: *Nature Photonics* 13.3 (2019), p. 214. DOI: 10.1038/s41566-018-0341-y.

[389] S. D. Silvestri, P. Laporta, and V. Magni. "Rod thermal lensing effects in solid-state laser ring resonators." In: *Optics Communications* 65.5 (1988), pp. 373–376. DOI: 10.1016/0030-4018(88)90106-x.

[390] N. Lilienfein, H. Carstens, S. Holzberger, C. Jocher, T. Eidam, J. Limpert, A. Tünnermann, A. Apolonski, F. Krausz, and I. Pupeza. "Balancing of thermal lenses in enhancement cavities with transmissive elements." In: *Optics Letters* 40.5 (2015), p. 843. DOI: 10.1364/ol.40.000843.

[391] K. Dupraz, K. Cassou, A. Martens, and F. Zomer. "The ABCD matrix for parabolic reflectors and its application to astigmatism free four-mirror cavities." In: *Optics Communications* 353 (2015), pp. 178–183. DOI: 10.1016/j.optcom.2015.05.021.

Bibliography

[392] J. Bonis, R. Chiche, R. Cizeron, M. Cohen, E. Cormier, P. Cornebise, N. Delerue, R. Flaminio, D. Jehanno, F. Labaye, et al. "Non-planar four-mirror optical cavity for high intensity gamma ray flux production by pulsed laser beam Compton scattering off GeV-electrons." In: *Journal of Instrumentation* 7.01 (2012), p. 1017. DOI: 10.1088/1748-0221/7/01/p01017.

[393] H. Carstens, S. Holzberger, J. Kaster, J. Weitenberg, V. Pervak, A. Apolonski, E. Fill, F. Krausz, and I. Pupeza. "Large-mode enhancement cavities." In: *Optics Express* 21.9 (2013), pp. 11606–11617. DOI: 10.1364/OE.21.011606.

[394] T. K. Allison, A. Cingöz, D. C. Yost, and J. Ye. "Extreme Nonlinear Optics in a Femtosecond Enhancement Cavity." In: *Physical Review Letters* 107.18 (2011), p. 183903. DOI: 10.1103/physrevlett.107.183903.

[395] J. Fischer, J. Drs, F. Labaye, N. Modsching, M. Müller, V. J. Wittwer, and T. Südmeyer. "Efficient XUV-light out-coupling of intra-cavity high harmonics by a coated grazing-incidence plate." In: *Optics Express* 30.17 (2022), p. 30969. DOI: 10.1364/oe.458946.

[396] J. Hollenshead and L. Klebanoff. "Modeling radiation-induced carbon contamination of extreme ultraviolet optics." In: *Journal of Vacuum Science and Technology B: Microelectronics and Nanometer Structures* 24.1 (2006), p. 64. DOI: 10.1116/1.2140005.

[397] R. Pappenberger. "Implementierung eines differentiellen Pumpsystems in einen optischen Resonator für einen Frequenzkamm im Ultravioletten." Bachelor thesis. Ruprecht-Karls-Universität, Heidelberg, 2019.

[398] Z. Filus, P. Ye, T. Csizmadia, T. Grósz, L. G. Oldal, M. D. Marco, M. Füle, S. Kahaly, K. Varjú, and B. Major. "Liquid-cooled modular gas cell system for high-order harmonic generation using high average power laser systems." In: *Review of Scientific Instruments* 93.7 (2022), p. 073002. DOI: 10.1063/5.0097788.

[399] C. M. Heyl, S. B. Schoun, G. Porat, H. Green, and J. Ye. "A nozzle for high-density supersonic gas jets at elevated temperatures." In: *Review of Scientific Instruments* 89.11 (2018), p. 113114. DOI: 10.1063/1.5051586.

[400] R. W. C. Hansen, M. Bissen, D. Wallace, J. Wolske, and T. Miller. "Ultraviolet/ozone cleaning of carbon-contaminated optics." In: *Applied Optics* 32.22 (1993), p. 4114. DOI: 10.1364/ao.32.004114.

[401] C. Corder, P. Zhao, X. Li, M. D. Kershis, M. G. White, and T. K. Allison. *Development of a tunable high repetition rate XUV source for time-resolved photoemission studies of ultrafast dynamics at surfaces.* 2018. DOI: 10.1117/12.2295232.

[402] C.-T. Chiang, M. Huth, A. Trützschler, F. O. Schumann, J. Kirschner, and W. Widdra. "Efficient and tunable high-order harmonic light sources for photoelectron spectroscopy at surfaces." In: *Journal of Electron Spectroscopy and Related Phenomena* 200 (2015), pp. 15–21. DOI: 10.1016/j.elspec.2015.04.001.

[403] R. Wallauer, J. Reimann, N. Armbrust, J. Güdde, and U. Höfer. "Intervalley scattering in MoS_2 imaged by two-photon photoemission with a high-harmonic probe." In: *Applied Physics Letters* 109.16 (2016), p. 162102. DOI: 10.1063/1.4965839.

[404] N. Griesbach. In preparation: Bachelor thesis. Ruprecht-Karls-Universität, Heidelberg, 2023.

[405] R. Hector. "Characterization of a Xenon-Recycling-System for an Extreme-Ultraviolet Frequency Comb." Bachelor thesis. Ruprecht-Karls-Universität, Heidelberg, 2022.

206

[406] D. R. Carlson, J. Lee, J. Mongelli, E. M. Wright, and R. J. Jones. "Intracavity ionization and pulse formation in femtosecond enhancement cavities." In: *Optics Letters* 36.15 (2011), pp. 2991–2993. DOI: 10.1364/OL.36.002991.

[407] J. A. R. Samson. *Vacuum ultraviolet spectroscopy*. Academic, 2000.

[408] D. R. Miller. *Atomic and molecular beam methods*. Vol. 1. Oxford University Press, 1988.

[409] N. Lackmann. "Development of a Focusing Beamline for an Extreme-Ultraviolet Frequency Comb." Bachelor thesis. Ruprecht-Karls-Universität, Heidelberg, 2021.

[410] R. V. Pound. "Electronic Frequency Stabilization of Microwave Oscillators." In: *Review of Scientific Instruments* 17.11 (1946), pp. 490–505. DOI: 10.1063/1.1770414.

[411] R. W. P. Drever, J. L. Hall, F. V. Kowalski, J. Hough, G. M. Ford, A. J. Munley, and H. Ward. "Laser phase and frequency stabilization using an optical resonator." In: *Applied Physics B* 31.2 (1983), pp. 97–105. DOI: 10.1007/bf00702605.

[412] E. D. Black. "An introduction to Pound–Drever–Hall laser frequency stabilization." In: *American Journal of Physics* 69.1 (2001), pp. 79–87. DOI: 10.1119/1.1286663.

[413] R. L. Barger, M. Sorem, and J. Hall. "Frequency stabilization of a cw dye laser." In: *Applied Physics Letters* 22.11 (1973), pp. 573–575. DOI: 10.1063/1.1654513.

[414] T. Hänsch and B. Couillaud. "Laser frequency stabilization by polarization spectroscopy of a reflecting reference cavity." In: *Optics Communications* 35.3 (1980), pp. 441–444. DOI: 10.1016/0030-4018(80)90069-3.

[415] S. Hannig, J. Mielke, J. A. Fenske, M. Misera, N. Beev, C. Ospelkaus, and P. O. Schmidt. "A highly stable monolithic enhancement cavity for second harmonic generation in the ultraviolet." In: *Review of Scientific Instruments* 89.1 (2018), p. 013106. DOI: 10.1063/1.5005515.

[416] D. Goldovsky, V. Jouravsky, and A. Pe'er. "Simple and robust phase-locking of optical cavities with >200 KHz servo-bandwidth using a piezo-actuated mirror mounted in soft materials." In: *Optics Express* 24.25 (2016), p. 28239. DOI: 10.1364/oe.24.028239.

[417] A. Chadi, G. Méjean, R. Grilli, and D. Romanini. "Note: Simple and compact piezoelectric mirror actuator with 100 kHz bandwidth, using standard components." In: *Review of Scientific Instruments* 84.5 (2013), p. 056112. DOI: 10.1063/1.4807859.

[418] T. C. Briles, D. C. Yost, A. Cingöz, J. Ye, and T. R. Schibli. "Simple piezoelectric-actuated mirror with 180 kHz servo bandwidth." In: *Optics Express* 18.10 (2010), pp. 9739–9746. DOI: 10.1364/OE.18.009739.

[419] T. Nakamura, S. Tani, I. Ito, M. Endo, and Y. Kobayashi. "Piezo-electric transducer actuated mirror with a servo bandwidth beyond 500 kHz." In: *Optics Express* 28.11 (2020), p. 16118. DOI: 10.1364/oe.390042.

[420] J. Zhang, R. J. Perez, and E. J. Lavernia. "Documentation of damping capacity of metallic, ceramic and metal-matrix composite materials." In: *Journal of Materials Science* 28.9 (1993), pp. 2395–2404. DOI: 10.1007/bf01151671.

[421] S. Khaple, R. G. Baligidad, M. Sankar, and V. V. S. Prasad. "Effect of Melting Process and Aluminium Content on the Microstructure and Mechanical Properties of Fe–Al Alloys." In: *ISIJ International* 50.10 (2010), pp. 1483–1487. DOI: 10.2355/isijinternational.50.1483.

[422] I. B. Chudakov, N. M. Aleksandrova, S. Y. Makushev, and R. V. Kakabadze. "High-damping alloys and steels based on Fe - Al: structure, properties, and application features." In: *Metal Science and Heat Treatment* 54.5-6 (2012), pp. 239–243. DOI: 10.1007/s11041-012-9489-0.

[423] Q. Zhou, K. H. Lam, H. Zheng, W. Qiu, and K. K. Shung. "Piezoelectric single crystal ultrasonic transducers for biomedical applications." In: *Progress in Materials Science* 66 (2014), pp. 87–111. DOI: 10.1016/j.pmatsci.2014.06.001.

[424] T. W.-Z. Lynn. "Measurement and control of individual quanta in cavity QED." PhD thesis. California Institute of Technology, 2003. DOI: 10.7907/PSPJ-6H44.

[425] B. Brandstätter, A. McClung, K. Schüppert, B. Casabone, K. Friebe, A. Stute, P. O. Schmidt, C. Deutsch, J. Reichel, R. Blatt, and T. E. Northup. "Integrated fiber-mirror ion trap for strong ion-cavity coupling." In: *Review of Scientific Instruments* 84.12 (2013), p. 123104. DOI: 10.1063/1.4838696.

[426] M. Uphoff, M. Brekenfeld, G. Rempe, and S. Ritter. "Frequency splitting of polarization eigenmodes in microscopic Fabry-Perot cavities." In: *New Journal of Physics* 17.1 (2015), p. 013053. DOI: 10.1088/1367-2630/17/1/013053.

[427] R. A. Chipman, W.-S. T. Lam, and G. Young. *Polarized Light and Optical Systems*. CRC Press, 2018. DOI: 10.1201/9781351129121.

[428] S. Miller, L. Jiang, and S. Pau. "Birefringent coating to remove polarization aberrations." In: *Optics Express* 30.12 (2022), p. 20629. DOI: 10.1364/oe.458859.

[429] P. Grelu. *Nonlinear Optical Cavity Dynamics From Microresonators to Fiber Lasers. From Microresonators to Fiber Lasers*. Wiley & Sons, 2015.

[430] L. A. Lugiato and R. Lefever. "Spatial Dissipative Structures in Passive Optical Systems." In: *Physical Review Letters* 58.21 (1987), pp. 2209–2211. DOI: 10.1103/physrevlett.58.2209.

[431] L. Lugiato, F. Prati, and M. Brambilla. *Nonlinear Optical Systems*. Cambridge University Press, 2015.

[432] T. Brabec, C. Spielmann, and F. Krausz. "Mode locking in solitary lasers." In: *Optics Letters* 16.24 (1991), p. 1961. DOI: 10.1364/ol.16.001961.

[433] P. Grelu and N. Akhmediev. "Dissipative solitons for mode-locked lasers." In: *Nature Photonics* 6.2 (2012), pp. 84–92. DOI: 10.1038/nphoton.2011.345.

[434] F. Leo, S. Coen, P. Kockaert, S.-P. Gorza, P. Emplit, and M. Haelterman. "Temporal cavity solitons in one-dimensional Kerr media as bits in an all-optical buffer." In: *Nature Photonics* 4.7 (2010), pp. 471–476. DOI: 10.1038/nphoton.2010.120.

[435] T. Herr, V. Brasch, J. D. Jost, C. Y. Wang, N. M. Kondratiev, M. L. Gorodetsky, and T. J. Kippenberg. "Temporal solitons in optical microresonators." In: *Nature Photonics* 8.2 (2013), pp. 145–152. DOI: 10.1038/nphoton.2013.343.

[436] F. X. Kärtner, N. Matuschek, T. Schibli, U. Keller, H. A. Haus, C. Heine, R. Morf, V. Scheuer, M. Tilsch, and T. Tschudi. "Design and fabrication of double-chirped mirrors." In: *Optics Letters* 22.11 (1997), p. 831. DOI: 10.1364/ol.22.000831.

[437] F. X. Kärtner, U. Morgner, R. Ell, T. Schibli, J. G. Fujimoto, E. P. Ippen, V. Scheuer, G. Angelow, and T. Tschudi. "Ultrabroadband double-chirped mirror pairs for generation of octave spectra." In: *Journal of the Optical Society of America B* 18.6 (2001), p. 882. DOI: 10.1364/josab.18.000882.

[438] E. Fedulova, M. Trubetskov, T. Amotchkina, K. Fritsch, P. Baum, O. Pronin, and V. Pervak. "Kerr effect in multilayer dielectric coatings." In: *Optics Express* 24.19 (2016), p. 21802. DOI: 10.1364/oe.24.021802.

[439] W. Rudolph, A. K. Oskouei, L. A. Emmert, M. Steinecke, M. Jupé, L. O. Jensen, and D. Ristau. "Nonlinear optics using interference coatings - opportunities and challenges." In: *Optical Interference Coatings Conference (OIC) 2019*. OSA, 2019. DOI: 10.1364/oic.2019.thb.1.

[440] S. Balendat, M. Jupé, M. Steinecke, L. Jensen, A. K. Oskouei, W. Rudolph, D. Zuber, U. Morgner, and D. Ristau. "Manufacturing and characterization of frequency tripling mirrors." In: *2021 Conference on Lasers and Electro-Optics Europe and European Quantum Electronics Conference*. Optica Publishing Group, 2021. DOI: 10.1364/CLEO_EUROPE.2021.cd_p_33.

[441] J. Petersen and A. Luiten. "Short pulses in optical resonators." In: *Optics Express* 11.22 (2003), pp. 2975–2981. DOI: 10.1364/OE.11.002975.

[442] A. Schliesser, C. Gohle, T. Udem, and T. W. Hänsch. "Complete characterization of a broadband high-finesse cavity using an optical frequency comb." In: *Optics Express* 14.13 (2006), pp. 5975–5983. DOI: 10.1364/OE.14.005975.

[443] F. Canella, E. Suerra, D. Giannotti, G. Galzerano, and S. Cialdi. "Low frequency-to-intensity noise conversion in a pulsed laser cavity locking by exploiting carrier envelope offset." In: *Applied Physics B* 128.11 (2022). DOI: 10.1007/s00340-022-07924-6.

[444] L. Zehnder. "Ein neuer Interferenzrefraktor." In: *Zeitschrift für Instrumentenkunde* 11 (1891), pp. 275–285.

[445] L. Mach. "Ueber einen Interferenzrefraktor." In: *Zeitschrift für Instrumentenkunde* 12 (1891), pp. 89–93.

[446] J. Hyyti, E. Escoto, and G. Steinmeyer. "Third-harmonic interferometric frequency-resolved optical gating." In: *Journal of the Optical Society of America B* 34.11 (2017), p. 2367. DOI: 10.1364/josab.34.002367.

[447] A. Galler and T. Feurer. "Pulse shaper assisted short laser pulse characterization." In: *Applied Physics B* 90.3-4 (2008), pp. 427–430. DOI: 10.1007/s00340-007-2924-z.

[448] J. Köhler, M. Wollenhaupt, T. Bayer, C. Sarpe, and T. Baumert. "Zeptosecond precision pulse shaping." In: *Optics Express* 19.12 (2011), p. 11638. DOI: 10.1364/oe.19.011638.

[449] S. Kerbstadt, L. Englert, T. Bayer, and M. Wollenhaupt. "Ultrashort polarization-tailored bichromatic fields." In: *Journal of Modern Optics* 64.10-11 (2016), pp. 1010–1025. DOI: 10.1080/09500340.2016.1271151.

[450] D. Pengel. "Dreidimensionale Kontrolle von freien Elektronenwellenpaketen mit polarisationsgeformten, ultrakurzen Laserpulsen." PhD thesis. Universität Oldenburg, 2018.

[451] G. Stibenz and G. Steinmeyer. "Interferometric frequency-resolved optical gating." In: *Optics Express* 13.7 (2005), p. 2617. DOI: 10.1364/opex.13.002617.

[452] R. Jafari, T. Jones, and R. Trebino. "100 percent reliable algorithm for second-harmonic-generation frequency-resolved optical gating." In: *Optics Express* 27.3 (2019), p. 2112. DOI: 10.1364/oe.27.002112.

[453] R. Trebino, R. Jafari, S. A. Akturk, P. Bowlan, Z. Guang, P. Zhu, E. Escoto, and G. Steinmeyer. "Highly reliable measurement of ultrashort laser pulses." In: *Journal of Applied Physics* 128.17 (2020), p. 171103. DOI: 10.1063/5.0022552.

[454] S. Kokh. "Pulse Characterization by Frequency-Resolved Optical Gating for Velocity Map Imaging of Xenon." Bachelor thesis. Ruprecht-Karls-Universität, Heidelberg, 2022.

[455] S. Kleinert. *Pyfrog*. [Online: `https://github.com/svenkleinert/pyfrog`; accessed 1-February-2023]. 2019.

[456] I. H. Malitson. "Interspecimen Comparison of the Refractive Index of Fused Silica." In: *Journal of the Optical Society of America* 55.10 (1965), p. 1205. DOI: `10.1364/josa.55.001205`.

[457] D. E. Zelmon, D. L. Small, and R. Page. "Refractive-index measurements of undoped yttrium aluminum garnet from 04 to 50 μm." In: *Applied Optics* 37.21 (1998), p. 4933. DOI: `10.1364/ao.37.004933`.

[458] F. Zernike. "Refractive Indices of Ammonium Dihydrogen Phosphate and Potassium Dihydrogen Phosphate between 2000 Å and 1.5 μ." In: *J. Opt. Soc. Am.* 54.10 (1964), pp. 1215–1220. DOI: `10.1364/JOSA.54.001215`.

[459] P. E. Ciddor. "Refractive index of air: new equations for the visible and near infrared." In: *Applied Optics* 35.9 (1996), p. 1566. DOI: `10.1364/ao.35.001566`.

[460] E. R. Peck and B. N. Khanna. "Dispersion of Nitrogen." In: *Journal of the Optical Society of America* 56.8 (1966), p. 1059. DOI: `10.1364/josa.56.001059`.

[461] A. Börzsönyi, Z. Heiner, M. P. Kalashnikov, A. P. Kovács, and K. Osvay. "Dispersion measurement of inert gases and gas mixtures at 800 nm." In: *Applied Optics* 47.27 (2008), p. 4856. DOI: `10.1364/ao.47.004856`.

[462] C. R. Mansfield and E. R. Peck. "Dispersion of Helium." In: *Journal of the Optical Society of America* 59.2 (1969), p. 199. DOI: `10.1364/josa.59.000199`.

[463] G. Fibich and A. L. Gaeta. "Critical power for self-focusing in bulk media and in hollow waveguides." In: *Optics Letters* 25.5 (2000), p. 335. DOI: `10.1364/ol.25.000335`.

[464] J. Weitenberg, T. Saule, J. Schulte, and P. Rusbuldt. "Nonlinear Pulse Compression to Sub-40 fs at μJ Pulse Energy by Multi-Pass-Cell Spectral Broadening." In: *IEEE Journal of Quantum Electronics* 53.6 (2017), pp. 1–4. DOI: `10.1109/jqe.2017.2761883`.

[465] K. Fritsch, M. Poetzlberger, V. Pervak, J. Brons, and O. Pronin. "All-solid-state multipass spectral broadening to sub-20 fs." In: *Optics Letters* 43.19 (2018), p. 4643. DOI: `10.1364/ol.43.004643`.

[466] M. Kaumanns, D. Kormin, T. Nubbemeyer, V. Pervak, and S. Karsch. "Spectral broadening of 112 mJ, 1.3 ps pulses at 5 kHz in a LG10 multipass cell with compressibility to 37 fs." In: *Optics Letters* 46.5 (2021), p. 929. DOI: `10.1364/ol.416734`.

[467] *Pressure Equipment Directive*. European Commision, 2022.

[468] P. Nagpal. In preparation: Master's thesis. Ruprecht-Karls-Universität, Heidelberg, 2023.

[469] J.-H. Oelmann, T. Heldt, L. Guth, J. Nauta, N. Lackmann, V. Wössner, S. Kokh, T. Pfeifer, and J. R. Crespo López-Urrutia. "Photoelectron tomography with an intra-cavity velocity-map imaging spectrometer at 100 MHz repetition rate." In: *Review of Scientific Instruments* 93.12 (2022), p. 123303. DOI: `10.1063/5.0104679`.

[470] I. León, Z. Yang, H.-T. Liu, and L.-S. Wang. "The design and construction of a high-resolution velocity-map imaging apparatus for photoelectron spectroscopy studies of size-selected clusters." In: *Review of Scientific Instruments* 85.8 (2014), p. 083106. DOI: `10.1063/1.4891701`.

[471] G. A. Garcia, L. Nahon, C. J. Harding, E. A. Mikajlo, and I. Powis. "A refocusing modified velocity map imaging electron/ion spectrometer adapted to synchrotron radiation studies." In: *Review of Scientific Instruments* 76.5 (2005), p. 053302. DOI: 10.1063/1.1900646.

[472] D. M. P. Holland and D. A. Shaw. "The design and performance of a velocity map imaging spectrometer for the study of molecular photoionisation dynamics." In: *Chemical Physics* 409 (2012), pp. 11–22. DOI: 10.1016/j.chemphys.2012.09.020.

[473] N. G. Kling, D. Paul, A. Gura, G. Laurent, S. De, H. Li, Z. Wang, B. Ahn, C. H. Kim, T. K. Kim, et al. "Thick-lens velocity-map imaging spectrometer with high resolution for high-energy charged particles." In: *Journal of Instrumentation* 9.05 (2014), p. 5005. DOI: 10.1088/1748-0221/9/05/p05005.

[474] M. L. Weichman, J. A. DeVine, D. S. Levine, J. B. Kim, and D. M. Neumark. "Isomer-specific vibronic structure of the 9-, 1-, and 2-anthracenyl radicals via slow photoelectron velocity-map imaging." In: *Proceedings of the National Academy of Sciences* 113.7 (2016), pp. 1698–1705. DOI: 10.1073/pnas.1520862113.

[475] S. J. Kregel, G. K. Thurston, J. Zhou, and E. Garand. "A multi-plate velocity-map imaging design for high-resolution photoelectron spectroscopy." In: *The Journal of Chemical Physics* 147.9 (2017), p. 094201. DOI: 10.1063/1.4996011.

[476] O. Ghafur, W. Siu, P. Johnsson, M. F. Kling, M. Drescher, and M. J. J. Vrakking. "A velocity map imaging detector with an integrated gas injection system." In: *Review of Scientific Instruments* 80.3 (2009), p. 033110. DOI: 10.1063/1.3085799.

[477] P. Mandal, G. Sikler, and M. Mukherjee. "Simulation study and analysis of a compact einzel lens-deflector for low energy ion beam." In: *Journal of Instrumentation* 6.02 (2011), p. 2004. DOI: 10.1088/1748-0221/6/02/p02004.

[478] J. B. Camp, T. W. Darling, and R. E. Brown. "Macroscopic variations of surface potentials of conductors." In: *Journal of Applied Physics* 69.10 (1991), pp. 7126–7129. DOI: 10.1063/1.347601.

[479] W. Demtröder. *Laser Spectroscopy*. Springer, 1996. DOI: 10.1007/978-3-662-08260-7.

[480] M. Krüger, M. Schenk, and P. Hommelhoff. "Attosecond control of electrons emitted from a nanoscale metal tip." In: *Nature* 475.7354 (2011), pp. 78–81. DOI: 10.1038/nature10196.

[481] B. Piglosiewicz, S. Schmidt, D. J. Park, J. Vogelsang, P. Groß, C. Manzoni, P. Farinello, G. Cerullo, and C. Lienau. "Carrier-envelope phase effects on the strong-field photoemission of electrons from metallic nanostructures." In: *Nature Photonics* 8.1 (2013), pp. 37–42. DOI: 10.1038/nphoton.2013.288.

[482] P. Dombi, Z. Pápa, J. Vogelsang, S. V. Yalunin, M. Sivis, G. Herink, S. Schäfer, P. Groß, C. Ropers, and C. Lienau. "Strong-field nano-optics." In: *Reviews of Modern Physics* 92.2 (2020), p. 025003. DOI: 10.1103/revmodphys.92.025003.

[483] A. Feist, N. Bach, N. R. da Silva, T. Danz, M. Möller, K. E. Priebe, T. Domröse, J. G. Gatzmann, S. Rost, J. Schauss, et al. "Ultrafast transmission electron microscopy using a laser-driven field emitter: Femtosecond resolution with a high coherence electron beam." In: *Ultramicroscopy* 176 (2017), pp. 63–73. DOI: 10.1016/j.ultramic.2016.12.005.

[484] M. Huppert, I. Jordan, and H. J. Wörner. "Attosecond beamline with actively stabilized and spatially separated beam paths." In: *Review of Scientific Instruments* 86.12 (2015), p. 123106. DOI: 10.1063/1.4937623.

[485] H. Srinivas, F. Shobeiry, D. Bharti, T. Pfeifer, R. Moshammer, and A. Harth. "High-repetition rate attosecond beamline for multi-particle coincidence experiments." In: *Optics Express* 30.8 (2022), p. 13630. DOI: 10.1364/oe.454553.

[486] A. R. Bainbridge and W. A. Bryan. "Velocity map imaging of femtosecond laser induced photoelectron emission from metal nanotips." In: *New Journal of Physics* 16.10 (2014), p. 103031. DOI: 10.1088/1367-2630/16/10/103031.

[487] O. Reinhardt and I. Kaminer. "Theory of Shaping Electron Wavepackets with Light." In: *ACS Photonics* 7.10 (2020), pp. 2859–2870. DOI: 10.1021/acsphotonics.0c01133.

[488] B. Barwick, D. J. Flannigan, and A. H. Zewail. "Photon-induced near-field electron microscopy." In: *Nature* 462.7275 (2009), pp. 902–906. DOI: 10.1038/nature08662.

[489] L. Piazza, D. Masiel, T. LaGrange, B. Reed, B. Barwick, and F. Carbone. "Design and implementation of a fs-resolved transmission electron microscope based on thermionic gun technology." In: *Chemical Physics* 423 (2013), pp. 79–84. DOI: 10.1016/j.chemphys.2013.06.026.

[490] L. Piazza, T. Lummen, E. Quiñonez, Y. Murooka, B. Reed, B. Barwick, and F. Carbone. "Simultaneous observation of the quantization and the interference pattern of a plasmonic near-field." In: *Nature Communications* 6.1 (2015). DOI: 10.1038/ncomms7407.

[491] G. Vanacore, A. Fitzpatrick, and A. Zewail. "Four-dimensional electron microscopy: Ultrafast imaging, diffraction and spectroscopy in materials science and biology." In: *Nano Today* 11.2 (2016), pp. 228–249. DOI: 10.1016/j.nantod.2016.04.009.

[492] A. Feist, K. E. Echternkamp, J. Schauss, S. V. Yalunin, S. Schäfer, and C. Ropers. "Quantum coherent optical phase modulation in an ultrafast transmission electron microscope." In: *Nature* 521.7551 (2015), pp. 200–203. DOI: 10.1038/nature14463.

[493] K. Wang, R. Dahan, M. Shentcis, Y. Kauffmann, A. B. Hayun, O. Reinhardt, S. Tsesses, and I. Kaminer. "Coherent interaction between free electrons and a photonic cavity." In: *Nature* 582.7810 (2020), pp. 50–54. DOI: 10.1038/s41586-020-2321-x.

[494] K. E. Priebe, C. Rathje, S. V. Yalunin, T. Hohage, A. Feist, S. Schäfer, and C. Ropers. "Attosecond electron pulse trains and quantum state reconstruction in ultrafast transmission electron microscopy." In: *Nature Photonics* 11.12 (2017), pp. 793–797. DOI: 10.1038/s41566-017-0045-8.

[495] M. Kozák, N. Schönenberger, and P. Hommelhoff. "Ponderomotive Generation and Detection of Attosecond Free-Electron Pulse Trains." In: *Physical Review Letters* 120.10 (2018). DOI: 10.1103/physrevlett.120.103203.

[496] A. Gorlach, O. Neufeld, N. Rivera, O. Cohen, and I. Kaminer. "The quantum-optical nature of high harmonic generation." In: *Nature Communications* 11.1 (2020). DOI: 10.1038/s41467-020-18218-w.

[497] P. Knauer. "Stabilization of thermal drifts in a femtosecond enhancement cavity." Bachelor thesis. Ruprecht-Karls-Universität, Heidelberg, 2019.

[498] J. Krummeich. "Development of a cooling system for mirrors in an UHV chamber." Bachelor thesis. Ruprecht-Karls-Universität, Heidelberg, 2019.

[499] M. Berg. "Tomographic reconstruction of photoelectron momentum distribution obtained through Velocity Map Imaging with a 100 MHz laser in a femtosecond enhancement cavity." Bachelor thesis. Ruprecht-Karls-Universität, Heidelberg, 2022.

[500] P. Knauer. "Automatic mode optimization of an optical resonator via hill climbing." Master's thesis. Ruprecht-Karls-Universität, Heidelberg, 2021.

Acknowledgments

Als ich mich vor etwa fünf Jahren auf den Weg zum Vorstellungsgespräch nach Heidelberg machte, ahnte ich noch nicht, dass mich die EBIT-Gruppe und ganz besonders die warmherzige Begrüßung von José Crespo und Janko Nauta innerhalb kürzester Zeit davon überzeugen würden, für meine Doktorarbeit nach Heidelberg zu kommen.

Lieber José, bei Dir möchte ich mich ganz besonders herzlich dafür bedanken, dass Du mir das Vertrauen geschenkt hast, bei Dir meine Doktorarbeit zu diesem spannenden Thema anzufertigen. Du hast mich mit Deinem kreativen Denken und der Eigenschaft Dinge zu hinterfragen sehr inspiriert. Für mich war Deine Hands-On Mentalität besonders wichtig und oft sehr hilfreich. Die Selbstverständlichkeit, mit der Du auch die neuesten Mitglieder Deiner Arbeitsgruppe bei ihrem persönlichen und beruflichen Fortkommen unterstützt, ist nur selten zu finden.

Des Weiteren möchte ich mich bei Prof. Werner Aeschbach für die Übernahme des Zweitgutachtens bedanken, sowie bei Prof. Selim Jochim und PD Dr. Zoltán Harman für die Vervollständigung des Prüfungskommitees.

Thomas, bei Dir möchte ich mich dafür bedanken, dass ich Mitglied Deiner Abteilung werden durfte. Für die großartige Unterstützung, die vielen Anregungen und das stets offene Ohr bin ich sehr dankbar.

Bei dieser Gelegenheit möchte ich mich bei der gesamten EBIT-Gruppe für die ausgesprochen gute Zusammenarbeit bedanken. Hier sind insbesondere Andrea, Christian, Elwin, Julian, Moto und Steffen hervorzuheben. Die ständige Hilfsbereitschaft, sowie die ausgezeichnete Arbeitsatmosphäre werden mir noch lange Zeit in bester Erinnerung bleiben - genauso wie die Kuchenkultur.

Während meines ersten, fast dreitägigen Bewerbungsbesuch in Heidelberg hast Du, Janko, mir die Stadt und das Heidelberger Schloss gezeigt. Dabei haben wir festgestellt, dass wir nicht nur mit knapp zwei Metern ähnlich groß gewachsen sind, sondern auch musikalisch und bei vielen anderen Dingen auf einer Wellenlänge sind. Ich habe unglaublich viel von Dir lernen dürfen und bin sehr dankbar, Dich als Kollegen und Freund gefunden zu haben.

Tobias, als Du Dich zu Beginn meiner Doktorarbeitzeit bei uns nach einer Masterarbeitsstelle umgeschaut hast, bist Du mir gleich als äußerst kompetent aufgefallen. Leider hast Du Dich zunächst nicht für unser Experiment entschieden, bist aber in der gleichen Abteilung gelandet. Für Deine Doktorarbeit wolltest Du dann aber doch noch einmal etwas anderes machen und hast wohl die 'XUV comb laser guys' noch in guter Erinnerung gehabt. Das war ein großes Glück, denn Du kamst genau zum richtigen Zeitpunkt. Ohne Deine Programmier-Zauberfertigkeiten würden viele Dinge im Labor vermutlich nicht oder nur deutlich langsamer funktionieren. Auch die Physik verstehst du schneller als die meisten anderen und hast immer gute Ideen. Es macht sehr viel Spaß mit Dir zusammenzuarbeiten und die Nächte gemeinsam im Labor zu verbringen. Ich bin sehr dankbar, Dich mit Deiner wertschätzenden Art als guten Freund gefunden zu haben!

Bei Dir, Lennart, möchte ich mich ebenfalls ganz herzlich bedanken. Mit Deiner Zielstrebigkeit und Sorgfalt bringst Du die Dinge zum Laufen, die schon viel zu lange liegen geblieben sind. Ich bin mir sicher, dass wir noch viele gemeinsame Stunden im Labor verbringen und phantastische